

Multi-axis Additive Manufacturing and 3D Scanning of Freeform Models

by

Mohammed Adamu Isa

A Dissertation Submitted to the
Graduate School of Sciences and Engineering
in Partial Fulfillment of the Requirements for
the Degree of
Doctor of Philosophy
in
Mechanical Engineering



December 24, 2018

Multi-axis Additive Manufacturing and 3D Scanning of Freeform Models

Koç University

Graduate School of Sciences and Engineering

This is to certify that I have examined this copy of a doctoral dissertation by

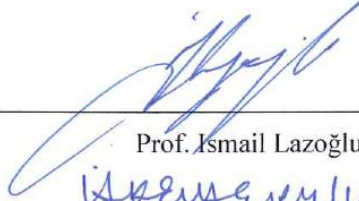
Mohammed Adamu Isa

and have found that it is complete and satisfactory in all respects,


and that any and all revisions required by the final

examining committee have been made.

Committee Members:




Prof. Ismail Lazoğlu



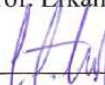
Prof. Iskender Yilgör



Assoc. Prof. Murat Sözer



Assoc. Prof. Erkan Günpınar



Asst. Prof. Lütfi Taner Tunç

Date: 24/12/2018

To my parents, brothers, sisters, teachers and friends

ABSTRACT

Additive manufacturing has earned reputation as an advanced manufacturing method capable of making revolutionary impact on the manufacturing sector. It emerged as a rapid prototyping method capable of fabricating complex products directly from digital models. In a world that has been molded by digitized data over last few decades, additive manufacturing progressed harmoniously to become a manufacturing method that spread into various fields. While the applications and compatible materials of additive manufacturing are continuously been discovered, there has been little change in the process of successive addition of layers of materials to produce parts. Fabrication using this common additive method is predominantly carried out using planar layers based on its established process plan.

The critical impediment of additive manufacturing is the poor quality of products, which can be partially attributed to the fixed build direction found in the common planar layering. As a result, the parts produced by additive manufacturing have jagged surfaces and lower mechanical strength along the build direction. Another problem that contributes negatively to the quality of products and the production time is the requirement of additional support structures.

The extension of additive manufacturing process to integrate multi-axis manufacturing results in production along variable build direction which can open up new avenues for improvements. This work studies the scope of multi-axis additive manufacturing in fabrication of overhang structures and freeform geometries. Multi-axis processes lack the additive-specific facilities and knowledge to address some of the issues holding back the progress of additive manufacturing. Hence, a 5-axis additive manufacturing scheme is suggested where the layering method and the build path are tailored based on the shape of a freeform NURBS-based 3D model. The manufacturing processes are investigated on an additive manufacturing system designed and built in the Manufacturing and Automation Research Center (MARC).

To digitize and assess the shape of existing physical objects, a new 3D scanner is designed with wide viewing space. By acquiring uniformly dense points, the scanner measurements are evaluated, and its uncertainty is analyzed. Benchmark geometries are used for both assessment of measurement accuracy and optimization of the 3D scanner parameters. Optimization of

influencing parameters based on the derived 3D scanner model is performed using least squares method. A standard measurement analysis is also carried out by uncertainty propagation using Monte Carlo simulation.

ÖZETÇE

Eklemeli üretim, imalat sektörü üzerinde büyük ve yenilikçi bir etki yapan gelişmiş bir üretim yöntemi olarak ün kazanmıştır. Başlangıçta, dijital modeller ile doğrudan kompleks ürünleri imal edebilen hızlı-prototip oluşturma yöntemi olarak ortaya çıkmıştır. Son birkaç on yılda sayısallaştırılmış verilerle kaplı olan bir dünyada, eklemeli üretim çeşitli alanlara yayılan bir üretim yöntemi haline geldi. Eklemeli üretim uygun malzemelerin sayısı ve uygulanması artmış olsa da, katmanların başarılı bir şekilde eklenmesi konusunda çok yol alınmadı. Bu güne kadar, bu üretim yönteminin uygulanması katmanların düzenli olarak üste üste konulması ile gerçekleştirilmiştir.

Eklemeli üretimin önündeki en büyük engel, ürünlerin düşük kalitesidir. Bu düşük kalite, üretimde, katmanların baskısının tek bir yöne (takım yönü) sabitlenmiş olması ürünlerin kalitesizliği ile de ilişkilendirilebilir. Sonuç olarak, eklemeli imalat ile üretilen parçalar pürüzlü yüzeylere ve baskı yönü boyunca daha düşük bir mukavemete sahip olur. Ürünlerin kalitesini ve üretim zamanını olumsuz etkileyen başka bir sorun da ek destek yapılarının gerekliliğidir.

Eklemeli üretim sürecini çok eksenli üretime entegre etmek yeni çalışma alanlarını ve fırsatları doğuracaktır. Bu çalışmada, “overhang” (sarkıtlı) yapıları ve NURBS serbest geometrilerin üretiminde çok eksenli eklemeli imalat konusunda çalışılmıştır. Geneline, çok eksenli eklemeli üretim üzerine çalışmalar yürüten tesisler ve ilgili yazılımlar konusundaki eksiklikler göze çarpmaktadır. Bu nedenden ötürü, çok eksenli eklemeli üretimde çok büyük bir gelişme kaydedilememektedir. Bu nedenle, bu çalışmada katman baskı yönteminin ve takım yolunun serbest forma sahip üç-boyutlu modelin şekline göre ayarlandığı bir üretim planı önerilmektedir. Üretim ve Otomasyon Laboratuvarı'nda (MARC) tasarlanan ve üretilen bir eklemeli üretim yazıcısı ile bu üretim yöntemleri araştırılmıştır.

Fiziksel objelerin şeklini değerlendirmek ve dijital ortama geçirmek için geniş görüntüleme alanına sahip bir üç boyutlu tarayıcı geliştirilmiştir. Düzenli ve yoğun noktalar elde edilerek tarayıcı ölçümleri değerlendirilmiş, belirsizliği analiz edilmiştir. Ölçümlerin doğruluğun değerlendirilmesi ve üç boyutlu tarayıcının parametrelerinin optimizasyonu için referans geometriler kullanılmıştır. Taranacak olan üç boyutlu modelleri etkileyen parametreler en küçük

kareler methodu kullanılarak optimize edilmiştir. Ayrıca, standart bir ölçüm analizi Monte Carlo simülasyonu kullanılarak belirsizlik yayılımı ile yapılmıştır.

ACKNOWLEDGEMENTS

I will first start by expressing my gratitude to my advisor Prof. Ismail Lazoglu for his endless support and motivation in this research, for his tutelage and insightful knowledge in manufacturing. Indeed, his vision is behind the advanced research and development going on in the invigorating environment of the research center. Gratitude to the other members of my thesis committee (Prof. Iskender Yilgör and Prof. Murat Sözer) for their comments and suggestions that helped in propelling this work.

I will also like to thank my present and graduated colleagues in the Manufacturing and Automation Research Center for the stimulating, inspiring and debatable discussions that helped in widening my views on many issues. Special thank goes to Muzaffer Abi for his practical expertise and assistance.

I will like to also thank my family, who have been altruistically supportive and encouraging throughout my studies.

TABLE OF CONTENTS

Multi-axis Additive Manufacturing and 3D Scanning of Freeform Models	1
ABSTRACT	4
ÖZETÇE	6
ACKNOWLEDGEMENTS	8
LIST OF FIGURES	12
Chapter 1	21
INTRODUCTION	21
1.1 Emerging Manufacturing Methods	21
1.2 Potentials of Additive Manufacturing	24
1.3 Standardization of AM	27
1.4 Reverse Engineering Introduction	30
1.5 Motivation and Organization	31
Chapter 2	33
ADDITIVE MANUFACTURING SYSTEMS	33
2.1 History and relevant literature on Additive Manufacturing	33
2.2 Types of Additive Manufacturing Systems	37
2.3 Additive Manufacturing Development in MARC	43
2.3.1 The first-generation AM machine	43
2.3.2 The second-generation AM machine	45
2.4 Fused Deposition on a Cartesian Machine	47
2.4.1 Fused deposition extrusion head	48
2.4.2 Composite production by AM	49
Chapter 3	54

MULTI-AXIS ADDITIVE MANUFACTURING USING EXISTING PROCESSES	54
3.1 Mechanical Design of Multi-axis AM System	55
3.2 G-code interpreter	61
3.3 Multi-axis Additive Manufacturing	64
3.4 Simple Path Generation Methods for Multi-Axis AM	68
3.4.1 Planar Slicing of By Part Decomposition	70
3.4.2 Application in Roofing Without Support.....	72
3.4.3 Use of Miscellaneous Paths	74
3.4.4 Discussion on the Need for a General Path Planner	76
3.5 Multi-Axis AM for Manufacturing of Overhang Structure	77
3.5.1 Multi-axis AM using 2D build platform.....	78
3.5.2 Additive manufacturing of parts with overhangs.....	80
3.5.3 Manufacturing and analysis of overhang structures	81
3.5.4 Discussion on results.....	87
Chapter 4.....	88
FIVE-AXIS ADDITIVE MANUFACTURING OF FREEFORM MODELS USING A NEW SCHEME	88
4.1 The 5-axis 3D printer	90
4.2 Path planning	92
4.3 Freeform solid representation	94
4.4 Side surface tangent tool orientation along 3D path.....	97
4.5 Toolpath for infill.....	103
4.6 Evaluation of build angles and kinematic error	112
4.7 Conclusion and discussion.....	116
Chapter 5.....	117

THREE-DIMENSIONAL SCANNING AND RECONSTRUCTION	117
5.1 Introduction to 3D Scanning and Reconstruction	117
5.2 Relevant Literature Work on 3D Scanning	120
5.3 Three-Dimensional Scanner Design	124
5.3.1 Previous Work in MARC	124
5.3.2 First Prototype	127
5.3.3 Second Prototype	131
5.3.4 Concluded Design	135
Chapter 6	150
THREE-DIMENSIONAL RECONSTRUCTION	150
6.1 Calibration	150
6.1.1 Camera Calibration	150
6.1.2 Calibration of lasers, and motion axes	155
6.2 Triangulation model	159
6.3 Laser stripe extraction using image processing:	161
6.4 Evaluation of Measurements	177
6.4.1 Uncertainty analysis of measured points	179
6.4.3 Least squares optimization	182
6.5 Mesh Fusion and CAD conversion	185
6.6 Conclusion	187
BIBLIOGRAPHY	189

LIST OF FIGURES

Figure 1: Survey on the impact of various advanced manufacturing method in the next five years [7].....	23
Figure 2: The future possible outcome of digital supply chain at different level of production [9]	24
Figure 3: Correlation between technological advancement level and industrial adoption[10]	25
Figure 4: Terminologies used to name Additive Manufacturing.....	28
Figure 5: Additive Manufacturing roadmap of standards following ASTM/ISO guidance structure	29
Figure 6: Timeline of Additive Manufacturing progress showing critical milestones[10]	35
Figure 7: a) Technology readiness level definition by NASA, and b) TRL values assigned to different applicational fields of AM from a keynote CIRP annals paper[34].....	36
Figure 8: Standard categories of Additive Manufacturing methods.....	38
Figure 9: List of various Additive Manufacturing equipment manufacturers [37]	39
Figure 10: Analysis of the publication trends in additive manufacturing using search of number of publications from the year 2000 to 2015 [34].....	40
Figure 11: Summary of literature works on the study of influencing parameters, their effects and optimization [38].....	41
Figure 12: Overview of IT-classes for various manufacturing processes [39].....	42
Figure 13: MARC's first generation Additive Manufacturing system setup	43
Figure 14: Sample parts produced with first generation machine	44
Figure 15: Second generation AM machine designed in MARC	46
Figure 16: Modified AM equipment for fused filament fabrication showing important components	48
Figure 17: Tensile test results of fabricated PETG (XT) and composite (XTCF20) compared with ABS strength from literature [44–46].....	50
Figure 18: Microscopic image of chopped carbon fibers after deposition showing their alignment and length.....	51
Figure 19: Fractography of broken surface of tensile-test coupon	52
Figure 20: Sample parts fabricated with chopped fiber composite.....	53

Figure 21: Cartesian and Delta designs of AM Systems in a) and b) respectively [58]. 2D print-head used in commercial machine[59]	56
Figure 22: Design of 2-degree-of-freedom rotation base added to Delta design.....	57
Figure 23: Static FEM stress analysis of supporting structural components	58
Figure 24: Manufactured table base, build support and complete design of the 5-axis 3D printer	59
Figure 25: 5-axis 3D printer design showing the function of the two-dimensional build platform	61
Figure 26: Data flow of Marlin firmware G-code interpreter with added functions	62
Figure 27: Schematic diagram of electronic board showing pins used to control additional motors [62].....	63
Figure 28: Microcontroller connection terminal pins of sensors and actuators.....	64
Figure 29: Manufacturing of a solid cuboid using two different build directions	65
Figure 30: Additive manufacturing of protruding components without the use of supports.....	66
Figure 31: Fused deposition modeling print-head showing the build direction and plane.....	67
Figure 32: Demonstration of multi-axis AM using two build directions.....	67
Figure 33: Slicing using intersection of part and z-plane	68
Figure 34: Demonstration of the goal of Multi-Axis AM.....	69
Figure 35: Demonstration of multi-axis AM using two build directions.....	70
Figure 36: Illustration of how MAAM can be used with planar slicers to 3D-print without supports	71
Figure 37: MAAM process using planar slicers on divided parts	71
Figure 38: a) An open cuboid to be covered b) and the path of the roofing operation for some layers with build direction shown.....	72
Figure 39: The roofing process with collision detection	73
Figure 40: Fabrication of a hollow component to demonstrate the roofing process	74
Figure 41: Generated support structure shown in a cross-section view of the component.....	74
Figure 42: Fabrication of a bent/revolved part in (a) and a feature manufactured from combination of circular and linear paths in (b).....	75
Figure 43: Sketch showing the ultimate 3D curved path desired	76

Figure 44: The constructed Multi-axis additive manufacturing system. b) Sketch showing the reference frames of the 3D printer and the 2D base platform where relative motion between the frames is achievable	79
Figure 45: Definition of a) the slice path and tilt angle used in manufacturing thin overhang components, b) overhang angle, and c) slice angle which is equated with the tilt angle	82
Figure 46: Fabrication of a) overhang part with high slice angle, b) low slice angle overhang using 5-Axis AM 3D printer. c) CMM measurement of surface deviation of manufactured sample parts	83
Figure 47: Error distribution at sample points on the top surface of the fabricated overhangs for various tilt angles. At the sides where the nozzle turns, there are extra accumulation resulting in elevation causing small elevations. The range of deviation in error shrinks when the tilt is increased.	84
Figure 48: Plot of average planar deviation on bridge components measured for used slice angle. These are the errors of the manufactured surface measured with the desired CAD model of the bridging overhangs.....	85
Figure 49: Image of sample overhang parts showing bridge, free hanging and roof components. Marked regions show the possible occurrence of folds. As the tilt angle is increased, the build building condition of the overhang improves, and better parts are produced.....	86
Figure 50: a) A freeform model where surface is used to generate AM toolpath with fixed tool orientation from the local normal b) Error of produced part surface from the designed model in a. c)The freeform roof in a is being fabricated on the 5-Axis AM system with 400 tool direction from the normal d) A flat roofing overhang components manufactured at 400 e) Error distribution on the flat surface of the roof in (d).	87
Figure 51: 5-axis 3D printer design showing actuators and mechanical components of the system	92
Figure 52: Procedure of representation of a CAD model as organized connected surfaces along with the data and function organizational structure	96
Figure 53: Alignment and arrangement of surfaces from a freeform model	97
Figure 54: Stairstep effect of an ideal part in fig. a is demonstrated on b) planar slicer, c) offset surface slicing and d) interior infill and outline (in red) of transition layers	99

Figure 55: The algorithm used to generate 3D curves from side surfaces. Connection of edge points p_1 and p_2 with surface curves is demonstrated.....	100
Figure 56: Tool orientation along the 3D path applied in manufacturing of impeller blades	101
Figure 57: Two impellers are manufactured, where a) traditional planar slicer is used, b) the blades are fabricated using the suggested path. Staircase effects are visible on the top wall of the impeller blades on the left. Retraction remnants are also visible on the hub and blade surfaces in a. The gaps in the blades of b can easily be filled using methods introduced in Section 3.3	102
Figure 58: : a) The surface (in blue $L(u, v)$) obtained by blending the top and base surfaces may not fit to the layer outline obtained using methods of Section 3.2. The shape of the blend surface needs to be transferred to the new layer $L'(u, v)$ b) Construction of the new surface $L'u, v$ by using combination of interpolated displacement vectors of the isoparametric curves of Lu, v	106
Figure 59: For some layers from a model, an illustration of a) Networks curves(NCs) blended from $T(u,v)$ and $B(u,v)$ (blue) and the modified NCs (brown) that fit inside the model, b) some transition surfaces obtained from the NCs, c) zigzag path drawn on some surfaces	107
Figure 60: Outline of stages of path planning from surfaces extracted from a CAD model	107
Figure 61: a) A sample freeform CAD model to be manufactured. b) Horizontal layer paths used in manufacturing the model for comparison. c) The manufactured sample using plan in (b). d) The base, top($n=85$), 5 th and 84 th layers with the 5-axis paths showing the layer gap distribution on the color scale and the tool directions e) The fabrication instant using the designed 5-axis 3D printer showing the infill of the proposed paths of transition layers. f) The final manufactured part using plan in (e).	109
Figure 62: A sample compound model composed of regional parts is tested using the 5-axis process plan to produce sections 2, 3, and 4. The parts 2,3,4 have total of 75, 21 and 17 layers respectively	110
Figure 63: a) The compound model in Figure 62 is produced by horizontal layer FDM for comparison. b) The 5-axis AM method is used to fabricate parts 2,3 and 4. Marked regions show the advantages of using the method in this work	111
Figure 64: Print-bed that can be oriented to a desired build direction. b) The four possible paths of θ solution c) Path simulation of the machine path obtained from G-code showing undesirable loops d) Reduced error after implementing the patching to the path of θ angle	113

Figure 65: a) Distribution of kinematic error and plot of interpolator trajectory along the deposition path of the impeller blade fabricated in Figure 57 b) The patching method using look-ahead algorithm.....	115
Figure 66: Grouping of 3D scanning using different basis.....	118
Figure 67: Process of reverse engineering in product development [110]	119
Figure 68: Illustration of variables used in estimation of Zhou’s central axis error.....	122
Figure 69: Map of some sources of uncertainty in 3D scanner	123
Figure 70: Previous 3D scanning device designed in MARC	125
Figure 71: Processed scan points using the old MARC 3D scanner.....	126
Figure 72: Image showing the new camera and laser used on the old 3D scanner setup	129
Figure 73: First results obtained from upgrade of the previous 3D scanner.....	130
Figure 74: New design concept to increase the scanning viewing space	131
Figure 75: The second prototype with added mobile lasers and lift frame fabricated from Plexiglas	132
Figure 76: Distortion of the lift frame measured through variation of relative positions between points C and S	133
Figure 77: Comparative deformation analysis of the camera and laser support frame using different materials.....	134
Figure 78: Alternative design considered for the 3D scanner.....	135
Figure 79: Components of the 3D scanner shown on the final design	136
Figure 80: Distortion of the final support frame measured.....	138
Figure 81: Deformation and stress analysis of the final lift frame made from AL7050.....	138
Figure 82: Cross-section showing turntable rotation system.....	139
Figure 83: Scanner setup showing relevant geometric axes, calibration grid and other design features with front and top views.....	141
Figure 84: The 3D scanner shown during reconstruction of a knight piece	143
Figure 85: Raw image obtained from the image sensor during the scanning of a knight piece .	144
Figure 86: The centroidal radius of a reconstructed stripe points in (a) is used in controlling step angle to maintain uniform spacing between points shown in (b)	146
Figure 87: Two cases where the vertical point spacing does not match the horizontal spacing..	147

Figure 88: The 3D scanner during scanning where motor drivers and microcontroller are shown	148
Figure 89: Electronic wiring used by the motor controllers[138].....	149
Figure 90: Image acquisition GUI for calibration of camera.....	151
Figure 91: Calibration pattern that looks like checker board is used along with small dark patch used for laser setting.	151
Figure 92: Detected pixel location of the square corners used for camera calibration.....	152
Figure 93: a) Reconstructed calibration patterns at several locations to visualize extrinsic parameters. b) Variation of some intrinsic parameters at different focus at stand off distance between 50mm to 120mm. c) The reconstructed lasers on the plane of calibrator. d) Computed laser beam planes used using reconstructed lines.	154
Figure 94: Mean deviation of reconstructed pixel points from the detected points which indicates accuracy of the camera model.....	155
Figure 95: Sketch showing camera and scanner object frame.....	156
Figure 96: a) Spin axis of 7 configurations with some calibration planes and center points of 1st Lift. b) Measured lift angles from fitted Spin axis data with their confidence interval.....	157
Figure 97: Procedure of calibration of the scanner variables using camera, lasers and a planar calibration grid.....	159
Figure 98: Pinhole camera model relation between pixel and world position.....	160
Figure 99: Triangulation diagram showing measurable range (MR), field of view, laser 1 plane and sample point (X, Y, Z)	161
Figure 100: laser width resolved as how it appears on the camera.....	162
Figure 101: Sketch showing measurable range and camera field of view.....	163
Figure 102: Raw red channel image sensor signal at two distances showing reflected laser beam	164
Figure 103: Filter and unfiltered images compared.....	165
Figure 104: a) Image shiny aluminum part and b) Image after it is painted.....	166
Figure 105: Reconstruction of rat knee without painting in (a) and with painting in (b).....	167
Figure 106: Local threshold method carried out in a local vicinity window	168
Figure 107: Cubic spline fitting of stripe points with and without filling of holes	169

Figure 108: Demonstration of how artificial texture can be introduced to the reconstructed part by over-interpolation.....	170
Figure 109: Omitted portion when applying global thresholding.....	170
Figure 110: Part on the left, reconstructed using global threshold shows more missing portions than the one on the right that is reconstructed using local thresholding.....	171
Figure 111: Normal estimation from image gradient	172
Figure 112: Sample point cloud with some normal directions indicated in green arrows.....	174
Figure 113: Mesh generation showing polygons at various locations.....	175
Figure 114: PLY file structure generated using points and normal vectors and the real-time point cloud processing application in MATLAB.....	176
Figure 115: Preliminary evaluation of dimensions of reconstructed part.....	177
Figure 116: Monte Carlo simulation of uncertainty propagation showing average sample distribution of radial deviation.....	181
Figure 117: Results of uncertainty propagation in X, Y, Z are shown in plots a, b, and c with 2-sigma confidence interval marked. The average least squares optimized radial deviation PDF of sample points on the sphere is shown in d.....	181
Figure 118: a) First laser scan fitted on sphere after optimization. b) Painted aluminum specimen. c) Second laser scan fitted on sphere after optimization.....	184
Figure 119: a) Frequency distribution of point radial deviations on sphere. b) Radial deviations of scan points on the sphere	185
Figure 120: a) and b) are the sphere image and its fused mesh respectively. c) and d) are image and fused meshes of a knight piece respectively.	186
Figure 121: a) Plane and sphere model used for measurement b) Reconstructed model used to measure Ds c) Error distribution of plane data	187

NOMENCLATURE

θ :	Rotation angle of a turntable
ϕ :	Tilting angle from a turntable
$[x, y, z]_P$:	The coordinate position from the 3D printer frame
$[x, y, z]_W$:	The coordinate position from the working-part frame
(w_x, w_y, w_z) :	Relative distance displacement between 3D printer frame and working-part frame
(u, v) :	
$S(u, v)$:	NURBS surface defined for parameters u and v
ΔE_i :	Amount of filament extrusion on the path of 3D printing
D_f :	Diameter of filament
w_t :	Width dimension (usually constant) of deposited raster in additive manufacturing
Δl_i :	Layer spacing (variable) at a local path of deposition
\hat{n} :	Unit vector representing the direction of the nozzle
\hat{t} :	Unit vector representing the direction of movement along a path
SST:	Side-Surface Tangent build orientation
TSN:	Transition-Surface Normal build orientation
$T(u, v)$:	NURBS surface representing the top layer of a freeform model
$B(u, v)$:	NURBS surface representing the base layer of a freeform model
$L(u, v)$:	NURBS surface representing a 3D printing layer
$L'(u, v)$:	NURBS surface representing a layer obtained by blending
$d^u(u, v), d^v(u, v), d(u, v)$:	Interpolated displacements using u-curves, v-curves their combination
n_b :	Build plate orientation in multi-axis additive manufacturing

β, β_1, β_2 : Angles laser plane makes with the camera axis, subscripts show 1st and 2nd lasers

$(X, Y, Z)_C$: Position coordinates in camera frame C

$(X, Y, Z)_S$: Position coordinates in workpiece-object frame S

$(X_{cam}, Y_{cam}, Z_{cam})$: Relative distance between the camera focal point C and point S.

(x_p, y_p) : Pixel location on an undistorted image

(f_x, f_y) : Pixel focal length of camera

(c_x, c_y) : Pixel principal axis location on an undistorted image

s : Scaling factor used in camera calibration

γ : Angle between scan surface and laser beam

FOV : Field of View of camera

R_{max} : The maximum radius measurable by the scanner

MR : The maximum range of the 3D scanner

$I(i, j)$: Image definition as a grayscale or binary

$h(k, l)$: Gaussian kernel used for smoothing

(n_x, n_y, n_z) : Normal vector on a part's surface

(n'_x, n'_y, n'_z) : Normal vector on a part in the camera reference frame

(u, u_1, u_2) : Array of scanner parameters, subscript represent the laser used

$(f_1^i(u_1), f_2^i(u_1), f_3^i(u_1, u_2))$: Functions minimized for optimization of scanner parameters

ICP: Iterative Closest Point algorithm

PCA: Principal Component Analysis

Chapter 1

INTRODUCTION

1.1 Emerging Manufacturing Methods

With the progressive growth in the global economy, manufacturing methods and processes are required to be in continuous evolution to cater for the demands of industries and customers. New frontiers emerging from research works in manufacturing need to be studied. Only through exhaustive investigation into new methods and ideas can the best decisions be made in production process selection and planning. With rigorous evaluation of strengths and weaknesses of various aspects of upcoming advancements, that are gauged against processes in prevalent manufacturing methods, reforms can be made in line with the technological pace. The motivation for research in manufacturing is usually the desire for nations to engage in widening the horizon of cutting-edge technologies and to keep industries up to date. It is not surprising that governments around the globe use increased research funding in manufacturing to bolster industrial production and improve competitiveness.

The direct effect research has on manufacturing output which then impacts positively on the economy of nations cannot be overemphasized. The importance of industrial growth is rooted and well-established in economic studies to the extent that economic principles have been built around the idea. Testing Kaldor's hypothesis where industrial growth is viewed as the powerhouse of economic growth [1,2], the correlation between the growth in production and Gross Domestic Product (GDP) is observed. Having attested to the significance of research and development to keep up with the best practices in manufacturing industries and possible update of existing processes.

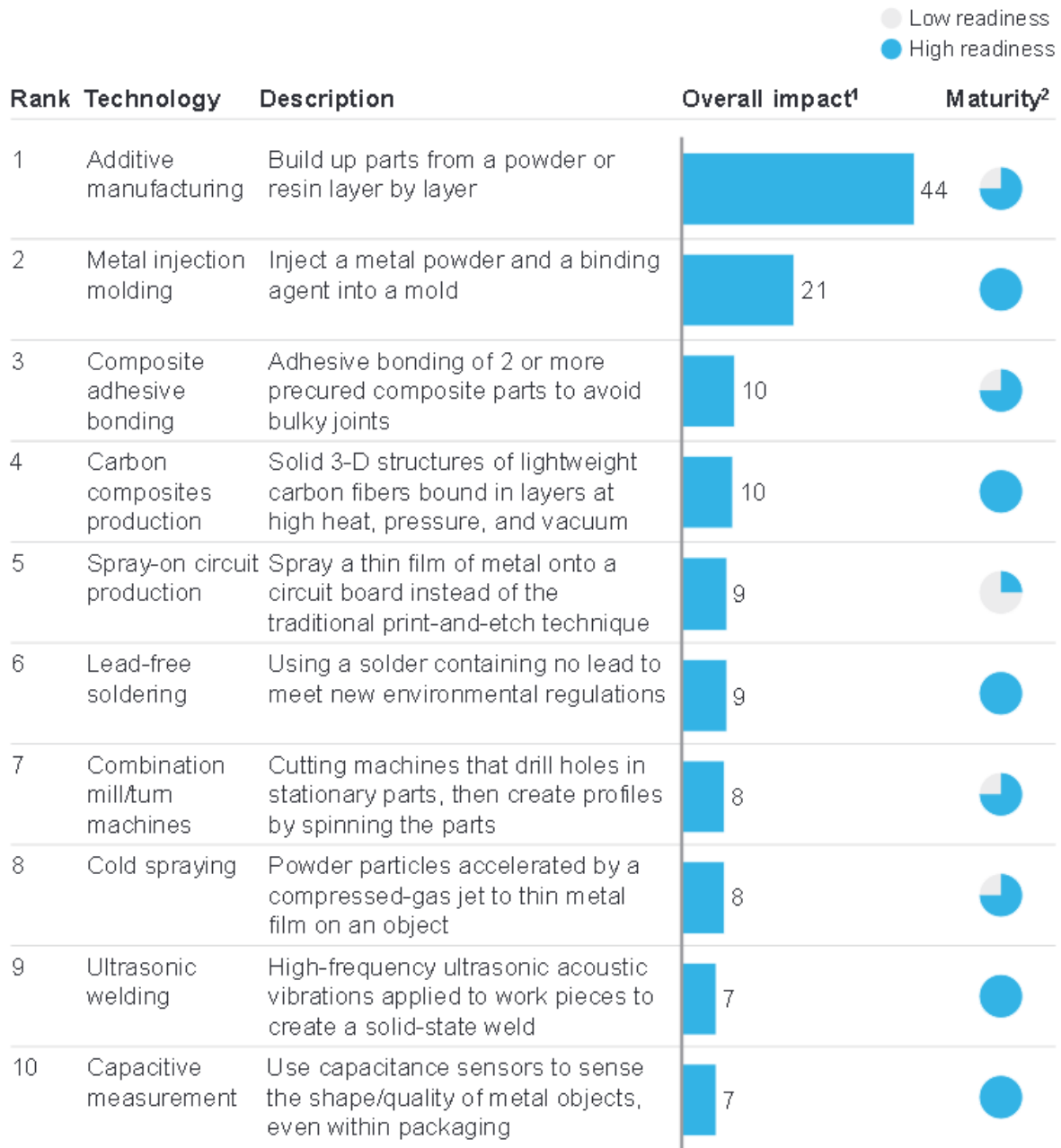
Classical categorization of manufacturing processes proves to be inadequate when it comes to incorporation of new methods. Manufacturing processes grouped into casting, forming, processes and fabrication [3] are reclassified to accommodate emerging technology [4]. Hence, a technology-based classification of manufacturing processes including joining, dividing, subtractive, transformative and additive technology groups was suggested [5]. New manufacturing

discoveries have led to increase in manufacturing flexibility and complexity that challenges proper utilization in the settings of conventional industries.

With progresses and innovations in manufacturing, design for manufacturing and process planning are constantly shaped to suit new capabilities. For instance, the advent of wider computer aided design (CAD) applications in the development of product has added new tools in design that target minimum part count and total cost. Using design for manufacturing, where the full information of manufacturing process is incorporated at the nascent stage of product design, improvements are observed in production [6]. The benefits of Design for Manufacturing and Assembly on the product design level has been shown to decrease cost and time significantly [3]. The new concepts and approaches can trigger a revolution in the manufacturing systems with regards to product design, information/data organization, process planning, machine shop structures and the nature of supply and demand.

Among the trending advanced manufacturing methods, additive manufacturing (AM) has been the most prominent and the dominating method that tailors the perception of the future of manufacturing. In a McKinsey report [7] on advanced manufacturing, AM was selected as the champion in the reformation of the future of manufacturing. The Figure 1, from the report, shows the result of an expert survey on the impact of advanced manufacturing methods in coming years. AM is seen to be the most influential considering the pace of development and interest it is accruing. Serving as a manifestation of imaginary predictions such as the 3 decades old vision of “prosumer” by the American futurist, Toffler [8], AM has the potential to place individual and private consumers at the center of production of goods making the consumer an integral part of the producer. The harmonious way AM integrates to the digital world is part of what makes it a modern and a promising new direction.

Critical factors that forces overhaul and adaptation of present manufacturing systems are regulatory pressure, competition in cost reduction, demand for high production rate, increase in part complexity, changes in data/process flow and the use of digital modes of demand and supply management.



¹ Percent of experts rating the technology as having high or very high impact on manufacturing over the next 0 - 5 years

² Derived from the Manufacturing Readiness Level assessment

SOURCE: McKinsey Advanced Manufacturing & Assembly survey

Figure 1: Survey on the impact of various advanced manufacturing method in the next five years [7]

1.2 Potentials of Additive Manufacturing

Additive manufacturing prioritizes the end-user perspective when it comes to production because of the more dominant role the consumer plays. Manufacturing industries and AM device manufacturers need to assist the user in providing more flexible and direct access to the systems or network engaged in production. The center for International Manufacturing [9] analyzed some possible future scenarios of digital supply chain of manufacturing are shown in Figure 2. The future manufacturing factory is expected to provide unhindered access to inline cloud-based designs reconfigurable by multiple users. Within the factory, higher flexibility in design and process is also possible through real-time scheduling, the use of flexible automation and digital production processes. The digital production processes are compatible with applications like AM that supports process monitoring. In addition, full production information regarding production lifecycle management (PLM), supply and trade can be made accessible to the consumer. The exact nature of how this grow into are not yet certain, but developments have already been observed in industry 4.0 and smart industry initiatives.

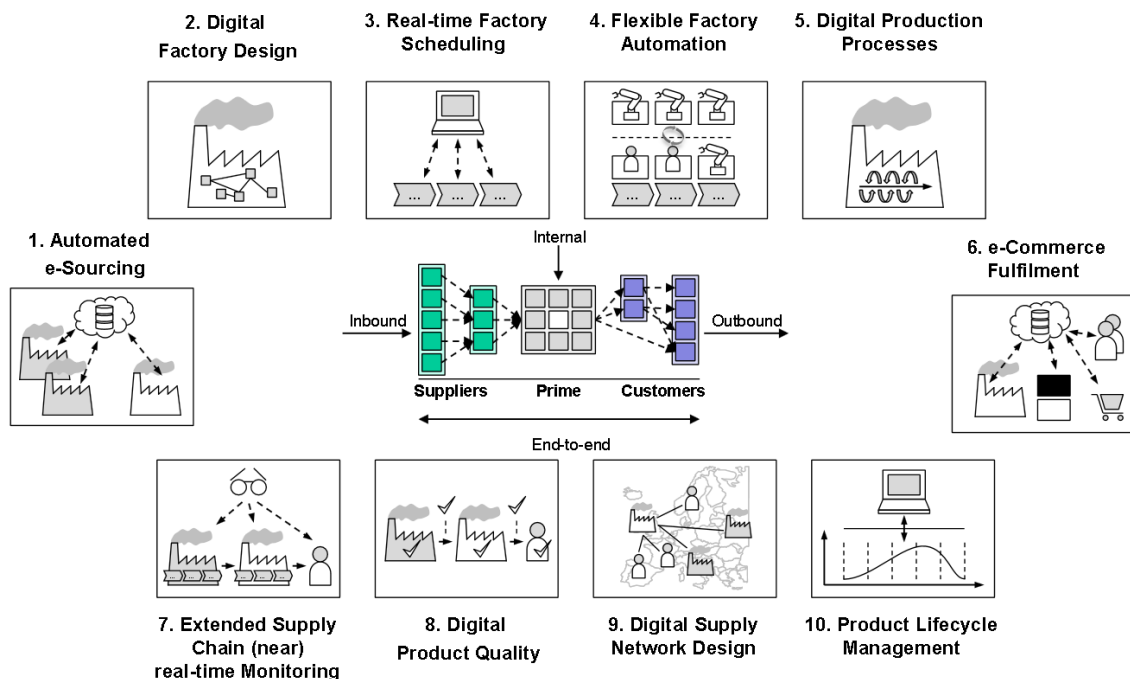


Figure 2: The future possible outcome of digital supply chain at different level of production [9]

The extent to which AM has been adopted in industries is related to the technological readiness of several aspects of the various additive production methods. Figure 3 (adapted from AM platform report [10]) shows the degree of industrial adoption of some popular AM techniques against the technological advancement level. The ranges delimited for each method represent the common applications in industries, hence there could be special applications not covered by the chart. The chart also compares the AM methods with some traditional manufacturing methods—CNC machining, injection molding and die casting. Methods that have been incorporated in low volume or mass production can be considered as approaching the peak of industrial adoption. It should be noted that not all the manufacturing methods necessarily go through all the industrial adoption. Some methods could only be suitable for low volume production at the peak of their adoption. Conversely, methods can be predominantly adopted in mass production rather than production in small volumes. The reason for this behavior is mainly due to production cost and speed. In processes, like molding, the unit cost of production is low in mass production.

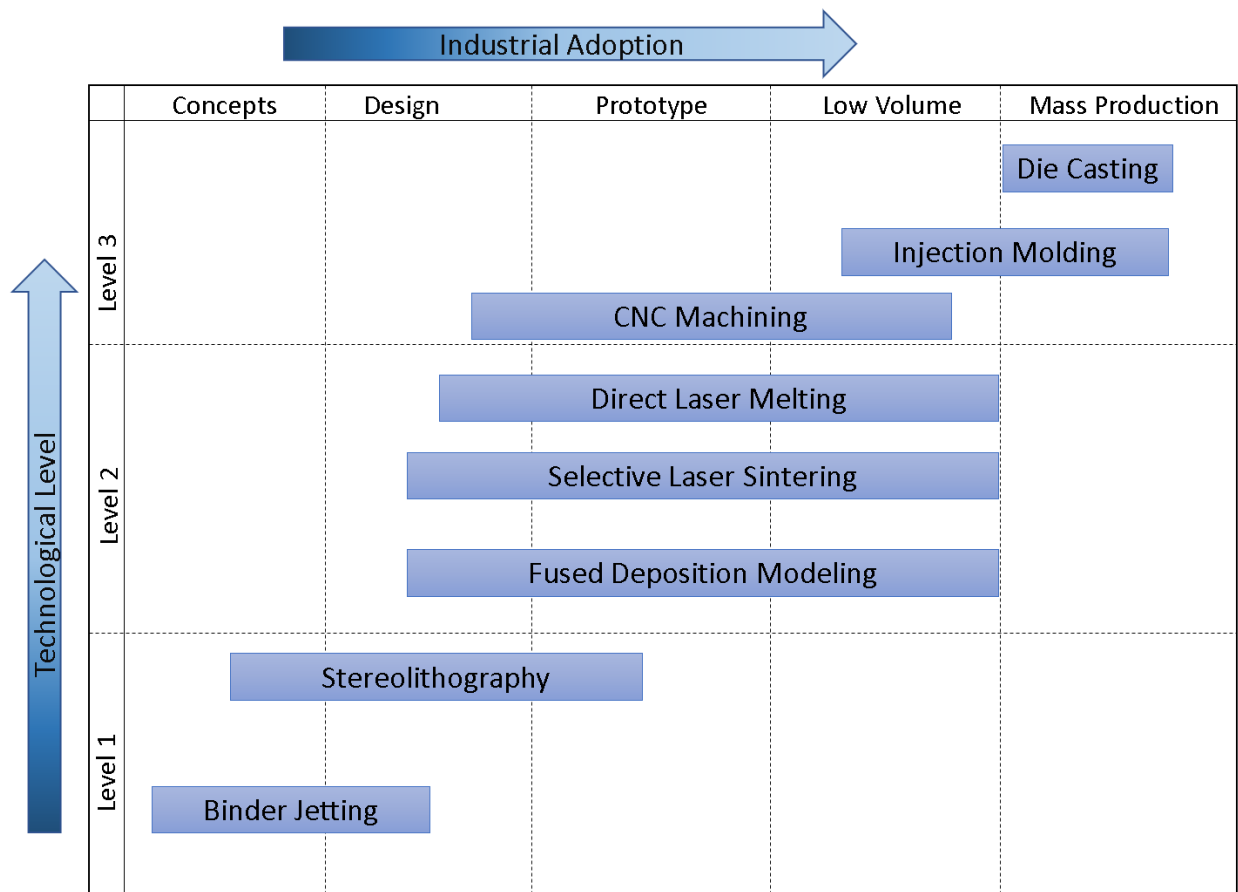


Figure 3: Correlation between technological advancement level and industrial adoption[10]

The four driving potentials of AM that puts it in competition with present manufacturing methods are given by Jiang et al. [11]. The critical factors mentioned are its power for exact replication (near net shape) of existing models [12], its improvement on function and weight of products [13], the capability for producing individualized products [14]. The fourth factor enhancing potential of AM is the minimization of dependence on assembly and part count [15]. The advantages and benefits of AM are discussed below.

- Production for CAD model to part: The capacity of producing any shape given with limited preprocessing and planning make AM the go-to method for fully automated manufacturing factory. Compared to other processes, like forging and machining, AM requires less breaking up of parts, therefore reducing assembly costs and in some cases, even production time is reduced.
- Customized designs: By complementation of AM with reverse engineering, a rapid prototyping strategy of generation of CAD model from an existing object, customized products can be realized and produced for a specific need with the ease other traditional methods cannot afford. Applications are common in the production of medical products, obsolete spare components, and the replication of geographical landscapes and artistic artifacts. In addition, AM presents a medium where customers can redesign or modify their own models without having much impact on the production process. This capability has opened up various online marketing avenues capable of making estimates on production feasibility, cost and time merely from by analysis of an uploaded design model.
- Function-based fabrication: Customarily, the burden of design decisions laid by how a product is going to be produced usually has more priority than how the product will be used. Using AM however, the decision on how to produce a part is less significant and can usually be given more room for complicated designs. Based on the application and the loading conditions of a part, AM filling patterns can be configured. Work on the use of topology optimization to generate optimal designs has evolved and major CAD software packages have started utilizing it.
- Material usage: Compared to subtractive manufacturing methods, AM does not leave much scrap materials. Some AM methods may require additional processing before a used feed material can be reused.

- **Productivity:** The initial material used for AM is the same and does not require preparation of blanks or cutting from stock. Consumables used by AM are easier and more productive to apply in machines mainly because they are identical. Unlike the use of non-uniform molding dies or machining blanks of different sizes, AM uses consumables like powders of graded sizes and filaments with uniform sizes. Additionally, use of less part counts, less assembly operations and limited human engagement makes AM more efficient.
- **Pollution:** AM methods contaminate the environment much less compared with other methods and does not have as much hazardous release to the environment [16]. The demand to reduced pollution and increased government regulations has made industries consider using AM. Additive manufacturing of plastics provides means of recycling unwanted plastics [17]. AM does not only provide more environmentally friendly manufacturing, it also serves as a means of cleaning the environment by recycling of plastics.

1.3 Standardization of AM

In the last 20 years, it has been observed that AM lacks the necessary standards that govern other processes. There is a need to have a common understanding between different groups associated with AM. The lack of standard in AM is a known fact among experts and work on standardization is ongoing. The American Society for testing and Materials (ASTM) and the International Standards Society (ISO) have begun work on the certification of AM processes, materials and naming.

Additive manufacturing was originally synonymously referred to as Rapid Prototyping (RP) [12] when it was initially conceived as a purely prototyping tool. Several names have been used to describe the it; the common ones used to describe AM are shown in the Figure 4. ASTM finally selected the name “Additive Manufacturing” to represent them. AM is defined officially by ASTM 2792-12 as “the processes of joining materials to make objects from 3D model data, usually layer upon layer, as opposed to subtractive manufacturing fabrication methodologies.” It is important for all the disciplinaries involved with AM to use the same standard vernacular in communication for effective transfer of information. The fields involved with AM is vast,

necessitating the clear uniform language to describe methodologies, processes and materials. Fields involved with design, technology, material and information communication need to be speaking the same AM languages. The capacity of AM to cut through industries is demonstrated in its growth into aerospace, medical, consumer products, automotive and even construction only intensifies the need for standardization. These industries will likely drive the future the growing manufacturing method [18]



Figure 4: Terminologies used to name Additive Manufacturing

The two big bodies that oversee the standardization of AM are the ASTM and ISO. In 2013, the two organizations agreed on collaborating to jointly formulate AM standards [19]. The structure is aimed at obtaining a single AM standard to be used all over the world and a common standard organizational structure of AM. The organizational structure [20,21] developed (shown in Figure 5) provides a common road map to related standards for a specific AM methodology. The structure retains consistency and avoids contradictions between standards among countries and companies across the globe. Within three hierarchical levels, the map of the AM standards is developed.

The top level, as shown in Figure 5, is for the general standards that covers all processes and methods. It contains the terminologies and definitions used in the field to describe the preferred names for consistency. The latest version of the standard of terminologies is the ISO/ASTM 52951. This standard contains terminologies and testing methodologies covering definitions of systems and devices. The terminology standard is complaint with ISO 841. Because AM depends on

computer numerical control. Most of its standards are made to obey ISO 841. The new AM terminologies are designed to complement the ISO 841 to tailor it for AM applications and not to overwrite it. The remaining general AM standards are the ISO 17296-2, ISO 17296-3 and ISO 17296-4. The second standard relates to processes, materials and their requirements. The next standard among the general standards is the testing method standard. Here, the specifications of the standard test specimen are given with the suggested types of testing. The ISO 17296-4 covers the design and data format of AM design files. The standard file format of AM has been the STereoLithography (STL) file format which commonly saves object model in the form of triangular tessellation meshes. The lack of the representation of texture, color, material and substructure features in the STL motivated the development of a new file standard for AM—the AMF file format. The AMF standard is based on the XML coding format.

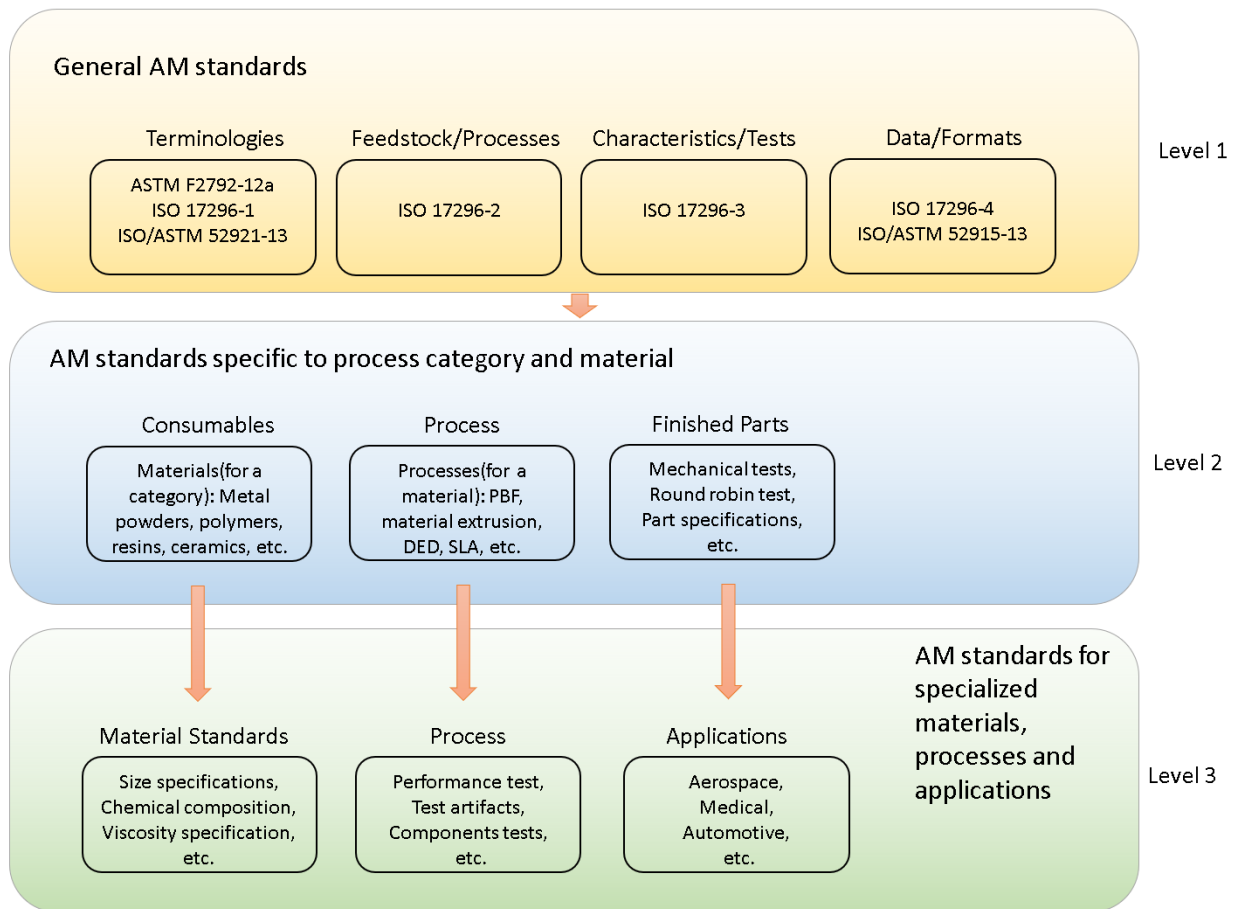


Figure 5: Additive Manufacturing roadmap of standards following ASTM/ISO guidance structure

The AM standards go beyond the general terms; there is the second level standards that make provisions for standards specific to a process or material. It contains standards for consumables, processes and finished parts. The consumables standard covers all necessary standard for the feedstock material for a certain AM method and process. The standard covers the powder, filament, resins and other material forms used in AM machines. Next is the category-based standards that covers the guidelines for the all the AM categories described in Chapter 2. The last standards in the second level covers the activities carried out on the finished part.

In the next level, the process standard for a some commonly used material-specific cases are given in details. For each material used in an AM method, the material features such as the size and composition specification are given. Some processes can accommodate fabrication using many materials that require some changes in standards. For instance, Powder Bed Fusion AM method can be used to produce both polymers like ABS and metals like titanium; the two materials require standard that are related to the Powder Bed Fusion process. The level 3 material standard covers these possible variations. The standards for AM processes also have their standards given in details in level 3. The details on the standards of testing of process performance and components properties are under the level 3 process. Last in level 3, the standards that cover a specific application like aerospace and medicine are outlined. The application condition of AM components does affect how it should be produced and the type of testing that should be used. Using the guidelines provided, up to level 3 standards, the required variation in standards is fully applied.

1.4 Reverse Engineering Introduction

Reverse engineering in this context refers to the generation of CAD model from an existing object. The term is used light to refer to all the processes involved in the obtaining this model. There is usually a measurement device (3D scanner), where points and mesh generation could follow. The whole data acquisition, processing, fusion and conversions are enveloped under the definition of reverse engineering in this text. To enhance the capacity of AM to produce parts that do not have digital models, reverse engineering can be used to generate freeform surfaces that can be modeled into CAD and produced by AM. Reverse engineering is a part of rapid prototyping tool that is used usually in the design or quality control stage of production.

Objects can be reconstructed to get a befitting design, for instance in bio-medical application where prosthetic limbs need to be customized. Consumer-specific products like shoe soles have also being manufactured using reverse engineering [22,23]. Aerial and terrestrial scanning is another growing application field of 3D scanning [24,25]. Stripes are made in making cars detect the geographic landscape to ultimately create fully automated smart vehicles.

In this paper, the application of RE considered with emphasis on using it a measurement device. It is interesting that RE can be used before and after production of a product for entirely different reasons. For new manufacturing methods, coordinate measurement of part may require full surface analysis to evaluate the deviation of manufactured parts. The potentials of using optical or non-contact measurement methodologies in RE for precision measurement of AM parts [26] is one critical issue. The conventional coordinate measurement machines are limited in speed; hence, there is need for a device that gathers measurement point without the need for mechanically touching each point.

Work on RE in the manufacturing lab was at early stage of verification of concepts. There was a laser scanner step-up and point cloud were acquired without a calibration, evaluation nor processing of the results. New prototypes of 3D scanner were built and analyzed in this work. Full calibration sequence and verification of measured surface accuracy are analyzed. Ways of improvement of measurement are also investigated alongside standard uncertainty evaluation and testing. The study on reverse engineering is deferred to Chapters 5 and 6 of this dissertation.

1.5 Motivation and Organization

Among the advanced methods of manufacturing, it is seen that AM has the most promising long-lasting effect on the manufacturing structure and facilities used in industries. It has capacity of expanding into many applications, as can be seen in its adoption into automotive, aerospace and medical fields. The most popular form of AM is the fused deposition modeling (FDM) or fused filament fabrication (FFF). Since the expiry of Stratasys patent [27], commercial FDM devices has expanded, making it the most familiar method of AM in industrial, educational and business settings. As an important method of AM, it still lacks the necessary research work to further its wider application and industrial adoption.

The process planning of AM has been established using common planar slicing and a movable fabrication point in three-axis for most of AM methods. Despite drawbacks in such systems, the ease and generality of the three-axis systems make them the default AM machines. Majority of AM work by solidification or binding of materials that is mainly carried out in a single direction. There is benefit in exploring the potentials of multi-directional AM to mitigate some of the existing impediments in application of AM.

In furtherance of work on multi-axis AM, the inadequacy of process planning for non-planar AM was acknowledged. A method of five-axis AM process planning for a freeform solid is suggested and tested by experiments. Without losing the universality of fabrication of parts by AM, freeform models are fabricated using new 3D paths aimed at alleviating deficiencies in present conventional AM process plan.

AM ushered in the capacity to fabricate freeform parts that are pre-designed as computer model directly. To complement the capacity of AM for objects that are not easily sketched as computer models, 3D scanning is also studied. The uncertainty of measured surface using a designed 3D laser scanner is evaluated and analyzed. Uncertainties of influencing parameters are propagated using the scanner model after optimization of the parameters.

Chapter 2 discusses the various types AM systems and the brief history of AM in Manufacturing and Automation Research Center (MARC). Chapter 3 covers the design of a multi-axis AM (MAAM) system together with preliminary manufacturing of certain parts. The benefits of MAAM system is also demonstrated using those simple geometries. For systematic part fabrication directly from a computer model, Chapter 4 introduces five-axis additive manufacturing (5AAM). The path and processes used to fabricate a model composed of enclosed solids bounded by freeform NURBS are suggested and implemented. Finally, Chapters 5 and 6 cover 3D scanning and reconstruction.

Chapter 2

ADDITIVE MANUFACTURING SYSTEMS

Additive manufacturing (AM) or Three-dimensional (3D) printing has grown continuously since its inception in the 1980s. Parts are manufactured by a successive layer-by-layer based material deposition directly from a digital design model. Manufacturing of various materials ranging from flexible polymers to strong metals can now be realized additively. The most ubiquitous AM technique is the fused deposition modeling® (FDM), which relies on the malleability of thermoplastics (TP) at low temperature for deposition of molten material to form the final part. FDM is significantly cheaper than other AM methods such as SLS/SLM used for metals, it is however still mainly confined to mainly fabrication of prototyping components that permits less structural applications [28]. The major setbacks of additive manufacturing are bad dimensional accuracy, lower production rate, small produced part size and poor mechanical properties of manufactured parts [29]. The effects of residual thermal stresses on form and dimensional accuracy of the final geometry of the manufactured part becomes very significant for large parts. As a remedy, measures are taken to improve uniform cooling and avoid excessive thermal gradient in the part by the use of cooling fans and heated bed. Most importantly, the lower accuracy and mechanical strength of the AM parts precludes its spread in vast application fields. To increase the applications of additively manufactured parts, it becomes necessary to address the issues holding back its promise of revolution in manufacturing.

2.1 History and relevant literature on Additive Manufacturing

The idea of using layered method in fabrication can be dated back to Blather's patent [30] where it is used for the construction of 3D relief maps by impression on wax mold. The earliest powder bed fusion type laser sintering was first described in 1979 through a patent in 1979 by Housholder [31]. He suggested binding and solidification of powder using laser heat for selective scanning or by using mask. Since the existence of AM depends on the invention and progress recorded in computing, it becomes necessary to acknowledge the role played by advancement in computers.

There was little promise that the early computers (such as Zuse Z3 and ENIAC) could make much impact; it was subsequent developments in transistors and microchips that brought higher speed, cheaper and small-sized computing systems to the forefront of technology[12]. Some indirect ways AM benefits from progress in computers include networking, graphics, processing power and machine control[12]. These functions are used in processing data and communicating with different entities to fabricate a part.

Despite earlier patent application on layered methods in topography and photo-sculpture, modern additive manufacturing is considered to date back to 40 year ago. The precise starting point of AM is rather hard to pinpoint, however there are many activities between 1950 and 1970 [12]. Notably, the invention by Charles Hull[32] introduced stereolithography(SLA) to the world in 1986, which rose to become the first commercialization of AM under the new company, 3D Systems. Figure 6 shows the timeline of important milestones in AM. The method of fused deposition modeling has its root in 1989 when a group from MIT invented and patented the 3D printing process. It became profusely utilized as consumer 3D printing method after the patent expired in 2009, making it the most popular AM process to date. AM continues to grow and its adoption in industries continue to supplant traditional manufacturing methods. Plans to use AM in mass production is underway as popular companies like general electric lead the way for implementation of the manufacturing method. Most of the progress in AM has been generally directed towards developing from a rapid prototyping method to a direct digital manufacturing method. The progress occurred in multiple fields simultaneously. Materials that can be used in AM systems have been advanced, processes have been improved and the accuracy, reliability and speed of the machines have also improved. These paved the way for commercially successful products like the fuel nozzle manufactured using powder bed fusion by GE Aviation[33]. This has reduced the amount of welding on the nozzle part from 25 counts to only 5.

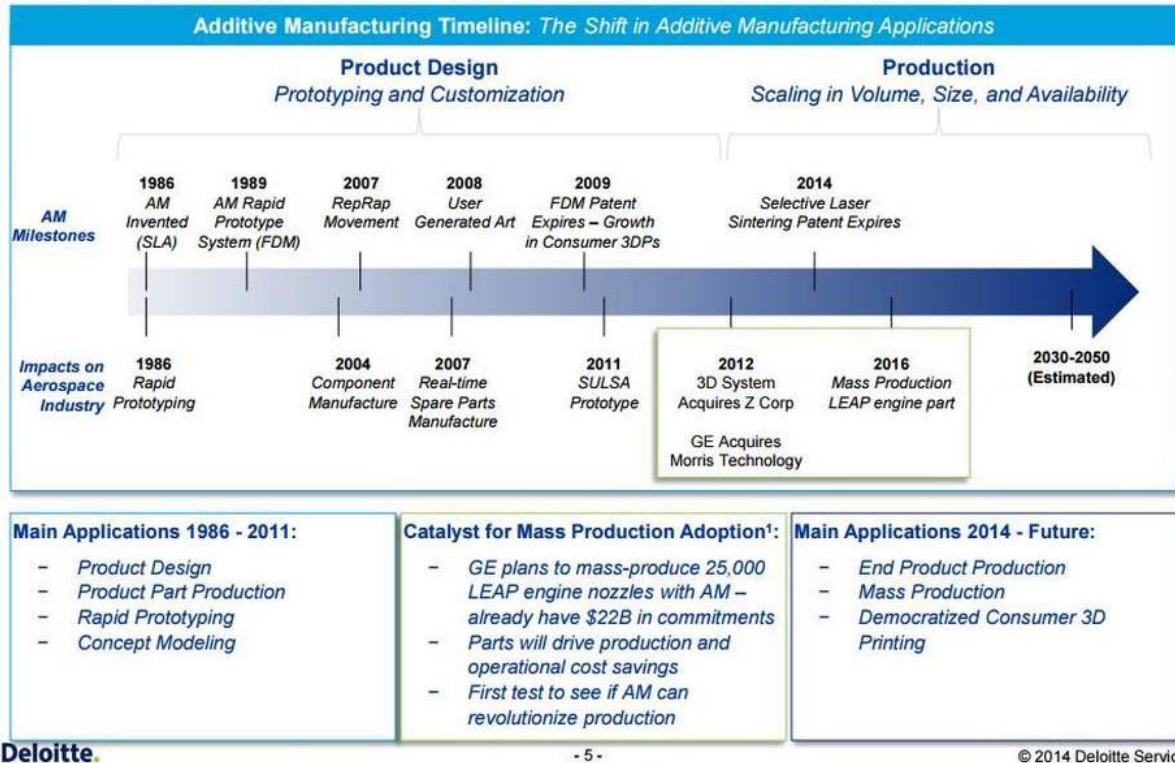


Figure 6: Timeline of Additive Manufacturing progress showing critical milestones[10]

An important factor that affects the adoption of a technology to the industry is the technological readiness level (TRL) of the technology. In an aim to bridge the gap between research done in universities, government research centers and commercial industries, America Makes gave the TRL in AM a value 4-7. The TRL levels, invented by NASA, are given in Figure 7a. The TRL serves as a method of estimating technological maturity across different types of technology. The readiness level of metal AM in some major application fields are provided in a keynote review paper[34], shown in Figure 7b. According to it, laser-based AM has reached the high maturity in aerospace, medical and tooling industries.

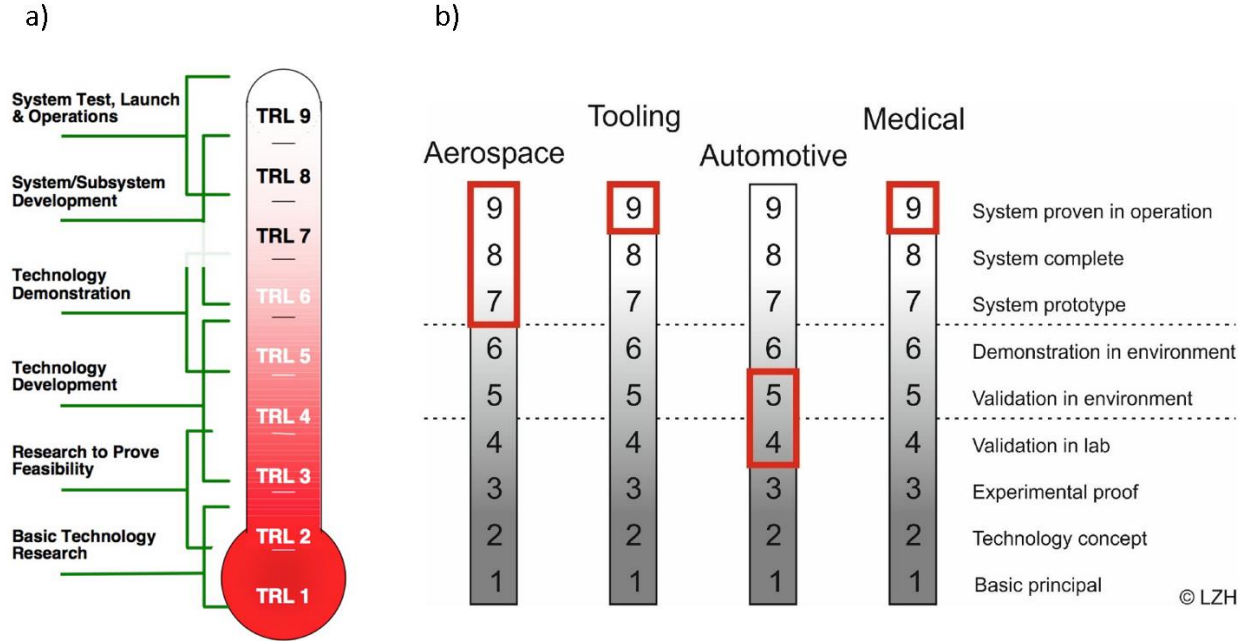


Figure 7: a) Technology readiness level definition by NASA, and b) TRL values assigned to different applicational fields of AM from a keynote CIRP annals paper[34]

Wessel[21] studied the potential of AM in the maintenance, repair and overhaul of existing machine parts where powder bed fusion and FDM are selected as the most likely AM method to dominate. Polymer FDM is assigned TRL level of 7-9 while Electron Beam Melting (EBM) and Selective Laser Melting (SLM) are given pre-production levels (3-7).

2.2 Types of Additive Manufacturing Systems

Additive manufacturing is defined as the selective layer-upon-layer based addition of material to consolidate a solid part to fit a known computer model. Additive manufacturing has evolved into various methods and applications with the trend of explosive growth of around 30% since 2010 [35]. Pham et. al. [36] classified AM technologies based on the mode of material addition. Initially most AM is carried-out by point-wise material addition and later droplets deposition technology in jetting methods introduced the possibility of deposition by array of point sources. The improvement from 1D source to array of 1D sources improves the manufacturing speed through increased throughput. In furthering this, 2D sources were introduced by the use of digital micro-mirrors and high resolution projection [12]. The 2D source, presently used in some stereolithography AM systems, is capable of projecting an entire surface at once. There is a possibility for a 3D source in the future using something like holographic technology. Pham's classification also demarcates the methods according to the materials used—liquid, powder, solid sheets or molten. The classification proves to be inadequate when classifying new methods such as composite extrusion where both particle/solid are deposited with molten material.

The AM standards on terminology broached in the previous chapter actually provides the standard classification of technologies. AM methods are grouped into seven categories: Vat Photopolymerization, Directed Energy Deposition, Material Extrusion, Material Jetting Powder Bed Fusion, Binder Jetting and Sheet lamination. Brief descriptions of the categories are given in Figure 8. This classification scheme allows new strategies to find their place easily among the groups without ambiguity.

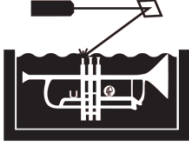
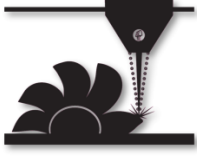
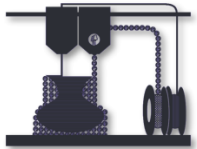
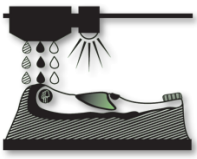
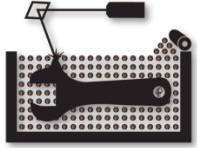
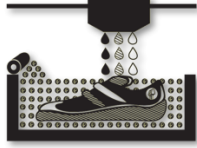

<p>Vat Photopolymerization</p>  <ul style="list-style-type: none"> • SLA: Stereolithography • DLP: Digital Light Processing • Resin is cured by UV light through laser or projector 	<p>Directed Energy Deposition</p>  <ul style="list-style-type: none"> • Uses metal powder or wire • Powered by laser or electron beam
<p>Material Extrusion</p>  <ul style="list-style-type: none"> • FDM/FFF: Fused Deposition Modeling • Uses filament, slurry or liquid 	<p>Material Jetting</p>  <ul style="list-style-type: none"> • Droplets are cured by UV light • Molten droplets are dispensed and allowed to solidify
<p>Powder Bed Fusion</p>  <ul style="list-style-type: none"> • SLS: Selective Laser Sintering • SLM: Selective Laser Melting • EBM: Electron Beam Melting 	<p>Binder Jetting</p>  <ul style="list-style-type: none"> • Bonding agent hold the powder particles • Part usually requires sintering in furnace
<p>Sheet Lamination</p>  <ul style="list-style-type: none"> • Sheets are laminated by welding, adhesives or chemical bonding 	

Figure 8: Standard categories of Additive Manufacturing methods

The mentioned categories of AM have been adopted in academia with analysis carried out on the bases of the classification. Huang and Leu [37] listed the commercial 3D printing machines on the basis of this categories. As indicated in Figure 9, each category has amassed enough interest in the private sector to record a number of commercial products.

Type	Process/Technology	Material	Manufacturer	Machine
Vat Photopolymerization	SLA (Stereolithography)	UV curable resins	Asiga	Freeform Pico
			3D Systems	iPro
			3D Systems	Projet6000/7000
			EnvisionTEC	Perfactory
			Rapidshape	S Series
		Waxes	DWS	DigitalWax
		Ceramics	Lithoz	CeraFab 7500
Material Jetting	MJM (Multi-Jet Modeling)	UV curable resins	3D Systems	Projet 3500 HD/ 3510/ 5000/5500
		Waxes	Stratasys	Objet
Binder Jetting	3DP (3D Printing)	Composites	Solidscap	3Z
		Polymers, Ceramics	3D Systems	Z Printer
		Metals	Voxeljet	VX Series
Material Extrusion	FDM (Fused Deposition Modeling)	Thermoplastics	Stratasys	Dimension
				Fortus
				Mojo
				uPrint
			MakerBot	Replicator
			RepRap	RepRap
			Bits from Bytes	3D Touch
			Fabbster	Fabbster Kit
			Delta Micro Factory Corporation	UP
			Beijing TierTime	Inspire A450
		Waxes	Choc Edge	Choc Creator V1
			Essential Dynamics	Imagine
			Fab@Home	Model
Powder Bed Fusion	SLS (Selective Laser Sintering)	Thermoplastics	EOS	EOS P
			Blueprinter	SHS
			3D Systems	sPro
		Metals	3Geometry	DSM
			Matsuura	Lumex Avance-25
	SLM (Selective Laser Melting)	Metals	Pherix	PXL, PXM, PXS
			EOS	EOSINT M
			SLM Solutions	SLM
			Concept Laser	LaserCUSING
			3D Systems	ProX
			Realizer	SLM
EBM (Electron Beam Melting)	Metals	Renishaw	AM250	
		ARCAM	Arcam A2	
		Sciaky	DM	
Sheet Lamination	LOM (Laminated Object Modeling)	Paper	Mcor Technologies	Matrix 300+
		Metals	Fabrisonic	SonicLayer
		Thermoplastics	Solido	SD300Pro
Directed Energy Deposition	LMD/LENS (Laser Metal Deposition / Laser Engineered Net Shaping)	Metals	OPTOMECH	LENS 450
			POM	DMD
			Irepa Laser	EasyCLAD

Figure 9: List of various Additive Manufacturing equipment manufacturers [37]

Upon studying the trend of AM in the academic environment, Figure 10 prepared by Schmidt et. al. [34] gives the number of publications from the year 2000. Academic interest in AM has been increasing in general with acceleration somewhere around the year 2012. The searches investigated in the figure include total AM, AM with laser, Laser Beam Melting (LBM), Laser Metal Deposition (LMD), Electron Beam Melting (EBM) and FDM. The publications in FDM is seen to overtake LMD and EBM in the last 3 years recorded in the figure. This trend is expected to keep up because of the industrialization of FDM and the emerging advancements in composites fabrication.

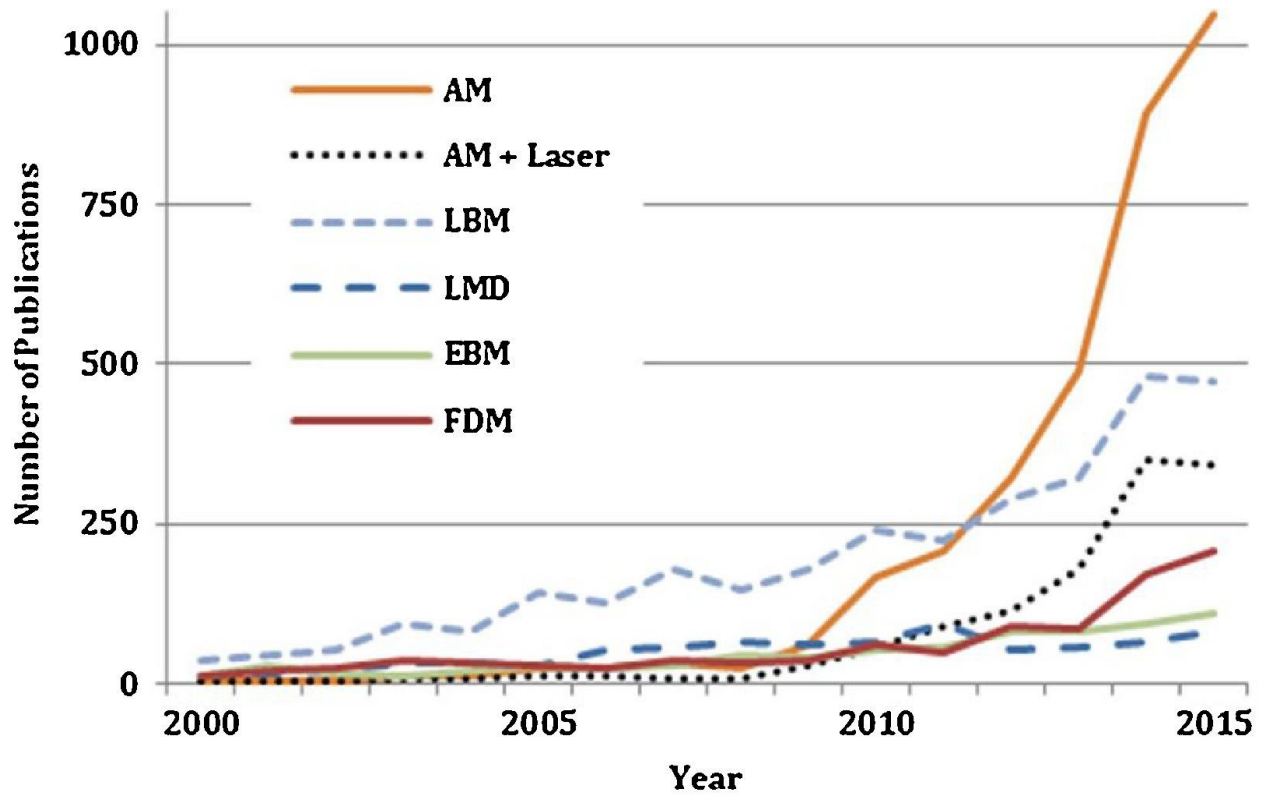


Figure 10: Analysis of the publication trends in additive manufacturing using search of number of publications from the year 2000 to 2015 [34]

Mohamed et. al. [38] studied the methods used in optimization of FDM process parameters. Methods such as response surface methodology, Taguchi method, full factorial, Artificial Neural Network (ANN) and many other methods. The parameters studied in literature are tabulated [38] and shown in Figure 11. Majority of the targeted optimized output is related to the surface and dimensional accuracy of the produced parts. Accuracy of produced part is indeed an important

factor in AM. Compared with other manufacturing methods, AM generally exhibits tolerances that are on the poor side.

References	Methods	Materials	Inputs	Outputs	Significant inputs
Anitha et al.	Taguchi method, (S/N) & ANOVA procedure	ABS	Layer thickness, road width, speed of deposition	Surface roughness	Layer thickness
Thrimurthulu et al.	GA	ABS	Slice thickness, build deposition orientation	Surface finish and build time	All input parameters
Nancharaiah et al.	Taguchi method, ANOVA procedure	ABS	Layer thickness, road width, raster angle, air gap	Surface quality and dimensional accuracy	All input parameters
Horvath et al.	2 ³ and 3 ² full factorial designs	ABS	Model temperature, layer thickness, part fill style	Surface roughness	Layer thickness
Wang et al.	Taguchi method, ANOVA along with gray relational analysis	ABS	Layer thickness, deposition style, support style, deposition orientation	Tensile strength, dimension accuracy and surface roughness	Layer thickness and deposition orientation
Sood et al.	Gray Taguchi method, ANN	ABS	Part orientation, road width, layer thickness, air gap, raster angle	Dimensional accuracy	Build orientation
Zhang and Peng	Taguchi method	ABS	Wire-width compensation, extrusion velocity, filling velocity, layer thickness	Dimensional error and warpage deformation	All input parameters
Sahu et al.	Taguchi method, fuzzy logic	ABS	Layer thickness, orientation, raster angle, raster width, air gap	Dimensional accuracy	All input parameters
Lee et al.	Taguchi method, ANOVA procedure	ABS	Air gap, raster angle, raster width, layer thickness	Elastic performance	Air gap, raster angle and layer thickness
Laeng et al.	Taguchi method, ANOVA procedure	ABS	Air gap, raster angle, raster width, slice height	Elastic performance	Air gap, raster angle and slice height
Ahn et al.	2 ⁵ full factorial design	ABS	Air gap, raster orientation, bead width, raster width, model temperature, color	Tensile strength, compressive strength	Air gap, raster orientation
Ang et al.	2 ⁵ full factorial design	ABS	Air gap, raster width, build orientation, build laydown pattern, build layer	Porosity, compressive yield strength, compressive modulus	All input parameters
Sood et al.	CCD, ANOVA procedure	ABS	Layer thickness, orientation, raster angle, raster width, air gap	Tensile, flexural and impact strength	All input parameters
Percoco et al.	CCD	ABS	Raster width, raster angle, immersion time	Compressive strength	Raster width
Rayegani and Onwubolu	2 ⁴ full factorial design, GMDH & DE	ABS	Part orientation, raster angle, raster width, air gap	Tensile strength	All input parameters
Masood et al.	Laboratory experiment	PC	Build styles, raster angle, raster width	Tensile strength	Not applicable
Arivazhagan et al.	Laboratory experiment	PC	Build styles, raster angle, raster width	Storage modulus, complex viscosity, loss modulus and Tan δ	Not applicable
Arivazhagan and Masood	Laboratory experiment	ABS	Build styles, raster angle, raster width	Storage modulus, complex viscosity, loss modulus and Tan δ	Not applicable
Jami et al.	Laboratory experiment	ABS	Build orientations	High-strain-rate behavior	Not applicable

Figure 11: Summary of literature works on the study of influencing parameters, their effects and optimization [38]

The achievable tolerances on systems using various manufacturing methods are tabulated by Lieneke et. al. [39], as displayed in Figure 12. The international tolerance grade, IT-classes, by ISO 286 standard of AM ranges from 11 to 16. These category of tolerance falls under large manufacturing tolerances that are usually useful for production of less rigorous parts. More demanding tight tolerance parts need to be produced using subtractive methods that manifest smaller tolerance. The large tolerance associated with AM also limits the how small a part can be produced.

Process	IT-Classes (DIN EN ISO 286-1)											
	5	6	7	8	9	10	11	12	13	14	15	16
Casting							■	■	■	■	■	■
Sintering					■	■	■	■				
Drop forging								■	■	■	■	■
Precision forging						■	■	■				
Cold extrusion			■	■	■	■	■	■				
Milling				■	■	■	■					
Cutting								■	■	■		
Turning			■	■	■	■						
Drilling								■	■	■		
Face milling			■	■	■	■	■	■				
Planing				■	■	■	■	■				
Stripping			■	■	■	■						
Circular grinding	■	■	■	■	■							
Additive manufact.							■	■	■	■	■	■
FDM							xyz	xyz	xyz	z		
LS									xyz	xyz	xyz	
LM							xy	xy	xy	xy	z	z

Figure 12: Overview of IT-classes for various manufacturing processes [39]

2.3 Additive Manufacturing Development in MARC

The development of AM system in the Manufacturing and Automation Research Center (MARC) were discussed in Bank's dissertation [40]. The history of the old generation of 3D printing research in MARC are obtained from the dissertation.

2.3.1 The first-generation AM machine

The beginning of additive manufacturing work in Manufacturing and Automation Research Center (MARC) was marked by a TUBITAK research project in 2005. The work targeted design of polymer extrusion head for AM. At that time, there was no much facilities developed, hence designs and processes decisions have to be carried out comprehensively. The mechanical structure designed was built on an open loop control where G-codes are used for communication. The design has an XY moving plate upon which Z-axis motor is attached. The extrusion of material was achieved by using a syringe controlled by an additional motor on the XYZ moving element shown in Figure 13. By the nature of the AM process, part can only be produced as using slurry or material paste.

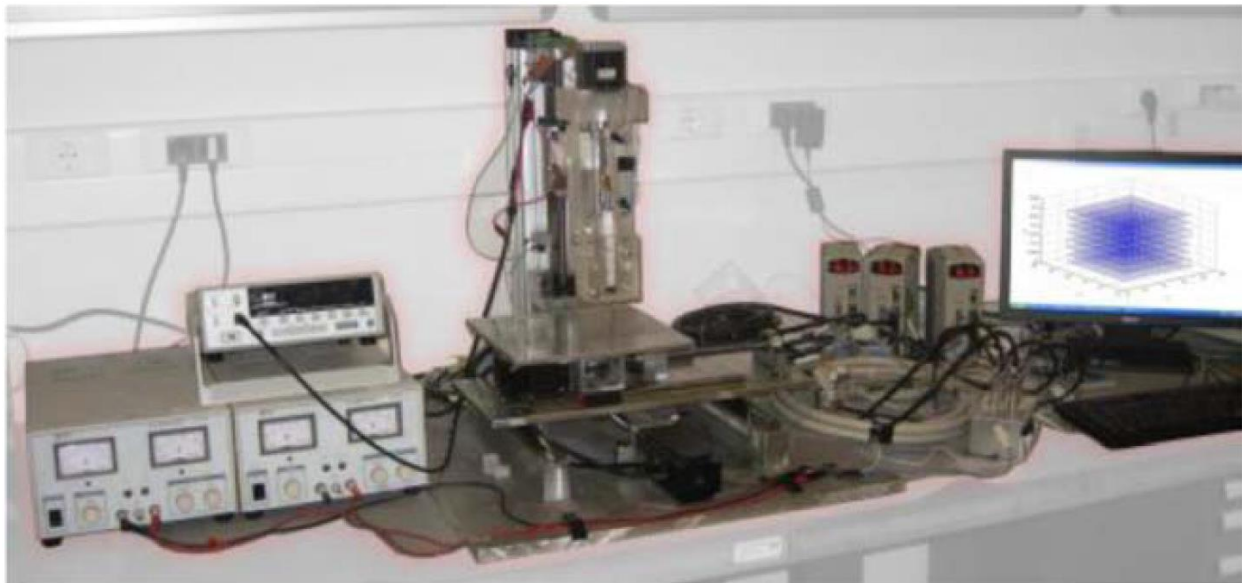


Figure 13: MARC's first generation Additive Manufacturing system setup

The first MARC prototype machine was a $2\frac{1}{2}$ D machine build as a cartesian positioning device. Even though the machine was aimed at delivering sub-millimeter level of tolerance, there was no deformation nor dynamic analysis to verify its precision. The work provides an introductory investigation of verification of ideas in AM but there are much more areas that require more studies to bring the research center at the contemporary level in the advanced manufacturing method. Some of the preliminary results obtained from the system are shown in the Figure 14.

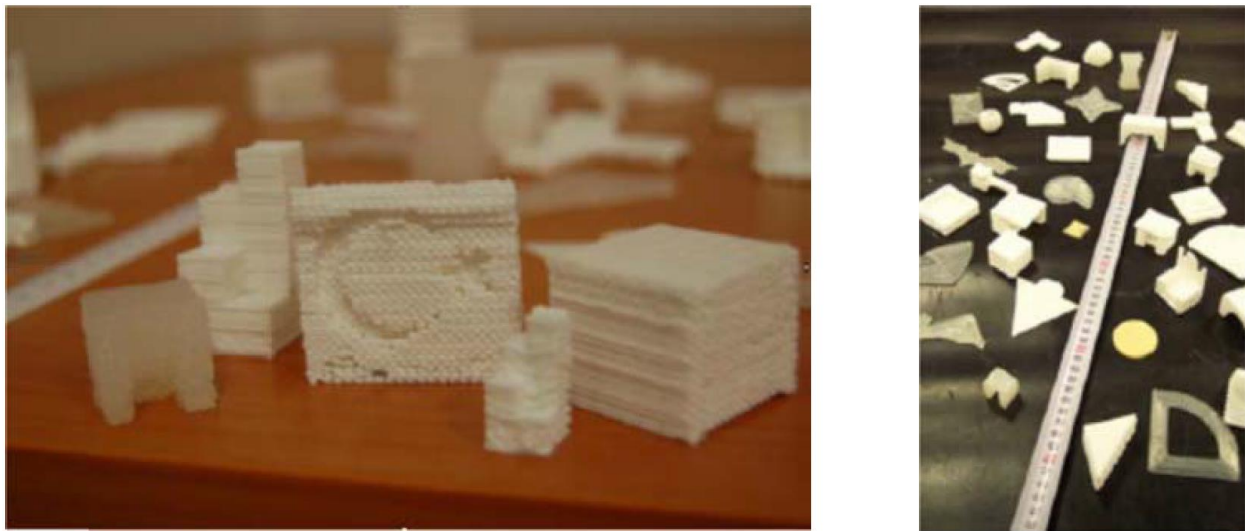


Figure 14: Sample parts produced with first generation machine

The tool location path was obtained from machining computer aided manufacturing (CAM) package. The path is then processed in MATLAB to make it suitable for AM and G-codes are developed to construct parts. Signals are transferred by RS-232 interface using serial protocol with the aid of microcontrollers and drivers. The machine does not support STL, and hence cannot produce many freeform parts. The geometrical complexity of the parts produced is severely limited. In addition, having to manually copy codes from one software to another is cumbersome and not user-friendly. There was a need to address the major issues with the first-generation rapid prototyping system in MARC.

The important issues observed by Bank[40] are outlined below:

- The temperature gradient in the extrusion head is not easily controllable. There way not proper analysis on the melting and the effects of heating.
- The viscosity is too low to allow construction of more complex objects. There is need for added layers to be fully supported during fabrication
- The lack of reverse control on extrusion makes material deposition continuous without full control on stoppage and taking material back.
- The software used is not for additive manufacturing but for machining. The two methods of manufacturing are very different, hence AM requires its own computer-aided software support.
- The syringe method used depends on the specific type of polymer used. The material used has limited applications; it will be better if a material-independent strategy is used.
- The structure is made out of heavy metal making it unwieldy and not easily carriable. z-axis is prone to errors.

2.3.2 The second-generation AM machine

The second-generation 3D printer was designed for the thesis titled “Open Architecture System for Biomanufacturing of Scaffolds for Tissue Engineering” by Daulet Izbassarov for Masters work in Mechanical Engineering. The system was designed mainly using the RepRap’s Fab@Home architecture.

For portability, the new system is designed from a Plexiglas body that significantly decreased the mass of the machine. However, due to the inaccuracies in the Plexiglas cutting method (laser cutting) and the inferior structural strength of the material, the second system has an unaccounted deformation. Basic machine design was not carried out on the machine. As a result, the build plate deforms by couple of millimeters during 3D printing. The alignment of X-axis is also questionable since it is done manually and slippage on the back belt can easily cause misalignment.

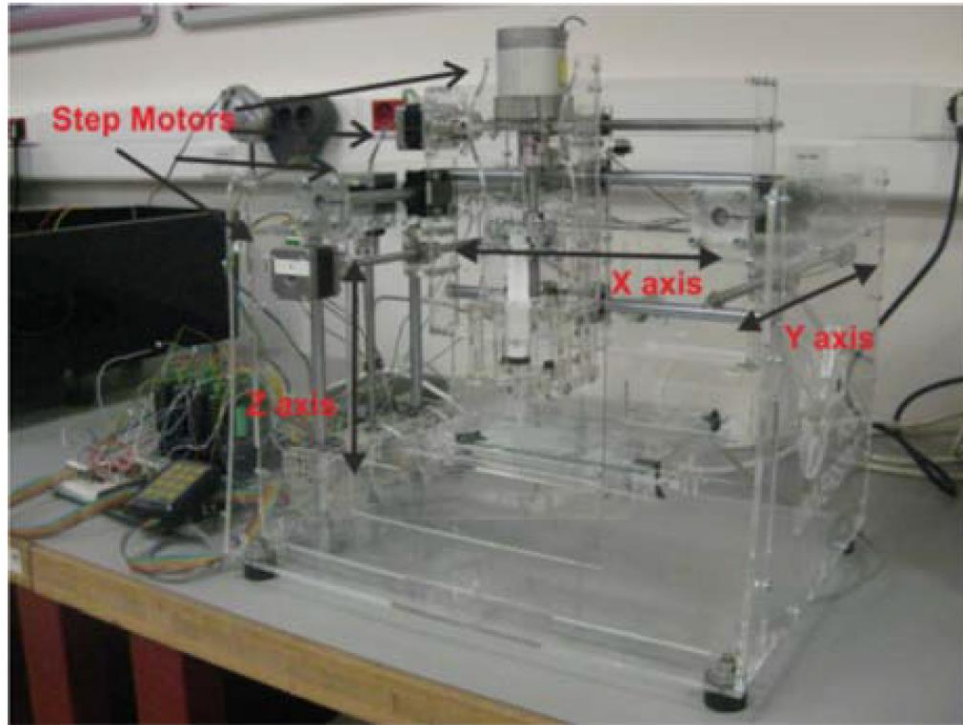


Figure 15: Second generation AM machine designed in MARC

The inherited problems of a syringe extruder head system still persist in the second-generation. However, the designed new syringe injection head is compatible with different types of syringes like 5-, 10- and 20-mL syringes, making it a great improvement on the old system.

The second-generation machine allows not only injection by pressing in the syringe plunger, but also it also permits the withdrawal of the plunger making it possible to relieve pressure quickly during deposition. This makes it possible to stop extrusion of material faster. The machine was produced to target the biomedical application of AM by attempting to produce scaffolds using some sample cell types.

The second system abandoned the 100MHz 8050 Cyrix microcontroller to apply a 20 MHz 16F877PIC microcontroller. The new controller allows micro-stepping which coupled with the 2.5 mm pitch lead screw provided very high resolution of position in X and Y coordinates at the cost speed. There is the need for a computer-aided means of producing geometries using G-codes.

After these AM machines are studied in MARC, the next research in AM focused on the use of laser energy in an open-architecture powder bed fusion machine. There were ways study of material-deposition AM can be furthered. This dissertation will focus on the used of fused filaments in material deposition AM to provide new ideas and test them.

2.4 Fused Deposition on a Cartesian Machine

The most ubiquitous AM technique is the fused deposition modeling® (FDM), which relies on the malleability of thermoplastics (TP) at low temperature for deposition of molten material to form the final part. FDM is significantly cheaper than other AM methods such as SLS/SLM used for metals, it is however still mainly confined to fabrication of prototyping components that permits less structural applications[28]. The major setbacks of additive manufacturing are lower production rate, small produced part size and poor mechanical properties of manufactured parts[29]. The effects of residual thermal stresses on form and dimensional accuracy of the final geometry of the manufactured part becomes very significant for large parts. As a remedy, measures are taken to improve uniform cooling and avoid excessive thermal gradient in the part by the use of cooling fans and heated bed. Most importantly, the lower mechanical strength of the AM parts precludes its spread in vast application fields. To increase the applications of additively manufactured parts, it becomes necessary to address issues holding back its promise of revolution in manufacturing.

Due to the demand of lightweight strong components such as in aerospace and automobile applications, specific strength of manufactured parts becomes a critical criterion in manufacturing decisions. A unidirectional continuously reinforced thermoplastic composite has been proven to exhibit potentially much superior specific strength of around 500Mpa in the fiber direction[41]. By tailoring the fiber embedding directions, it is possible to achieve structurally enhanced parts. It has been shown that metallic parts can be supplanted by such fiber enhanced TP composite[42]. It is noteworthy that even though high-performance TPs are already in used in aircraft applications, there is still need to study their freeform fabrication and reinforcement by AM since this will expand their applicability.

2.4.1 Fused deposition extrusion head

The second-generation machine was modified to replace the syringe head with a filament extruder, shown in Figure 16. The result of which is makes the device a polymer 3D printer capable of printing different materials sold as standard filaments. Since FDM has been studied sufficiently in literature and many commercial products and parts are available, there are open source FDM components for design, control and planning. Open source RepRap control is used to guide the motion of the 3D printer and communicate via serial port to receive position commands. The extrusion actuation is carried out using a pinch-roll mechanism to precisely feed or retract the filament during AM process.

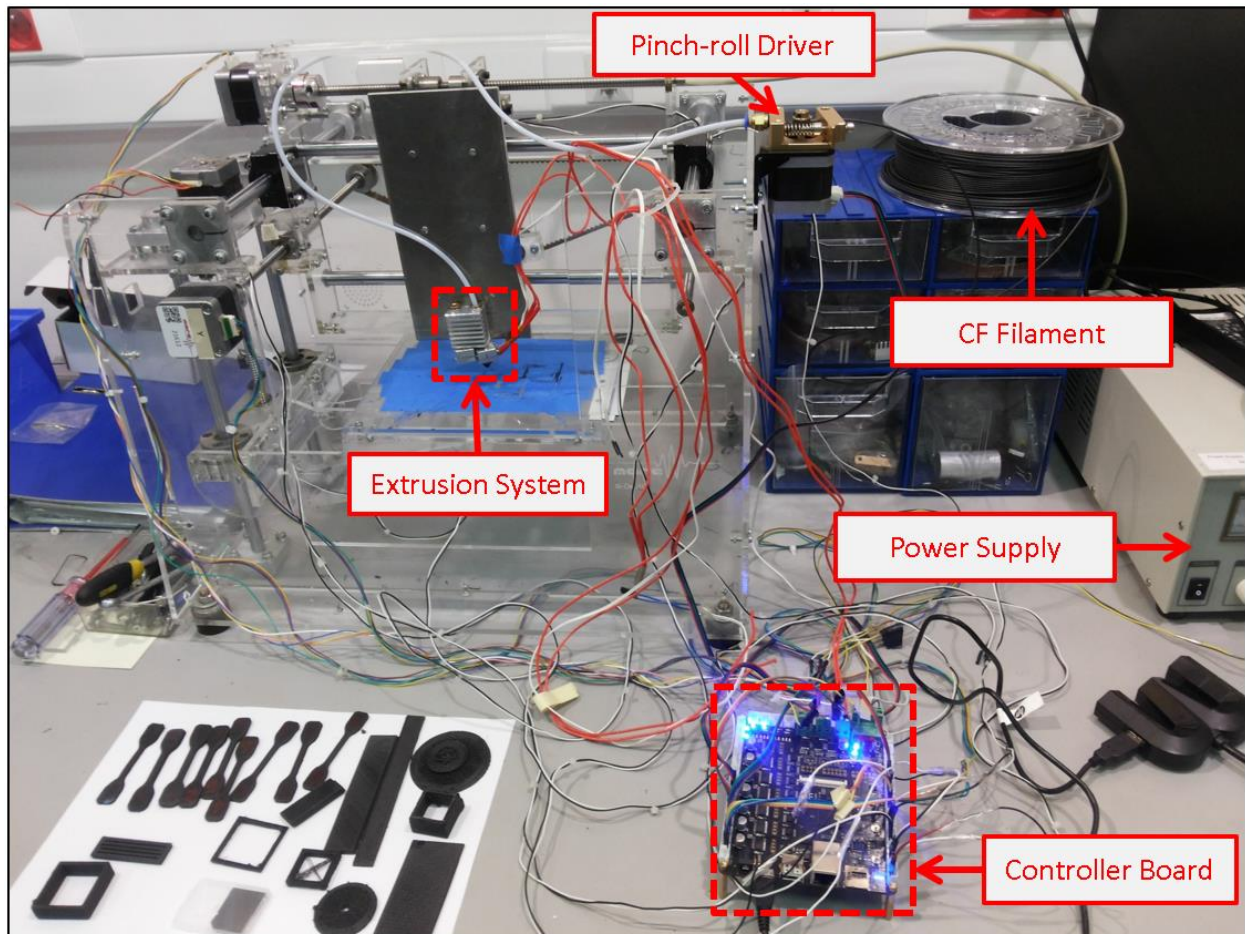


Figure 16: Modified AM equipment for fused filament fabrication showing important components

2.4.2 Composite production by AM

Carbon fiber is used to reinforce parts in the form of powder, chopped fiber or continuous fiber. Commercially, there are many continuous fiber preform as sheets and tapes made by braiding the fiber into woven structures. The length of the dispersed fiber significantly determines how the mechanical property of the resulting composite is enhanced. The theoretical strength expected from changing fiber length when perfect bond is assumed at the interface for some critical fiber lengths [43]. The reinforced strength seems to converge as the fiber length is increased. Particular to additive manufacturing, chopped fibers are added to a thermoplastic matrix to form filaments that enable fabrication of stronger parts. Various commercial filaments are sold with chopped fiber reinforcement. For this report, an Eastman co-polyester brand Amphora which is blended with small fibers by Colorfabb is used as filament. The filament named Colorfabb XT CF20 is loaded with no less than 20% carbon fiber.

Using the new extrusion head, composites of carbon fiber are produced on the cartesian 3D printer. The carbon fiber (CF) reinforced polymer needs to be characterized to assess the improvement in mechanical strength. Using a standard token dimension defined by DIN EN ISO 527-2 Type 5A, tensile strength is measured. The filament is made from PETG produced from pellets made by Eastman's Amphora co-polyester that was mixed and winded into filament by the company Colorfabb. Two versions, one having 20% volumetric carbon fiber content, are tested. The result of the tensile test along XY direction of 3D printing direction are shown in Figure 17.

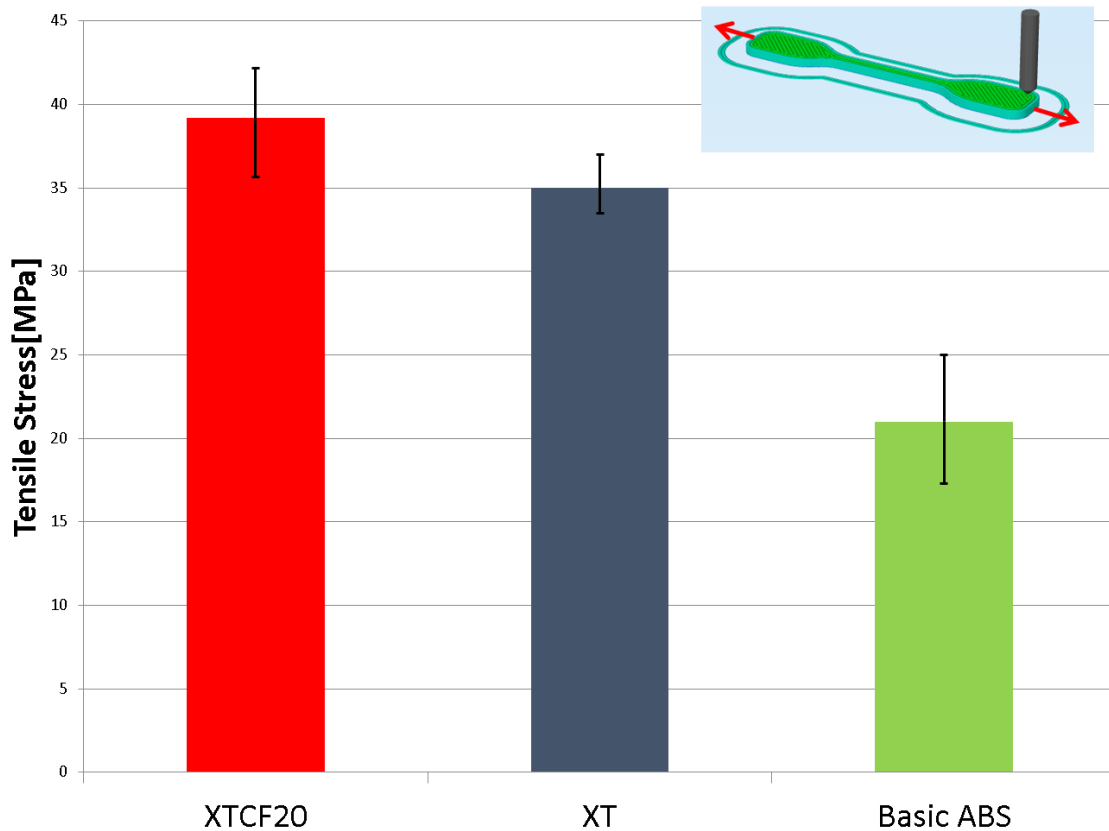


Figure 17: Tensile test results of fabricated PETG (XT) and composite (XTCF20) compared with ABS strength from literature [44–46]

The chopped carbon fibers tend to align with the deposition direction as shown in the microscopic image in Figure 18. The small improvement in tensile strength of the reinforced part sample is attributed to these fibers. The estimated fiber lengths are around 50 to 130 μm .

In general, the strength of the composite improves as the average fiber length is increased. The tensile modulus of the composite (E_m) is expected to conform to the rule of mixture where it is a superposition of the fiber and matrix modulus (E_f, E_m) in proportion of their volumetric content assuming there is a non-porous sample. $E_c = E_f v_f + E_m(1 - v_f)$, where v_f is the fiber volumetric content. As the fiber content gets high however, the tensile strength is found to decrease. As a result, most commercially available short fiber filaments are made with fiber content less than 30% due to a higher chance of clogging in the printing nozzle. Another reason why a higher volumetric ratio is avoided is because there is usually not enough thermoplastic resin to encapsulate the fibers.

In a more recent emergence, interest in embedding continuous fibers using AM techniques has surfaced through new startups and a couple of research papers. Continuous fibers provide the maximum possible reinforcement. A trademarked 3D printing filament with continuous fiber in the core has been developed by Markforged [47] to be used with their FFF 3D printers. Composites made using this printer have been shown rival aluminum parts in their specific strength[42]. A comprehensive investigation on literature work on fiber reinforced FDM can be found in the review paper by Brenken et. al [48].

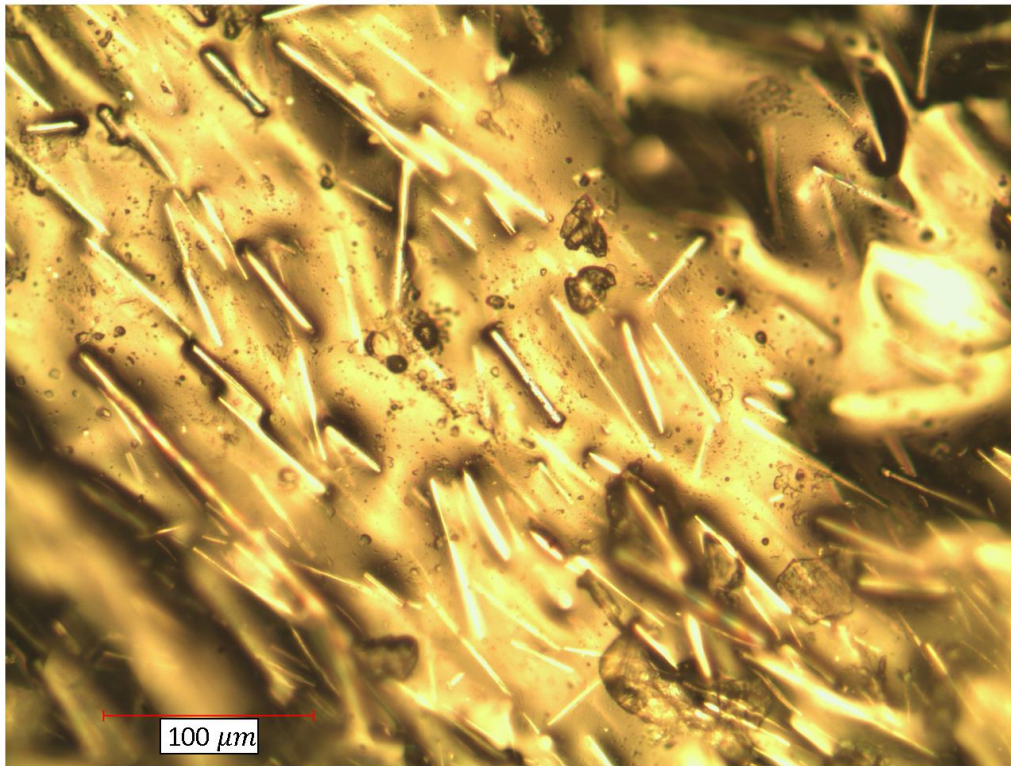


Figure 18: Microscopic image of chopped carbon fibers after deposition showing their alignment and length

The study of the fractured surface after destructive test usually reveals some information about the part. This fractography study is useful in understanding the dynamic behavior involved during breakage. For the tensile test coupons, the microscopic image of the fracture surface shows the pulling of fibers from the polymeric matrix, hence the holes in Figure 19. This indicates that most of the load applied is carried by the matrix rather than the stronger fibers.

Apart from the need for longer fibers, it should be noted that when the tensile test is carried out on a coupon that is aligned with the Z-direction of 3D printing the tensile strength is very weak. This shows the weak point of fiber reinforcement where strength cannot be tailored in a particular direction on the AM machine. The interest in application of new manufacturing innovation in composite fabrication has led to multi-national projects like the Directional Composites through manufacturing Innovation (DiCoMI) project[49]. With the inspiration of tailoring local structural and physical properties, this study looked into possibilities of applying multi-axis AM in fabrication of parts.

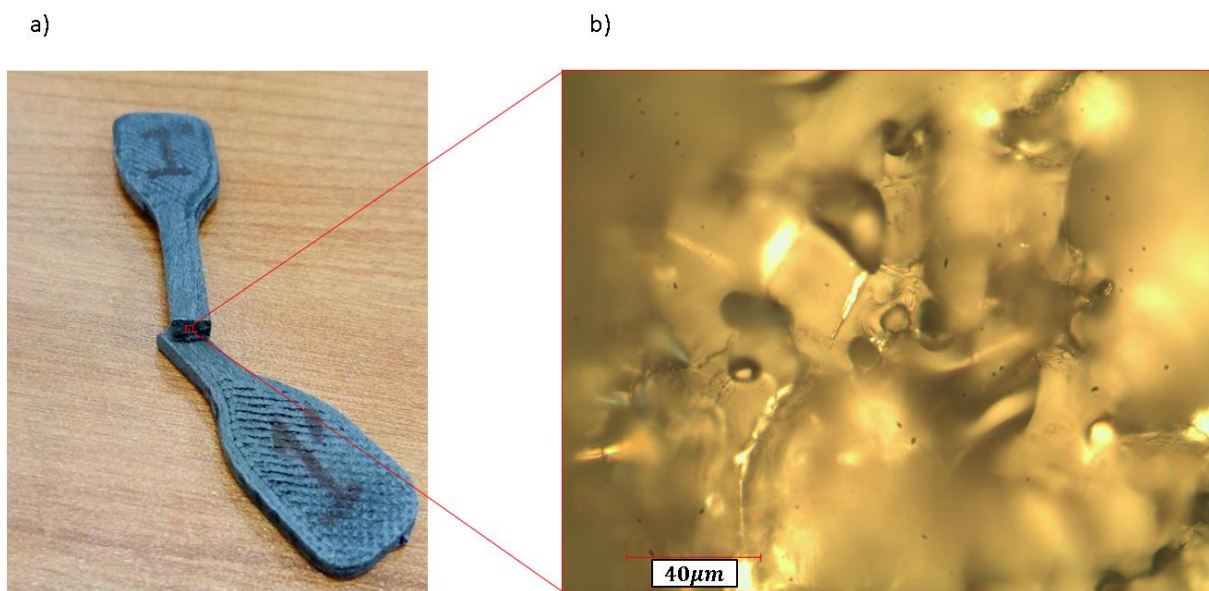


Figure 19: Fractography of broken surface of tensile-test coupon

Despite the bendable build plate of the machine, the following sample parts are fabricated with CF reinforcement. An airfoil and sample impeller were tested using the AM setup.



Figure 20: Sample parts fabricated with chopped fiber composite

Chapter 3

MULTI-AXIS ADDITIVE MANUFACTURING USING EXISTING PROCESSES

Multi-axis manufacturing which is popular in machining literature, generally refers to manufacturing process done with more degree(s) of freedom(s) in addition to the native spatial three axis in machining centers. For machining systems, the flexibility of multi-axis machines is exploited in production of more complex free-form parts and in improvement of overall machining efficiency of parts. The growth in interest and application of it has led to wide research in four(five)-axis machining [50] and existence of several commercial multi-axis machining centers. On the contrary, most additive manufacturing (AM) is carried out using 3-axis of movement leaving multi-axis AM in adequately studied. This is the case for major AM methods, such as fused deposition modeling (FDM) and selective laser sintering (SLS). Even though AM is known for its ability to fabricate complex geometries, many AM methods are constrained by the need for a support beneath each layer [51]. Consequently, in most AM part manufacturing planning, overhangs are supported by an additional support structure which negatively affects production time, labor and part quality [52].

Analogous to how the extension of axes of motion in machining can enhanced the machining process, AM can also benefit from multi-axis promotion to mitigate some of its inherent limitations. Despite being in its primitive stage, multi-axis additive manufacturing (MAAM) is shown to eliminate the need for support structures and improve part strength and surface quality [53]. Due to the anisotropic property of parts manufactured by AM [45], with the weakest direction being along the build direction [54], the possibility of varying the build direction within a part can go long way in strength improvement of the part. With the flexibility offered by variable build direction in MAAM, the part strength can be tailored to substantially improve the load bearing capacity of the part [55].

Section 3.1 and 3.2 cover design of a MAAM system and its control. Section 3.3 introduction manufacturing of parts using the multi-axis machine. Work on fabrication of simple parts without the need for support structure is discussed in Section 3.4. The work on analysis of overhang structures and fabrication of freeform overhangs previously published in proceedings of Solid Freeform Fabrication is discussed in Section 3.5 [56].

3.1 Mechanical Design of Multi-axis AM System

Initially, parts were manufactured using a Cartesian 3D printer used for scaffold manufacturing as mentioned in Chapter 2. The need for a new design of AM device was realized immediately. Apart from the structural and mechanical issues, addition of two extra degrees of freedom served as the reason for the new design. From available open source architecture of 3D printers, the Cartesian and delta designs were considered. A multi-axis Cartesian system was found to be bulky and composed of many connecting members. This is due to the commonly movable build platform and lack of space for addition of additional moving components. As a result, the delta type design was selected as starting basis for the five-axis machine. Delta design has a fixed build plate which is suitable for addition of multi-directionality. The delta design can achieve faster linear motions and maneuverability than traditional designs [57]. The actuators in Delta design are usually similar and the positioning method is more suitable for 3D curves. Cartesian design, on the other hand, usually has faster X and Y motion with slower Z motion making it particularly featured for horizontal motion. The common target speed for AM is between 20 to 100 mm/s with build volume that can contain a cube of length 100 mm.

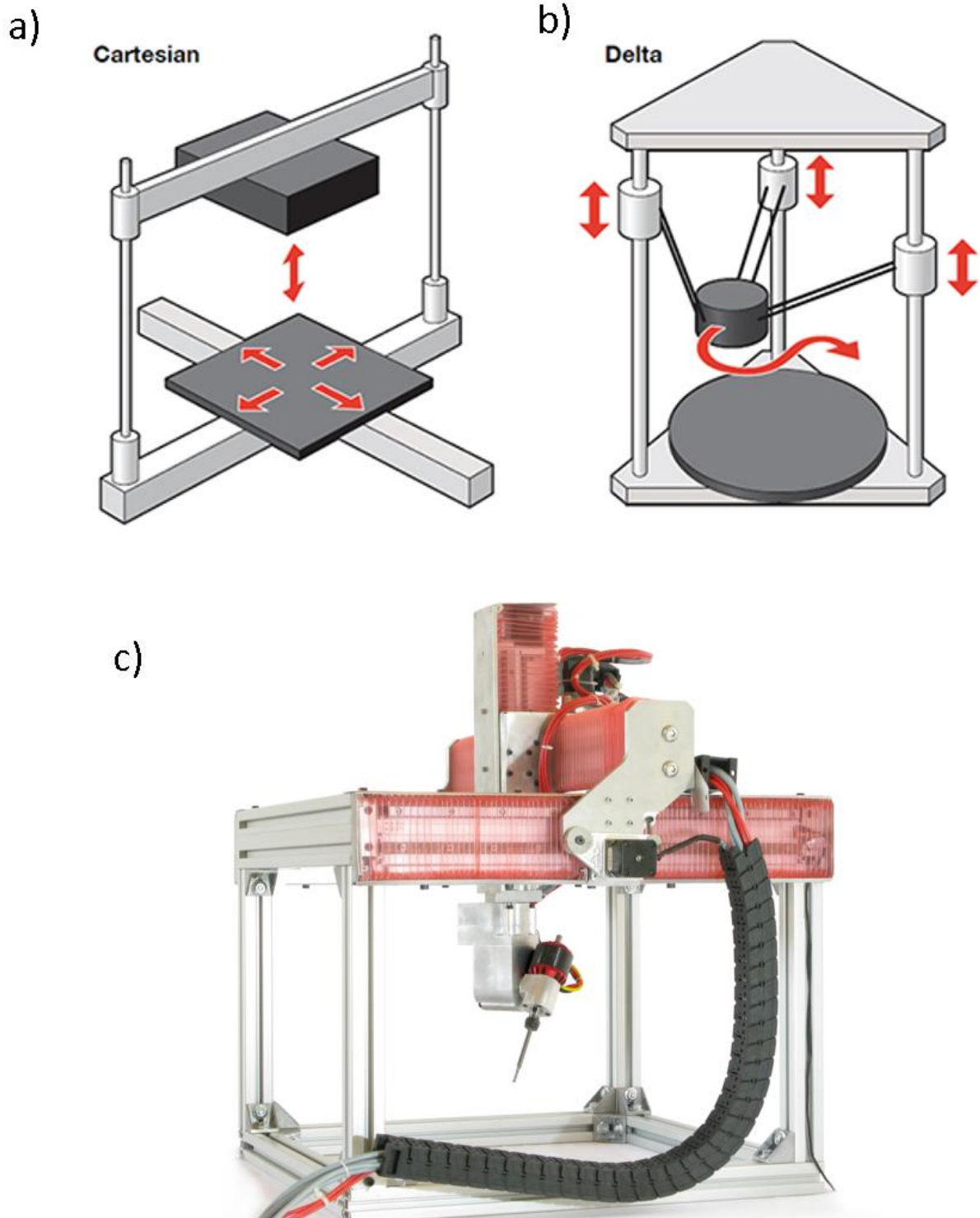


Figure 21: Cartesian and Delta designs of AM Systems in a) and b) respectively [58]. 2D print-head used in commercial machine[59]

The needed degrees of freedom could be attached to extrusion head or the base. In other words, either the tool is given additional axis of motion or the otherwise rigid base is made to rotate. It can be observed that positional freedom is already achieved in 3D printing, but rotational motions are restricted. To avoid adding load to the delta arm, two rotational motions are introduced to the base plate. In the other case, the added rotational motions can be given to the print-head instead of the print platform as shown in the commercial gantry in Figure 21c. Decision on adding motion to the platform rather than the print-head is based on both simplicity [57] and concern of added load on the parallel arms. Besides, keeping the nozzle aligned with gravitational acceleration assists in material deposition.

After several considerations on application, manufacturing and feasibility, the following design having movable build is suggested for the two degree of freedom requirement.

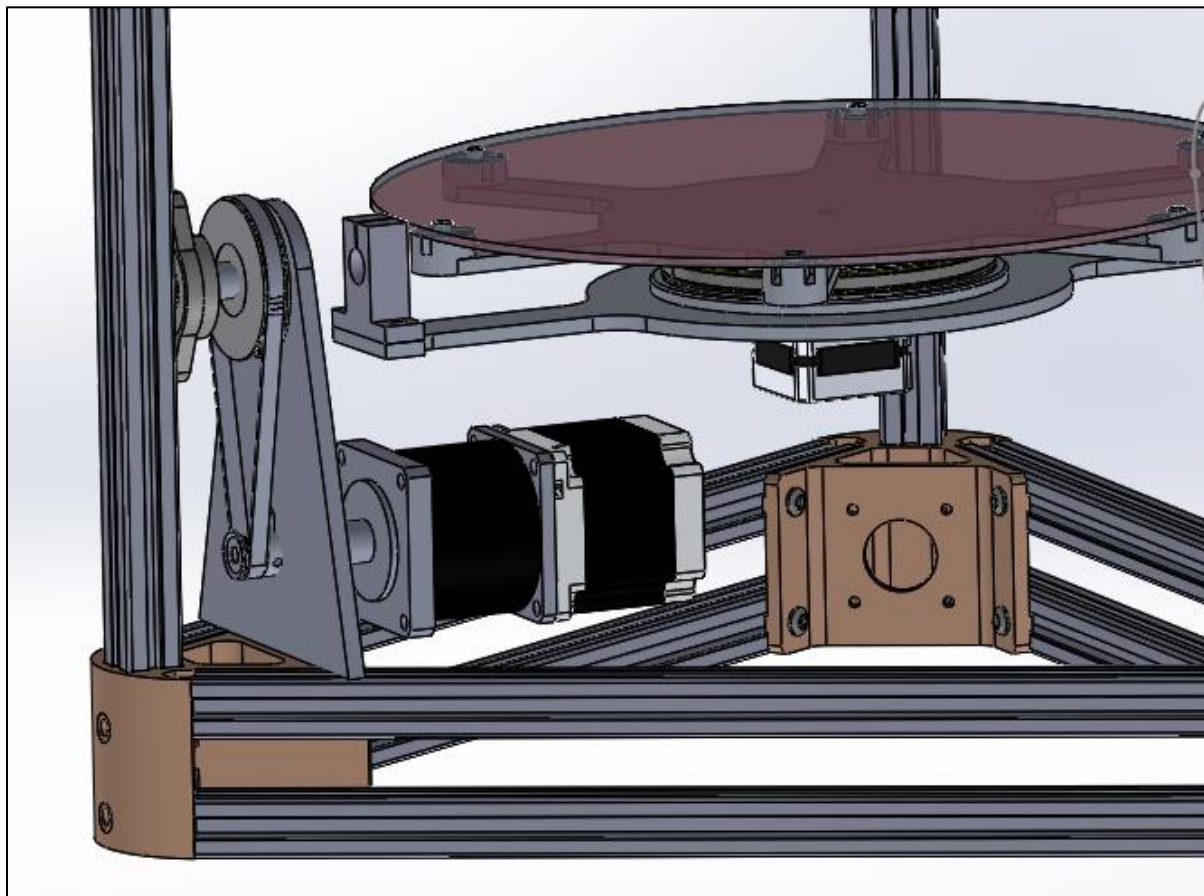


Figure 22: Design of 2-degree-of-freedom rotation base added to Delta design

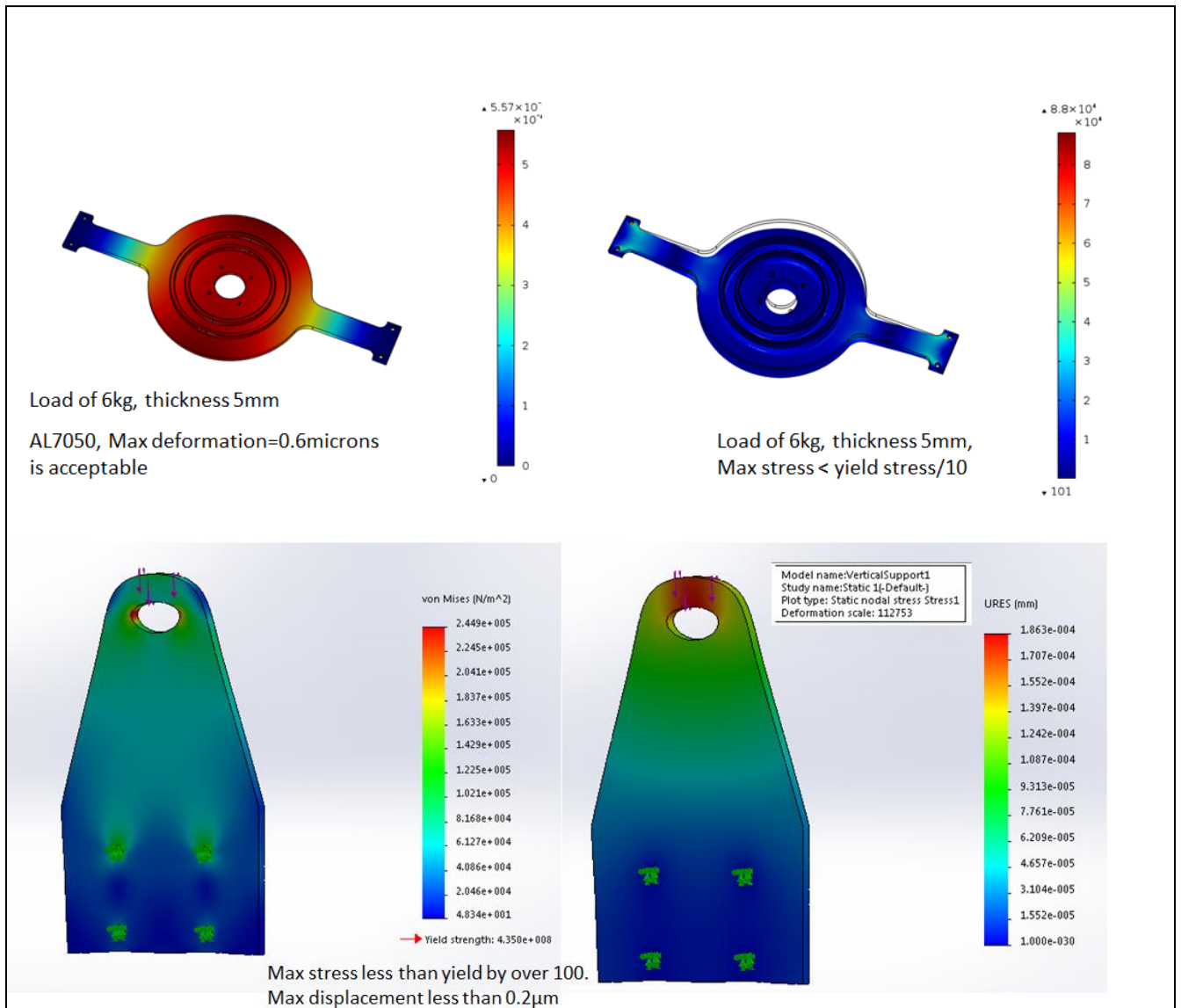


Figure 23: Static FEM stress analysis of supporting structural components

A planetary gearbox attached to 3Nm stepper motor with backlash less than 0.25° powers the tilting of the base. As for the azimuthal axis, a 1.2Nm stepper is used connected to a thrust bearing which supports the build plate. Static analysis was carried out by finite element analysis on critical components for dimensional decisions. With a load of 6 kg (The maximum weight of 3D printed object is rated to be 4kg) on the build plate, the stress and deformations of the support structures are checked using stationary analysis in COMSOL multi-physics. The results are shown

in Figure 23. Fine meshes are used with the assumed fixed boundary condition at the location of integration with the system.

The base, build plate, and vertical supports in Figure 24 are manufactured from aluminum 7075 using CNC milling machine center. The detailed manufacturing process of the parts are carried out in Unigraphics CAD/CAM environment. Frame is made from aluminum profile and parallel arms are cut from carbon fiber tubes. The complete design of the printer is shown in Figure 25 below.

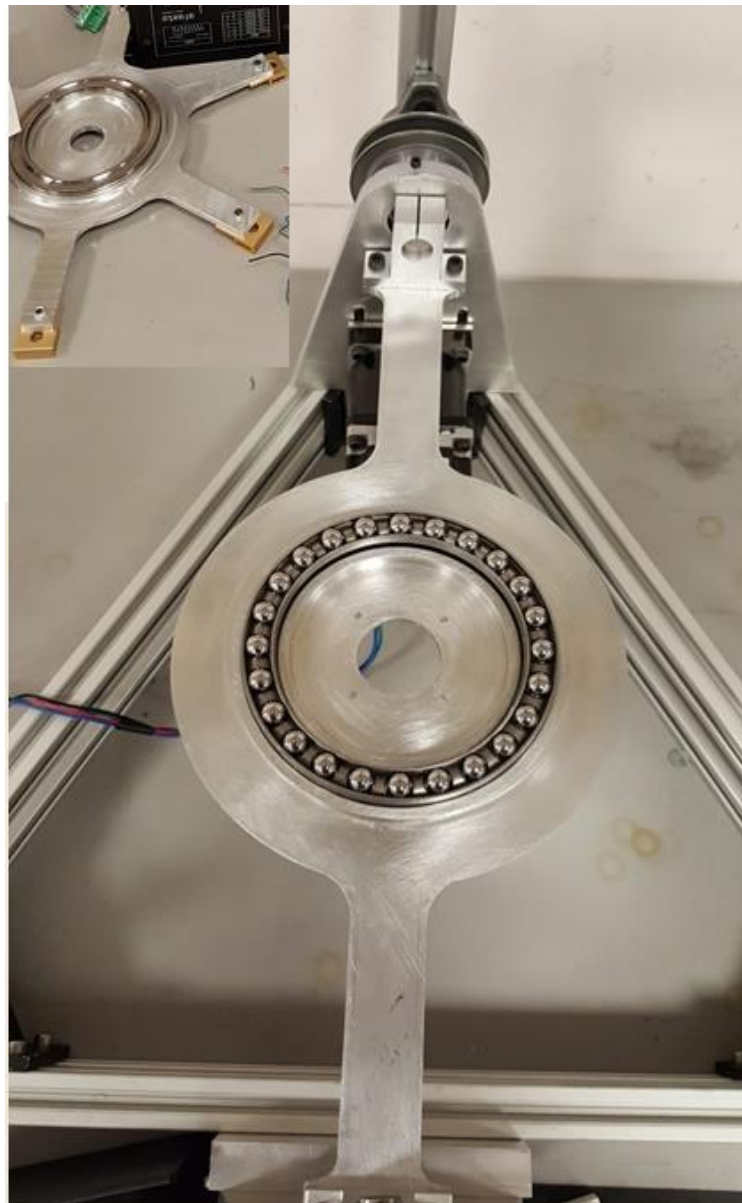


Figure 24: Manufactured table base, build support and complete design of the 5-axis 3D printer

Delta type 3D printers, along with other common 3D printing designs, are capable of manipulating 3D printing nozzle only in the translational axes X, Y and Z. The build direction which is along the nozzle deposition direction is usually fixed in the Z direction for such 3-axis systems. Confined by the constant build direction, the scope of AM is diminished to the incorporation of only Z planar deposition paths. In this study, a 3D printer inspired by the described delta-type concept is designed with two additional degrees of freedom resulting from the rotation and tilting of the print-bed, as shown in Figure 25. The print-bed rotation about C axis is controlled by the motor attached to the base of the bed platform. The second rotation, about B axis, permits tilting of the whole print-bed via a belt that is linked with a planetary geared motor. The designed printer has a cylindrical working space of about 210mm diameter and 200mm height.

Expansion of 3D printing tool movement with respect to the workpiece beyond 3-axis unleashes new possibilities in toolpath design. In literature, 5-axis AM system with two additional rotational have been tested. Yerazunis et al. [55] added an AB type rotary table to a 3D printer where manufacturing of hemispherical pressure cap is studied. Shen et al. [60] utilized an interference-free nozzle in 5-axis AM to test surface guided offset toolpaths for different modes of 3D printing.

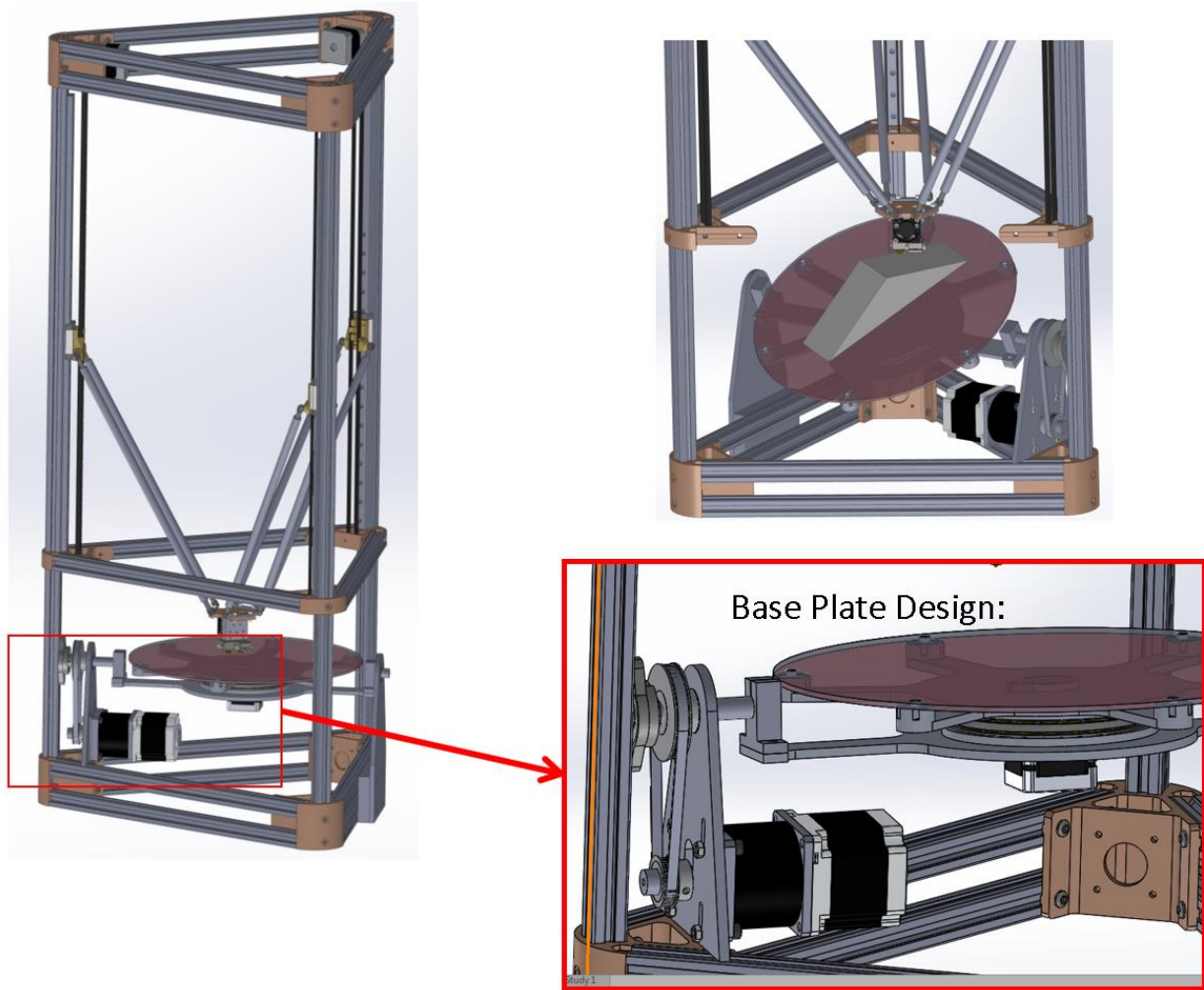


Figure 25: 5-axis 3D printer design showing the function of the two-dimensional build platform

3.2 G-code interpreter

From the open source GRBL project of CNC G-code interpreter in 2011, the open source community has developed a firmware called Marlin that works with many 3D printers and control boards. Communication is established via serial port protocol and commands are sent from any applications that support serial communication. The commands are in the form of G-codes and control position, temperature, end-stops, feed and filament extrusion. These are processed by a microcontroller like Atmel atmega2560.

Marlin firmware accepts G-code commands, parses them and stores them in a command buffer. Each command in the buffer is redirected to subroutines that handle the G-code. For the new device

created, new G-codes routines are added to the module. “G6” and “G7” commands are accepted, parsed and stored to the buffer. G6 commands takes rotation values of the base table together with amount of filament extrusion. G7 accepts all the 6 motor commands and redirects them to G1 and G6 commands. How the motors are driven is controlled by stepper planer where a trapezoidal acceleration profile is found for a given feed rate.

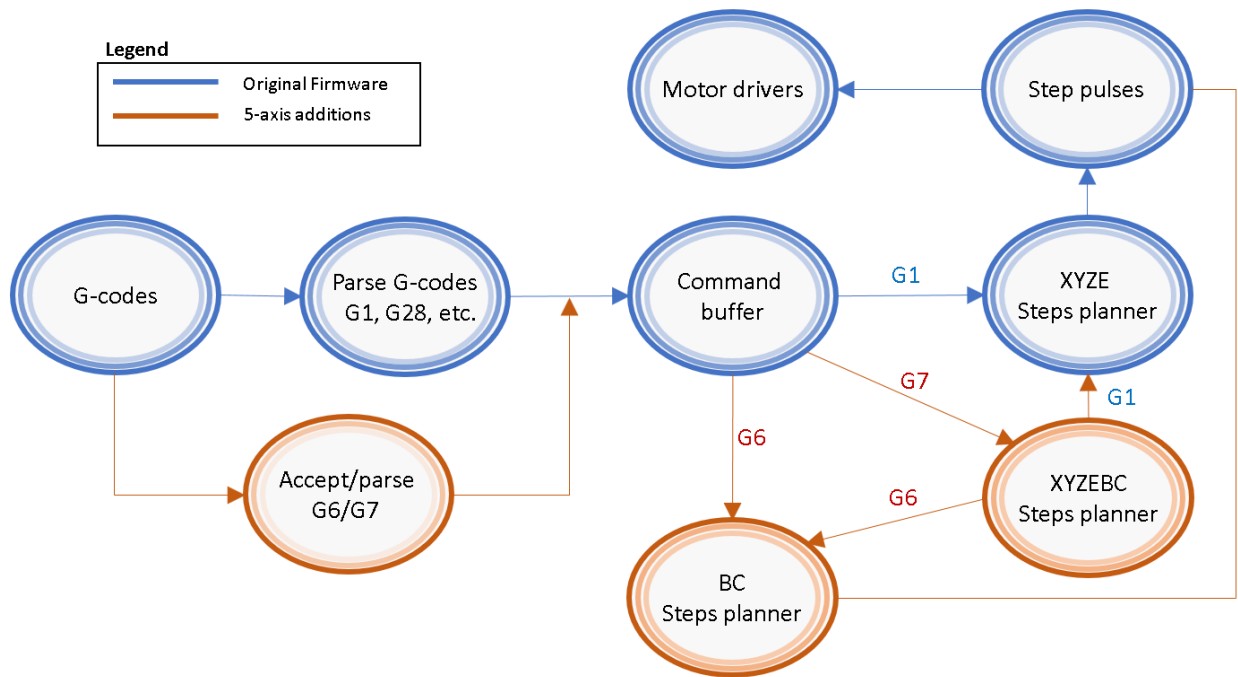


Figure 26: Data flow of Marlin firmware G-code interpreter with added functions

Having designed and assembled the 3D printer, it is necessary to control the motion of the nozzle and print-bed. Just like in computer numerical control (CNC) systems, there is need for a central control unit, where all the actuation and sensory signals are processed. In 3D printing jargon, the control unit is synonymous to a microprocessor board with an installed compatible firmware software. ATmega2560 microprocessor loaded with a designed software based on the opensource framework, Marlin firmware [61], is used in this work. Since the original firmware only supports 3-axis 3D printers, new submodules are programmed to extend it to support 5-axis functions. Figure 26 shows the simplified data flow in the control unit. The commands are classified and added to the command buffer for queuing and redirection to the motion planner. The motion planner mixes the required motion steps of each motor smoothly and the pulse signals are

sent to the motor drivers. New G-code commands, G6 and G7, are introduced to handle 2D rotation of the build platform. The control unit supports only positional and orientational commands in the joint space of the machine. Therefore, the required transformation of 3D printing path is carried out in the post-processing stage (before generation of the G-codes) because the control unit cannot handle complex calculations with the required speed. More details on the computer-aided manufacturing and post-processing are provided in Chapter 4.

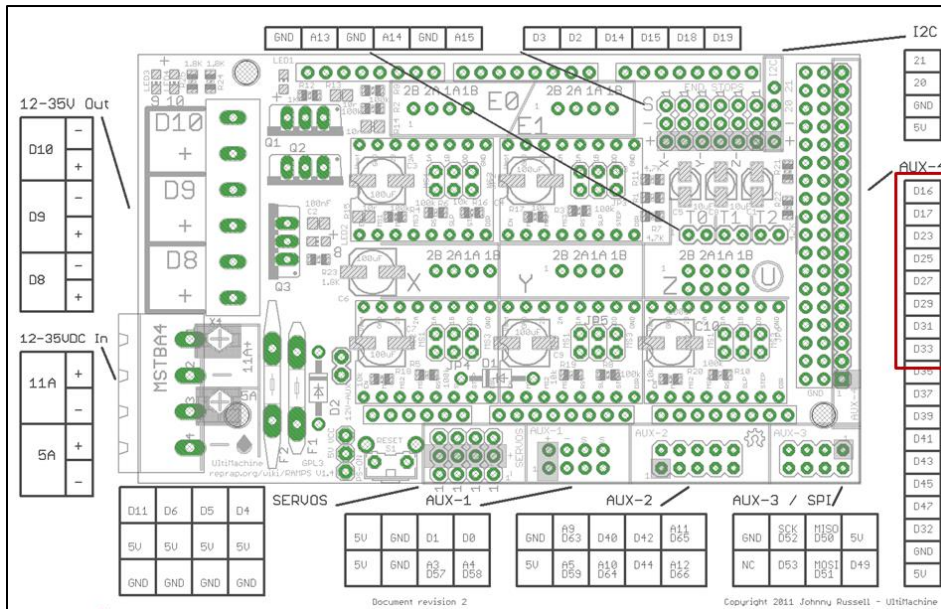


Figure 27: Schematic diagram of electronic board showing pins used to control additional motors [62]

RepRap Arduino Mega shield is used as a control board where auxiliary pins for LCD screen are used to control the two additional motors. The connection points with the motor drivers and sensors are given in Figure 28. For most of the additive manufacturing tasks, G-codes are generated from Rhinoceros CAD software where an AM plugin is designed to process digital models and provide path files. The details on path planning is covered in Chapter 4.

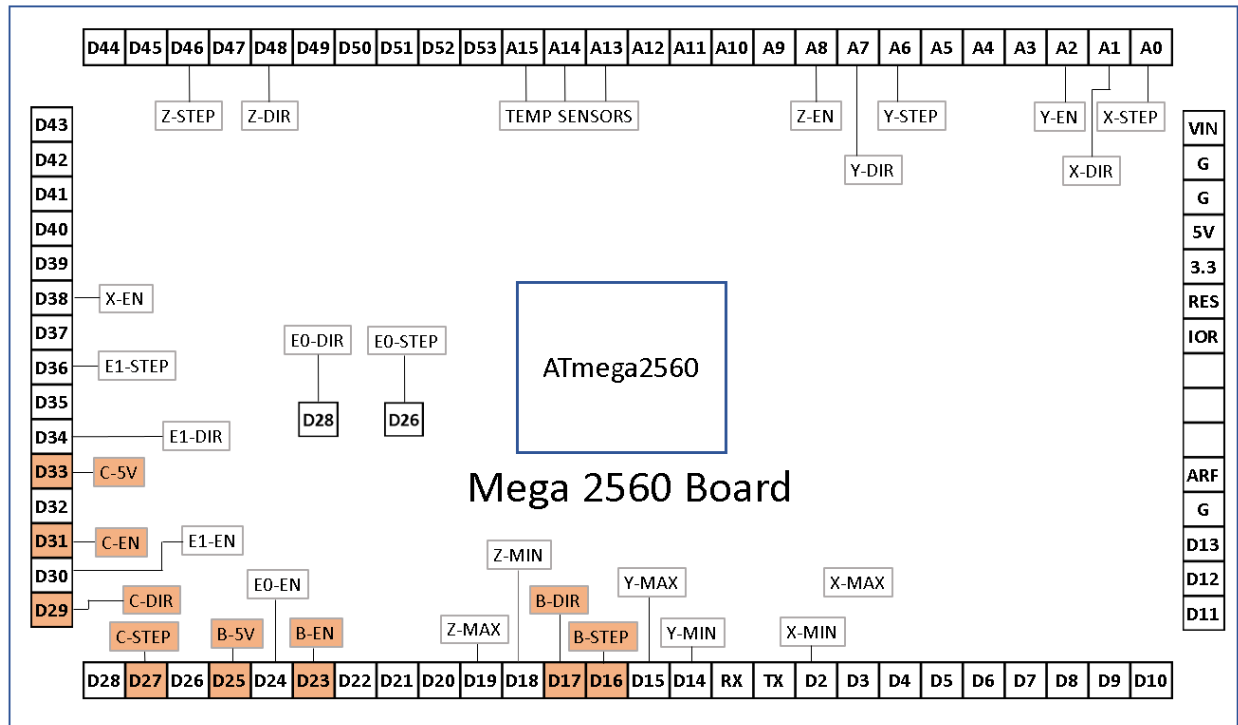


Figure 28: Microcontroller connection terminal pins of sensors and actuators

3.3 Multi-axis Additive Manufacturing

The traditional 3D printing can only deposit material onto a plane with the same axis along the tool. With the 5-axis additive device, the part being manufactured can be oriented and materials can be deposited in other configurations. Some of the advantages of multi-axis additive manufacturing are explored by manufacturing simple parts shown in this section. Features of multi-axis AM such as the ability to print on multiple planes, on freeform surfaces and 3D print of bend parts without supports are demonstrated in each figure.

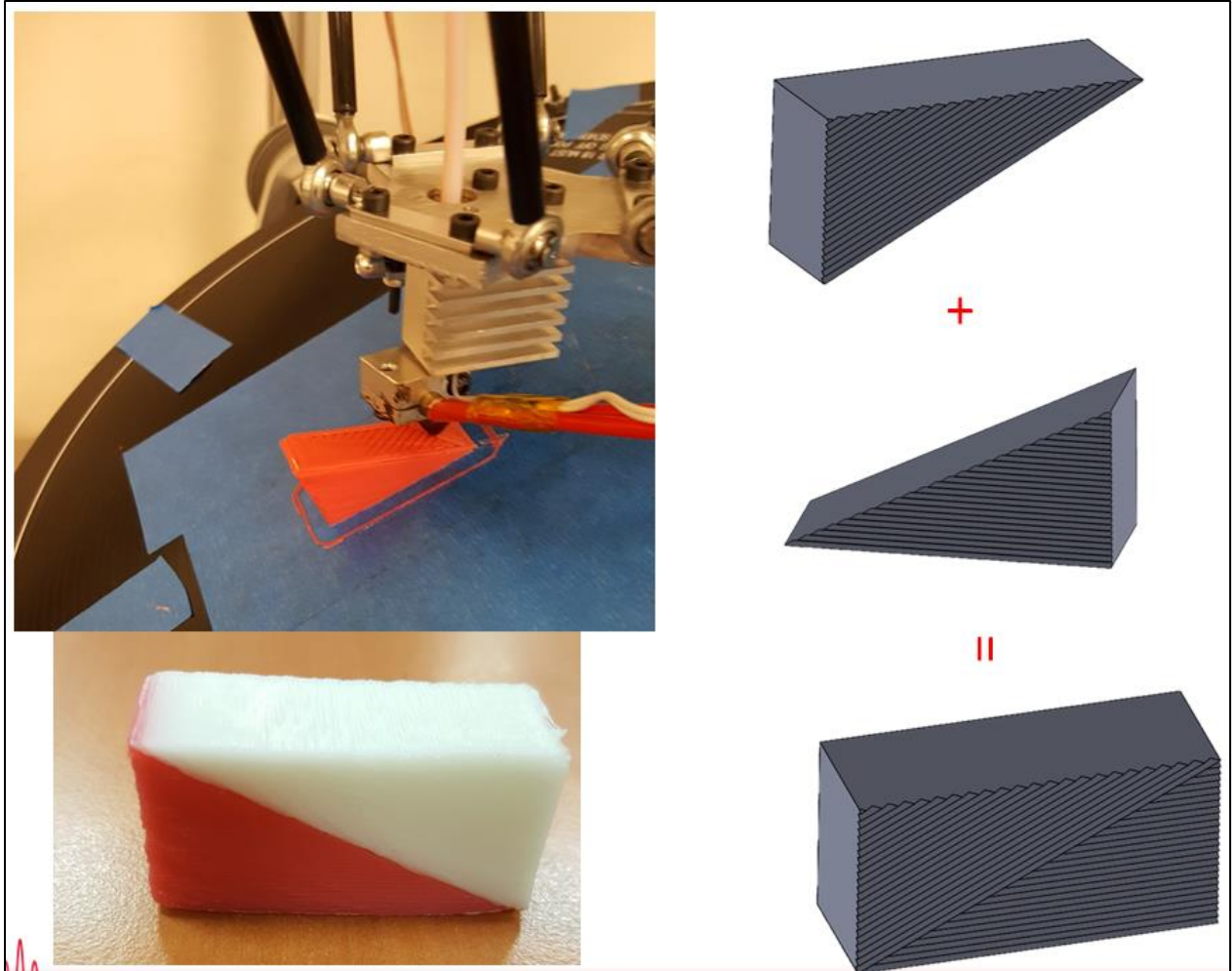


Figure 29: Manufacturing of a solid cuboid using two different build directions

Figure 29 shows the ability to produce parts on different build directions. Another simple demonstration of the MAAM is in its application in fabrication of overhang parts. The part shown in Figure 30 will normally require support, but since the build direction is variable, it can be produced directly.

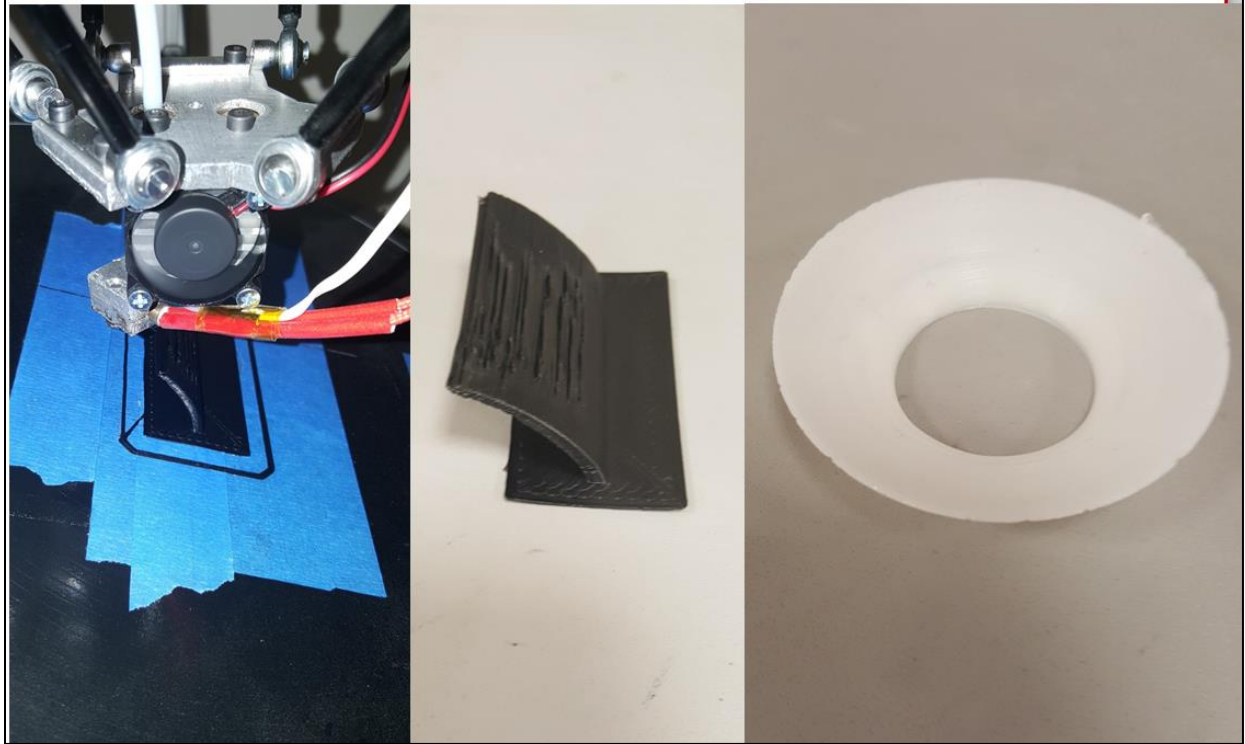


Figure 30: Additive manufacturing of protruding components without the use of supports

For a complete MAAM system, it is required to construct the 3D printer, evaluate its kinematics, program the numerical controller to listen and interpret commands, and finally design the path planner. Each of the mentioned requirements can be set out as an individual scope of research. The 3D printer used in this work is designed to perform fused deposition AM process, depicted in Figure 31. As shown in Figure 32, the gantry that carry the deposition print-head is constructed from RepRap Delta design concept[63] with the addition of tilting and rotation of the build platform. Additional details on the specific computer-aided design, kinematics and controller are discussed in Chapter 4. This chapter will concentrate on how the MAAM 3D printer can be used in manufacturing specific parts that cannot be produced on normal planar 3D printers without support structures.

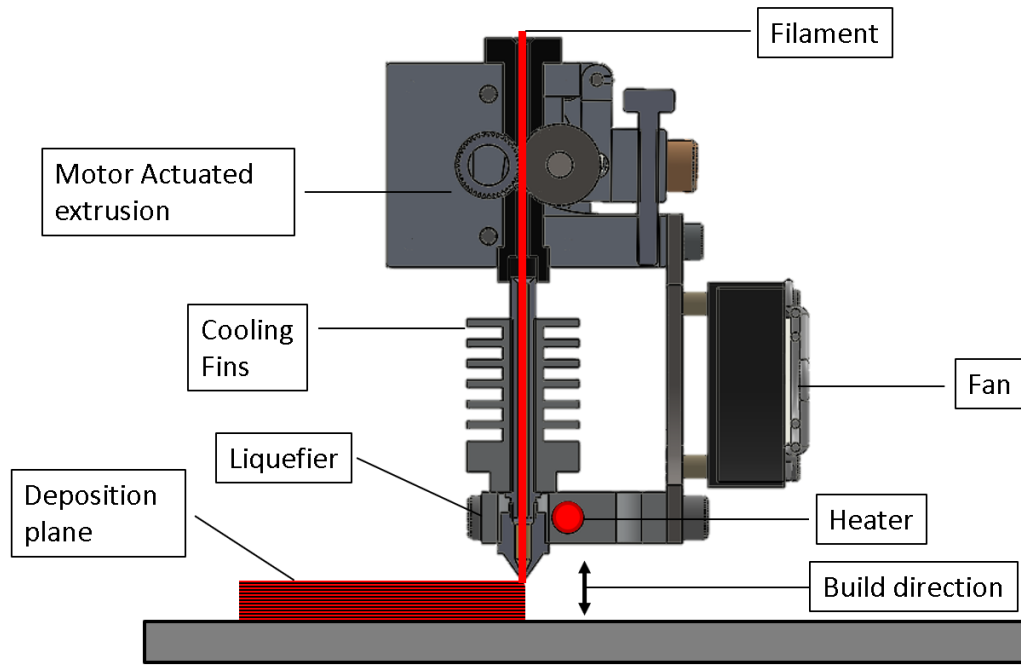


Figure 31: Fused deposition modeling print-head showing the build direction and plane

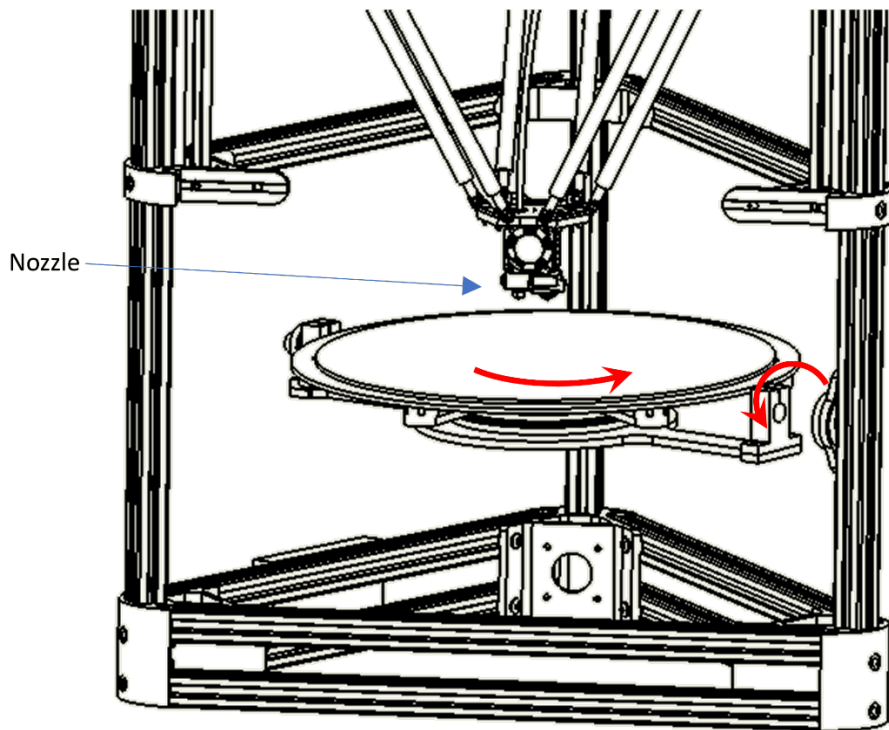


Figure 32: Demonstration of multi-axis AM using two build directions

During planar AM, the boundaries of successive layers do not have to be precisely vertically aligned. Depending on the layer spacing and the wall thickness, it is possible for the boundaries to slant away from the vertical to some extent. This slant angle popularly termed overhang angle is critical for a successful AM process. For both FDM and SLS, a typical overhang angle not exceeding 45° is usually permissible[45,64,65]. Support structures are usually generated before or during slicing of parts. Regions on the part that protrude by an angle greater than the critical overhang angle must therefore be supported.

For the Subsections 3.4 and 3.5, ways of fabricating parts with changing build direction will be investigated. Simple parts whose path can be formulated easily are demonstrated in Section 3.4. Section 3.5 looks into the fabrication and analysis of overhang structures. The complete process of fabricating freeform models using 3D curves will be discussed the next chapter.

3.4 Simple Path Generation Methods for Multi-Axis AM

It should be noted that the simple paths do not provide a solution to Multi-Axis process planning and a more general solution is necessary. All the parts manufactured using the 5-axis AM in this section (Section 3.4) are planned were planned manually using MATLAB where 3D line segments are generated and written into G-code command files. The final geometry is not known nor defined initially. This method is time consuming and almost impossible for complex parts. There is a need for a path planar that generates 3D curve paths that when followed through can produce a known CAD file. For traditional planar 3D printing, slicing is done obtain intersection of STL files with XY planes at z-positions as shown in Figure 33.

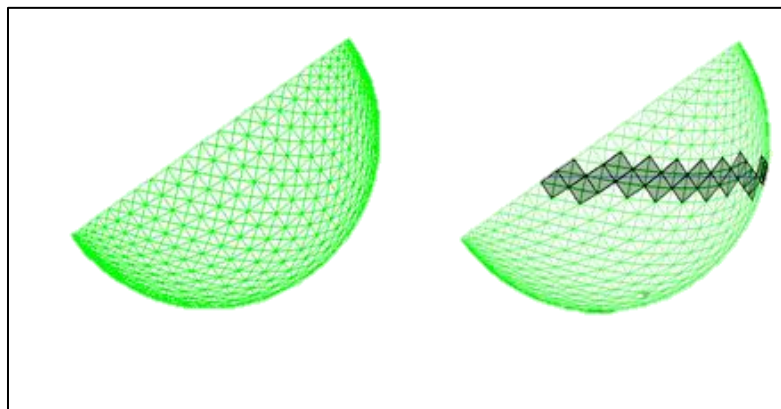


Figure 33: Slicing using intersection of part and z-plane

3D paths can be obtained based on the final surface form of the part. The paths can be designed to follow paths that ensure that the final deposition on the surface is normal to the path. An idea on how this kind of path should be is provided in Figure 34. This minimizes discontinuities on the final part surface and eliminates staircase effect.

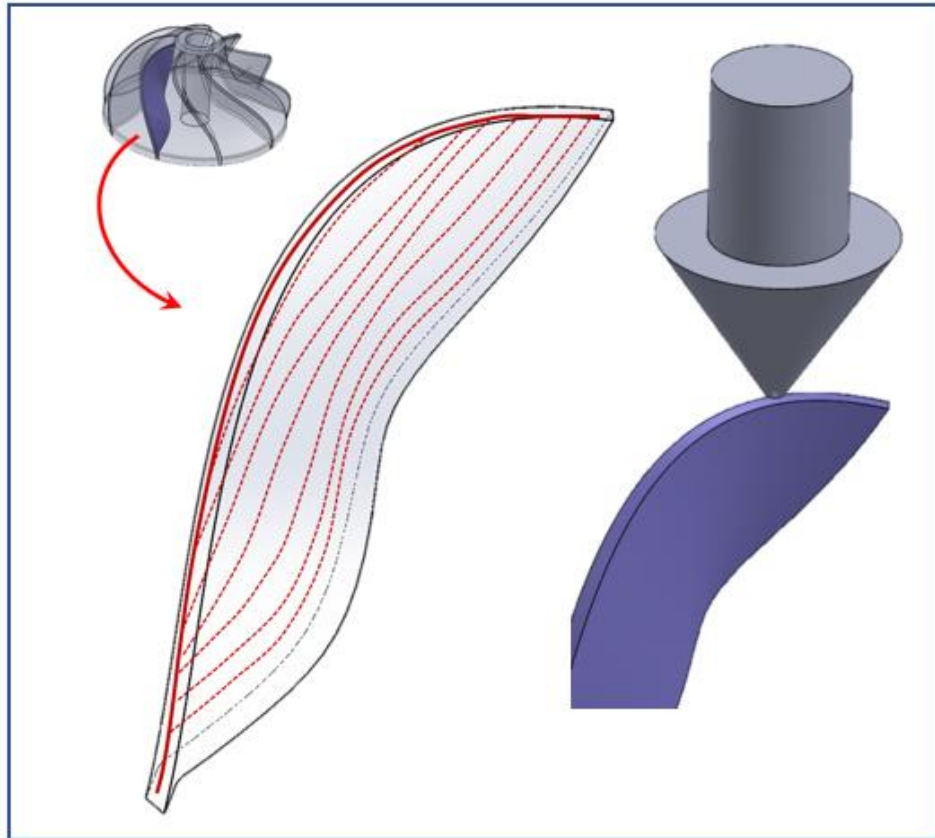


Figure 34: Demonstration of the goal of Multi-Axis AM

This section discusses strategies that can be used to apply simple paths to fabricate parts using the designed Multi-Axis AM system. By combining pre-existing methods and using simple intuitive patterns of toolpath, the capacity of MAAM is studied.

3.4.1 Planar Slicing of By Part Decomposition

The usual fused deposition AM can only eject molten filament in a uniaxial direction, leading to parallel deposition planes. The 3D printing paths are therefore in a stack of parallel layers that are generated by planar slicers[66]. In this section, the ability of MAAM to produce a part using more than one build direction is demonstrated using a part that is divided into two and sliced with the usual slicer. A diagonally split cuboid is sliced horizontally at the lower portion while the top part is sliced diagonally. While the first part is 3D printed with zero tilt, the second is manufactured on the first part at a tilt angle of 26.57° when the diagonal surface becomes perpendicular to the build direction as shown in Figure 35.

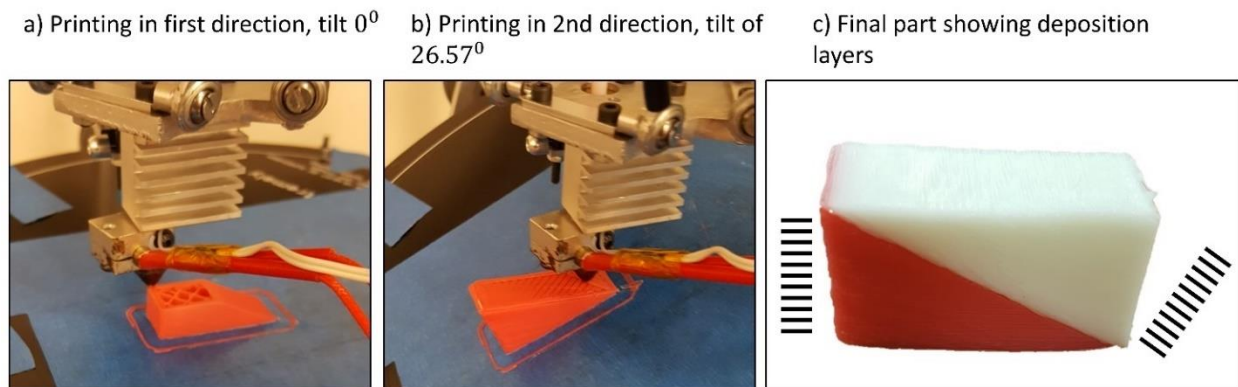


Figure 35: Demonstration of multi-axis AM using two build directions

Using the same rationale mentioned above, it is possible to fabricate parts that will usually require support such as the part shown in Figure 36a without any support. The part to be fabricated needs to be dissected into smaller parts, where each of the trimming planes serves as a build direction. With respect to each of the build directions, there should not be any overhang exceeding the critical overhang angle in each of the divided parts.

To avoid using the supports shown in Figure 36, the part is divided into 5 regions. Each of the region is to be fabricated in a suitable build direction—which must start from the build platform direction. The subdivided parts must be transformed in such a way that the initial plane coincides with the horizontal plane of the slicer. Popular open-source slicers such as Cura, Skeinforge and

Slic3r can generate support structures together with the complete planar path for a tessellated model in STL format. Using such slicers, the 3D printing path of each division can be found. If the division is done right, there should be no necessity of support when slicing each subdivision. Finally, using the path, each region should be 3D printed at the determined build directions. The process of MAAM using slicers is summarized in Figure 37.

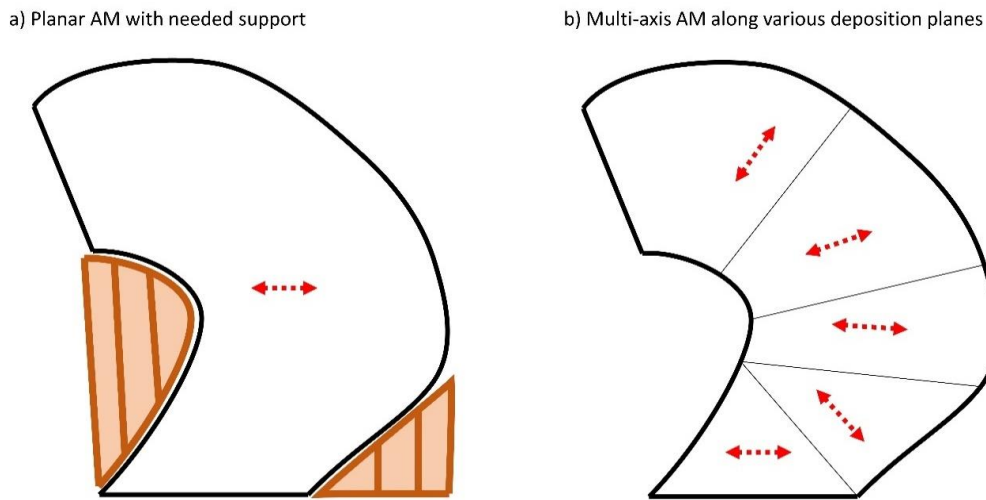


Figure 36: Illustration of how MAAM can be used with planar slicers to 3D-print without supports

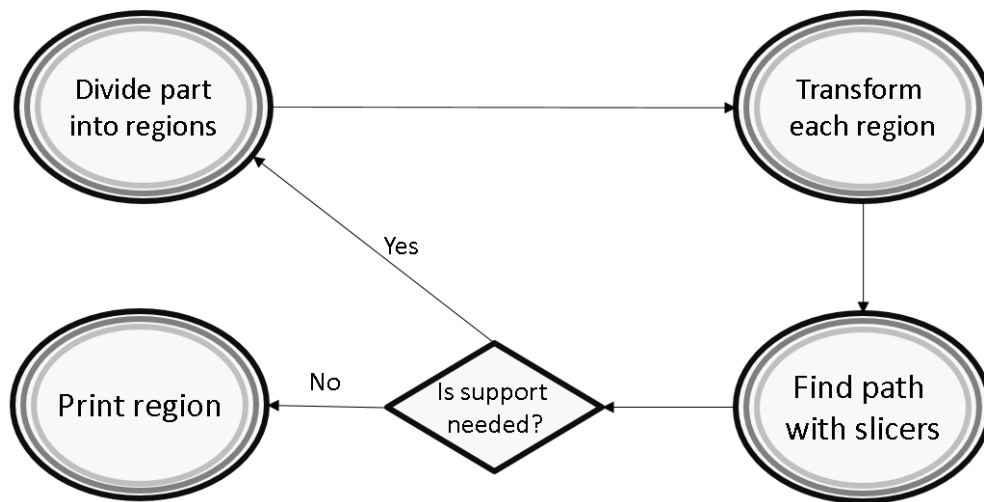


Figure 37: MAAM process using planar slicers on divided parts

3.4.2 Application in Roofing Without Support

In this section, a method of adding a roof over an open 3D printed part will be discussed. Laying such roof is not possible on planar AM because the overhang angle of a typical roof is around 90°. However, when the open part is tilted by some angle, it becomes possible to incrementally fabricate the roof component at an overhang angle that is less than the critical overhang angle.

It should be noted that in some cases, even for planar AM, it is possible to 3D print at an angle greater than the critical angle. When the gap between two vertical pillars is only a few centimeters, a bridging process where small horizontal overhangs are created without support is possible [67]. It is therefore possible to carry out a roofing process in planar AM if the opening is small. However, for a part with significant size, obtaining good outcome without support requires a multi-axis method.

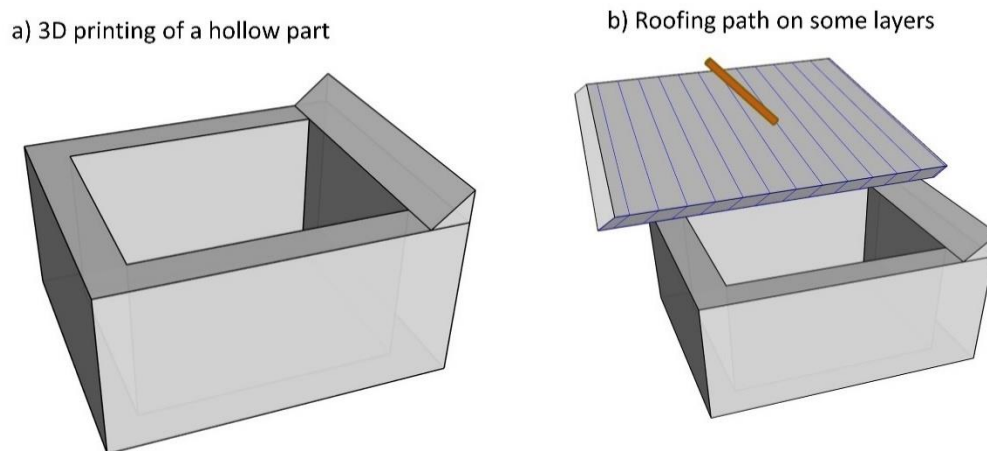


Figure 38: a) An open cuboid to be covered b) and the path of the roofing operation for some layers with build direction shown

The roofing strategy requires the lid to be separated from the part as illustrated in Figure 38. A prescribed tilt angle of the print platform should be chosen such that the already manufactured portion will not collide with print-head during manufacturing. The roofing process

starts by using one side of the hole as start layer. Adding a small wedge at one side of the hole is found to improve the first layer deposition. The whole process is summarized in Figure 39.

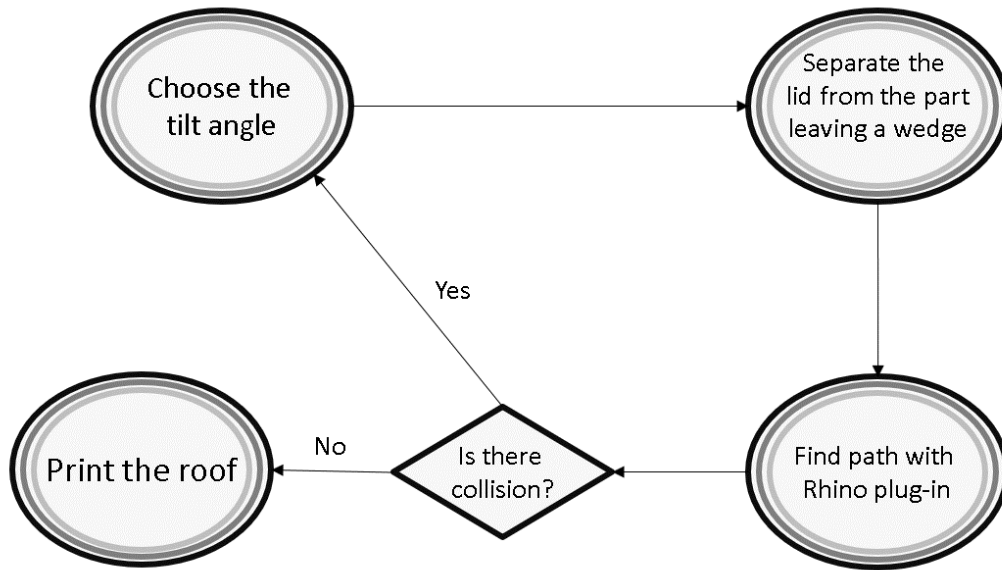


Figure 39: The roofing process with collision detection

With the aid of Rhinoceros® CAD software, geometric data of the roof is used in a programmed plugin script to plan the path of the AM. Using this path along with the given tilt angle, g-code is generated in the plugin script. The path starts from a layer that is on the wedge surface as shown in Figure 40. Subsequent layers are then added until the roof structure is complete. It is found that decreasing the speed of deposition, especially around the edges, helps in ensuring better binding with hollow part.

If the roofing specimen is fabricated using a planar slicer, the interior of the part will require support structure like the one shown in Figure 41. The proposed roofing method makes it possible to manufacture the part without the additional structures.

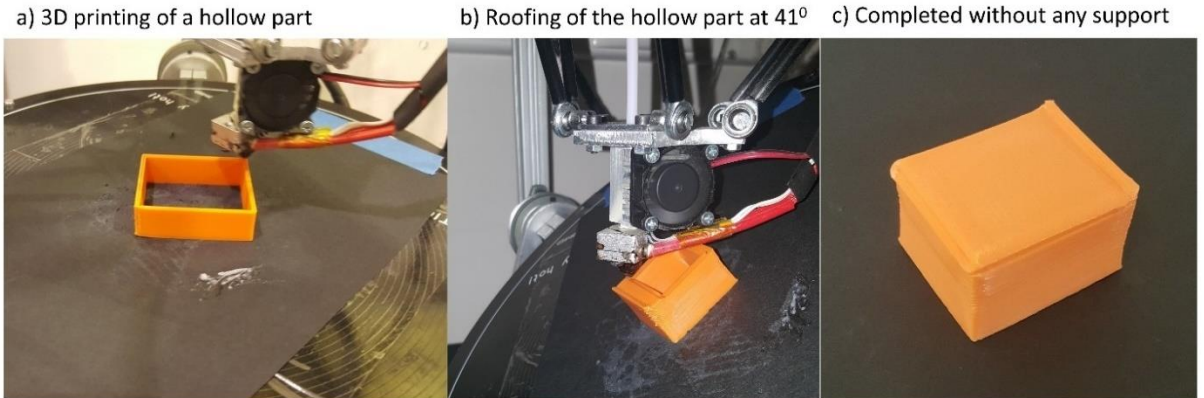


Figure 40: Fabrication of a hollow component to demonstrate the roofing process

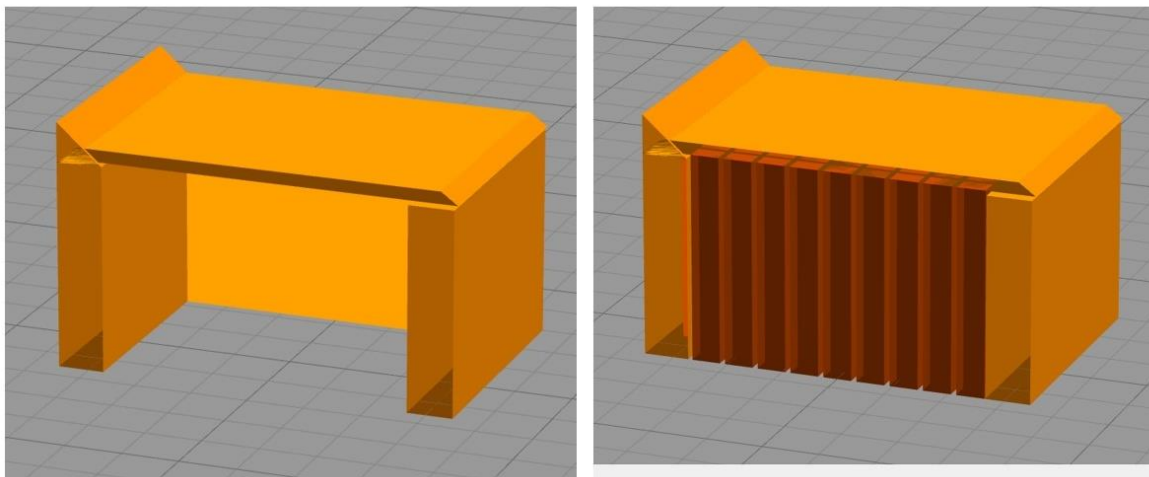


Figure 41: Generated support structure shown in a cross-section view of the component

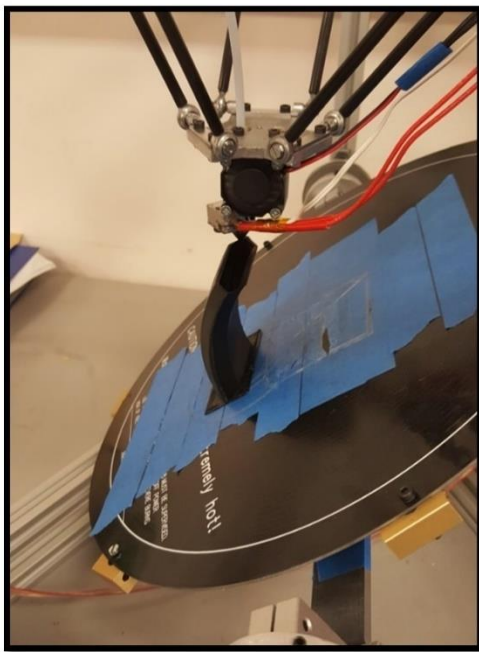
3.4.3 Use of Miscellaneous Paths

There are other ways of multi-axis 3D printing of parts that require support in planar AM. Just like the previous methods, these strategies depend on the nature of the part. For some parts that are obtainable by revolution or sweeping of a cross-section, the cross-sections can be manufactured incrementally at different platform orientation. The platform orientation must be changed slowly between consecutive layers so that each cross-section is supported. The way the

print platform moves determines how the cross-section is swept or revolved. Figure 42-a shows a sample revolved part constructed without any support structure.

It is also possible to make use of non-linear layer paths in multi-axis part construction without support. A sample of application of non-linear path is shown in Figure 42-b. A combination of linear and circular passes in each layer is used in the MAAM. When making the path, caution must be given to the gap between the nozzle and the deposited part especially during the circular pass. The nozzle must not jam into the part and the gap should not be greater than a few micrometers. It should be observed that since the layers are non-planar, an initial base part needed to be constructed.

a) Manufacturing of a revolved section



b) Part with straight and circular layer path

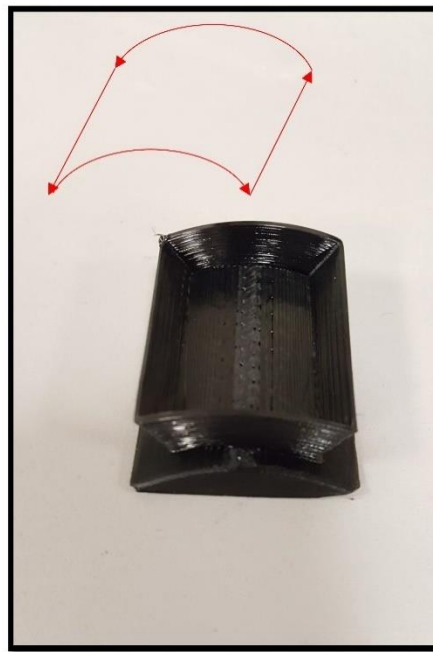


Figure 42: Fabrication of a bent/revolved part in (a) and a feature manufactured from combination of circular and linear paths in (b)

3.4.4 Discussion on the Need for a General Path Planner

For the two parts discussed in the previous section, each of the solid part is constructed as a byproduct of a sequentially arranged set of 4-axis motion to produce a 3D part by mere intuition. In fact, there are many different solid parts that can be manufactured with the 5-axis AM machine, but producing their path manually can be difficult. In engineering application, designs are made in solid models and there is usually no information on the manufacturing motion path. As a result, precedence needs to be given to finding a 5-axis path from a given solid model. The multi-axis path can be generated from a collection of 3D curves, as shown in Figure 43. Despite the significant progress in multi-axis path planning in machining, path planning needs to be studied for additive manufacturing since the two types of manufacturing methods are characterized by different constraints. Nevertheless, multi-axis machining literature can still provide some guidance on MAAM path planning.

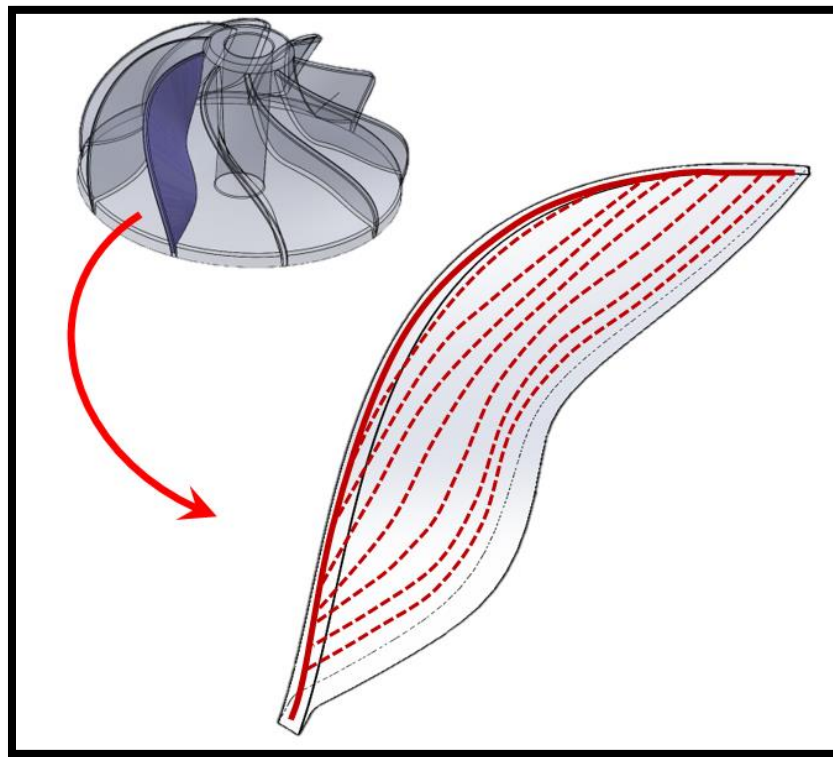


Figure 43: Sketch showing the ultimate 3D curved path desired

3.5 Multi-Axis AM for Manufacturing of Overhang Structure

Additive manufacturing (or 3D printing) became a popular rapid prototyping method since its beginning in the 1980s. It has since then expanded in application to various fields in engineering and sciences. It is now prevalent in the rapid prototyping, biomedical, construction and multi-functional applications. The most popular AM method is the fused filament fabrication (FFF) where molten material is deposited in layers to construct a part directly from a digital model. The layers are commonly extracted and filled from a tessellation model called StereoLithography (STL). This format represents an approximation of the actual analytical model using triangular surface meshes. The inaccuracy in STL files are usually negligible and do not affect the ability of AM to fabricate complex parts. Despite the complexity of parts obtainable by AM compared to other traditional manufacturing methods, the requirement for each layer to be supported limits the types of features realizable. Parts with overhanging structures like branch, roof and bridge components may not be directly manufacturable by AM. In such cases, preprocessing is commonly carried out by addition of support features to model. The additional support adversely affects production time, efficiency and quality of the part [52].

An alternative way of 3D printing overhanging features is by reorientation of the part. The reorientation is aimed at repositioning the part so that a feature can be 3D printed support-less. To evaluate the amount of tilting required, it is relevant to know the overhang angle. The overhang angle is the angle by which a layer contour deviates from the vertical build direction. Features that deviate from the vertical by an angle greater than a tentative angle of 45° are usually required to be supported [45,64,65]. This critical overhang angle serves as the criterion to use in deciding if a part can be additively manufactured. By reorienting a part, a new equivalent overhang angle below the critical angle can be obtained. However, such reconfiguration needs to be carried out on a multi-axis AM(MAAM) system because many complex parts do not have any orientation where overhangs can be eliminated. MAAM is not a new concept since it has been utilized in manufacturing. In machining, it improves machining efficiency of freeform parts. Even though AM is already compliant with freeform parts, multi-axis benefits has been demonstrated in overhang manufacturing [55]. By determination of part orientation for every overhanging portion

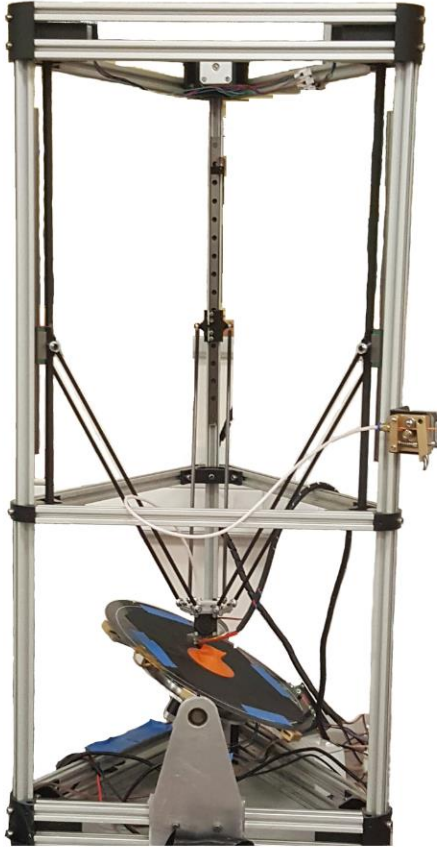
in STL, partitioning method has developed to fabricated in stages at various suitable part orientation [68].

There are few studies on application of multi-axis positioning in additive manufacturing. A robot arm platform has been used for AM using multi-plane toolpaths [69]. Non-planar slicing paths has been developed for MAAM robot to reduce need for supports and improve production time [70]. Recently, A new slicing method termed inclined layer printing has been developed to 3D print overhang features in uniaxial AM systems [71]. The use of an inclined surface allows AM of overhangs beyond the critical slant angle. However, the pressure of compaction during deposition is less when the deposition layer is not perpendicular to the build direction. To reposition the relative build direction normal to the sliced layer, MAAM can be introduced. Research on MAAM is multifaceted comprising of design, control, process planning, path planning and analysis of manufactured parts. Most of these categories occupy an entire scope of research. Hence this paper will focus on the analysis of overhang features produced by AM.

3.5.1 Multi-axis AM using 2D build platform

A 5-axis AM system has been developed to facilitate variable axis of fabrication. As stated in the previous section, MAAM can be used to change part orientation to avoid unsupported features in a model. Figure 44 shows the constructed system where a motorized build platform is attached to a 3D printer designed from Delta design concept [63]. The arms carry the print-head, which distributes material melted from the filament. The build table configuration is defined by the angles θ and ϕ .

a)



b)

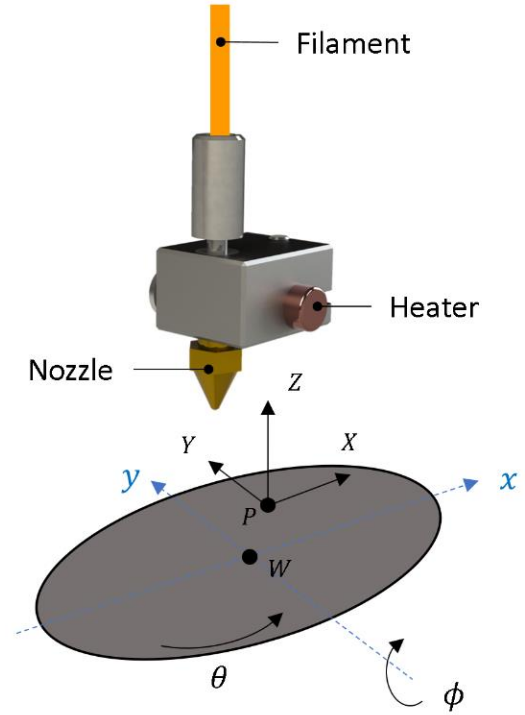


Figure 44: The constructed Multi-axis additive manufacturing system. b) Sketch showing the reference frames of the 3D printer and the 2D base platform where relative motion between the frames is achievable

An initial stage in fabrication of a part is the 3D printing path planning. The path is planned within the workpiece frame of reference. Since the part manufactured moves with the build table, it is necessary to transform each point in the part's path to a fixed frame P. Equation 1 provides the transformation relation from the workpiece frame W to the 3D printer frame P. Where the relative position of workpiece origin O with respect to the printer origin P is $\langle w_x, w_y, w_z \rangle$.

$$\begin{bmatrix} x \\ y \\ z \end{bmatrix}_P = \begin{bmatrix} \cos(\phi) & 0 & -\sin(\phi) \\ 0 & 1 & 0 \\ \sin(\phi) & 0 & \cos(\phi) \end{bmatrix} \cdot \begin{bmatrix} \cos(\theta) & -\sin(\theta) & 0 \\ \sin(\theta) & \cos(\theta) & 0 \\ 0 & 0 & 1 \end{bmatrix} \cdot \begin{bmatrix} x - w_x \\ y - w_y \\ z - w_z \end{bmatrix}_W + \begin{bmatrix} w_x \\ w_y \\ w_z \end{bmatrix} \quad (1)$$

The transformed path in P frame is send to the printer control system where actuation takes place. The control unit of the 5-axis 3D printer is designed to receive commands of positions X, Y, Z, rotations θ and ϕ and filament extrusion E.

3.5.2 Additive manufacturing of parts with overhangs

Complex parts used in various applications can have overhanging regions that necessitates the use of support in AM. The setbacks introduced by the supports has led to research in how the use of support structures can be minimized. Supports, commonly generated as vertical columns, patterns or tree-like structures, are usually minimized to improve AM productivity. Given a design model, usually in STL format, regions requiring supports are identified. Bounding regions (surfaces and edges for meshes), that incline by an angle greater a critical overhang angle, are considered for support generation. Vanek et. al[72] and Mao et.al[73] sampled points at such regions to generate support structures. In horizontal AM case where build direction remains fixed, studies have been carried out to either modify the desired part to reduce support structure or optimize the needed support structures.

By changing general designed model orientation, using multi-objective optimization, Jibin [74] and Pandey et. al.[75] obtained improved part orientation with respect to surface quality, support volume and production time. Optimal direction for simple models has also been studied to minimize geometric dimensioning and tolerancing errors[76]. Recent studies in design for AM have suggested inclusion of support minimization constraint at part design stage using topology optimization[77,78]. Hu et. al. investigated shape optimization and transformation of models to reduce supports. The design of support structure itself has also been studied. The goal is to use the best part orientation and generate the minimum amount of support since fully self-supporting part cannot be guaranteed on a uniaxial AM system.

3.5.3 Manufacturing and analysis of overhang structures

With the ability to change part orientation in the making, several types of overhang structures are fabricated and analyzed in this section. The instances where the outlines of a model slants significantly away from the build direction usually results in rough surface. This is attributed to the fact that the new line of deposited material on the outline may be entirely or partially unsupported. Figure 45 shows the overhang angle θ_0 , slicing angle θ_s , and the print platform tilt angle. Free overhangs (Figure 45b), bridges (Figure 45c) and roof components are studied in this paper.

The lack of research and tools in non-planar slicing has been acknowledged[60,79]. Hence most MAAM systems are used to fabricated parts using planer slicers at different build orientation. The overhangs need to be identified as explained in the previous section. Moreover, for MAAM, the model is required to be partitioned after identification of support requirement. Lee et. al.[80] used adjacent layer features classification to label features and partition them into buildable and unbuildable regions. In this study, the overhang features are predesigned separately to investigate them. A common two-pass printing path is used to fabricate the overhang structures. The path obtained directly from the analytical model of an overhang part using a developed Rhino plugin. A solid overhang model, in STEP or IGES file format, is first selected. After the starting layer is specified, the plugin generates the 3D printing paths.

The three types of overhang parts considered can be constructed in similar matter. It is observed that fabrication of bridge components is harder than roof components because roofs are supported at the sides. The side supports on roofs makes deposition of each raster easier due to the supports on both ends. Also, the free hanging component can be manufactured using similar design with the bridge, with elimination of the end wall. Hence, the analysis of overhang structures is carried out using the model in Figure 45a. Small variation in the design is used to study roof and free-hanging parts. The free-hanging part does not require collision check like the bridge component. The filament used is Colorfabb PETG filament of diameter 1.75. Fabrication of the base region of the designed model that holds the overhang structures is fabricated using normal horizontal AM using Simplify3D[®] for g-code generation.

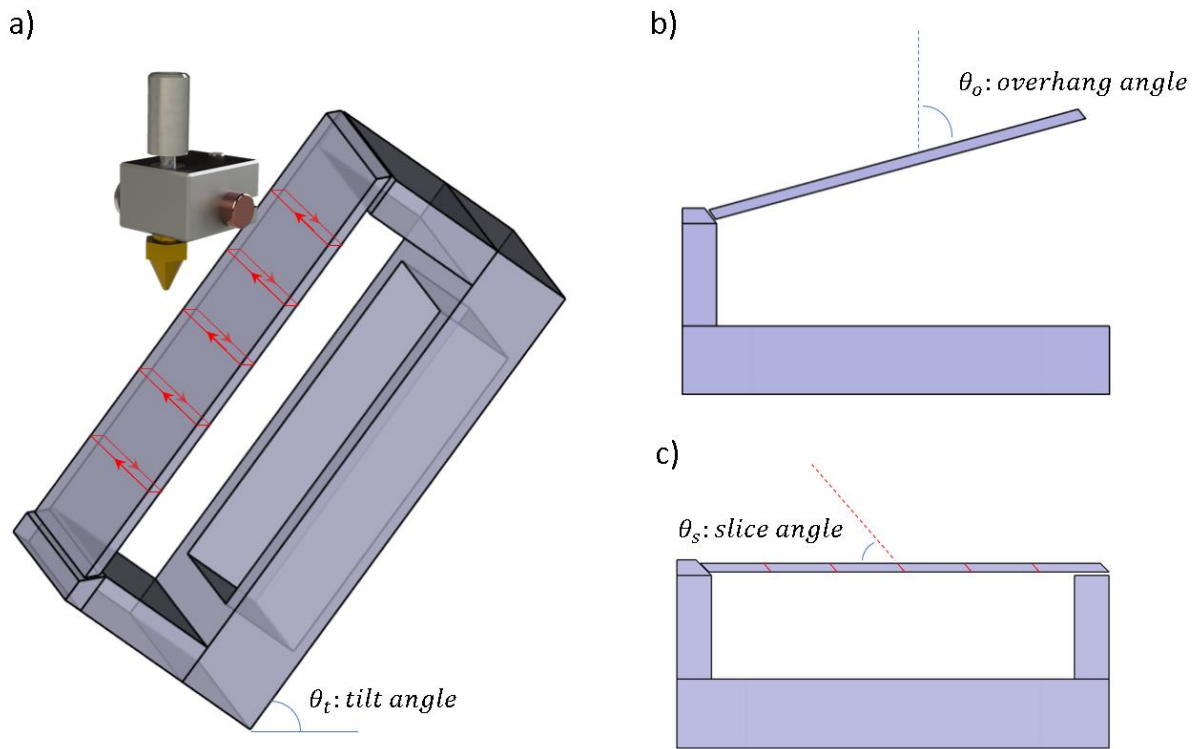


Figure 45: Definition of a) the slice path and tilt angle used in manufacturing thin overhang components, b) overhang angle, and c) slice angle which is equated with the tilt angle

The bridge component introduced has an overhang angle of 90^0 . For bridge length greater than 10mm[81], there should be added supports to prevent deposition on air. Upon tilting the bridge, the effective overhang (θ_e) can be decreased $\theta_e = \theta_o - \theta_t$. The tilt angle is chosen to be equal to the slice angle. For slice angles ranging from 25^0 to 70^0 , the bridge component is manufactured.

Figures 46a and 46b shows an overhang fabrication with high and low slice angles respectively. While deposited material in Figure 46a rests on a rigid layer, the one in Figure 46b hardly touches the bridge with insufficient support. Another issue with low slice angle is the blade-like ends. The sharp end of the low slice angle bridge makes the supporting structure less rigid and less heat dissipative. Hence, for small slice angles, the tip of the bridge during fabrication is fragile and neither supports the deposited material nor dissipate the heat away from the nozzle. The top surface of the component is analyzed using contact type CMM with Renishaw MH 20 probe of

1mm diameter, as shown in Figure 46c. It is used to study the form of the bridge surface at various slice angle.

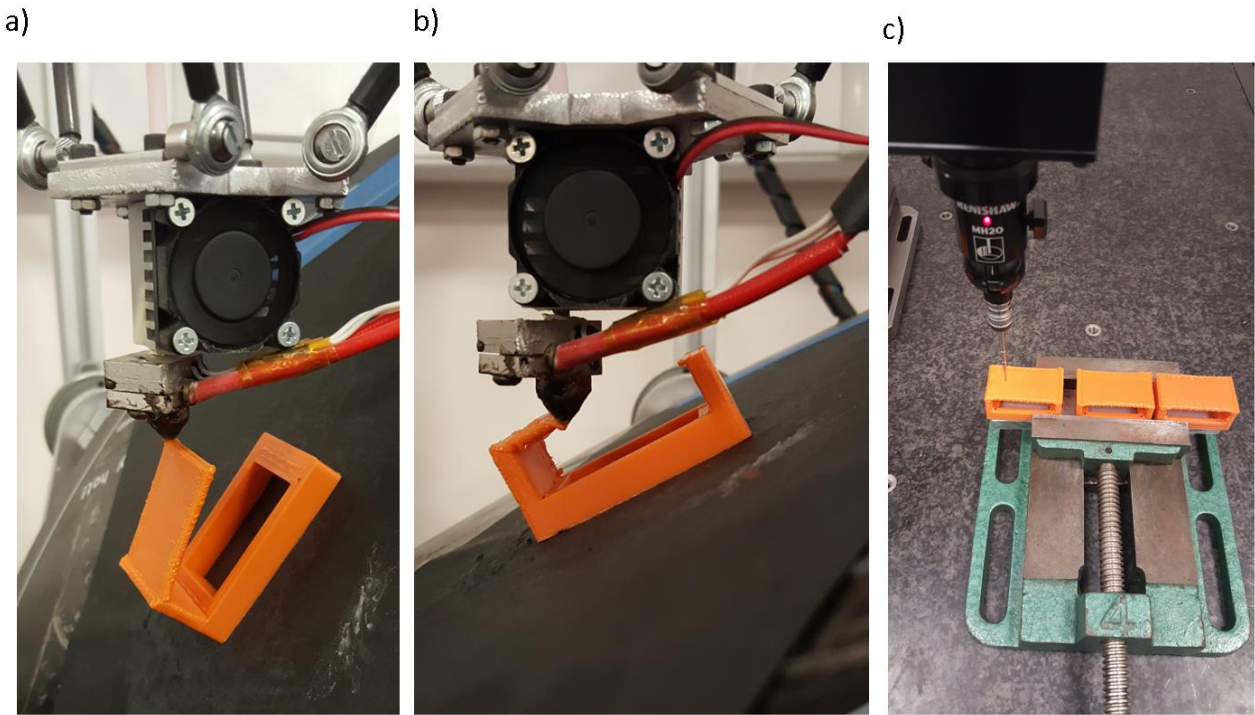


Figure 46: Fabrication of a) overhang part with high slice angle, b) low slice angle overhang using 5-Axis AM 3D printer. c) CMM measurement of surface deviation of manufactured sample parts

The CMM results of four slice angles are shown in Figure 47. Around 150 points are sampled from each surface and the deviations from the expected planar surface are analyzed. From the results found, it is observed that it is not only the surface roughness that is affected by slice angle[71], but also the overall shape of the surface. The complete results of average deviations from the plane at different slice angle is given in Figure 48.

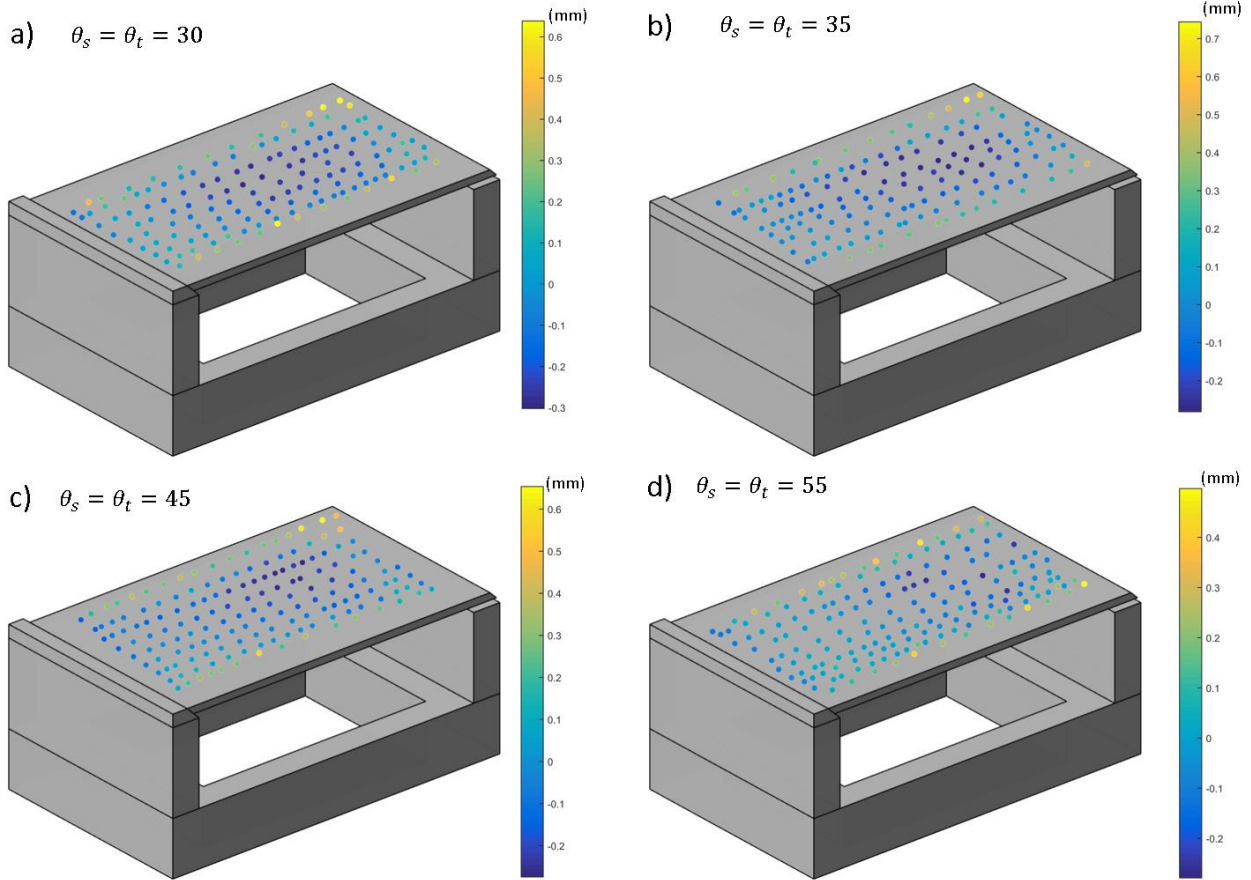


Figure 47: Error distribution at sample points on the top surface of the fabricated overhangs for various tilt angles. At the sides where the nozzle turns, there are extra accumulation resulting in elevation causing small elevations. The range of deviation in error shrinks when the tilt is increased.

Some similarities are observed in Figure 47. There is a common dent at the center of the bridges and sides of the bridges are raised. Since the bridge parts are thin, the motion of the nozzle at the sides carries unsolidified material to form a fold shown in Figure 49. This is what accounts for the raised sides. Figure 49 also shows that the folding phenomenon also decreases as the tilt angle is increased. It can also be observed that this behavior does not exist on the roof sample because of the side walls that increase heat dissipation at the side corners of the roof. For the roof sample that is fabricated at slice angle of 40° , the average deviation is 0.051mm. This is less than all the bridge samples measured.

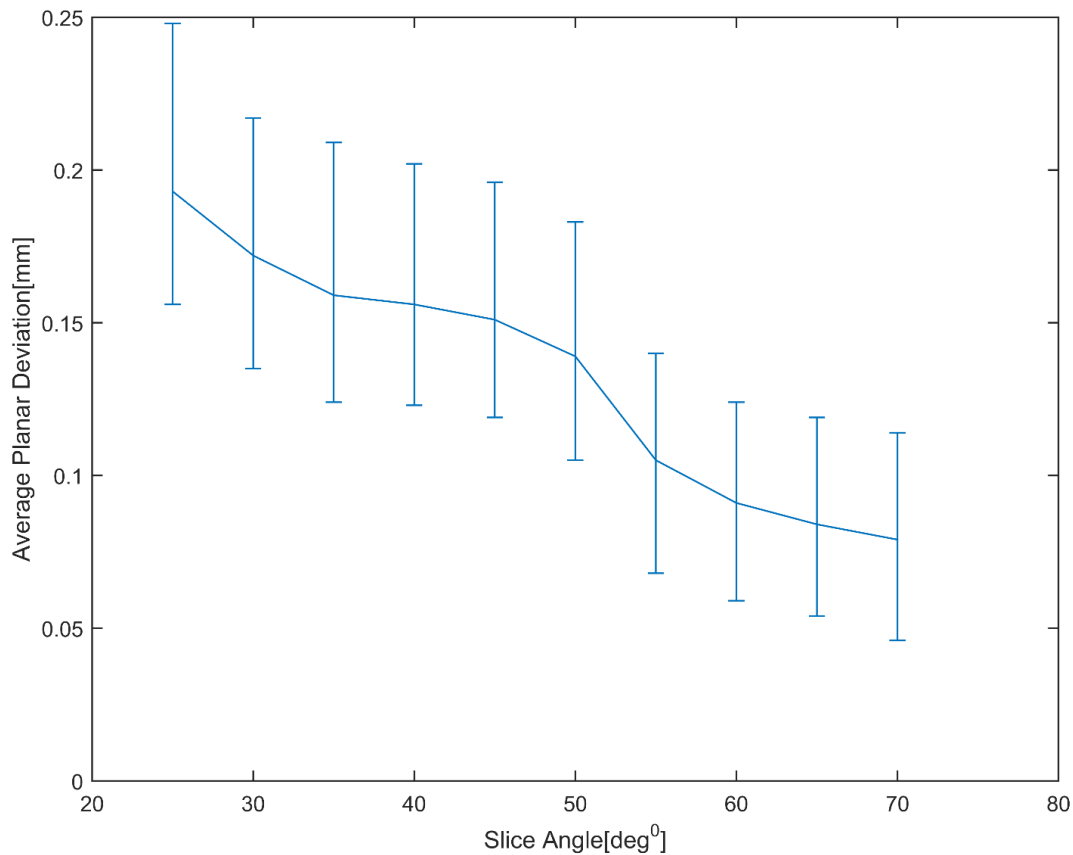


Figure 48: Plot of average planar deviation on bridge components measured for used slice angle. These are the errors of the manufactured surface measured with the desired CAD model of the bridging overhangs.

The shape deviation plot in Figure 48 is obtained using repeated measurements from two samples of each part at the slice angles. The deviations of the fabricated surface from the ideal model are analyzed in MATLAB.

The higher the slice angle (which is set to match the tilt angle), the lower the effective overhang angle, which is expected to produce better surface. The tilt angle serves the purpose of changing the part's altering the build direction on the part. From the work of Zhao et.al.[71], where the slice angle and overhang angles are studied, there are combinations of the slice and overhang angles that lead to failure in part fabrication. In mentioned the paper, part failures are classified into two types. For slice angles that deviate too much from the overhang angle, the mode of failure is collapse failure. The other failure mode is the adhesion failure where slice planes deviate from

the build direction. The adhesion failure is completely resolved by multi-axis AM in this section. The collapse failure can be avoided by choosing appropriate slice angles. Introduction of tilt angle expands the possible fabrication ranges of the slice and overhang angles.

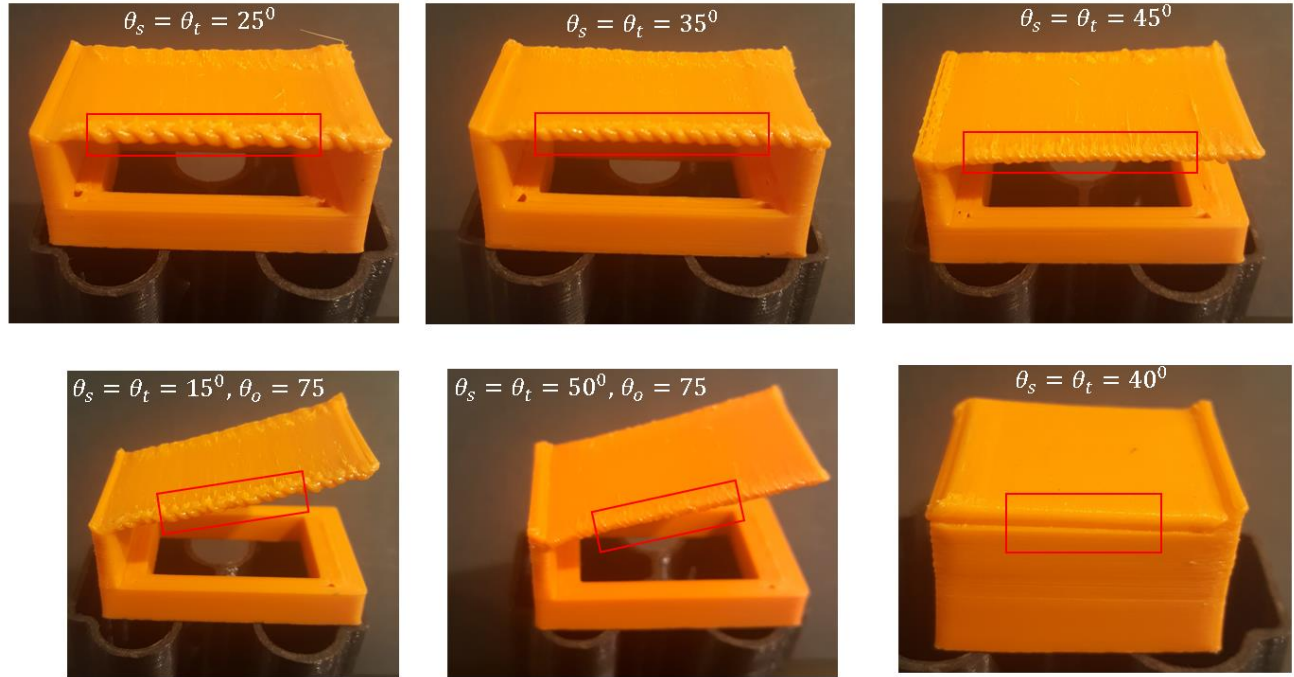


Figure 49: Image of sample overhang parts showing bridge, free hanging and roof components. Marked regions show the possible occurrence of folds. As the tilt angle is increased, the build building condition of the overhang improves, and better parts are produced

The path planning script enables manufacturing of freeform overhang structures as well. This is because the AM toolpaths are obtained from the actual overhang geometry surface. For a curved surface, a new angle θ is introduced as indicated in Figure 50a. The angle defines the tool orientation. It is chosen and fixed from the local surface normal direction while maintaining perpendicularity with the relative tool velocity vector. An identical two-pass paths are generated in each layer using 3D curves on the overhang surfaces. Figure 50b and c show error measurement and fabrication of a freeform roof component respectively. The surface normal relative tool direction is 40° . A flat roof fabricated with the same angle in Figure 50d is shown to have less error in Figure 50e.

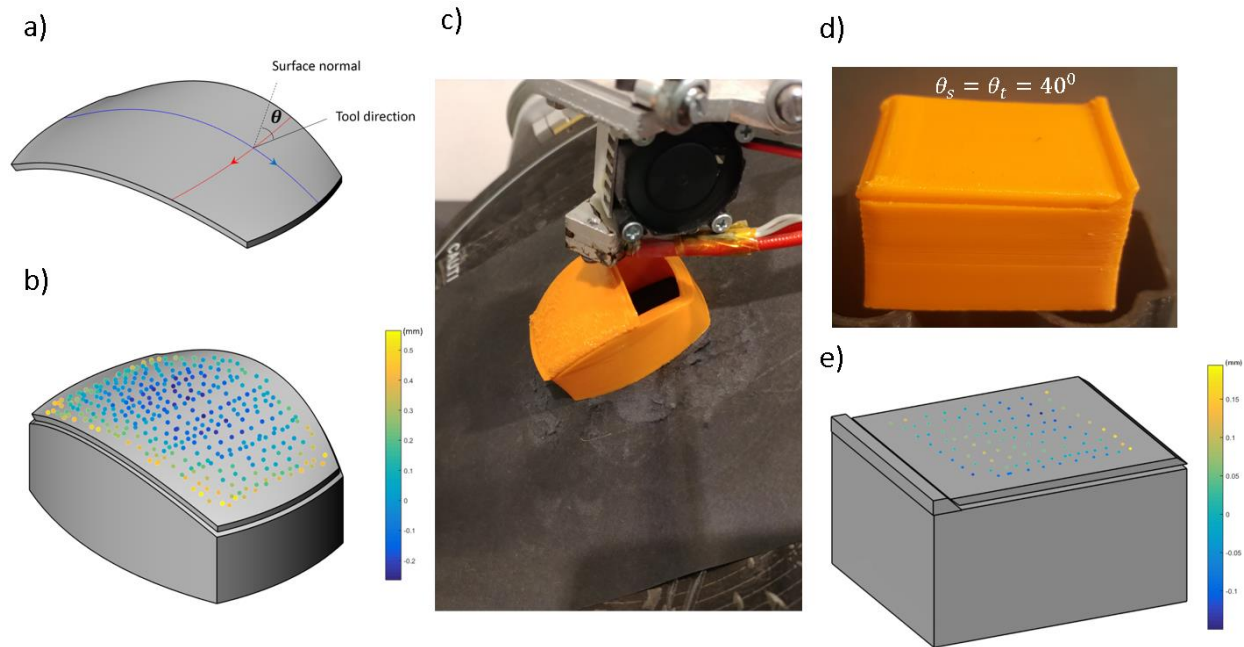


Figure 50: a) A freeform model where surface is used to generate AM toolpath with fixed tool orientation from the local normal b) Error of produced part surface from the designed model in a. c) The freeform roof in a is being fabricated on the 5-Axis AM system with 400 tool direction from the normal d) A flat roofing overhang components manufactured at 400 e) Error distribution on the flat surface of the roof in (d).

3.5.4 Discussion on results

The effects of changes in build direction on the shape of overhang features are studied in this paper. The slice angle is matched with each build direction to study the effect on the shape of overhangs. For an overhang angle of 90° , the inclined layer slicing can only be used for slice angles between 40 to 50 degrees. However, using a changing build direction, thin overhangs are produced with slice angles from 25 degrees and above. It is shown that with the aid of tilting, slice angles from 25° angle and above is obtainable using a PETG filament.

Some factors that can affect the test like overhang thickness, printing temperature, filament feed rate and speed are kept constant for all the tests. Analytical and numerical thermomechanical modeling of the overhang parts can be used to study the part deformations. A good knowledge of overhang fabrication without support can improve production time, reduce postprocessing labor and decrease material usage.

Chapter 4

FIVE-AXIS ADDITIVE MANUFACTURING OF FREEFORM MODELS USING A NEW SCHEME

Additive manufacturing (AM) or three-dimensional (3D) printing has grown continuously since its inception in the 1980s. Parts are manufactured by a successive layer-on-layer based material deposition along paths that are generated directly from a computer-aided design (CAD) model. Manufacturing of various materials ranging from flexible polymers to strong metals can now be realized additively. AM applications has also proliferated to a wide scope of research stretching from nano-scale bio-fabrication to large architectural constructions [82]. The most ubiquitous AM method is the fused deposition modeling® (FDM) or fused filament fabrication (FFF), which relies on the malleability of thermoplastics at low temperature for deposition of molten material to form the solid part. FDM is significantly cheaper than other AM methods, such as selective laser sintering/melting (SLS/SLM) used for metals, however, it is still predominantly confined to the fabrication of prototyping components [28]. The lack of reliability and consistency in material properties and dimensional accuracy hinders the adoption of AM in the rigorous industrial production environment [83]. For AM to satisfy more demanding applications, it becomes necessary to address the hurdles holding back its promise of revolution in manufacturing.

To open up new avenues of research, classic uniaxial AM design can be expanded to multi-axis AM (MAAM) concept. In addition to the common three-axis relative motion between tool and workpiece, multi-axis systems have one or more additional direction(s) of movement that allows variable tool orientations. Multi-axis manufacturing is not a new notion seeing that it has gained ground in machining field with an extensive research background and advanced application in production of complex parts. On the contrary, when it comes to AM, the available research, hardware and software in MAAM is inadequate and requires an overhaul of the present facilities [84].

Mechanical strength and geometric accuracy of produced parts are major concerns in AM. The surface quality of additively manufactured parts is affected by stairstep (or staircase)

phenomenon which leaves ridges in the size of layer thickness on surfaces that are supposed to be smooth. In addition to deviation in shape, staircase effect also necessitates postprocessing operations like polishing [85]. Surface quality of top and side profiles in FDM have been analyzed by Jin et al. [86], where mathematical models of surface deviations are explored.

By the addition of z-axis to common 2D layer path of three-axis 3D printers, Chakraborty et. al [87] introduce the idea of curved layer fused deposition (CLFD) modeling. This method uses a curved layer where deposition path normal vectors deviate only slightly away from the vertical. Llewellyn-Jones [88], Allen and Trask [89] demonstrated CLFD application in manufacturing of skin surfaces in composite and multi-material structures to reduce staircase effects. Recently, in the modeling and process planning of CLFD [90], the demand for a universal slicing method for arbitrary model is emphasized. The disadvantages of using three-axis 3D printers for curved layers includes limited surface geometry and the possibility of shearing and scraping during deposition. Since the CLFD in literature uses uniaxial deposition, issues like requirement of support structure and staircase effects (especially on side surfaces) are still predominant. As a result, an ideal curved layer 3D printing is envisioned using 5-axis gantry [87,90]. Pertaining to mechanical strength, It has been shown that 3D printed parts are anisotropic and have the highest strength along the deposition raster's direction [45]. The incorporation of fiber reinforcement in this direction can further increase this strength manifold [28]. Singamneni et al. [91] showed that using curved layer path can improve the load a part can withstand. In light of these prospects, it becomes necessary to explore new paradigms in additive fabrication of parts where tailoring 3D raster direction is feasible.

An important aspect of most manufacturing methods is path planning. For subtractive and additive manufacturing alike, the toolpath determines the quality of the part produced. Considering the nature of machining, parts can be machined starting from any region and orientation as long as it leads to the desired geometry. Hence, for the many machining operations, various toolpath have been studied with objectives like optimization of production time [92] and geometric accuracy [93]. On the other hand, AM is constrained to begin from a given build layer and configuration. Perhaps, this is the reason why AM has less diverse toolpath and its multi-axis strategies has not been equally studied exhaustively. There are several commercial multi-axis CAM packages for machining, but there is lack of such for AM [60]. Using conventional slicers, it is possible to

sequentially 3D print parts in discrete build orientations. To eliminate the need for supports, a digital model, in STL (StereoLithography) file, can be partitioned algorithmically and fabricated at different build orientation using a multi-axis system [80]. The use of these planar slicers narrows the applicability of MAAM by restricting depositions to planar paths. For instance, it will not be possible to carry out 5-Axis AM, where 3D printing paths of 3D curves demand instantaneous mingling of the all the axes of motion. Grutle [79] designed a 5-axis 3D printer to show the possibility of fabrication with better surface quality and without requirement of supports. These improvements are demonstrated on simple parts and the lack of a 5-axis slicer for general 3D printing is mentioned as a main issue. In another work [94], the build table is attached to a robotic arm to accomplish multi-axis AM using commercial machining CAM software for path planning. Most recently, Shen et al. [60] proposed slicing methods of 5-axis AM by intersection of offset surfaces for non-planar sculpture-printing and tangential tool direction for shell parts. Concerning the amount of material deposited, development of AM process where the shape of layers deforms—contrary to the use of parallel planes or offset surfaces—will require non-uniform material buildup and variable material extrusion rate within each layer. Indeed, the prospects of studying new AM layering combined with the new realm of possibilities facilitated by MAAM, commonly affirmed in the available studies, can extend AM development and application. With a complete multi-axis AM process for freeform parts, integration to combined additive and subtractive scheme can be a promising endeavor [95].

In this chapter, a new approach in model representation, geometric computation and path planning is explored to address some of the setbacks of AM. Initially, Section 2 presents design alternatives of a 5-axis 3D printer, introduces the selected mechanical design, and outlines features of its control system. Next, Section 3 proposes methods of path planning for arbitrary shell and solid models. Considering build orientations requirements and shape of model's geometry, strategies in construction of buildup layers and path are explored. Finally, Section 4 covers the evaluation of build angles and analysis of kinematic error.

4.1 The 5-axis 3D printer

A 5-axis 3D printer is designed and reconstructed by extension of a modified open-source design. As introduced in Chapter 3, RepRap project [96] brought 3D printing to the open-source

community in 2011 and has been expanded to many designs ever since. One of such designs is the delta-type prototype [63], whose variant forms include three pair of moving parallel arms that hold the print-head in place during 3D printing operation. A more popular design is the Cartesian gantry design that is usually composed of drives along the X and Y axes and a moving platform along Z. It is observed that augmentation of additional realm of motion in the delta-type model is less bulky compared with the Cartesian type. Besides, Cartesian design is shown to be slower and less productive [57]. Figure 51 shows the Delta design with its parallel-arm mechanism that supports and positions the print-head. A slider connected to each pair of arms is positioned vertically by a belt that is attached to the slider in a pulley-belt system, which is solely controlled by a motor above each tower. The positions of the sliders on the three towers dictate the 3D position of the print-head, where the essential process of additive manufacturing takes place. Within the print-head, a thermoplastic filament is injected, heated and deposited through the nozzle. The filament is fed with the aid of an additional motor and the heating is carried out by a resistive cartridge heater where temperature is regulated by a thermistor.

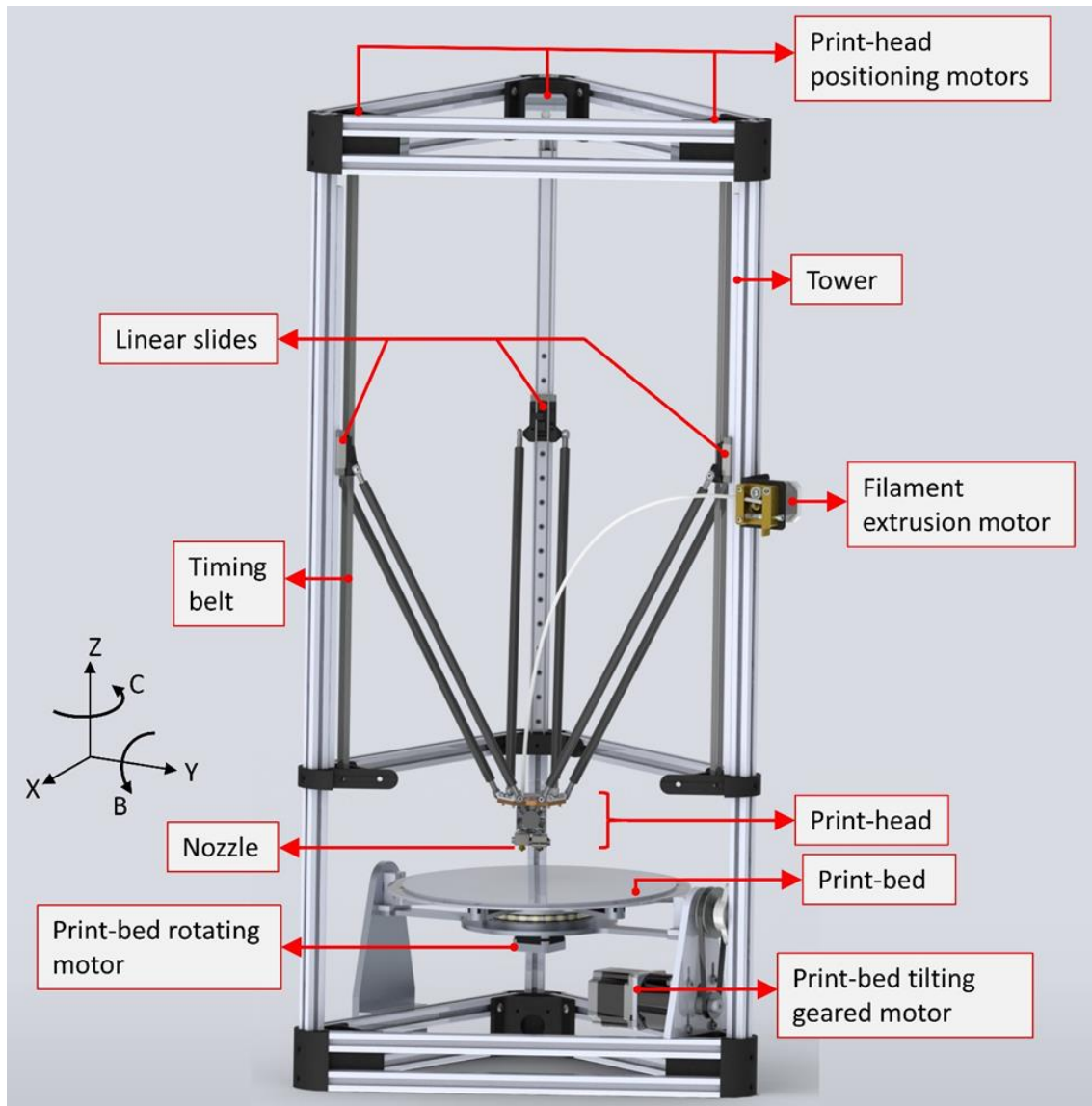


Figure 51: 5-axis 3D printer design showing actuators and mechanical components of the system

4.2 Path planning

A vital process in AM, and most of other manufacturing methods, is toolpath planning. At the path planning stage, a set of position coordinates—including orientation information for multi-axis systems—is chosen with respect to the workpiece that is to be manufactured. Regardless of whether or not the part remains stationary during the manufacturing operation, the path generated in the workpiece frame remains equally useful. This is because the path can be transformed to any position the workpiece is moved to. As a result, a complete toolpath can be used in any

manufacturing setup such as 3-axis, multi-axis and robotic manufacturing processes. In general, the toolpath is prepared to conform with the nature of the manufacturing method. Extrusion-based additive manufacturing work on the condition that each point on the toolpath must be structurally supported along the deposition direction. Hence, when building a part, choosing a layer path containing points that cannot be supported by preceding layers should be avoided. This is a significant constraint on AM toolpath design that limits how freely lines and curves can be chosen to fill a freeform model. For common 3-axis systems, several toolpath methods have been conventionalized for both machining and AM in the Literature.

Most of path planning in additive manufacturing comes from slicing a workpiece in the format of STL (STereoLithography), a tessellation of a CAD model obtainable in major modeling software packages. The basic slicing relies on finding intersection of tessellation triangles and parallel horizontal planes equally spaced to find the outline of each slice. Due to staircase effect that significantly affects the surface quality, layer and region based adaptive slicing methods are introduced [97]. These methods can only improve the surface quality at the cost of additional deposition layers that increases production time. In fact, the production time increases exponentially as the number of layers increases [85]. In MAAM, planar slicers can be used when the workpiece is partitioned so that separate build directions can be used for each partition to avoid the use of support structures [80]. However, the use of planar slicers in MAAM does not address the problem of stairstep effects.

In addition to producing good surface quality, each point on the path of AM is required to be supported by a solid membrane beneath the point along the build direction. Since the build direction cannot be changed in 3-axis AM, use of support structures may be inevitable [84]. Despite endeavors in CLFD and inclined layer AM [71], 3-axis manipulation of extruder is inadequate in ensuring good surface quality of parts without the use of support structures. For the MAAM in this chapter, with the aim of improving surface quality, paths will be constructed without considering the option of using supports. This section covers freeform model representations and the proposed path and build orientation of 5-axis additive manufacturing.

4.3 Freeform solid representation

The two types of commonly used internal solid representation are the Boundary representation (B-rep) and the Constructive Solid Geometry representation (CSG-rep) [98]. For CAD and geometric modeling within engineering applications, B-rep is widely adopted and employed by most modern modeling software packages. Freeform shapes in this work are represented by B-rep as a collection of trimmed non-uniform rational B-Spline (NURBS) faces, edges and vertices. A NURBS surface $\mathbf{S}(u, v)$ is a bivariate vector-valued piecewise rational function [99], which can be evaluated for any parameter values $u \in [u_0, u_1]$ and $v \in [v_0, v_1]$. From the book titled “The NURBS book” [99], the definition provided in Equation 2 is for a NURBS surface of degrees p and q in u and v directions respectively. The points $\mathbf{P}_{i,j}$ are the control points and the weights of the points are given by $w_{i,j}$. $N_{i,p}(u)$ and $N_{j,q}(v)$ are the nonrational B-spline basis functions defined on the knot vectors of both parametric directions. The definition of the B-Spline basis functions is most useful when they are in a recurrence formula due to computer implementations. The basis function $N_{i,p}(u)$ defined in Equation 2 is a result of the many work in the 1970s[99–102]. A similar definition for j th basis function $N_{j,q}(u)$ for the second direction can be defined by substituting j for i and q for p in the given equation using a new knot vector in the second direction. Unlike the popular tessellation based slicers, the direct use of NURBS preserves the surface accuracy of a CAD model [103]. The modeling package Rhinoceros® is used to access shape data from CAD features that is used to plan the multi-axis toolpath. All surface data—like parametric domain, location, derivatives, etc.—are reachable through the scripting environment. To be able to carry out toolpath planning for freeform geometry, a conventional system of organizing the surfaces is adopted.

$$\mathbf{S}(u, v) = \frac{\sum_{i=0}^n \sum_{j=0}^m N_{i,p}(u) N_{j,q}(v) w_{i,j} \mathbf{P}_{i,j}}{\sum_{i=0}^n \sum_{j=0}^m N_{i,p}(u) N_{j,q}(v) w_{i,j}} \quad (2)$$

For knot vectors of non-decreasing sequence $U = \{u_0, \dots, u_m\}$, $V = \{v_0, \dots, v_m\}$ the i th and j th B-Spline basis functions $N_{i,p}(u)$ and $N_{j,q}(v)$ of p -degree and q -degree are given iteratively by:

$$N_{i,0}(u) = \begin{cases} 1 & \text{if } u_i \leq u \leq u_{i+1} \\ 0 & \text{otherwise} \end{cases}$$

For which
$$N_{i,p}(u) = \frac{u-u_i}{u_{i+p}-u_i} N_{i,p-1}(u) + \frac{u_{i+p+1}-u}{u_{i+p+1}-u_{i+1}} N_{i+1,p-1}(u),$$

and the second parameter has:

$$N_{j,0}(v) = \begin{cases} 1 & \text{if } v_j \leq v \leq v_{j+1} \\ 0 & \text{otherwise} \end{cases}$$

where
$$N_{j,q}(v) = \frac{v-v_j}{v_{j+q}-v_j} N_{j,q-1}(v) + \frac{v_{j+q+1}-v}{v_{j+q+1}-v_{j+1}} N_{j+1,q-1}(v)$$

A plugin script is programmed to process freeform solids in STEP, IGES and Rhino model formats. A CAD model of a freeform part is disintegrated into its component surfaces and edges through the process depicted in Figure 52. Initially, the extracted surfaces undergo an organizational process of parametric flipping and reversing, which is carried out automatically by the plugin. The requirement for closed surfaces is that each edge of a surface, which is coincident with the bounding isoparametric line, is paired with other edge from another surface. The parametric directions of the surfaces are to fit a specific conventional order shown in Figure 53. The figure shows the parametric directions of top $T(u, v)$, base $B(u, v)$, and side surfaces of a freeform solid after they are aligned. The parametric directions of the top and base faces are aligned to match each other along the build direction. The side surfaces (S_1, S_2, S_3, \dots) are enumerated starting from the parametric origin edge and continuing in counterclockwise directions. The v parametric direction is chosen as upward build direction on the bounding side faces.

The script is organized in an objected oriented structure where a 3D printing process is represented by “layer stack” objects that comprise of the attributes and functions necessary to plan, stored and process data for additive manufacturing. A “layer stack” object is comprised of multiple layer objects representing the additive manufacturing layers and some interlayer functions. The layer-stack stores the closed freeform model as closed set of NURBS surfaces. It also keeps an

array representing the sorted 3D printing path organized in the sequence they will be used to generate G-codes. Figure 52 illustrates the data structure of the Rhino script used as plugin.

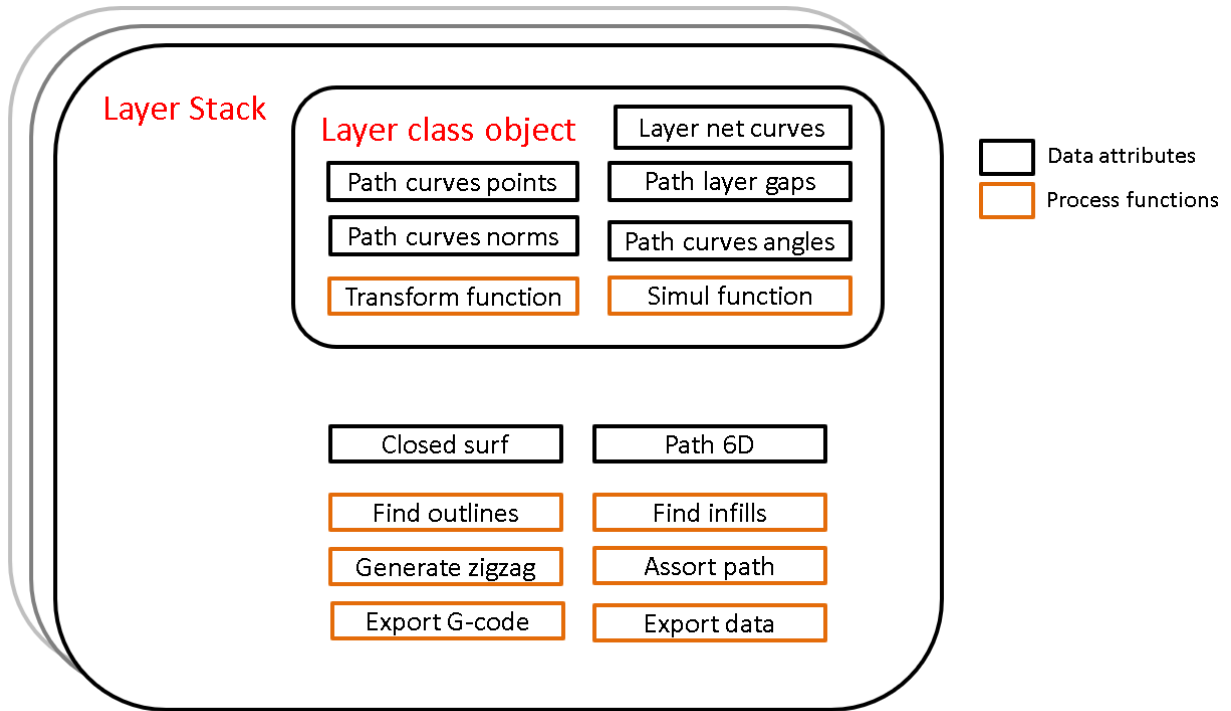
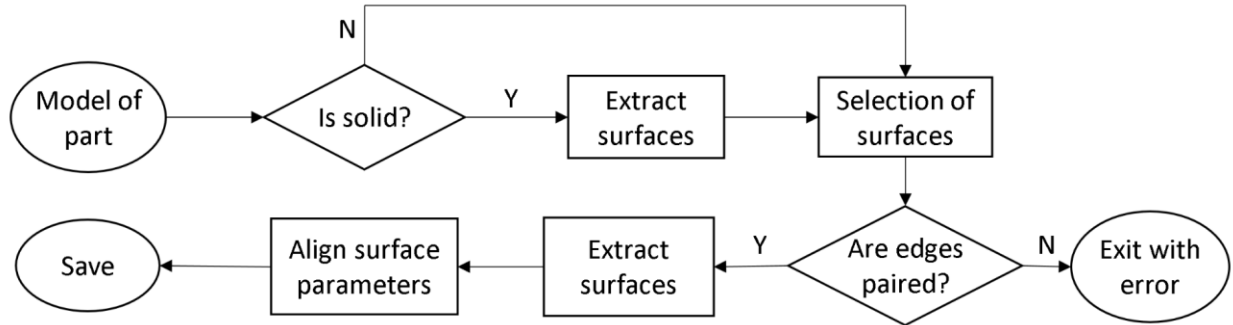


Figure 52: Procedure of representation of a CAD model as organized connected surfaces along with the data and function organizational structure

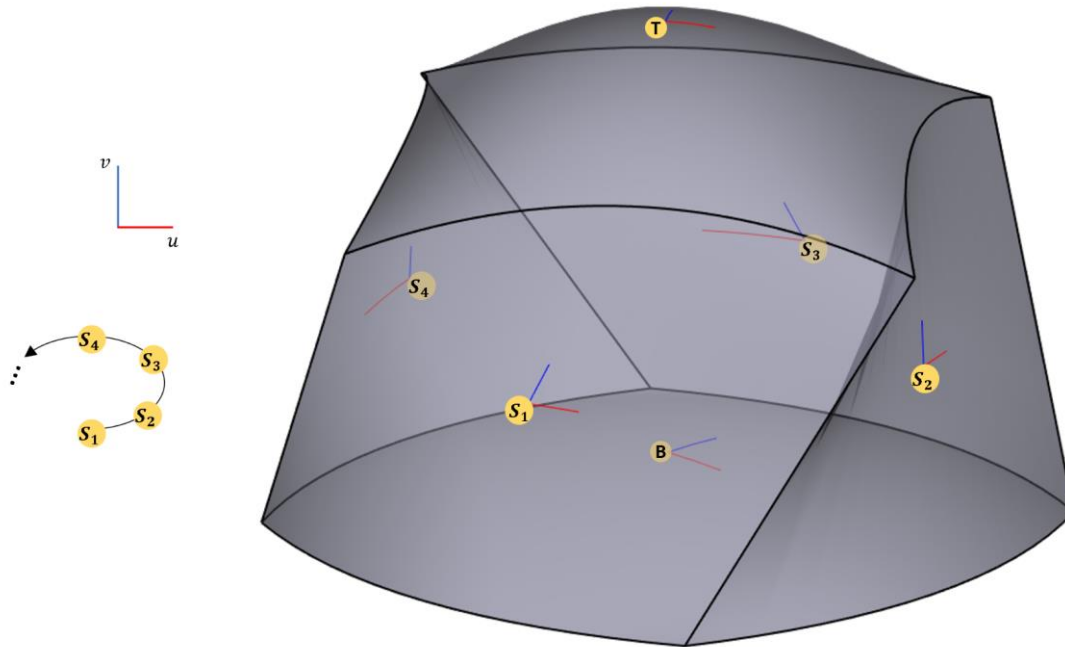


Figure 53: Alignment and arrangement of surfaces from a freeform model

4.4 Side surface tangent tool orientation along 3D path

Surface quality of parts manufactured by planar slicing are affected by staircase effect, which becomes more pronounced as shift in the outline of consecutive layers increases. With the introduction of MAAM, it is possible to theoretically eliminate this effect by changing the local nozzle direction [60]. When the build orientation is chosen to remain tangent to the side surfaces, the deviation caused by the staircase effect becomes significantly diminished. Hence, the side surface tangent (SST) tool orientation is adopted as a constraint on the orientation of outline paths of all layers. Since the top surface of a freeform model can also have this effect, the staircase effect is not limited to the side surfaces. This chapter also suggests compelling the toolpath at the final layer to remain normal to the top surface. To accomplish this, the intermediate layers used in filling a model to its top surface are constructed as 3D surfaces where the tool direction must remain normal to the surfaces. The described transition surface normal (TSN) tool orientation ensures that the top surface has no stairsteps. The generation of such surfaces and paths challenges present 3D printing layering methods.

Apart from the popular planar slicing methods, an offset method suggested for 3D printing on a non-planar base surface has been studied [60,70]. In this method, by using either mesh or parametric model, a successive offset of nonplanar base surface is intersected with the model to generate layer contours. Despite the added flexibility in layers, the offset method does not address staircase effect on any portion of the manufactured part. Figure 54 shows three layering methods for a solid model with an exaggerated demonstration of how layers are constructed. The planar slicing method (Figure 54b) is the most restrictive because it cannot be used for parts that do not have planar base. The offset layering (Figure 54c) works for nonplanar path, but it only considers the base surface and not the form of other bounding surfaces of the part. Hence, it does not provide solution for staircase effect on the final product. The method suggested in Figure 54d is based on using a gradual shapeshifting transition layers to fill solid model from the base to top surface. The method also proposes the use of side NURBS surface in constructing the outline portion of each layer (represented in color red). The curves used in generation of the outline path also exhibit the same progressive shape bending to fit the top outline from the base. In this sub-section, generation of paths on side surfaces are discussed for the fabrication of a shell part or the side-exterior portion of a solid model. Together with the strategies developed in this sub-section, Section 3.3 will discuss the transitional layering method of filling a solid model as imagined in Figure 54d. By comparing how the jagged profiles differ from the desired model in Figure 54a, it is obvious that the new approach provides the best surface quality among the three methods.

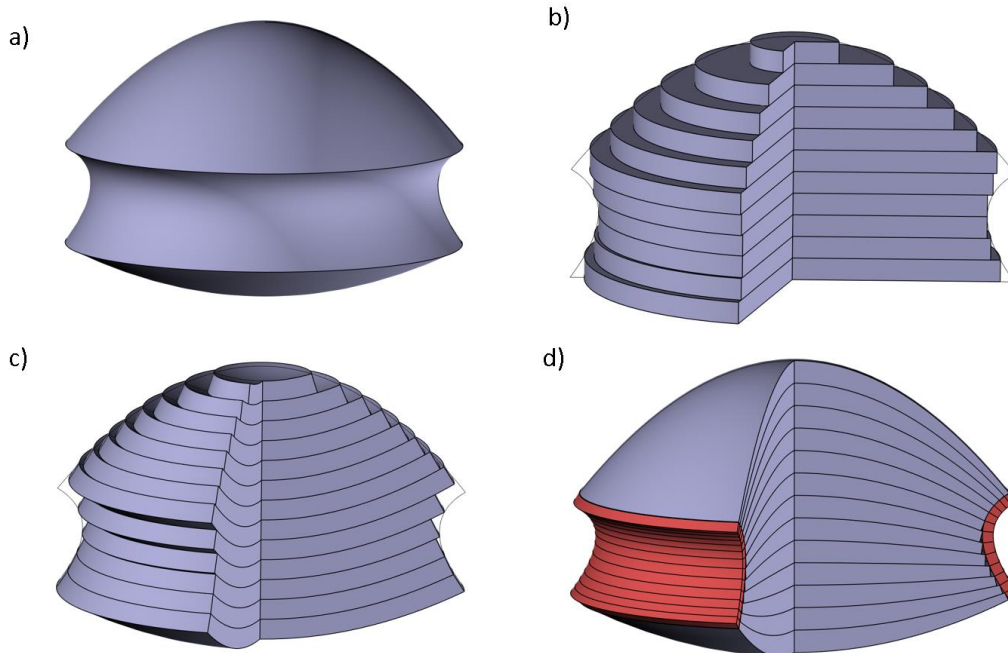


Figure 54: Stairstep effect of an ideal part in fig. a is demonstrated on b) planar slicer, c) offset surface slicing and d) interior infill and outline (in red) of transition layers

Mapped parametric lines provide curves that initially take the shape of the base and slowly morph to the shape of the top. The form change is possible only if the gaps between consecutive curves varies within a layer. This intra-layer variable thickness can be achieved if the amount of filament extruded at each point reflects this thickness. By conservation of volume, a cylindrical filament, with a diameter D_f deformed into a raster of rectangular cross-section of width w_t and length spanning from (x_i, y_i, z_i) to $(x_{i+1}, y_{i+1}, z_{i+1})$ at a point of local layer thickness of Δl_i , should have filament extrusion length (ΔE_i) given by Equation 3.

$$\Delta E_i = \frac{4w_t\Delta l_i\sqrt{(x_{i+1}-x_i)^2+(y_{i+1}-y_i)^2+(z_{i+1}-z_i)^2}}{\pi D_f^2} \quad (3)$$

In common FDM printers, the material extrusion rate is known the moment the path positions are found, because the rate of material extrusion is uniformly correlated with the tool velocity. For the shape-changing layers, the rate of material extrusion varies based on the spatial variation in the build of each layer. The length ΔE_i given in Equation 3 is added to the previous E -motion value in the path and is appended to the g-code sent to the numerical controller. Even

though the path points are sampled at a uniform distance within the range 0.4-0.8mm along the path curve, raster thickness remains uniform throughout the length. The reason for the uniformity is attributed to the linear interpolator in the numerical controller.

For a thin walled freeform part or sides of a filled part, where the side walls are to be fabricated, Figure 55 shows how the path is constructed. After the surfaces are aligned according to the convention mentioned, the required number of layers is determined. By determining the length of the longest curve from the base to the top edges, using a target maximum layer thickness, the number of layers (N) can be evaluated by dividing the length by the thickness. Next, N points are uniformly distributed along each of the common edges of the surfaces. Curves are mapped to connect the found points for each side surface at all the N layers. A mapped parametric line from point $p_1(u_1, v_1)$ to $p_2(u_2, v_2)$ on an arbitrary side surface $S(u, v)$ demonstrated in Figure 55, will result in a curve $C(t)$ defined by Equation 4 for $0 \leq t \leq 1$. Although these curves may differ a bit from the surface isoparametric curves, they provide the desired transition from the base to the top edges in the build direction.

$$C(t) = S(u_1 + (u_2 - u_1)t, v_1 + (v_2 - v_1)t) \quad (4)$$

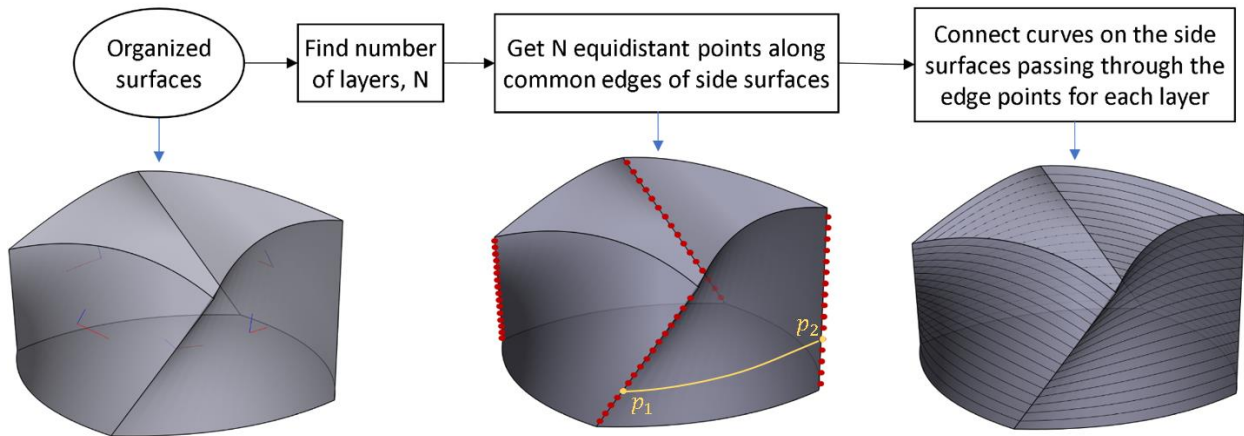


Figure 55: The algorithm used to generate 3D curves from side surfaces. Connection of edge points p_1 and p_2 with surface curves is demonstrated.

The tool orientation is determined by the combination of SST orientation and the curved path directions found. The ideal orientation of the nozzle along a curve is perpendicular to the local

curve tangent \hat{t} . Similarly, the SST condition constrains the orientation to be perpendicular to the local surface normal \hat{n}_s . With the constraints, illustrated in Figure 56b, the tool orientation can be expressed by Equation 5. Figure 56 also points to an application of the path on an impeller blade side-surfaces where the hub and blade regions can be exclusively fabricated.

$$\hat{n} = \frac{\hat{n}_s \times \hat{t}}{|\hat{n}_s \times \hat{t}|} \quad (5)$$

The use of the elaborated curve path and orientation is expected to result in no staircase effect on neither the side surfaces nor the top wall of the blade. An additional merit of the new path strategy is reduced retractions and non-extrusion passes which results in cleaner surfaces. Figure 57 compares the fabrication methods of the impeller model shown Figure 56a. Figure 57a shows the impeller that is manufactured using path generated by a planar slicer on an STL version of the model with the aid of Simply3D software. The other impeller, shown in Figure 57b, is created by initially manufacturing the hub using normal planar path g-codes. Afterwards, by appending the derived freeform path commands to the hub's g-codes, the impeller blades are fabricated.

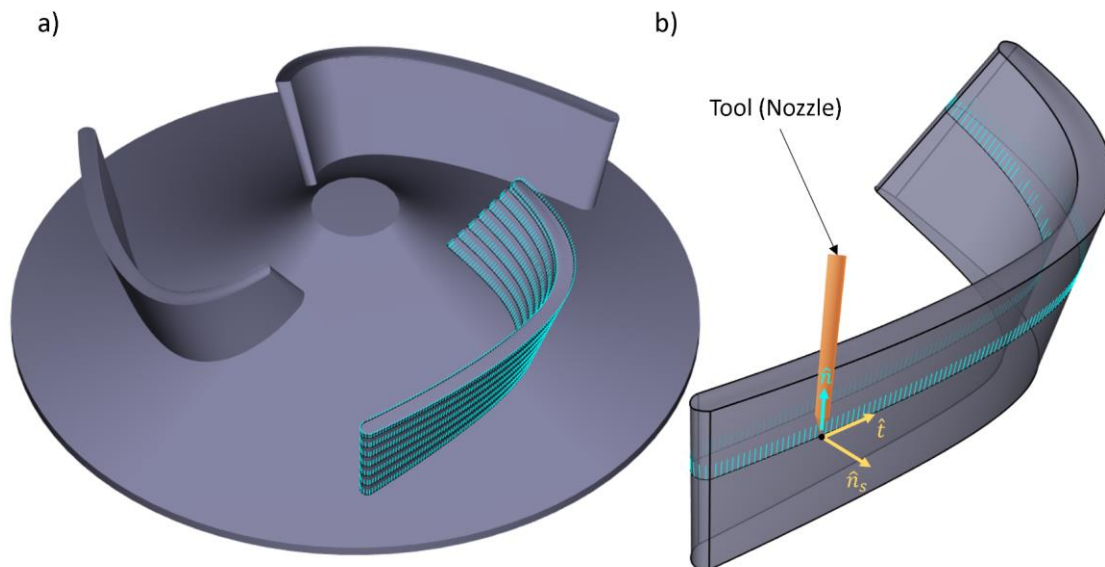


Figure 56: Tool orientation along the 3D path applied in manufacturing of impeller blades

The impeller fabrication process using planar slicer did not consider the form of the part manufactured. Hence, the occurrence of multiple islands and non-extrusion path could not be mitigated. The retraction and reloading of filament, made necessary by existence of islands, affect the surface quality of the part. The multi-axis path used allows tailoring of path for individual component in the model thereby ensuring good surface quality with minimal non-extrusion passes.

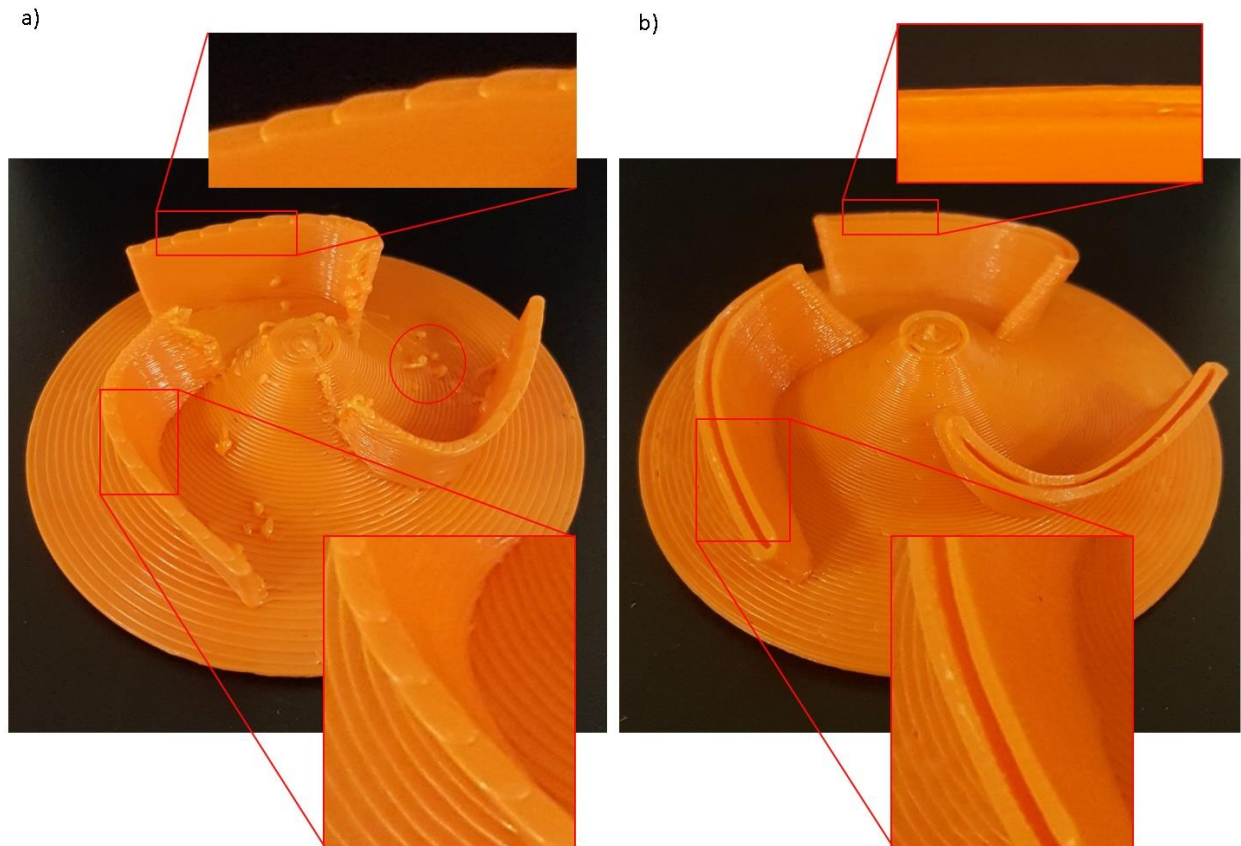


Figure 57: Two impellers are manufactured, where a) traditional planar slicer is used, b) the blades are fabricated using the suggested path. Staircase effects are visible on the top wall of the impeller blades on the left. Retraction remnants are also visible on the hub and blade surfaces in a. The gaps in the blades of b can easily be filled using methods introduced in Section 3.3

4.5 Toolpath for infill

The toolpath path for manufacturing the thin exterior surfaces of a given freeform part is studied in the previous section. However, as most models are required to be enclosed solids in applications, a method of fabricating the interior filled portion of a model is paramount to AM. Usually, due to high production time and the nature of FDM, solid model is hardly produced void-free. As a result, taking advantage of the ability to tailor infill density, use of completely gapless toolpath is rare. Rather, solids are usually manufactured using topological infill patterns that are easily filled after the outline of each layer is found. A common continuous pattern that can be easily generated is the zigzag pattern [104]. This filling pattern, commonly designed for planar toolpath, can be extended to fill a freeform surface with 3D curves.

From the model representation defined in section 3.1, the freeform surfaces are not manufactured accurately using the present toolpath strategies in AM because of staircase effect. As mentioned in the previous section, SST tool orientation resolves this issue on the side surfaces. A method of filling the freeform model that results in staircase-free top surface is proposed in this section. Since the necessary tool orientation condition for a smooth top surface is the to keep the tool direction normal to the top surface, the proposed TSN orientation chooses the final deposition layer to coincide with the top surface. Furthermore, the infill layers can be designed in a way that they take the form of the top surface as they approach the final layer from the base surface. In other words, for n less than a total of layers N , a layer surface $\mathbf{L}(u, v)$ is such that $\mathbf{L}(u, v) = \mathbf{B}(u, v)$ and $\mathbf{L}(u, v) = \mathbf{T}(u, v)$ as $n \rightarrow 0$ and $n \rightarrow N$ respectively. To support compound models that can be expressed as combinations of multiple solid models of Section 3.1, material is deposited for the layers $n=1$ up to $n=N$, since the base layer $\mathbf{B}(u, v)$ is assumed to be coincident with an existing base on a previously fabricated part without any gap. With the tool orientation on each layer maintaining the surface normal (TSN) condition, the top surface can be fabricated as the final layer without staircase effect. The transition layers should support the top layer while maintaining variable intra-layer thickness that do not exceed the maximum layer thickness, which is usually less than the nozzle diameter.

The concept of surface transition from one form to another is common in computer graphics [105], where it is usually referred as morphing. This study applies this notion to develop surfaces—as blends of the base and top surfaces—upon which infill paths are generated. The

blending function is formulated as a mapping where one-to-one correspondence is established between the two surfaces. Fortunately, the organization of surfaces adopted in section 3.1 ensures alignments of the (u, v) parameters of the two surfaces which can be matched to guarantee correspondence. Due to more even inter-layer thickness distribution along the build direction, a linear combination [106] or linear morph is chosen as the preferred blending function. The new surface representing n th layer is defined by Equation 6.

$$\mathbf{L}(u, v) = \left(1 - \frac{n}{N}\right) \mathbf{B}(u, v) + \frac{n}{N} \mathbf{T}(u, v) \quad (6)$$

The transition layers do not take into consideration the shape of the side surfaces. Consequently, it is expected that the boundaries of the layers may not coincide with the side surfaces. In fact, the layer outline fits into boundary surfaces only when the side surfaces are obtained by lofting outline of the top surface linearly towards that of the base surface or vice versa. Figure 58a demonstrates the possible mismatch where the blue surface boundaries lay outside the part's bounding surface(s) and the surface outline does not match the desired layer outline obtained by algorithm in Section 3.2. It should be noted that the shape of outline of the blue surface may deviated considerably from the orange outline in Figure 58a, hence, mere translation cannot fix the issue. Evidently, as long as the mapping function does not take the boundary surfaces into consideration, the intermediate layers are bound to deviate from the model. It becomes pertinent to resolve this layer deviation issue to have a complete path planning scheme for a general freeform model.

Using methods outlined in section 3.2, for each layer, the accurate outline can be extracted directly from the boundary surfaces. To get a proper surface, a new layer $\mathbf{L}'(u, v)$ is constructed by first designating the outline curves as its boundary. Hence, the curves $\mathbf{L}'(u, v_0)$, $\mathbf{L}'(u_1, v)$, $\mathbf{L}'(u, v_1)$ and $\mathbf{L}'(u, v_0)$ serve as the bounds of the surface $\mathbf{L}'(u, v)$. Where (u, v) are arbitrary parameters of the new surface with $u \in [u_0, u_1]$ and $v \in [v_0, v_1]$. Next, a method of transferring the shape of $\mathbf{L}(u, v)$ to the new surface $\mathbf{L}'(u, v)$ is proposed. With correspondence established between the two surfaces, a point on the surface $\mathbf{L}(u, v)$ on the u -directional isoparametric curve can be displaced by a vector $\mathbf{d}^u(u, v)$ interpolated between the determinable displacement vectors $\mathbf{L}'(u, v_0) - \mathbf{L}(u, v_0)$ and $\mathbf{L}'(u, v_1) - \mathbf{L}(u, v_1)$. The same point considered on the v -directional

isoparametric curve will have an interpolated displacement vector given by $\mathbf{d}^v(u, v)$. The displacement vectors $\mathbf{d}^u(u, v)$ and $\mathbf{d}^v(u, v)$ are expressed in Equations 7 and 8 respectively.

$$\mathbf{d}^u(u, v) = \mathbf{L}'(u, v_0) - \mathbf{L}(u, v_0) + \frac{v-v_0}{v_1-v_0} [\mathbf{L}'(u, v_1) - \mathbf{L}(u, v_1) - \mathbf{L}'(u, v_0) + \mathbf{L}(u, v_0)] \quad (7)$$

$$\mathbf{d}^v(u, v) = \mathbf{L}'(u_0, v) - \mathbf{L}(u_0, v) + \frac{u-u_0}{u_1-u_0} [\mathbf{L}'(u_1, v) - \mathbf{L}(u_1, v) - \mathbf{L}'(u_0, v) + \mathbf{L}(u_0, v)] \quad (8)$$

It should be noted that the two displacements $\mathbf{d}^u(u, v)$ and $\mathbf{d}^v(u, v)$ are not equal. Since each carries some information on the shape of the new surface, a weighted average of the two is used to find the displacement given in Equation 9. The overall displacement $\mathbf{d}(u, v)$, indicated in Figures 58b and 58c, can be computed at any arbitrary (u, v) and can be used to create a proper transition layer.

$$\mathbf{d}(u, v) = \gamma \mathbf{d}^u(u, v) + (1 - \gamma) \mathbf{d}^v(u, v) \quad (9)$$

Where γ and $(1 - \gamma)$ represent the weights on the displacement vectors of the isoparametric u -curves and v -curves respectively. Upon adding the displacement vector to the blend surface, as expressed in Equation 10, new transition surfaces can be explicitly obtained.

$$\begin{aligned} \mathbf{L}'(u, v) = & \mathbf{L}(u, v) + \gamma \left(\mathbf{L}'(u, v_0) - \mathbf{L}(u, v_0) + \frac{v-v_0}{v_1-v_0} [\mathbf{L}'(u, v_1) - \mathbf{L}(u, v_1) - \right. \\ & \left. \mathbf{L}'(u, v_0) + \mathbf{L}(u, v_0)] \right) + (1 - \gamma) \left(\mathbf{L}'(u_0, v) - \mathbf{L}(u_0, v) + \frac{u-u_0}{u_1-u_0} [\mathbf{L}'(u_1, v) - \right. \\ & \left. \mathbf{L}(u_1, v) - \mathbf{L}'(u_0, v) + \mathbf{L}(u_0, v)] \right) \end{aligned} \quad (10)$$

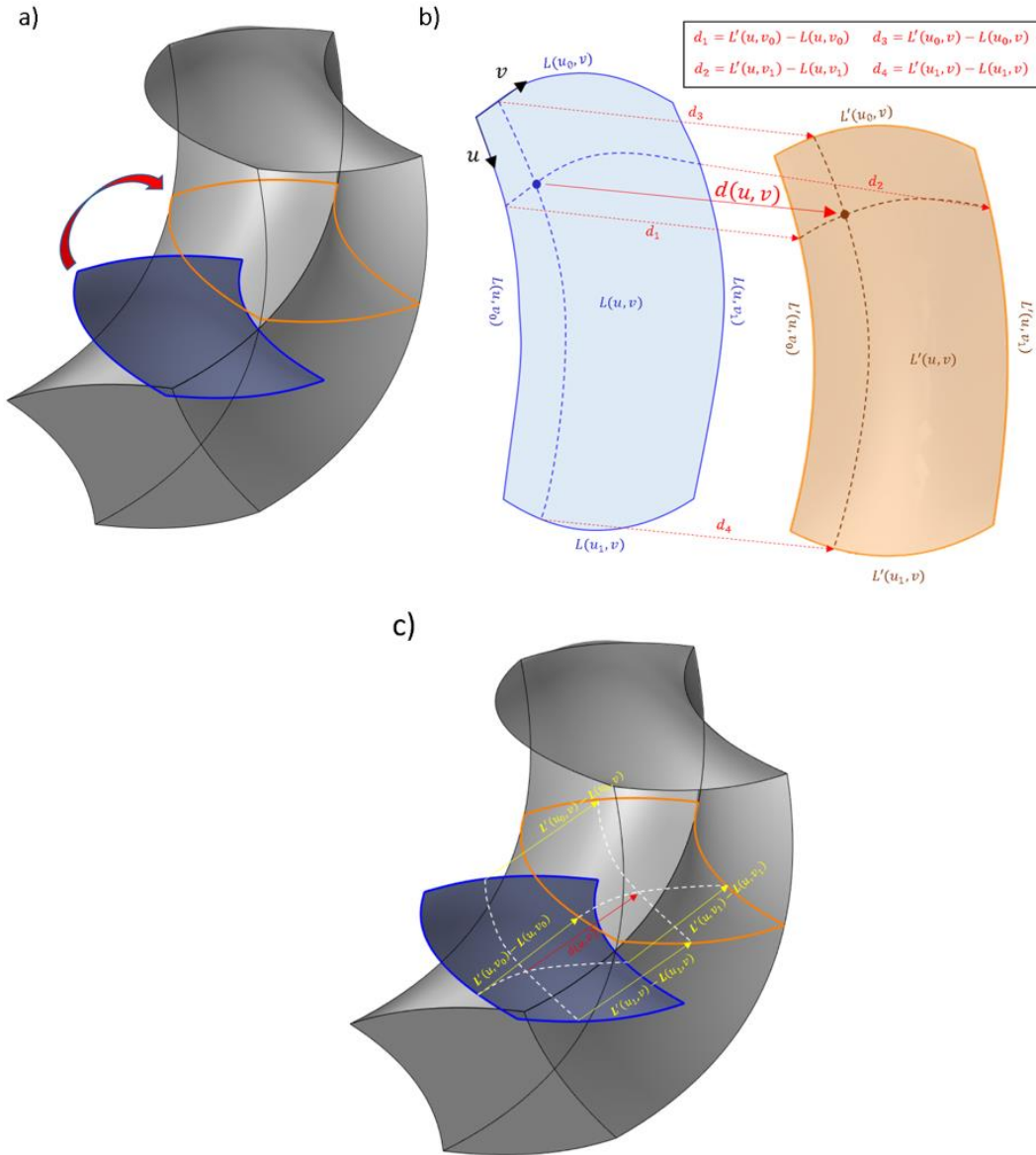


Figure 58: : a) The surface (in blue $L(u, v)$) obtained by blending the top and base surfaces may not fit to the layer outline obtained using methods of Section 3.2. The shape of the blend surface needs to be transferred to the new layer $L'(u, v)$ b) Construction of the new surface $L'(u, v)$ by using combination of interpolated displacement vectors of the isoparametric curves of $L(u, v)$

To construct the actual transition surfaces, network curves (NCs) are developed by mapping the isoparametric curves of $L(u, v)$ to $L'(u, v)$ using Equation 10. Figure 59a illustrates the resulting NCs in brown color. The designed plugin in this work generates all the AM layers using features that permit surface creation from NCs. The generated surfaces for some layers are

shown in Figure 59b. The general process of path generation of a closed freeform solid in the plugin is summarized in Figure 60. Zigzag patterns are laid out for all layers in alternate directions on the rectangular parametric domain of the surfaces. After mapping those paths, 3D curve paths are obtained on the surfaces. Figure 59c shows the 3D path on some layers, with the last couple of layers designed to have airtight hatch spacing.

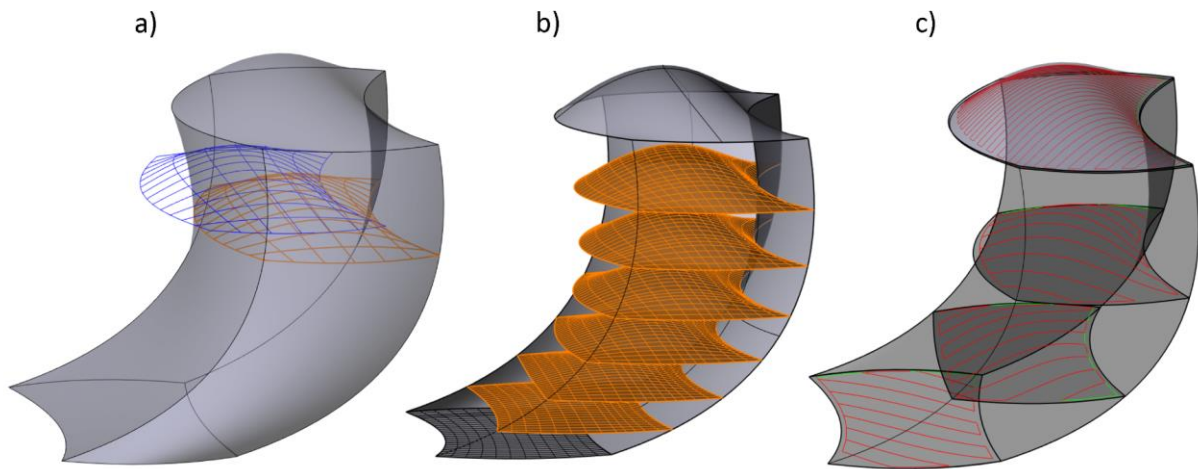


Figure 59: For some layers from a model, an illustration of a) Networks curves (NCs) blended from $T(u,v)$ and $B(u,v)$ (blue) and the modified NCs (brown) that fit inside the model, b) some transition surfaces obtained from the NCs, c) zigzag path drawn on some surfaces

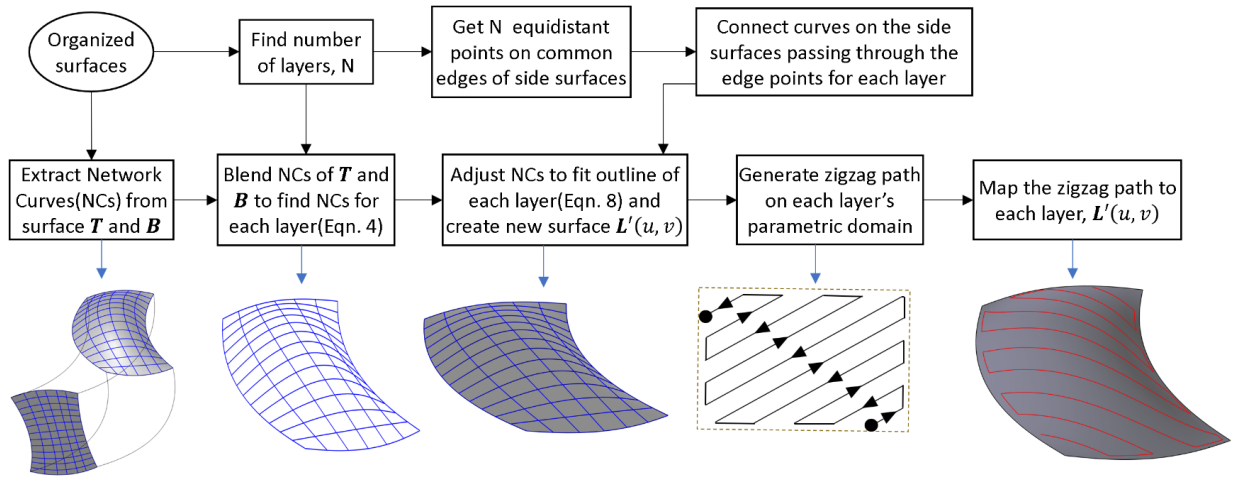


Figure 60: Outline of stages of path planning from surfaces extracted from a CAD model

A sample freeform part enclosed by completely non-planar surfaces is fabricated using the strategy discussed in this section. Figure 61a shows the freeform model whose base surface is attached to an initial part that was fabricated by normal planer 3-axis path. For comparison, the model is fabricated as a traditional 3-axis FDM using the flat layers shown in Figure 61b. The formulated 5-axis path, shown in Figure 61d, is applied to the model from the base to the top layers using a material deposition that corresponds to the variable layer spacings demonstrated in the figure. The manufacturing instant shown in Figure 61e reveals the infill pattern obtained by the generated layer paths. The same paths smaller hatch spacings are used in the final 3 layers to obtain the top surface. All the paths used, including the layer outlines paths, have tool direction defined by the TSN tool orientation. By comparing the objective of layering and infilling method, the top surfaces of the manufactured samples are compared in Figure 61c and Figure 61f.

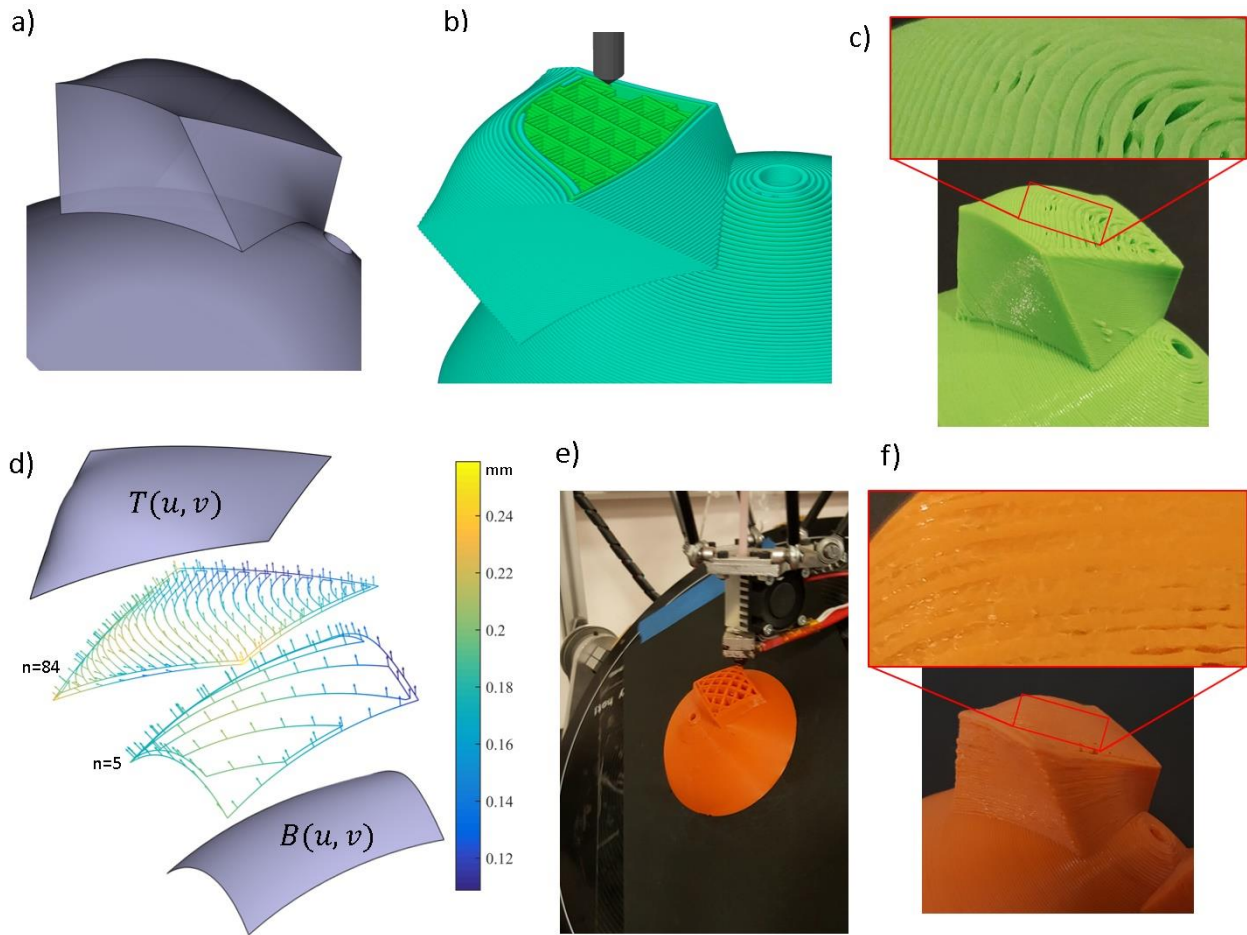


Figure 61: a) A sample freeform CAD model to be manufactured. b) Horizontal layer paths used in manufacturing the model for comparison. c) The manufactured sample using plan in (b). d) The base, top($n=85$), 5th and 84th layers with the 5-axis paths showing the layer gap distribution on the color scale and the tool directions e) The fabrication instant using the designed 5-axis 3D printer showing the infill of the proposed paths of transition layers. f) The final manufactured part using plan in (e).

For parts that can be expressed as compound models composed of the freeform model schemes introduced, the developed process plan can be adopted for such parts where the individual freeform model is fabricated in sequence. Figure 62 shows a sample compound model where the 5-axis scheme is applied for the parts 2,3 and 4. The sample layer paths, thickness distributions and tool directions are shown in the figure. The regions are fabricated in sequence part 1,2,3 and4, where the initial part is produced using planar layers.

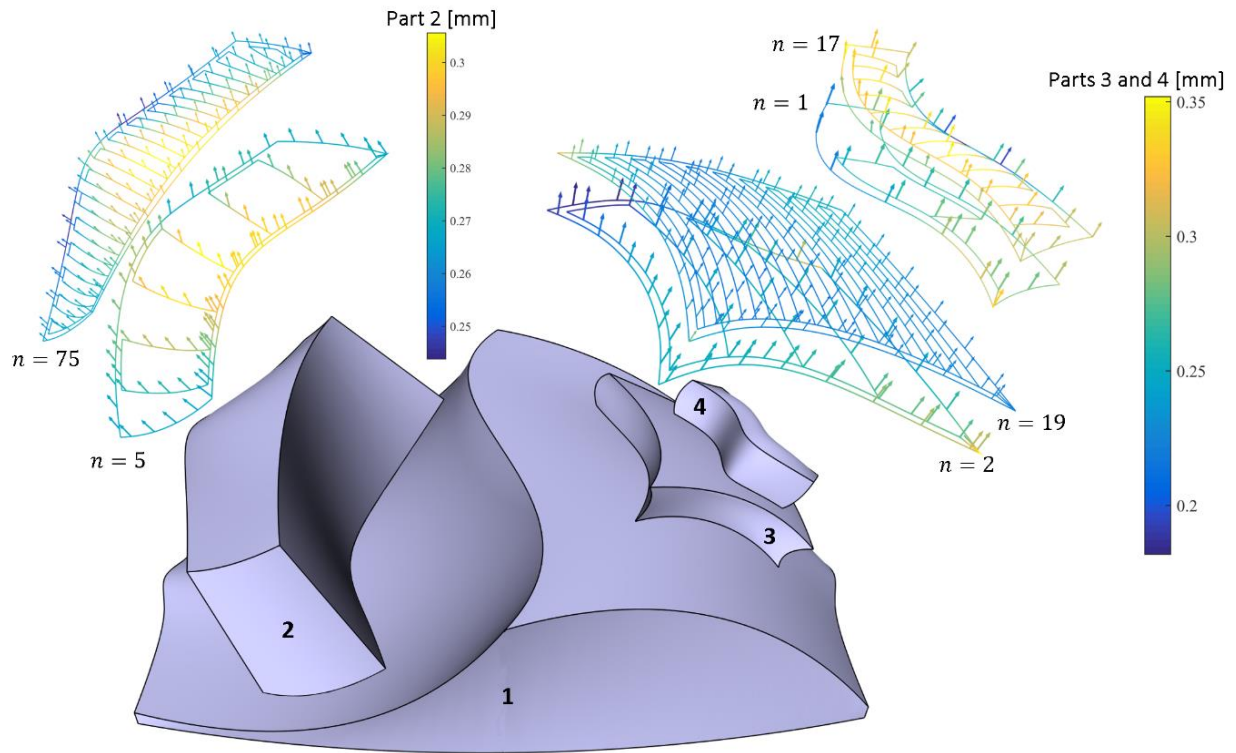


Figure 62: A sample compound model composed of regional parts is tested using the 5-axis process plan to produce sections 2, 3, and 4. The parts 2,3,4 have total of 75, 21 and 17 layers respectively

For comparison, the 5-axis additive manufacturing of the sample compound model is also compared with the horizontal layer FDM in Figure 63 .Top surfaces are showcased with reduced breaks and unevenness in many regions. The added advantage of more efficient path with less non-extrusion motion shows reduced residual drops caused by tool retractions.

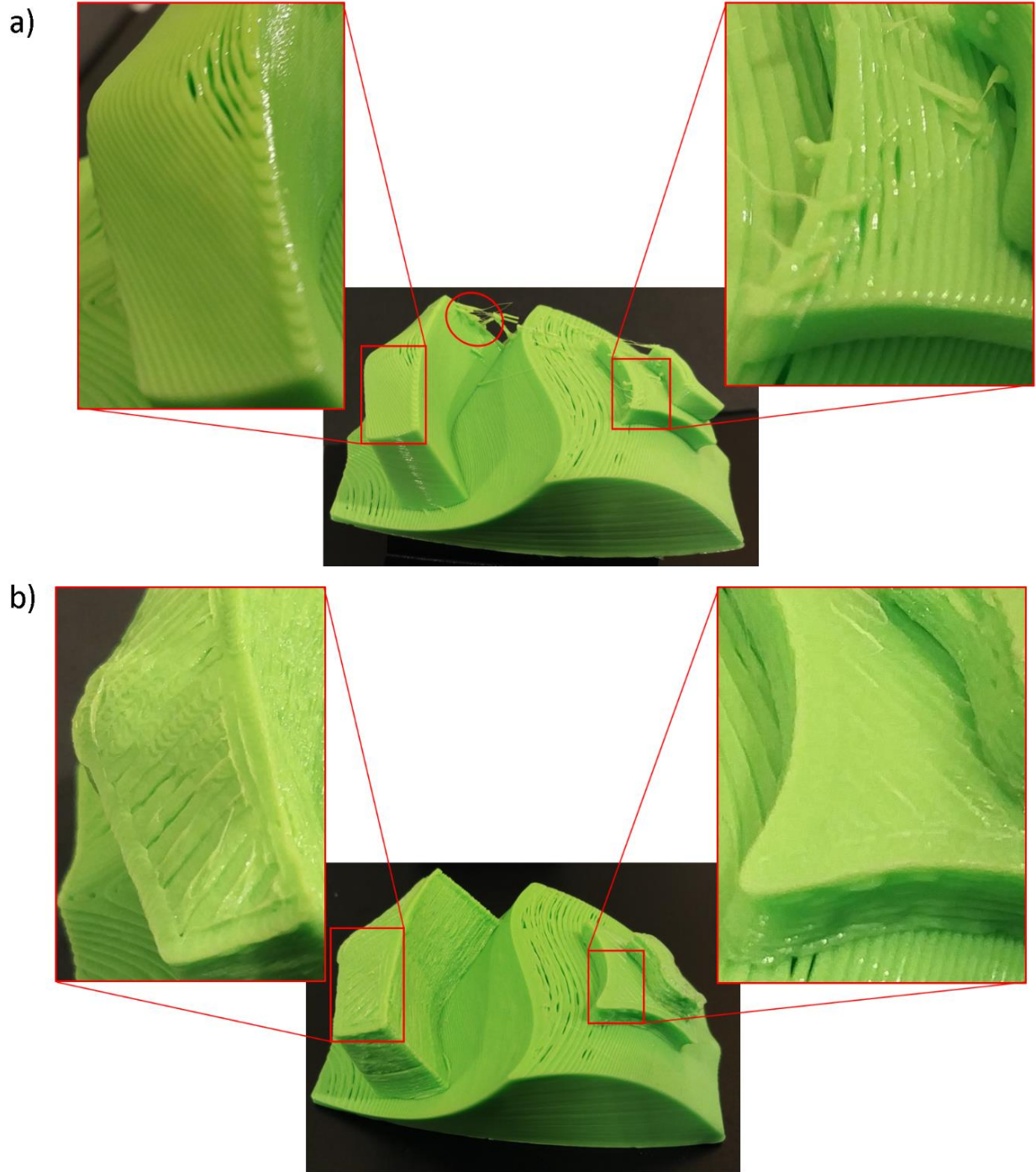


Figure 63: *a) The compound model in Figure 62 is produced by horizontal layer FDM for comparison. b) The 5-axis AM method is used to fabricate parts 2,3 and 4. Marked regions show the advantages of using the method in this work*

4.6 Evaluation of build angles and kinematic error

Generated toolpath for multi-axis AM comes with tool directions which represent the desired relative orientations of the tool with respect to the part. It is therefore required for either the tool or the part to transform to positions that correspond to the configurations. In the case of the built 5-axis 3D printer, a movable print-bed accomplishes the task of orientation.

For a desired build orientation given by the unit vector $\mathbf{n}_b = \langle n_x, n_y, n_z \rangle^T$ the corresponding angles $\phi \in \left[-\frac{\pi}{2}, \frac{\pi}{2}\right]$ and $\theta \in [-\pi, \pi]$ shown in Figure 64a are found by transforming the print-bed from the default orientation facing Z-direction ($\langle 0, 0, 1 \rangle^T$) to \mathbf{n}_b . By evaluating the inverse kinematics of the platform transformation, $\mathbf{n}_b = \mathbf{R}_z(\theta) \cdot \mathbf{R}_y(\phi) \cdot \langle 0, 0, 1 \rangle^T$, Equation 11 is obtained. Equating Equation 11 with the components of \mathbf{n}_b leads to the expressions in Equations 12 and 13. The angle θ has two solutions $\theta_1 = \text{atan2}(n_y, n_x)$ and $\theta_2 = \text{atan2}(-n_y, -n_x)$ for which ϕ is positive and negative respectively. Considering a preceding angle θ_{i-1} , there are four possible paths from θ_{i-1} to θ as indicated Figure 64b. Among the four possibilities, there is always the shortest path where the change in θ , $|\Delta\theta| \leq \frac{\pi}{2}$. The decision on the next value of θ is made using Equations 12 and 13, where the value of σ is found by Equation 14. The firmware is programmed to make the decision on which direction of rotation is shorter.

$$\mathbf{n}_b = \begin{bmatrix} -\cos(\theta) \sin(\phi) \\ -\sin(\theta) \sin(\phi) \\ \cos(\phi) \end{bmatrix} \quad (11)$$

$$\theta = \text{atan2}(\sigma n_y, \sigma n_x) \quad (\text{For the case } n_x \neq 0 \text{ or } n_y \neq 0) \quad (12)$$

$$\phi = \text{atan}\left(\frac{\sigma \sqrt{n_x^2 + n_y^2}}{n_z}\right) \quad (13)$$

Where the value of σ is given by Equation 14.

$$\sigma = \begin{cases} 1 & \text{if } |\theta_1 - \theta_{i-1}| \leq \frac{\pi}{2} \text{ or } 2\pi - |\theta_1 - \theta_{i-1}| < \frac{\pi}{2} \\ -1 & \text{if } |\theta_2 - \theta_{i-1}| \leq \frac{\pi}{2} \text{ or } 2\pi - |\theta_2 - \theta_{i-1}| < \frac{\pi}{2} \end{cases} \quad (14)$$

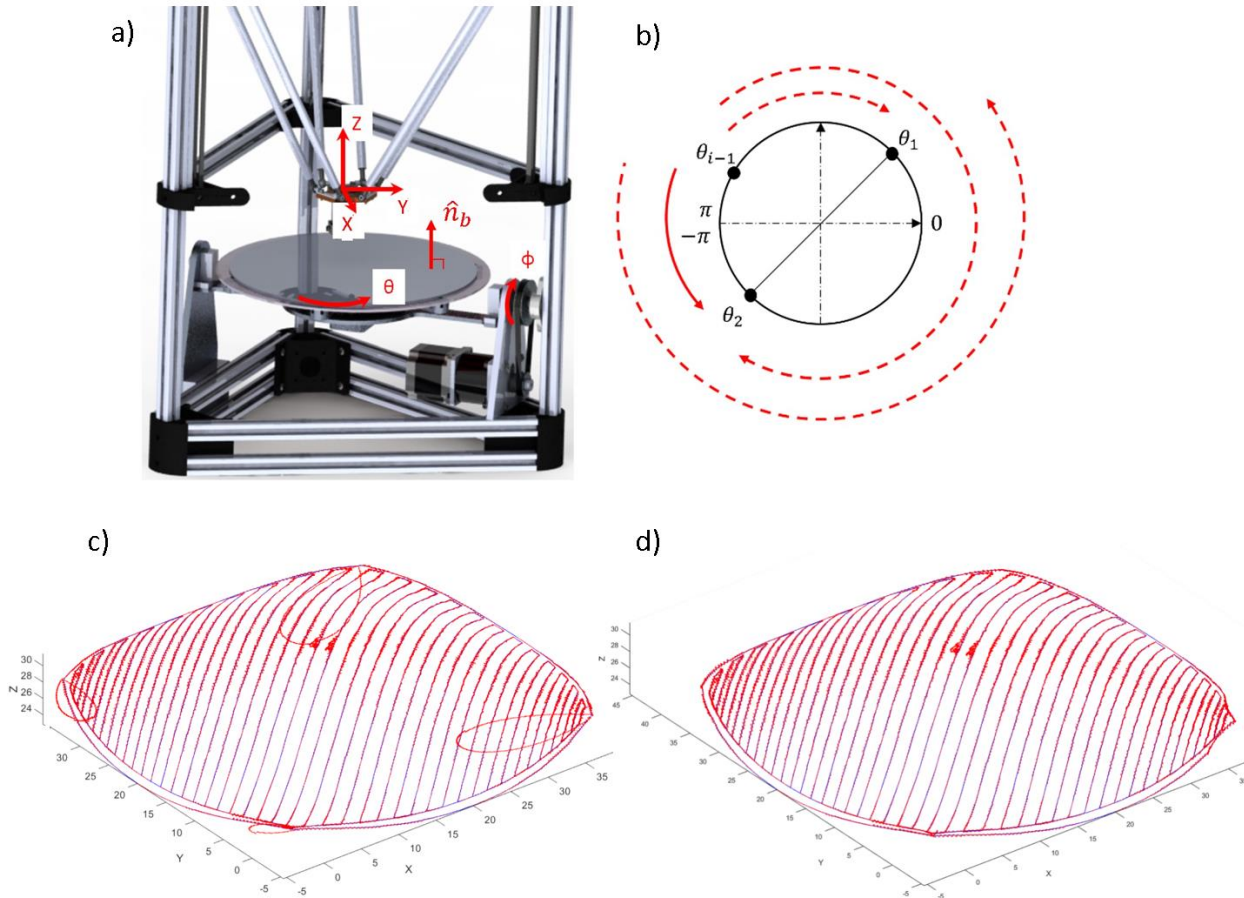


Figure 64: Print-bed that can be oriented to a desired build direction. b) The four possible paths of θ solution c) Path simulation of the machine path obtained from G-code showing undesirable loops d) Reduced error after implementing the patching to the path of θ angle

A critical point in 5-axis inverse kinematics is when $n_x = 0$ and $n_y = 0$. Theoretically, Equation 11 does not have a solution for θ at this location, and axis C does not have any influence on the orientation of the print-bed. Practically, near this point, dangerously abrupt motion of axis C can occur. This complication is ascribed to the interpolation carried out in the numerical control units in joint space of the base platform. Within the interpolation spectrum, the singularity can be

traversed and large non-linear deviation from the planned path can be observed. The large deviation is caused by the fact that the change in consecutive θ values can be large even when the change in \mathbf{n}_b is very small. As a remedy, Affouard et al. [107] adopted the concept of singularity cone to account for the uncertainties in the angle ϕ . It provides a range close to the singular point where the solution using Equations 11 can lead the tool to traverse the singularity point. Whenever a path points are detected within the singularity cone, the values of angle θ are obtained by patching between two points, one before entering the cone, the other after exiting it. Decision on how far the points must be from the cone is made based on the path length and change of angle θ between the two points. The method used in for the developed system is the combination of the singularity cone idea [107] with a C-axis patching strategy [108] proposed by Grandguillaume et al. A look-ahead scanning and correction of the sharp changes in the angle θ is implemented as shown in Figure 65b. Improvement of achievable by this patching is demonstrated in Figures 64c and d.

It is important to point out that interpolation on the transformed position implemented in the firmware generates kinematic error at all interpolation steps within a line segment. The presence of angular positions makes the error different from mere linearization error. Although, the error increases when the configuration of the bed is close to singularity. It becomes crucial to estimate the magnitude of these errors for every path g-code before the commands are sent to the 3D printer. Kinematic errors are computed using the method outlined by Makhanov et al. [109]. The errors are obtained through evaluation of the difference between re-transformed path (from printer to workpiece frame) of interpolated g-code points with the original desired path. The estimated result of the kinematic error of the impeller blade path is shown in Figure 65a. During path planning, the path is sampled at curve length of 0.6mm while the interpolation resolutions of 0.1mm for each of XYZ positions, 0.02mm for filament extrusion, 0.06° for B axis and 0.1° for C axis are used. It should be noted that decreasing these resolutions will not improve the kinematic error and decreasing the sampling curve length will lead to increase in manufacturing time and large size of g-code files. The estimated error plot is used for g-code inspection before 3D printing.

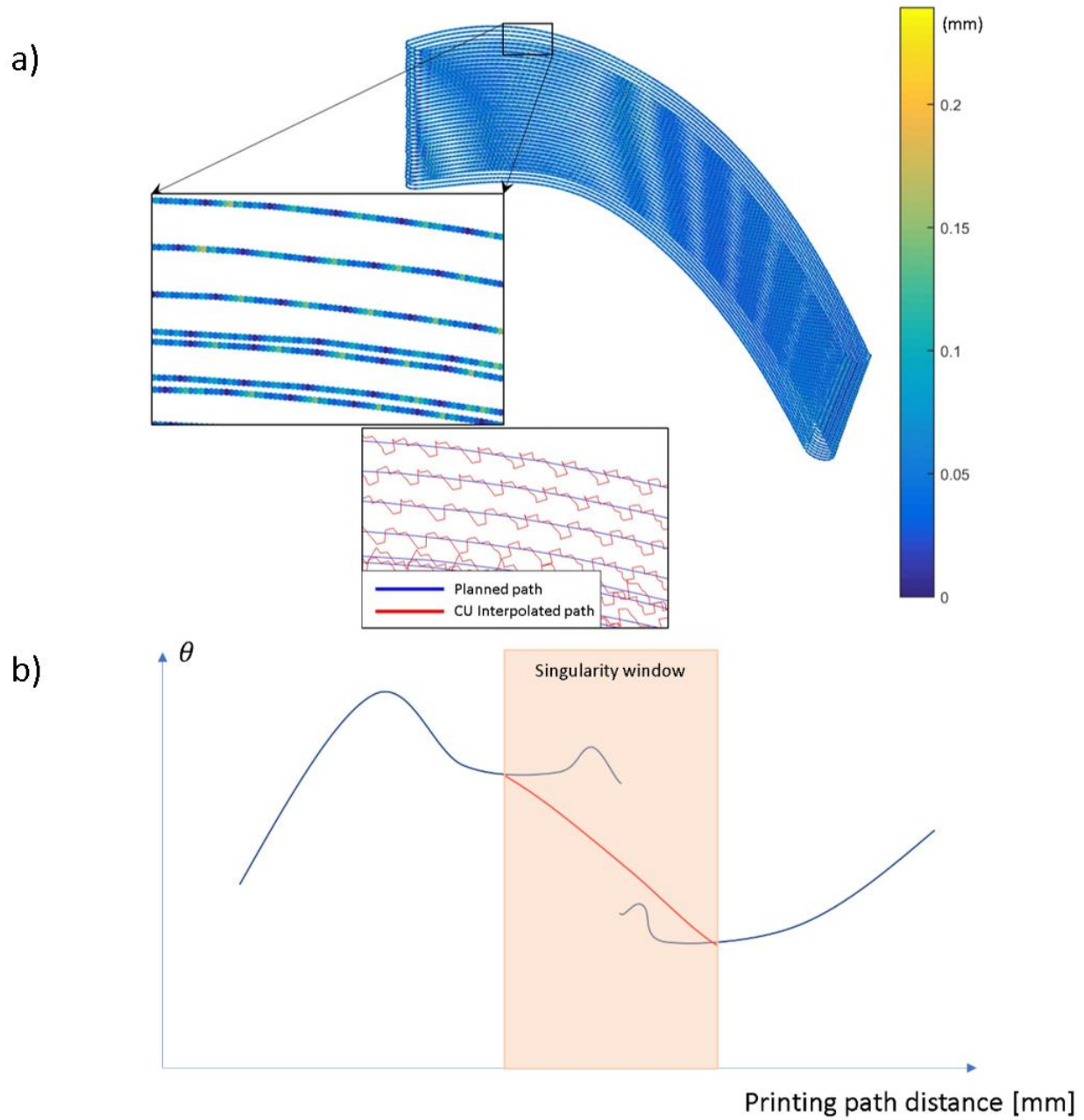


Figure 65: a) Distribution of kinematic error and plot of interpolator trajectory along the deposition path of the impeller blade fabricated in Figure 57 b) The patching method using look-ahead algorithm.

4.7 Conclusion and discussion

Using a designed and built 5-axis additive manufacturing system, process and path planning techniques are studied for arbitrary shell and solid freeform components. Software script that performs the functions of both toolpath generation and postprocessing are programmed. By connecting mapped parametric lines on the side NURBS surfaces of a solid part, 3D curves that transition from the base to the top profile of the wall are obtained. Using these curves along with side surface tangent tool orientation, shell parts are shown to be fabricated without staircase effects. The idea of transition layering from base to top surface of a solid freeform part is introduced. AM paths are planned on the constructed surfaces with surface-normal tool orientation to prevent staircase effects on the top portion of the freeform solid parts.

Even with the presence of kinematic errors, the benefits of using the stipulated path planning strategies are apparent on test specimens. For the freeform filled sample fabricated in this chapter, the ideal tool orientation along the outline of each layer should be obtained by the SST rule indicated in Section 4.4. This orientation is not used because of the requirement for numerous fast retractions that cannot be realized on the 3D printer. When the retracted nozzle in a layer is not repositioned quick enough, the filament material oozes out, thereby affecting surface quality of subsequent layers. This is caused by limitations on speed of the control system and motors.

This study explores new methods of 5-axis additive manufacturing of freeform models to maintain surface quality and provide efficient toolpaths. Improvements are still required in actuation, control system, and reduction of kinematic errors.

Chapter 5

THREE-DIMENSIONAL SCANNING AND RECONSTRUCTION

5.1 Introduction to 3D Scanning and Reconstruction

3D scanning (or digitizing) refers to the use of a 3D scanner or any measurement device to acquire data for the purpose of reconstruction of shape and computer-model features. The device used for such data acquisition in 3D scanning are referred to as 3D scanner, or in some cases 3D digitizers. The data acquired by a scanner can include point positions texture and color. 3D scanners are grouped into contact-type and non-contact-type 3D scanners. The non-contact 3D scanner can be further divided into active and non-active groups. While active scanners usually make use of a light source, the passive ones do not have such additional energy requirement. For most of the scanners, there is usually a measurement head attached to a positioning mechanism for control of measurement location.

While 3D scanning is closer in definition to the derivation of primary data from an actual physical object, reverse engineering (RE) has a wider definition where the whole process of creation of virtual model from an object is enveloped. Hence, 3D scanning is used to refer to the measurement portion of reverse engineering while reverse engineering is expected to culminate in the complete development of a computer model. In product design process, an engineer usually begins with drawing up details of a part, with which solid or surface models are constructed and processed to obtain a complete CAD model, which can be used to make manufacturing plan. The designed product undergoes a manufacturing stage where the model is accurately fabricated into a physical object with a mechanical and chemical characterization. The process of reverse engineering is given in Figure 67 [110]. The “reverse” in RE alludes to the converse process which starts with an actual object and ends with a virtual model. This virtual model is three-dimensional (3D) computer representation of the object. 3D models can be volumetric or surface representations depending on the type of data represented. Volumetric 3D model contains local properties of internal features while surface 3D model contains only external features. Volumetric reconstruction will require radiative methods like computer tomography to see inside of an object [111]. As such study is out

of the scope of this work, the term “3D model” will be delimited in definition to refer to 3D surface models. For the construction of a surface model, the primary data is the positional information that define how the shape of the surface is. The position information is usually in a collection of points termed points cloud. The virtual model or data structure obtained by RE can be used in the design stage of product development. It may also serve as a means of part replication or aid in part inspection and quality control. RE can be carried out in single-point, points-array, 2D-points, or 3D-points depending on the nature of the application. For single-point systems, the data acquisition of carried out in point-wise basis. Most CMM devices can be used to measure surfaces by acquiring positional data point by point. The drawback of the 1D systems is that they are not suitable for large data acquisition due to the limited speed and excessive cycles needed.

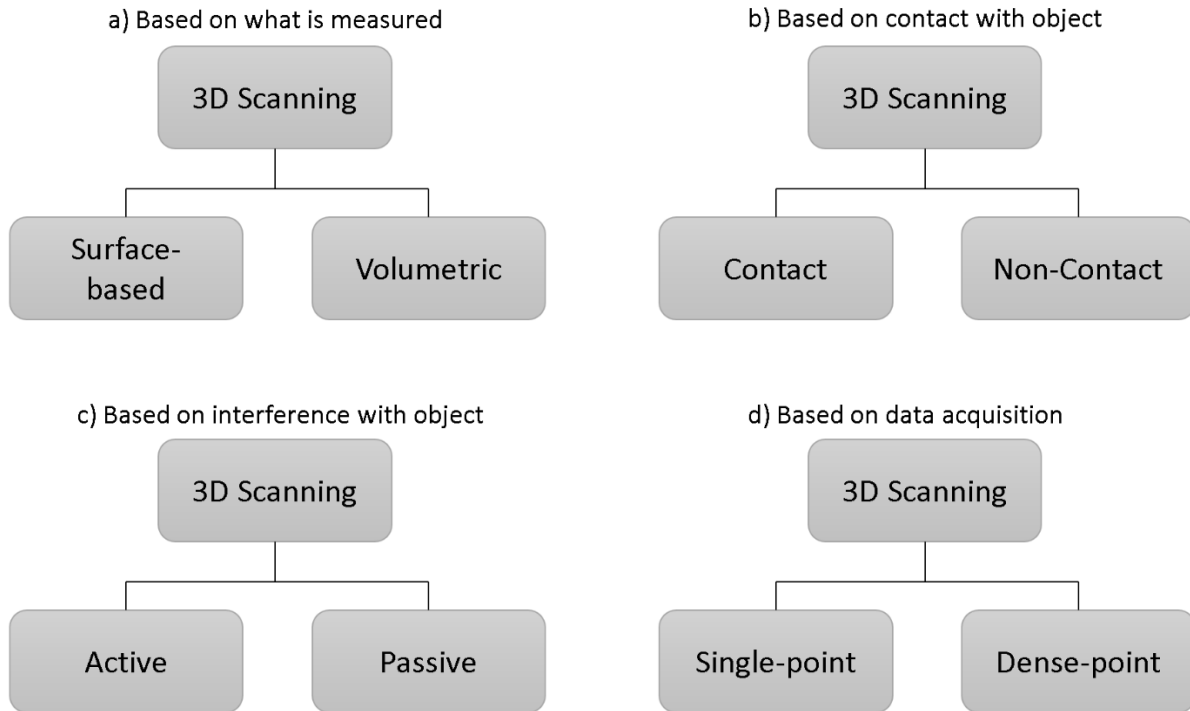


Figure 66: Grouping of 3D scanning using different basis

3D scanning can be grouped based on four different criteria shown in Figure 66. When the nature what is measured is considered, we can classify 3D scanners as surfaced-based and volumetric measuring devices. Surface scanners analyze the exterior of an object with no regards to what is

within. Volumetric scanners, on the other hand, measure the interior of an object usually without destroying it. The second criterion of classification is based on requirement of force to be exerted on the object. Based on this criterion, 3D scanners can be grouped into contact and non-contact types. Contact type scanners are characterized measurement through physical touching of an object's surface. They require that the object being scanned do not get deformed or damaged on the exertion of force as that could lead to an erroneous measurement. Coordinate Measurement Machines (CMM) fall under this type of scanner. A tactile probe is attached to a robotic structure that controls probe location. Through displacements along each axis, the probe issued to measure surface of objects manually or by automated computer routine. For the non-contact types, there are Time of flight, phase shift and laser triangulation scanners.

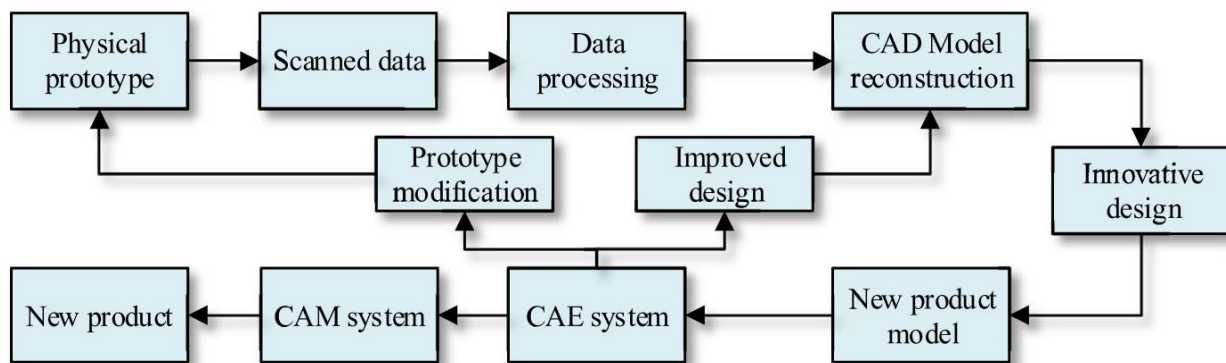


Figure 67: Process of reverse engineering in product development [110]

The process of reconstruction to a virtual model is particularly important for three classes of objects. First class consists of object that do not have computer models. Such objects do not undergo any systematic product development process. They can be biologically created entities—like human face [112,113], tooth [114] and plant leaves [115]—that result from cellular growth and development. Whenever these parts require accurate geometric reconstruction, reverse engineering needs to be conducted. For instance, when designing a prosthetic limb, it is required to match the interface region of the limb with the prosthetic. In addition, attempts at reconstruction of human face from image to analyze identity or emotions is an example of RE application in biological system. Applications seeking to interface natural objects with the digital world lean to

RE, as in computer generated imagery (CGI) in the entertainment industries, patient-specific digital model integration in medicine and augmented reality. The first class also contains naturally and chemically formed entities, the likes of landscapes mapping and urban reconstruction. There are also obsolete components and objects whose shape changes in application. The former kind of parts are usually not an outcome of the modern engineering product life cycle process. This type of parts may be a result of a natural, artistic or uncontrolled process where there is no sufficient virtual planning in form of a computer model. Reconstruction of the mentioned objects find applications in fashion design, medicine, terrain mapping, archeology and entertainment industry. There is a computer-vision-interest in human-like intelligent feature extraction[116]. An automated scanning device was designed by Chan et. al.[117] to make preliminary scan of different faces of a sample model with unresolved registration and refraction problems.

5.2 Relevant Literature Work on 3D Scanning

3D scanning systems emerged around the 1960s where light sources, projectors and cameras are used to carry out reverse engineering job[118]. It was a time consuming and laborious process because of the limitation in equipment. The development of in CMOS sensor was predicted to have great impact on 3D digitizers[119]. The required improvements then were enhancements in low-light sensitivity and noise.

The reason why conventional coordinate measurement machines (CMM) have been widely utilized as a standard measurement device for over 40 years is due to their high precision contact sensors that satisfy industrial standard[120]. Beyond their accuracy, CMM can be expensive and slow. The low speed is due to the fact that data acquisition is carried out point-wise as the probe is displaced continuously. It does not support fast and efficient instantaneous linear or 2D data acquisition prevalent in image sensors. Moreover, probe-type measurement devices are incompatible with flexible or deformable parts and reaching some points in complex geometry can be challenging. Therefore, there is benefit in exploring possibilities in non-contact multi-points acquisition-based scanners for geometric reconstruction.

In light of contact-type CMM drawbacks, non-contact measurement devices have gained some interest in recent years and have taken an integral part in various industrial applications.

Several commercial products—referred to as 3D scanners or digitizers—have also emerged. Most of the scanners use led-based projectors or lasers as illumination source. As outlined by Molleda et al. [121], led projectors provide more uniform illumination and sharper edges. However, due to size and cost constraints, a class of non-contact scanners that uses laser as a source of light to project known pattern on geometry is of particular interest in this work. In addition to illumination, an important feature of scanners is image sensing. The popular camera sensor types are complementary metal oxide semiconductor (CMOS) and coupled-charge device (CCD). Based on size, functionality, performance and cost, CMOS is preferable in most machine vision applications [120]. The choice of camera resolution is made based on computation capacity and speed requirement.

Theoretically, by optical diffraction limitation imposed by Rayleigh’s criterion, the scanner camera used should be able to resolve distances greater than about 3 micrometers taking a typical lens f-number as 4 [121]. However, the actual accuracy of triangulation laser scanner can hardly reach around 30 microns even in a controlled environment [122]. Systematic errors arising from laser source, reflection surface, lens defects and environmental non-uniform illumination are the cause of increased uncertainty. In addition, image sensor noise adds error to measurements and partially occluded width of the light beam will give wrong data at some regions.

An important estimation made in scanners is assuming that peak point or center of laser image corresponds directly to the central axis of the incident beam. It is not always the case as Zhou[123] found an expression that estimated form error originating from deviation of stripe beam mass center shown in the equation (Equation 15) below with variables illustrated in Figure 68. The laser stripe with width l_0 is assumed to obey Lambertian reflection law and lens radius is assumed to be small. It was shown that the expression corresponds with the experimental form error [123]. This expression applied to our scanner gives less than 15 micrometer error.

$$\Delta x = \frac{l_0 r_l \tan(\gamma)}{a \tan(\beta)} \left(1 - \frac{R \cos(\beta)}{a}\right) \left(1 + \frac{2R \cos(\beta)}{a}\right) \quad (15)$$

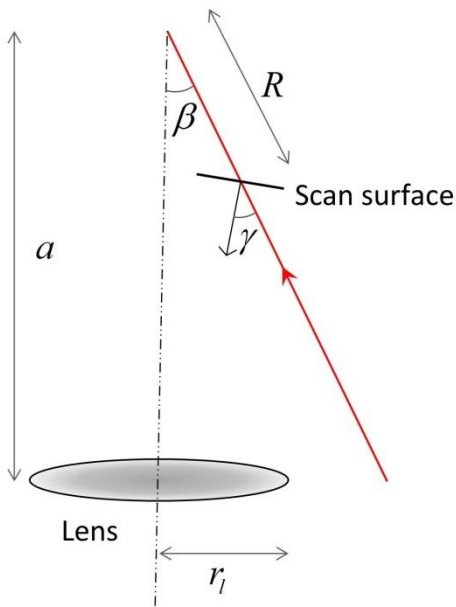


Figure 68: Illustration of variables used in estimation of Zhou's central axis error

Studies on estimation of uncertainty in laser reconstructions of geometric part have helped shed some light on how the magnitude of error is implicitly related to the part geometry. Isheil [124] found that angle between laser plane and camera axis, significantly affects local error of measured part. Angles exceeding 400 for regions around 100mm from camera were observed to contribute systematic error higher than 15 micrometers. The random error is also found to have magnitude reaching 30 micrometers. Common sources of error in 3D scanners are displayed in Figure 69. By geometric intuition, Curless and Levoy [125] provided instances where positions of sensor, surface and illuminant could result in erroneous measurement. Occlusion and discontinuities in reflectance or shape were mentioned as sources of errors. Laser scanners extract stripes resulting from the intersections of central plane of incident laser line beam with the scan object. The laser line beam is not a perfect plane because it has width of about 0.5mm to 1mm depending on the imaging sensor. It becomes critical to quantify the form error that arises from the surface form of a measured object. Zhou[123] derived an expression that estimates form error originating from deviation of reflected stripe beam center and the original central incident plane for a Lambertian reflection with relatively very small lens radius. Uncertainty approaching magnitudes of 15 micrometers were ascribed to the mentioned form errors. The form dependence

of laser structured light scanners has made standardization rather difficult. In most cases, a known geometric model is used as measurement benchmark of such scanners. In the designed laser scanner, the benchmark geometry is used for not only validation of scan results but also to reduce positional and systematic errors. In general, the global error in commercial 3D laser scanners has been analyzed in detail in literature [122,124,126], they generally possess errors ranging from 40 to 300 micrometers. Their uncertainties are usually about one order more than contact type scanners [127], which is why probe-type CMMs are still predominantly in use.

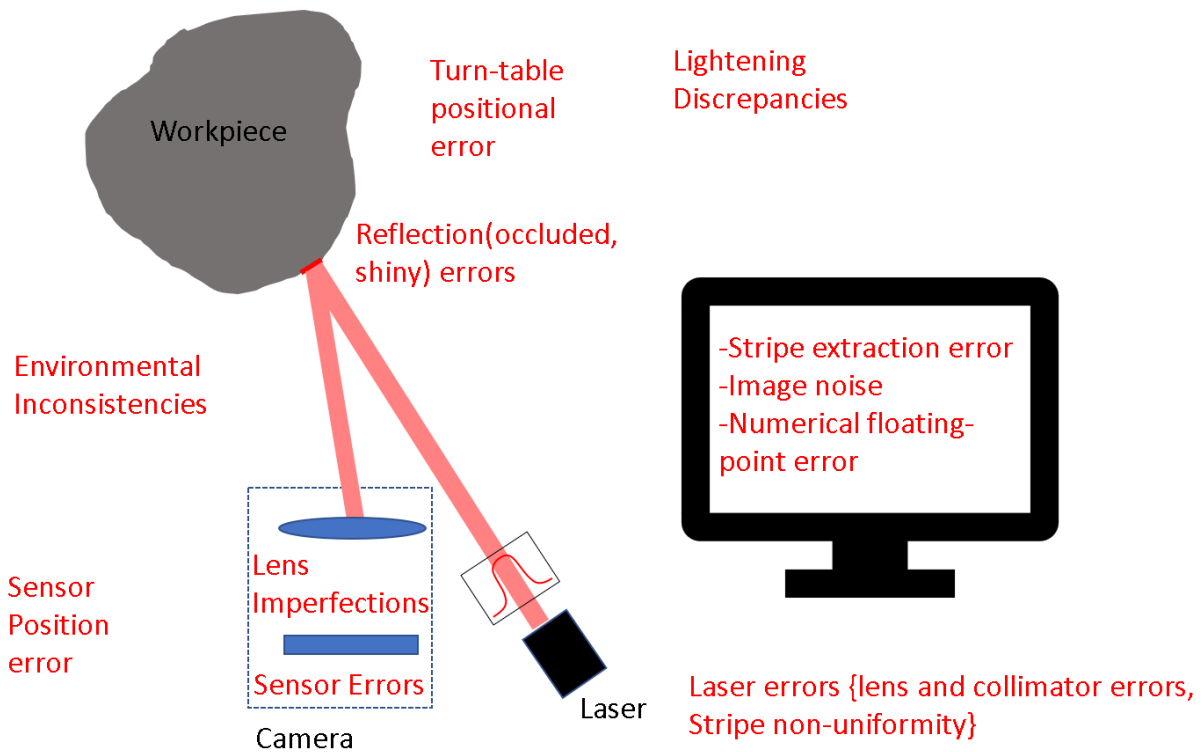


Figure 69: Map of some sources of uncertainty in 3D scanner

5.3 Three-Dimensional Scanner Design

Laser scanner designed with two cameras is suggested by Davis and Chen [128] to avoid moving parts that lack repeatability during calibration to reduce cost and complexity. The multiple views from the scan space are sent to each camera with the aid of mirrors. There are various designs 3D scanners, with some having multiple lasers or imaging sensors. The use of multiple lasers is to make the reflected laser beam more visible at some regions by varying the incident beam angle.

In the work of Fan et. al. [129], Structured light scanning system is placed on a 3D gantry with two planar motion and a rotation to capture rigid objects in large areas. Objective function is developed to determine the optimum scanning view after an initial space exploration scan. The designs of the positioning mechanism is usually a cartesian gantry, a parallel arm or a robotic arm. Some are designed to be handle by human hand, the simplicity of which cost this type of devices' accuracy and precision.

5.3.1 Previous Work in MARC

As part of the process of CAD file construction for additive manufacturing, Bank [40] worked on 3D scanning in the Manufacturing and Automation Research Center(MARC). It works by image acquisition of the reflected laser beam from a scan object placed on a rotating stage. The image is acquired using an image sensor and a red-light line beam generator is used to project a thin beam of light vertically on an object (Figure 70).

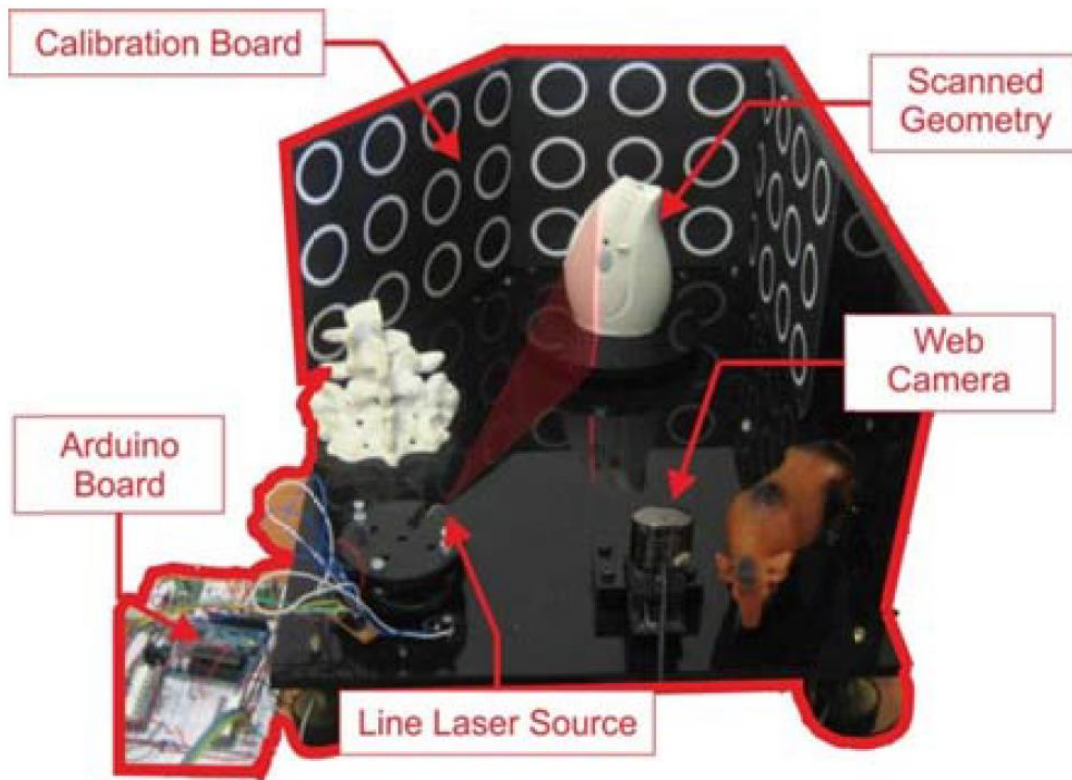


Figure 70: Previous 3D scanning device designed in MARC

Known planar circles are used to calibrate the transformation matrix between the camera and the measurements from the laser images captured. The decrease in cost of sensors and equipment led to the increase in 3D scanning application in rapid prototyping. As part the work on open architecture hardware systems for rapid prototyping, the economically feasible components like off-the-shelf camera and lasers are used to demonstrate the possibility of reverse engineering to acquire points. The laser stripe image captured with the webcam is processed using MATLAB's Image processing Toolbox. The triangulation phenomenon where three points consisting of a camera, laser and a point on the reflected laser light on the object form a triangle is used to obtain the depth information from a 2D image.

Sample results from the 3D scanner are shown in Figure 71.

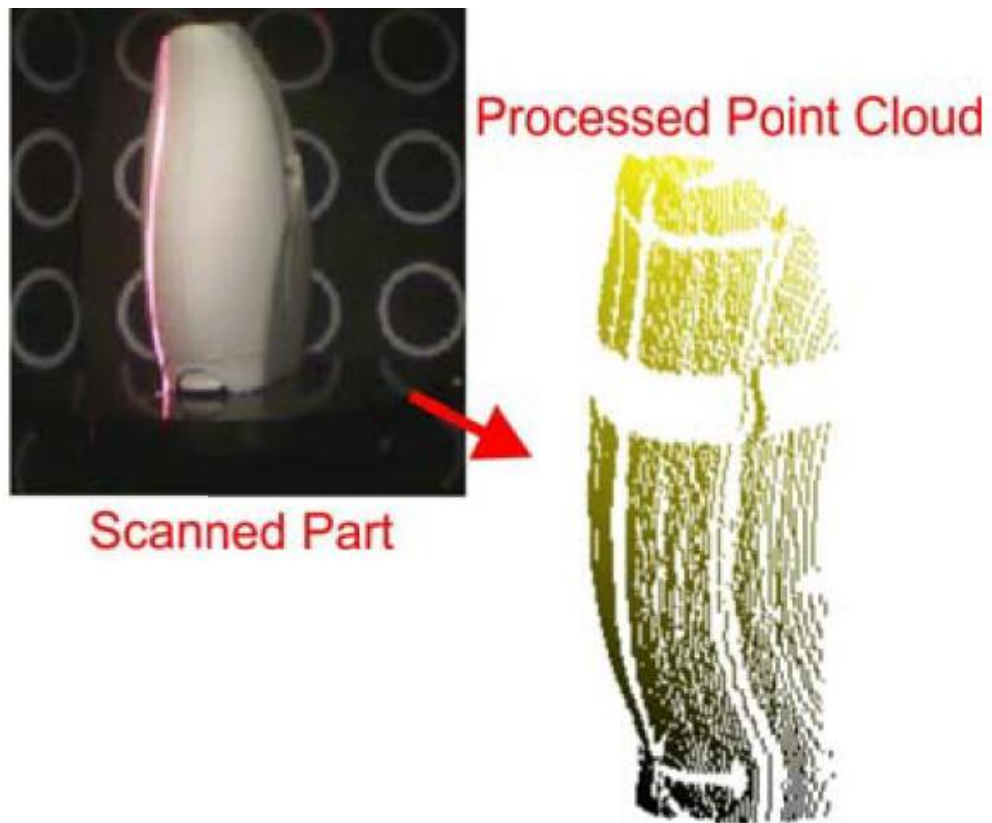
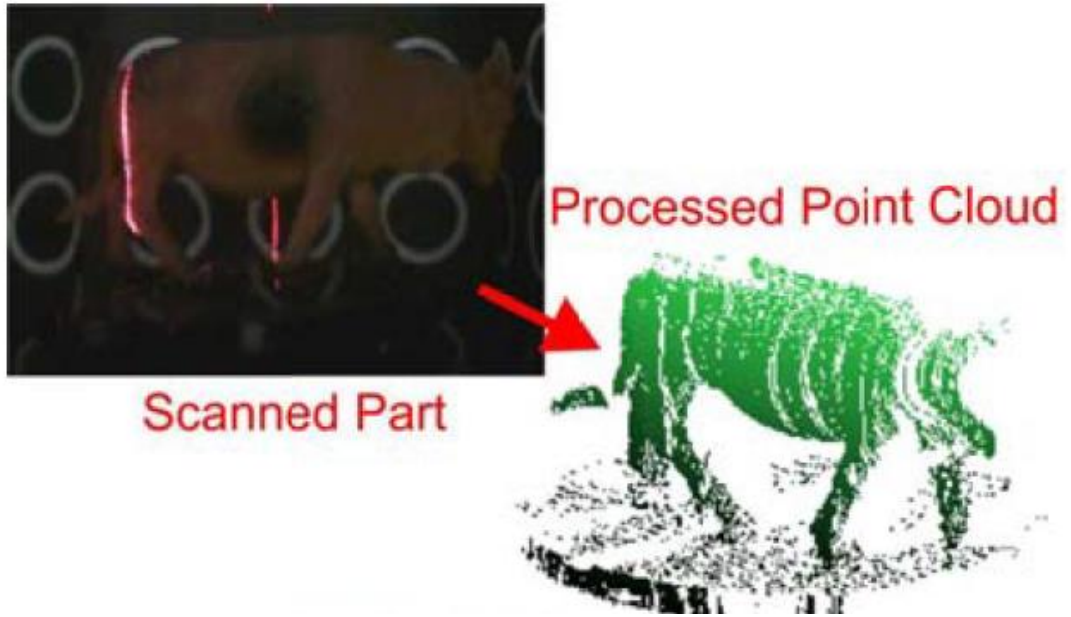


Figure 71: Processed scan points using the old MARC 3D scanner

In Figure 71 shown, there are visible inconsistencies in the point cloud with several portions missing point representation even though there are no observable changes in the actual part in those regions. There are two possible reasons for those omitted data. First, the laser angle used could be too large rendering many of the reflected laser stripe invisible to the camera. This is the major disadvantage of using large laser angle against the advantage of obtaining higher resolution along the stripe. The required compromise usually tilts towards making the laser stripe more visible since high resolution is worthless without the ability to access the data. Secondly, some empty regions in the scan point cloud result seem to occur along some step rotation steps. Such can be caused by errors in the step motor or in its control. There is a need to resolve this issue and obtain more uniform distribution of points for better reconstruction of surfaces. While point clouds were generated using this set up, there was no attempt to evaluate the accuracy or consistency of the measurement. A measurement method is only as good as its verified reliability in accuracy and precision. There is also the requirement for wider views/poses, standard deviation evaluation and accurate or optimum ways of measuring relative positions and orientation of relevant sensors and actuators. An additional preferred feature is the ability to scan in normal environment (not just closed dark environment).

5.3.2 First Prototype

The drawbacks of the first MARC 3D scanner were studied and some changes were done on the same setup. The equipment used was changed since there are better sensors, actuators, lasers and adapters. To be prevent having the undesired gaps in the point cloud, the following improvements were made:

- The line laser was changed because the previous one was not generating uniform light beam and most of the light was barricaded by a tape attached to half of the beam aperture to convert a cross-beam to a vertical line beam. As a matter fact, the wrong type of laser was used, and the laser beam was non-uniform along the line. Considering that, a new line laser was purchased and tested as shown in Figure 72 setup.
- The camera was changed to Logitech's full HD C920 camera that can capture High Definition videos at 30fps. The camera is a major improvement on the old one where very

low-quality videos can be captured and only software-based 10-megapixel photos can be capture with lots of noise, low contrast and severe distortion. The old camera also had a bad plastic lens and weak light sensor. The new upgrade consist of a 1/3'' sensor (or 6mm diagonal) light sensor and a high precision glass lens.

- As pointed out previously, the high laser angle (the defining angle between the camera focal axis and the laser plane) causes more reflected laser beam to be occluded from the camera. As a result of this, the laser angle is kept below 18^0 . The lower angle increases the possibility of the visibility of the beam. As mentioned by Sliwa et. al.[130], it is common to reduce these omitted points by reducing the laser angle and increasing viewing options.
- Finally, the turn-table rotation was improved with better micro-stepping control board that supports more current. This results in more precise rotational motion that should eliminate the missed stripe points in the preceding results.

The resulting point clouds after specified adjustments are shown in Figure 73 . There are more points scanned and fewer empty patches are seen. Those patches are more visible at the polygonization stage of the points which is explained and carried out in chapter 8.

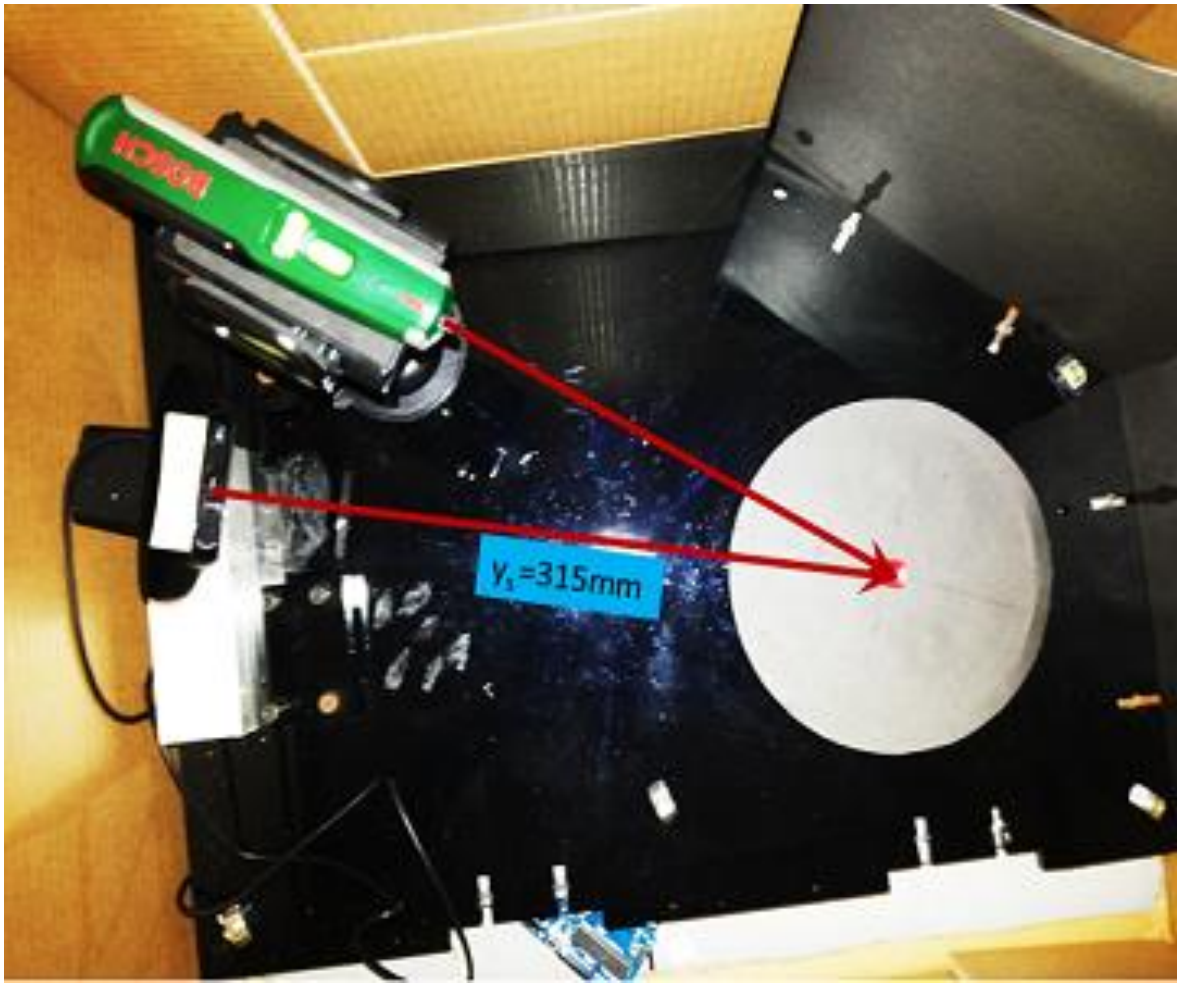


Figure 72: Image showing the new camera and laser used on the old 3D scanner setup

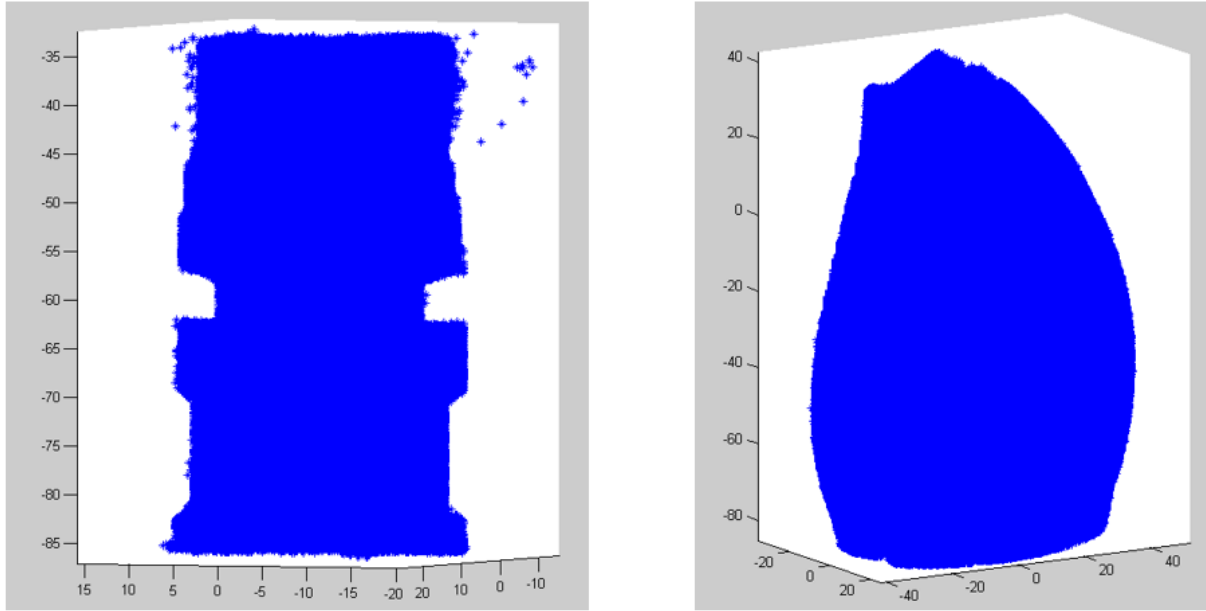


Figure 73: First results obtained from upgrade of the previous 3D scanner

A common limitation observed in the setup with fixed camera, fixed laser and rotating a scan-object, which is also the same limitation available in commercial products[131,132], is that it cannot scan regions that are at the top of the object. In fact, surfaces whose normal direction deviate too much from the camera view (any angle above tentative angle of 60°) when the laser beam is incident on it will not be visible enough to the camera. This problem hinders this type 3D scanners in their applicability in the rigorous industrial environment where there can be very complicated parts. While most of the available motorized scanning systems sample view space by uniform rotation on a turntable[129], Having only one degree of freedom does not provide enough viewpoint to capture all of the scan-part. To address this, A new design concept is envisioned, where a lifting frame that supports the camera and laser system is movable over the object to be scanned. Figure 74 shows the initial physical design considered where the motion of the lift frame is controlled by another motor placed on the rigid platform.

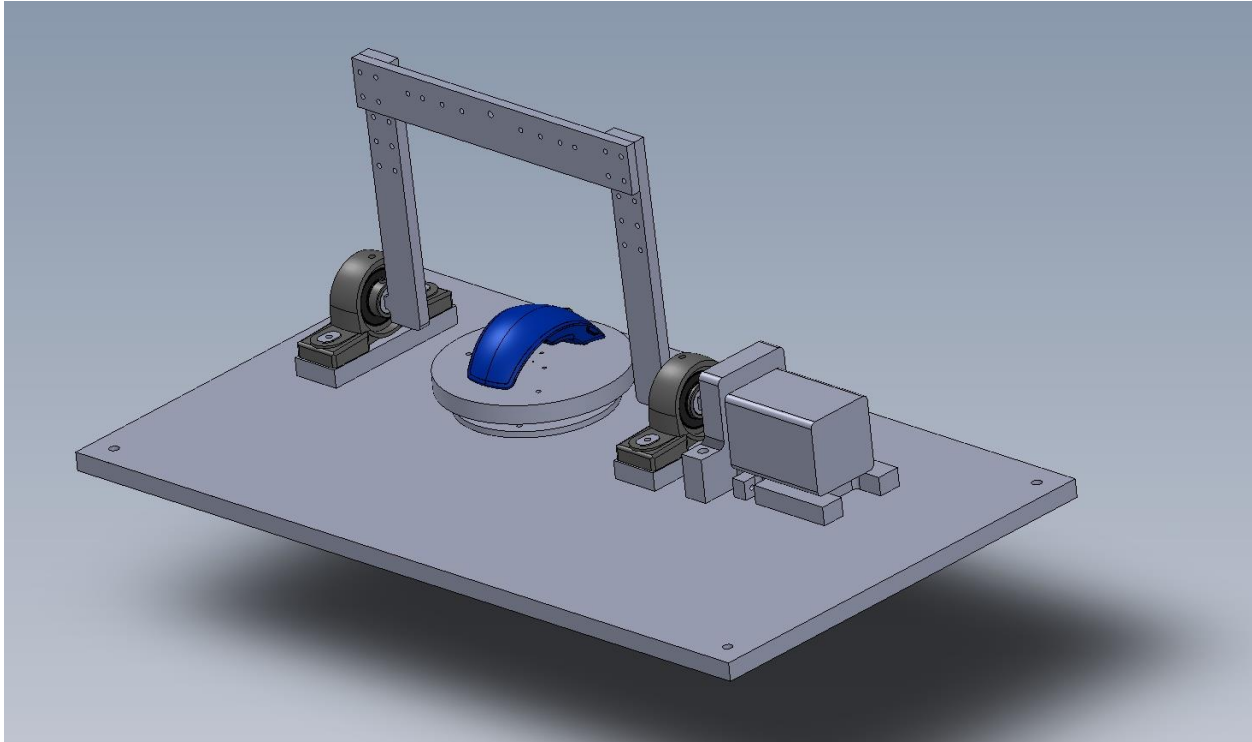


Figure 74: New design concept to increase the scanning viewing space

5.3.3 Second Prototype

The second prototype of the 3D scanner is aimed at providing more flexible motion freedoms to capture image from as many poses of the object. The scanning system where the scanner and laser are fixed do not provide sufficient mobility scan the top of an object. On account of this, the idea of using a moving frame that carries the camera and laser was proposed. The system provides a spherical motion system between the workpiece and the camera frames.

The physical design with the movable camera-laser system was initially conceived using three beams to construct the frame as shown in Figure 74 . The design in the figure was manufactured and tested to obtain proof of concept. By studying the components design, it was observed that the lift frame is the most critical design component because the lifting mechanism requires the highest power and design of the lifting frame is critical in ensuring accurate positioning and flowless motion. The frame designed by joining 3 beams could not satisfy the positioning accuracy required because the frame whose prototype was made from acrylic plastic

also known as polymethyl methacrylate (PMMA). The frame was observed to tilt with the beam on the side where motor is attached always positioned above the other beam making the camera to make an undesirable tilt sideways. The tilting was so much that it could be seen by eyes and the frame was measured to deform by over 6mm.

A more efficient design of the lift frame is the U-shaped design shown in Figure 75 . It has shorter center-of-mass moment arm which ensures lower energy demand from the motor. In addition, the new frame must be manufactured as a single piece to avoid assembly joints that worsen the initial frame distortion.

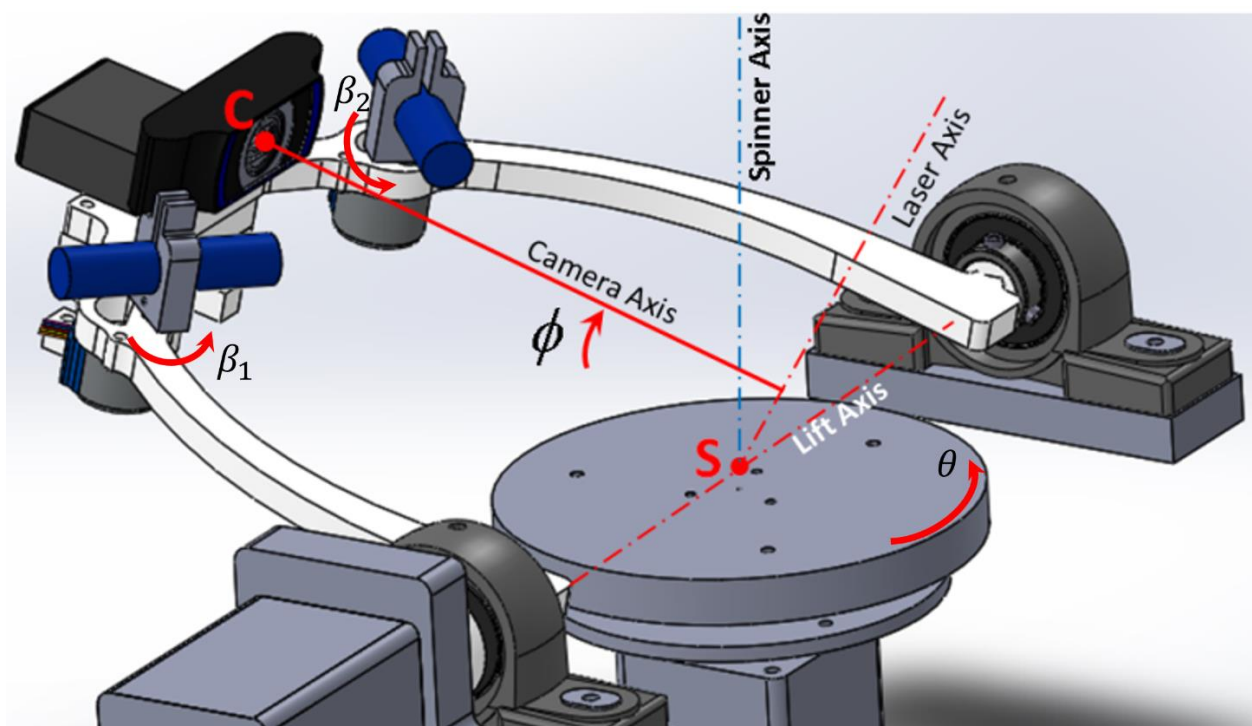


Figure 75: The second prototype with added mobile lasers and lift frame fabricated from Plexiglas

For this second prototype, the is designed out of acrylic plastic as well and it supports the camera, two lasers and two small motors to control the laser planes. The maximum torque requirement for the lifting the frame is around 1.9Nm, hence, a 3.0Nm rated motor is used for this function. Overall, there was a big improvement in the bending of the lift frame. Using the scanner calibration methods outlined in Section 5, the positional changes in the relative position of the

camera origin and the workpiece origin is shown in Figure 76 . Despite the additional weight of the two motors, the camera was more stable than the design with lift frame made with beams.

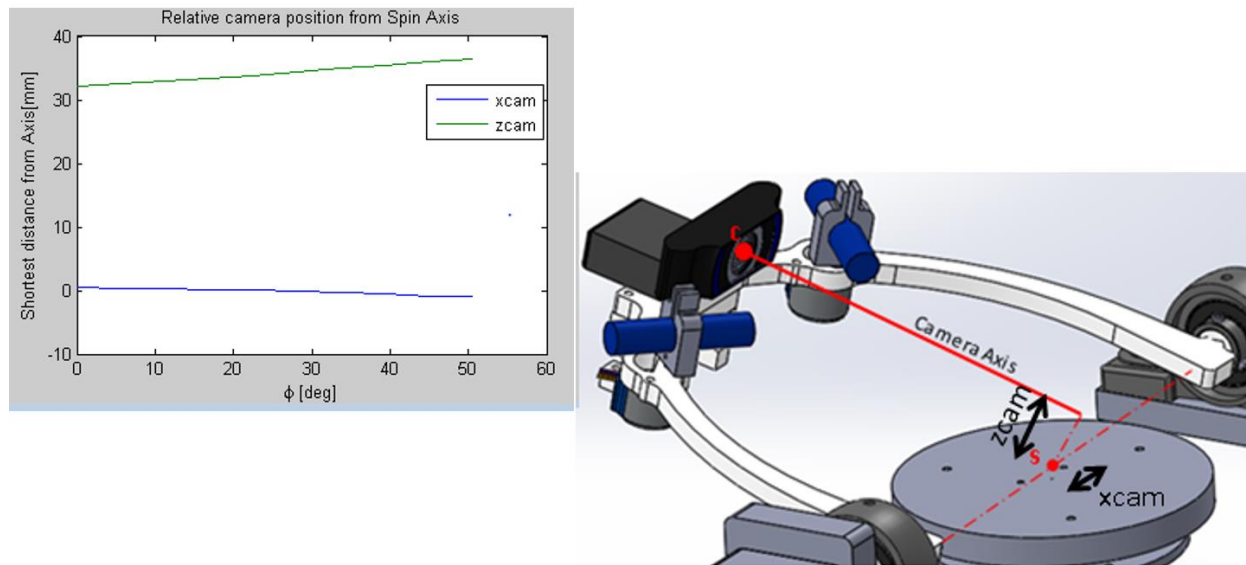


Figure 76: Distortion of the lift frame measured through variation of relative positions between points C and S

Apart from the deformation of the lift frame, the laser positioning motors were found to be inaccurate too flexible. They do not provide the needed repeatability for the 3D scanner. In fact, it was impossible to make a scan by only moving lasers because the step size was not precise and step resolution was inadequate. Scan were carried out using fixed laser angles with this system. Since the laser motors are not essential in setting laser angles (angles can be set manually or measured by calibration), the two small motors became redundant.

Obviously, the second prototype did not satisfy the needed positional accuracy for the optical system. Even though the effects of the bending of the lift frame can be measured and be compensated, it cannot be done during the scanning process of a workpiece. Hence, the repeatability of the positional changes becomes significant. The repeatability of the relative position of the camera with respect to the rigid frame happens to deteriorate with more deformation of the lift frame.

Max deformation Plexiglas=20microns

Max deformation AL5050=0.3microns

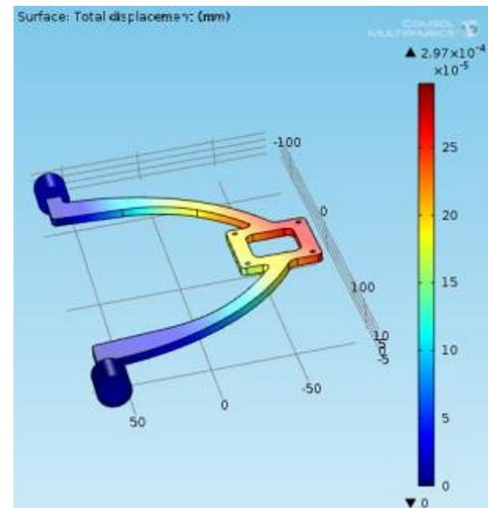
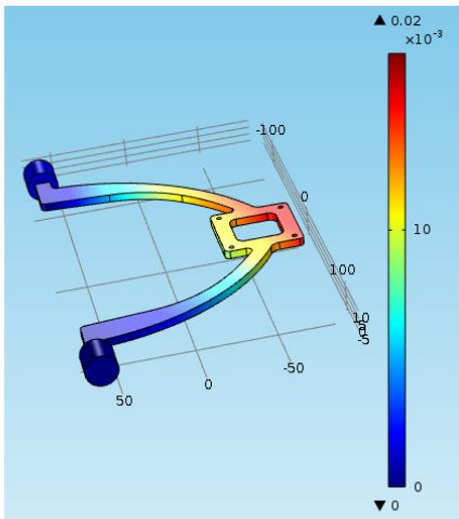
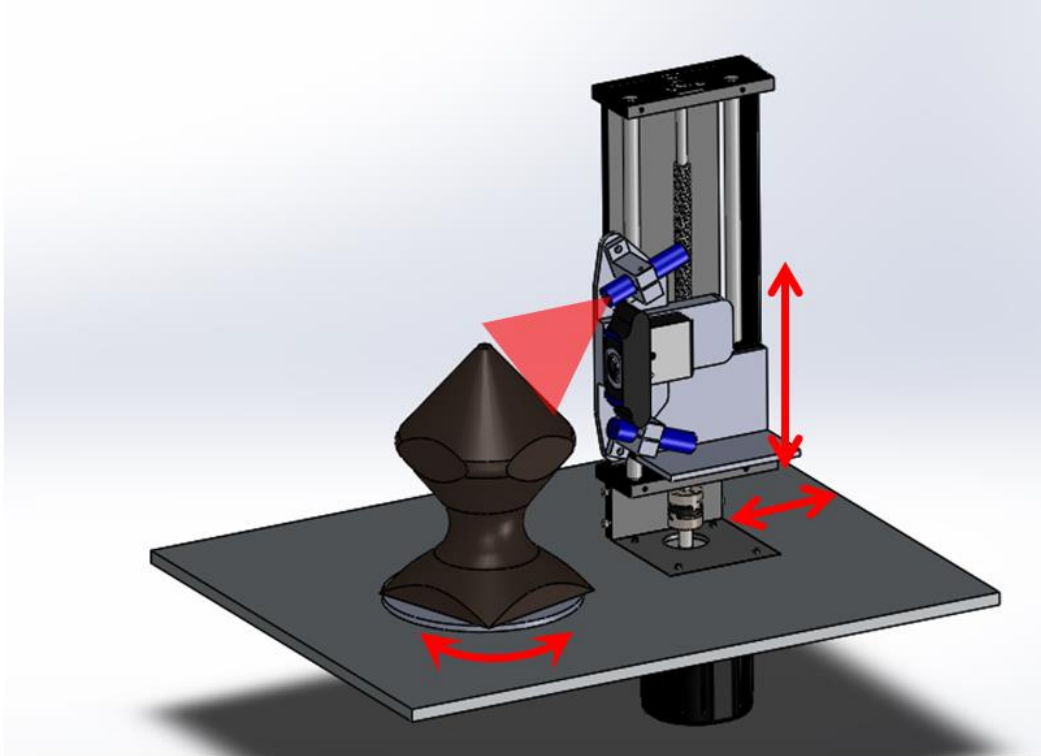


Figure 77: Comparative deformation analysis of the camera and laser support frame using different materials

New designs and adjustments were explored and considered to build the final prototype of the 3D scanner. Apart from the use of better load carrying material like aluminum, the new prototype eliminates the laser motors because they add to the load and do not help much in the scanning process. The comparison of deformations estimated by Finite Element Method using Plexiglas and AL5050 is given in Figure 77 . There was too much inconsistency and errors associated with the laser motor rotation that makes them completely useless during scanning. To support the reverse engineering of object of various size, a radial axis is introduced in the new model. An alternative design also considered is the one shown in Figure 78 . The concept design in the figure was later re-conceived by “Matter and Form 3D scanner”[133] which later entered the market using a product of similar design.



The resolution of the linear system is of order of few microns, it gives better resolution regardless of workpiece rotation step size.

Figure 78: Alternative design considered for the 3D scanner

5.3.4 Concluded Design

The 3D scanner in this work is designed based on the demand of a scanner with good accuracy and wide coverage of points of view of a workpiece by allowing multiple camera view angles. This was an observed limitation observed in affordable commercial products like MakerBot 3D digitizer [131] and DAVID scanner [132]. Therefore, designing a scanner that promises satisfactory relative displacement between camera and workpiece is investigated. Every measurement device and most optical devices require very accurate and precise positioning. Some of the most expensive manufacturing processes are carried out for optical devices. To make a scanner prototype on limited budget, the scanner components' stiffness and integrity must not be compromised. Hence, each component of the final design underwent deformation analysis under operational loads. As can be seen in Figure 79 , a design that warrants wide camera view direction

that covers a scan space of hemispherical dome was designed and constructed. The design, model and measurement evaluation from this scanner was published in a journal article [134].

An object is scanned by placing it on the turntable where it can be rotated by up to 360° . The camera-laser setup can be lifted to new viewing pose by up to 90° . The total positional accuracy, which influences the whole measurement, depends on the consistency of the step positions in spinning and lifting as well as the uncertainty in some vital scanner geometric dimensions. For this reason, the calibration influencing parameters that dictate the scanner motion must be accurate. Figure 79 shows the embodiment of the system showing some components used in scanning.

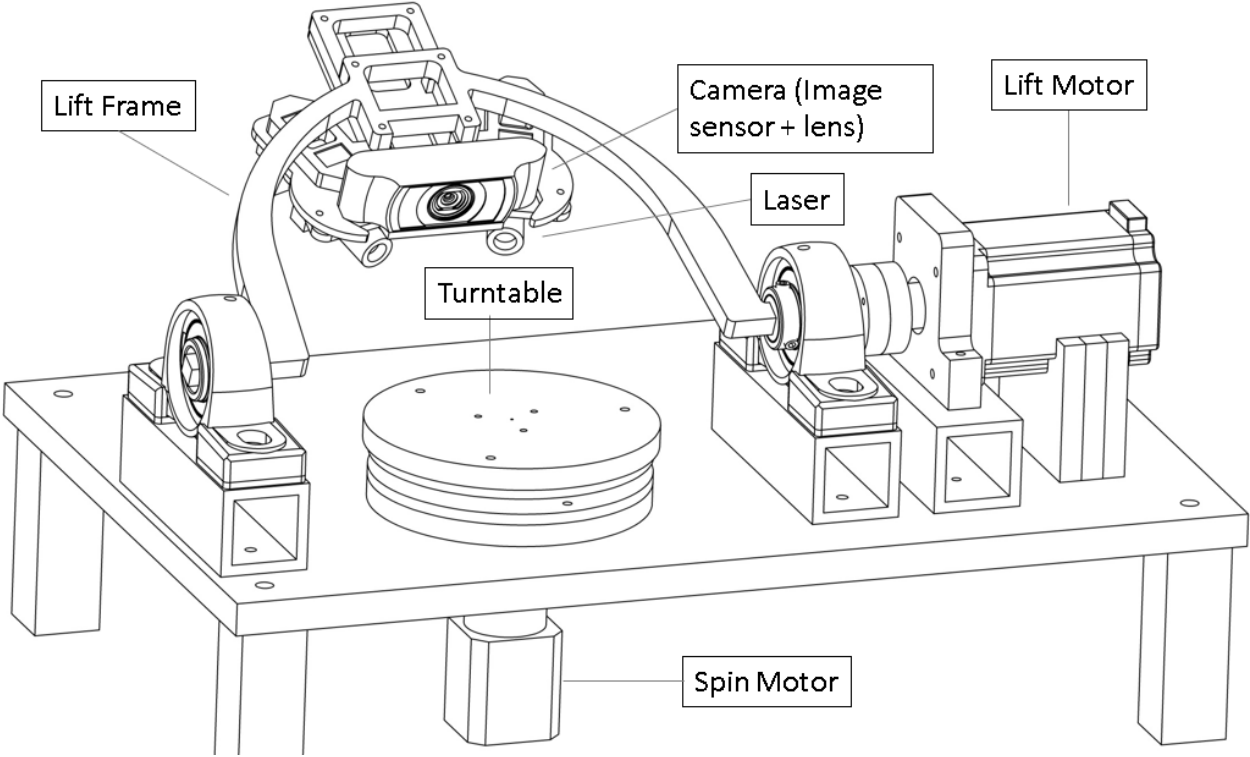


Figure 79: Components of the 3D scanner shown on the final design

All the structural components were carefully chosen, and deformations of the parts are checked to ensure that positional uncertainty is reduced. The lift frame, which supports the camera and lasers, is found to be particularly critical since it must not exert a torque the motor cannot withstand. Consequently, the final design is fabricated from aluminum sheet 12mm thick and designed in a u-shape. All other components were found to exhibit negligible deformations compared to the lift frame and their deformations are from this point neglected. In addition, the influence of vibration during lifting is also negligible since the motor is operated slowly and enough time elapses, providing the system sufficient time to stabilize before image capture. It is noted that the stabilization time of about 0.5 seconds is ideal. The vibration is hardly an issue because most of the scanning is carried out at a fixed lift position. The stabilization time provides an opportunity to carry out other computations and processing of data. While the frame-lifting motor is controlled by a micro-stepping with a step driver, the workpiece-spinning motor has a gear reduction attached to the motor; these ensure small incremental steps are used to decrease the vibration amplitude of the frame and the workpiece.

Compared to the second prototype design, there is decrease in the load on the frame due to the elimination of the laser motors. The frame was produced using Aluminum by laser cutting and machining. The results of the static analysis by Finite Element Method (FEM) of the loads on the frame using safety factor of 2 is shown in the Figure 81 . The measured change in the relative distance between points C and S is below 0.05mm which is acceptable for the 3D scanner. Figure 80 shows the changes in this distance with the lift angle ϕ . Compared with the results in Figure 76 , it is clear that the final prototype has improved positional accuracy.

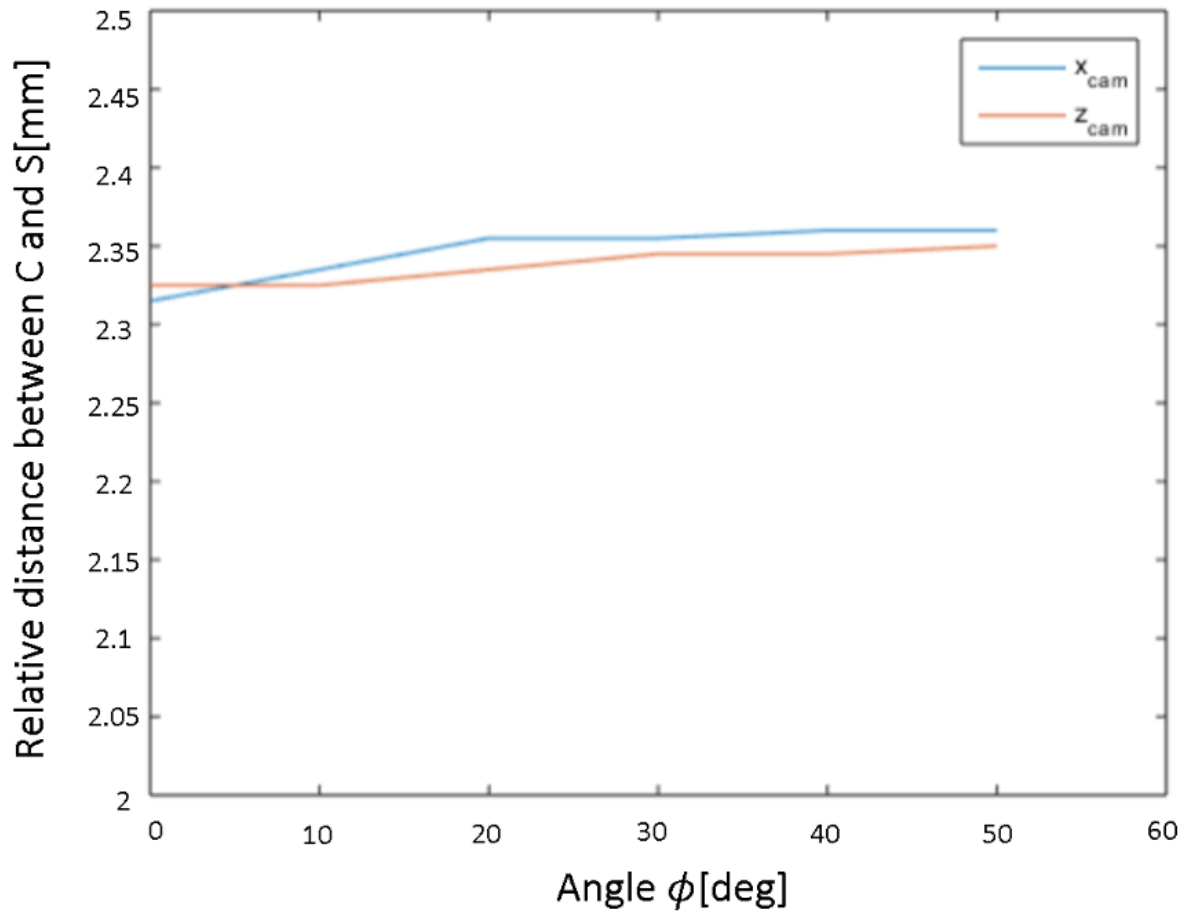


Figure 80: Distortion of the final support frame measured

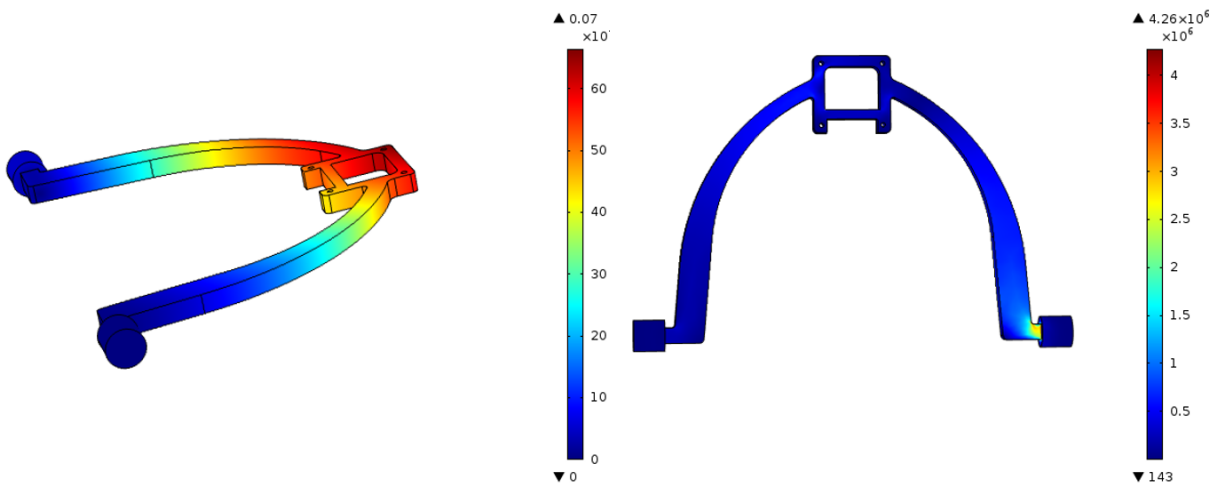


Figure 81: Deformation and stress analysis of the final lift frame made from AL7050

There is need to ensure that the rotation of the turntable is along a fixed axis without any wobbling. To that end, the turntable designed with a thrust ball bearing to support a workpiece by ensuring that rotation is along a fixed axis—defined as Spin axis in Figure 83 . A step motor is equipped with a planetary gear that reduces steps to very fine motion of about 70 to 225 thousand steps per rotation. The gear increases the torque that can be delivered without even using micro-stepping feature of the motor driver that is known to diminish incremental torque [135]. The motor and gearbox system is attached to the turntable through a stiff coupling. Figure 82 shows the cross-sectional view of the turntable with the motion components. The weight that can be supported by the scanner is up to 10 kg and the scan space is a hemi-sphere of 100 to 150mm radius.

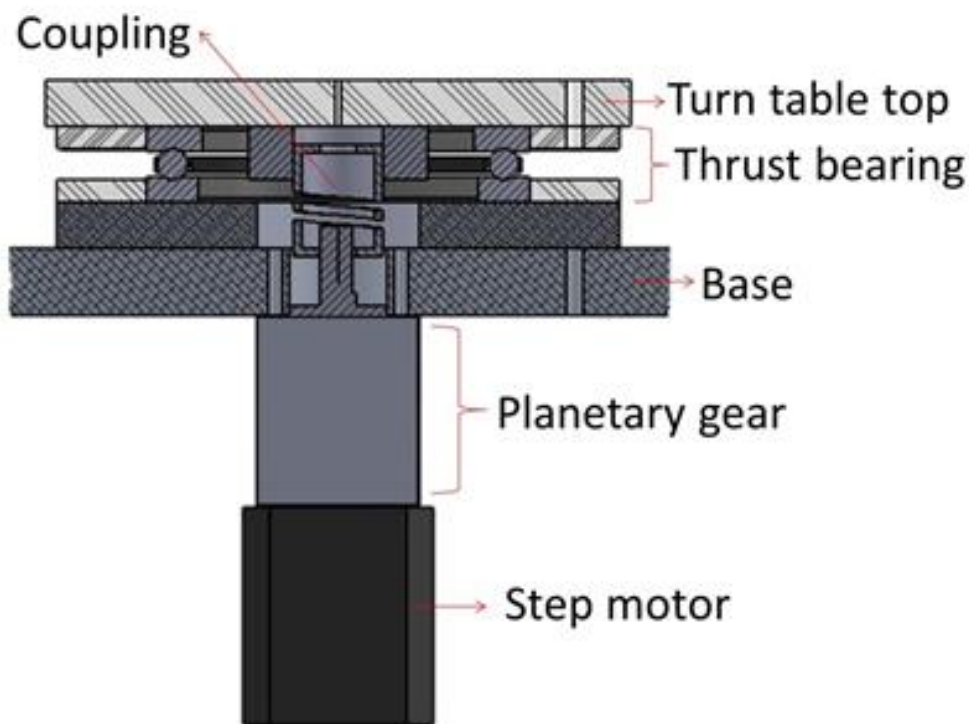


Figure 82: Cross-section showing turntable rotation system

Most laser scanners operate by positioning the image sensor and laser through Cartesian gantry, hand-held use, use of robotic arm and the use of turntable. Some laser 3D scanners use

trackers to register measured results allowing measurements at any configuration. Others use fully automated known positions and configurations to measure parts. Among the handheld scanners, there are scanners fixed to robot-arms for manual scanning where the arm joint encoders provide accurate scanning position and configuration with less calibrations. These scanner find applications in production environments like forging industries[136]. Other handheld scanners depend on trackers placed on the part to register scan data. The use of trackers on the scan object places limitations on the type of part that can be scanned. In some cases, the tracker pattern significantly decreases the working space of the 3D scanner. Other 3D scanners using less accurate registration methods or inadequate viewing configurations may only be usable for less rigorous applications.

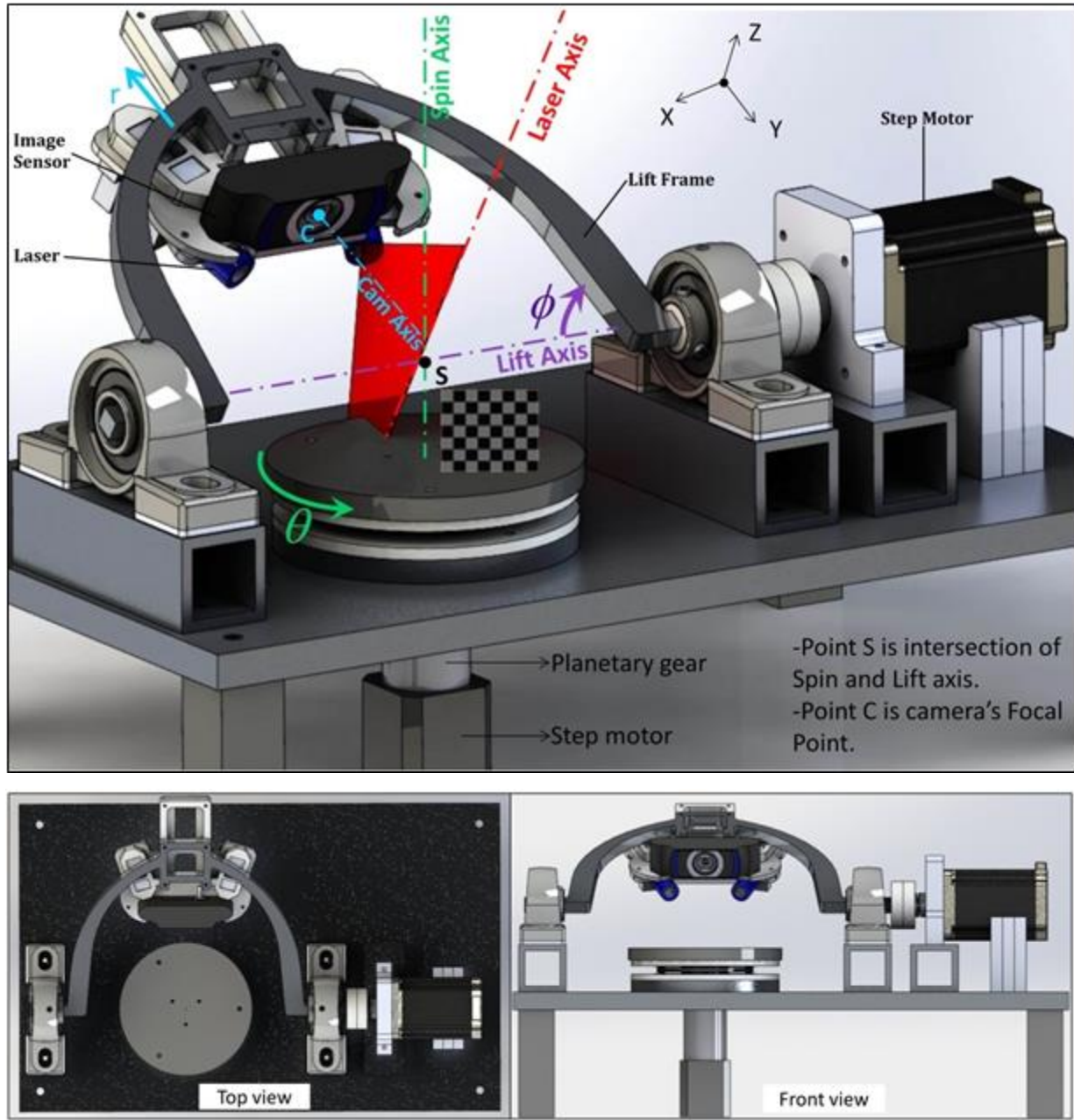


Figure 83: Scanner setup showing relevant geometric axes, calibration grid and other design features with front and top views

In this project, the scanner is constructed to allow movement around the spherical coordinate r, θ and ϕ , providing multiple pose possibilities of the object. As Figure 83 clearly indicates, the first motor is responsible for rotating the object on the horizontal turntable. The first motor rotation is the primary scanning process because of the high resolution of the rotation

motion. The support frame which holds the camera and laser system, is controlled by the second motor. Scans are usually conducted with at some lift positions for desired scan regions. The third positional variable, the radial position r , which represents the y-axis distance between the focal point C from point S, is used to adjust the standoff distance of the scanner allowing placement of test object within the scanning configuration space. While the θ and ϕ positions are controlled programmatically, the radial r position is set manually for each scan depending on the size of the object. The focus of the image sensor changes significantly at various standoff values; hence, the scanner calibration process is repeated for all the used radial values. For each of the radial locations of around 100, 150 and 200 mm of point C from central point S, sensor calibrations are performed and recorded. Specifically, for the measurements in this study, a radial location of 100mm and 150mm from S have been used in reverse engineering cases. Figure 84 shows a sample knight piece used as object to be scanned at a radial distance of 100mm. This chosen distance provides the right standoff distance as can be seen in Figure 85 . It is desirable to have the image almost filled with the laser stripe but not too large to trim off some regions.

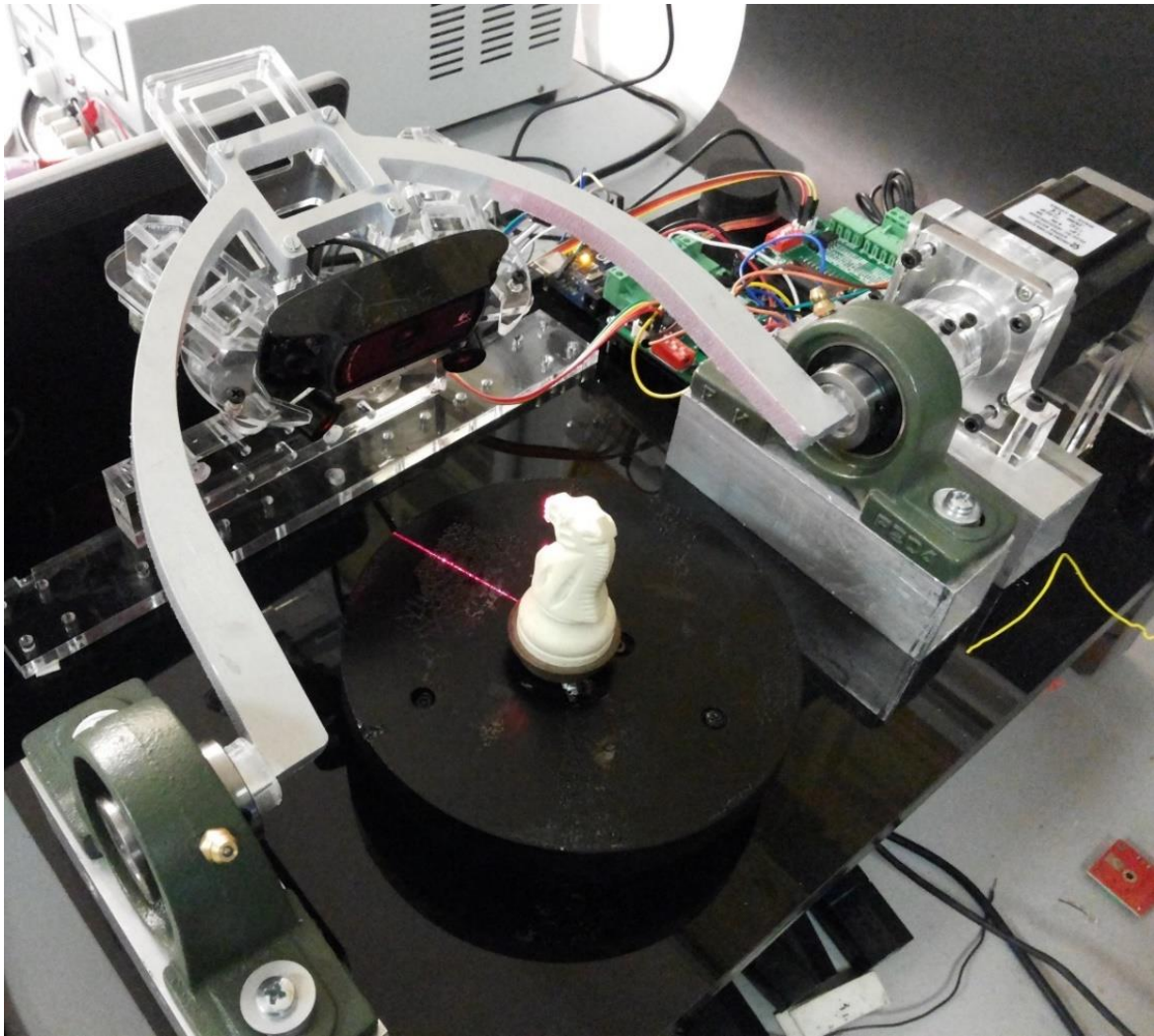


Figure 84: The 3D scanner shown during reconstruction of a knight piece



Figure 85: Raw image obtained from the image sensor during the scanning of a knight piece

There are three important axes labelled in Figure 83 as the laser, Spin and Lift axes, which defined from the camera axis, become critical in the design and analysis of the 3D scanner. In this consideration, the camera axis is taken as the default frame of reference. Hence, it is fully defined and represents the y-axis of the camera frame from where all image measurement are carried out. Each of the three axes are measured when the scanner setup is fully assembled to avoid accumulation of uncertainties.

The laser axis is defined as a portrayal of the intersection axis of the laser plane with the vertical camera plane, shown as YZ plane. This axis is set to remain strictly vertical with respect to the camera frame. In practice, a feedback from reconstruction of the laser stripe on an object is used in setting the laser perfectly vertical by iterative adjustments. The laser plane control sequence has to do with the checking the constructed laser plane orientation using the camera feedback that will be discussed in the coming section.

Next, the Spin axis is defined as the rotation axis of the turntable where the scan object is attached. A sample object to be scanned must to be fixed rigidly to the top of the turntable throughout a scanning process. A method of axis calibration is discussed in the calibration section. The rotating axis can be reconstructed after a complete camera calibration. Sample rotating pattern points at generation and proper regression of the points can be used to estimate the axis. Axis points, measured with respect to the camera, are utilized in the estimation of the axis for every φ lift angle of interest. Further detail about the axis estimation methods are provided in the calibration section.

For the last axis (Lift axis), a method of capturing axis data identical to the one used for the Spin axis can be used by capturing known points at φ locations to reconstruct the rotational transformation axis. The intersection point S of the two axes, Spin and Lift, is important for transformations of scan results from the scanner. In the case that the two axes do not intersect, then Necessary translations will need to be carried out before rotational transformations. MATLAB subroutine has been written to carry out these calibrations along with majority of the computational tasks of the 3D scanner.

The turntable is made to rotate by a changing step angle, ranging from a unit step angle of 0.02^0 - 0.4^0 , where the total step for each image is determined depending on average vertical spacing of previously measured laser stripe characteristics. The motor used for the turntable is significantly reduced to the extent that little or no micro-stepping is required to generate fine motion. To obtain a uniform point distribution, the horizontal spacing s_x should have approximately equal magnitude as the vertical point spacing s_y as illustrated in Figure 86 . Using the scanning automation motion, only the horizontal point spacing can be controlled because the vertical spacing is controlled by the image vertical pixel while the horizontal spacing is determined by the angular steps. The average vertical spacing is estimated based on the radial location of the center of mass of the last saved laser stripe data, which is illustrated in Figure 86 . Knowing that the camera's vertical field view is $\varphi_v = 43.3^0$ and center of mass of the precedent stripe is $(\bar{X}_{n-1}, \bar{Y}_{n-1}, \bar{Z}_{n-1})$, the target step angle in radians for nth stripe measurement can be estimated using Equations 16 and 17. Y_{cam} is the y-location of camera point C with respect to object fixed point S shown in Figure 83 . The benefits of using this variable step angle can be seen in the Figure 87 . In the top scan, the step

angle used between each image capture is too small and should be increased to obtain uniform data. Conversely, the result at the bottom of the figure requires the step spacing to be decreased. The effect of this non-uniform directional spacing of data on reconstructed part is discussed further in upcoming sections.

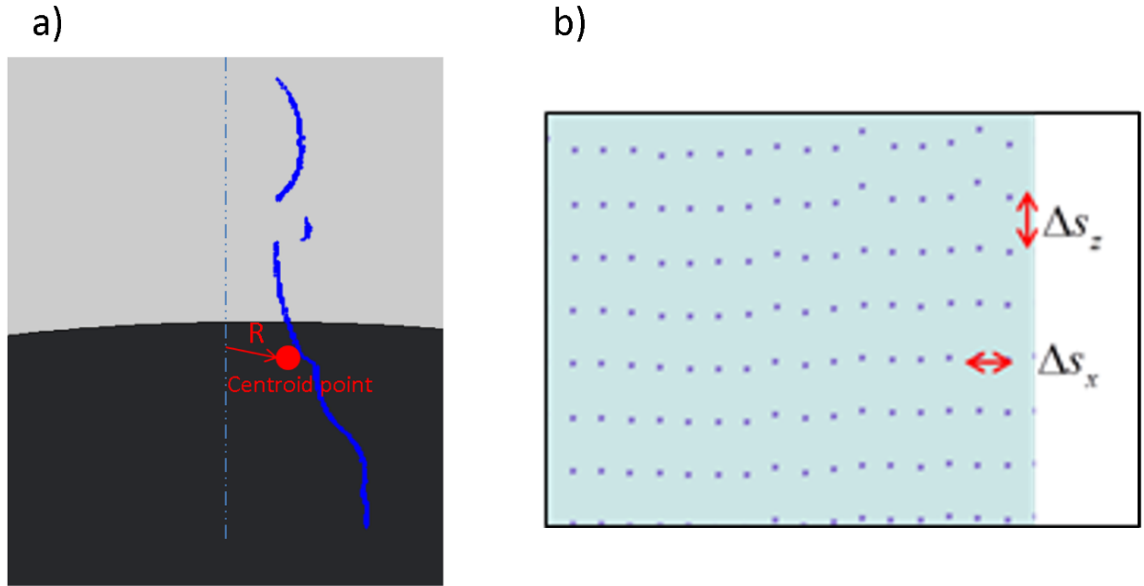


Figure 86: The centroidal radius of a reconstructed stripe points in (a) is used in controlling step angle to maintain uniform spacing between points shown in (b)

$$\Delta s_z = \frac{2(\bar{Y}_{n-1} - \bar{Y}_{cam})}{p_y} \tan\left(\frac{\phi_v}{2}\right) \quad (16)$$

$$step \approx \frac{\Delta s_z}{\sqrt{\bar{X}_{n-1}^2 + \bar{Y}_{n-1}^2}} \quad (17)$$

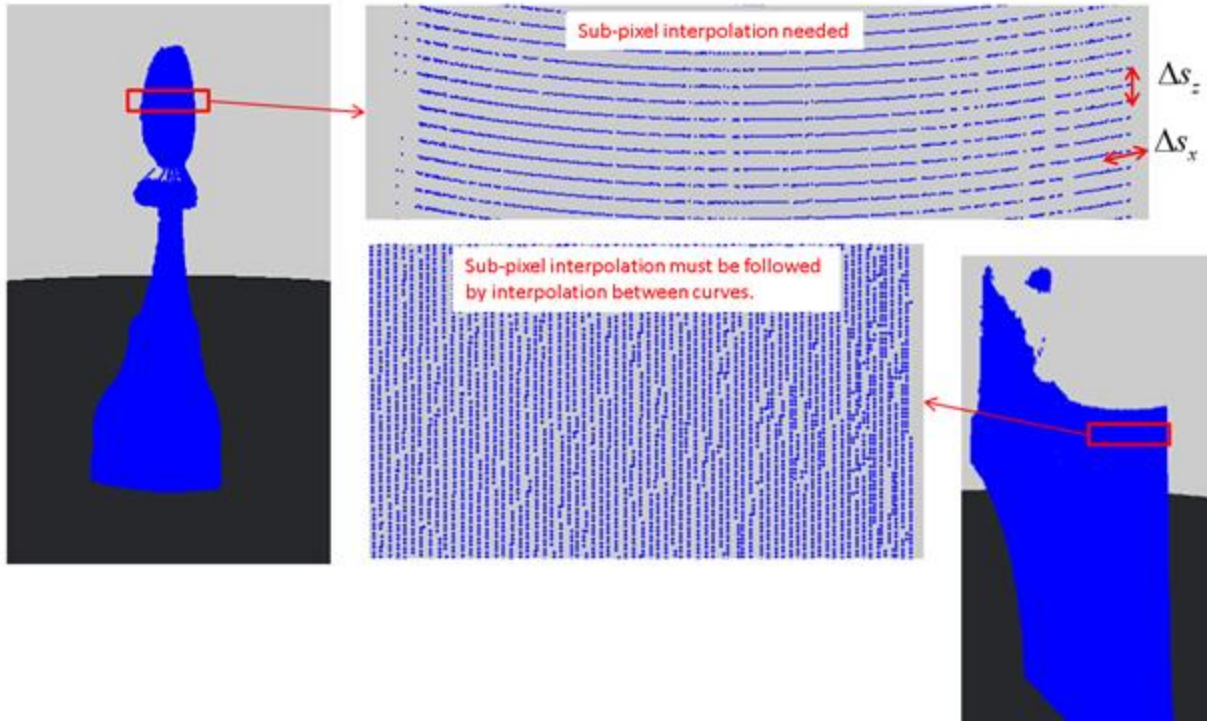


Figure 87: Two cases where the vertical point spacing does not match the horizontal spacing

The final issue pertaining to the design is the control of the motors. The rotation of the turntable about the Spin axis and the lifting of the frame about the Lift axis are all accomplished using step motors that are controlled by the use of microcontroller that sends signals to the motor control breakout boards. Each stepper motor has four coils terminals whose sequence of activation rotates the motor's rotor transferring motion through the shaft. The activation sequence of the coils is generated by the control board.

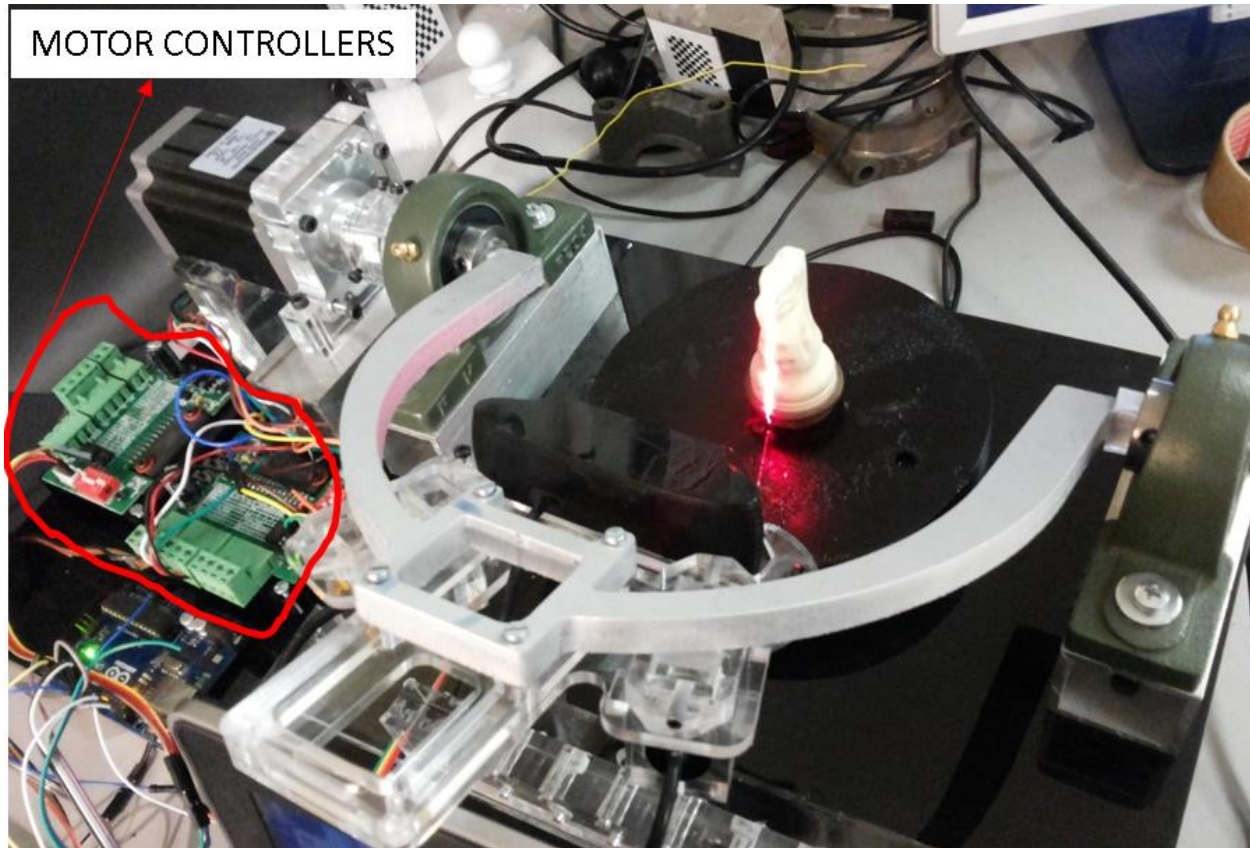


Figure 88: The 3D scanner during scanning where motor drivers and microcontroller are shown

Figure 88 illustrates the control breakout boards used in the control of the motors. They convert pulse signals to coils currents required to rotate the motors by a step. Motors are controlled using breakout boards that implements the Toshiba TB6600HG pulse width modulation (PWM) chopper type-type micro-step motor controller Integrated Circuit (IC). The schematic[137] of the required electric diagram is given in Figure 89 . Each control board has four input terminals—the Step, Direction, Enable and Ground terminals—that are connected to pins on the microcontroller. The PWM signal is sent to the Step terminal of the motor control board while binary values of the voltage sent to the direction terminal determines the direction of rotation of the motor. Similarly, the Enable pin takes the value of on/off to disable the function of the motor. The ground pin is required to be connected to the microcontroller's Ground pin for proper voltage synchronization.

TB6600hq bipolar stepping motor driver
CuteMinds.com

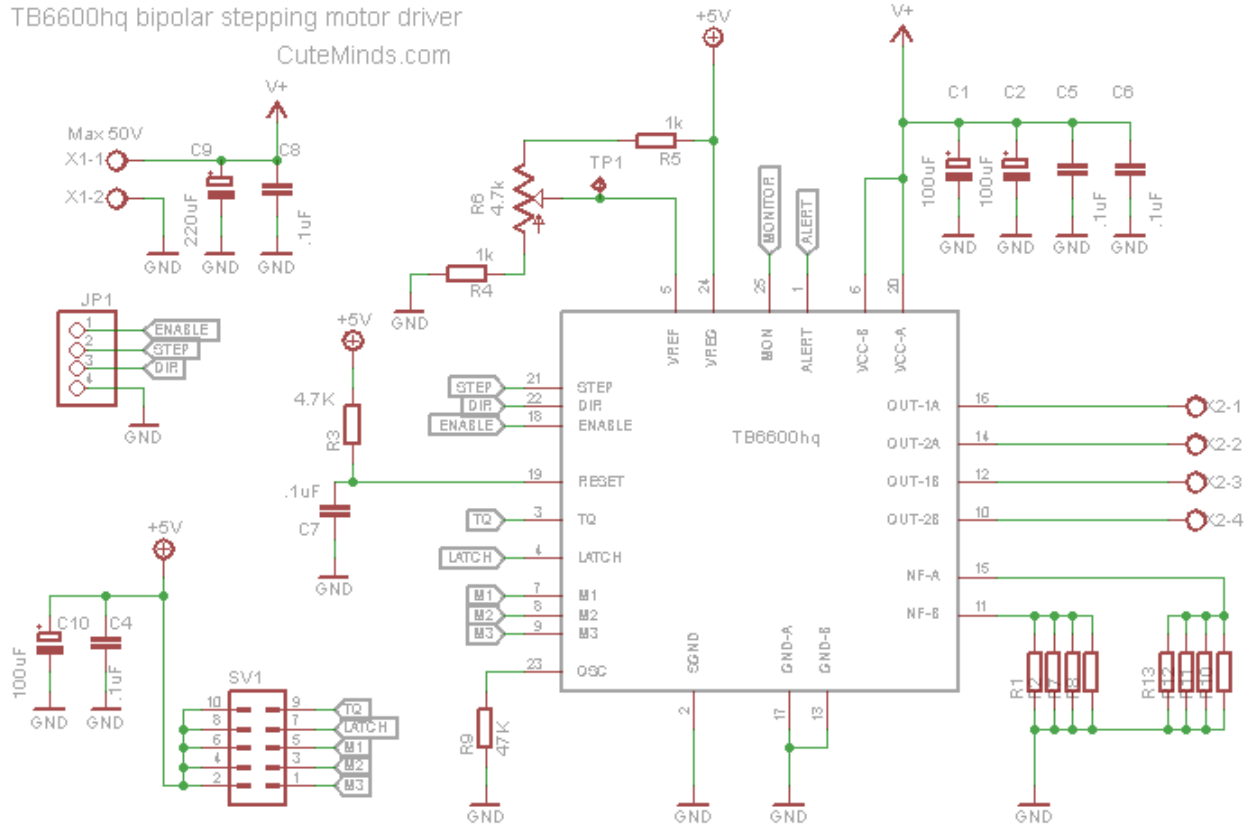


Figure 89: Electronic wiring used by the motor controllers[138]

Chapter 6

THREE-DIMENSIONAL RECONSTRUCTION

6.1 Calibration

This section covers the calibration of the camera, laser, motions of the turntable and the lift frame. The methods used in ensuring that each of the quantities defining the position, calibration and size of the scanner parameters are known within some uncertainty bounds are explained. The section begins with the camera calibration followed by the calibration of other entities.

6.1.1 Camera Calibration

For a computer vision camera, there is need to identify how the images captured relate to the real object they represent. To accomplish this, an imaging calibration is necessary. Cameras are composed of image sensors that function as converters of incident photons to electrical signals. This photoelectric conversion, together with charge accumulation, signal transfer and analog-to-digital conversion makes the image sensor the most important component of a camera. For the purpose of light direction and focusing, camera lens is also required. How the incident light from the real world gets bent and transferred to the sensors through the lens and micro-lens must be modelled. In addition, the charges accumulated and their pixel-locations on the sensor should also be correlated with the physical entities they represent.

The individual codes tested for calibration, image acquisition, storage/retrieval of images from video, image processing, curve extraction and cloud point representation are united into to a user-friendly environment. This makes it easier to add new features and study effect of each parameter individually.

General code that can work in all PC using any camera is implemented. It allows selection of installed cameras and acquisition of images for calibration. For application on computer that does not have MATLAB, a runtime library provided by MATHWORKS can be installed for free and the application should work. The complete the calibration are process is in the codes used in MARC.

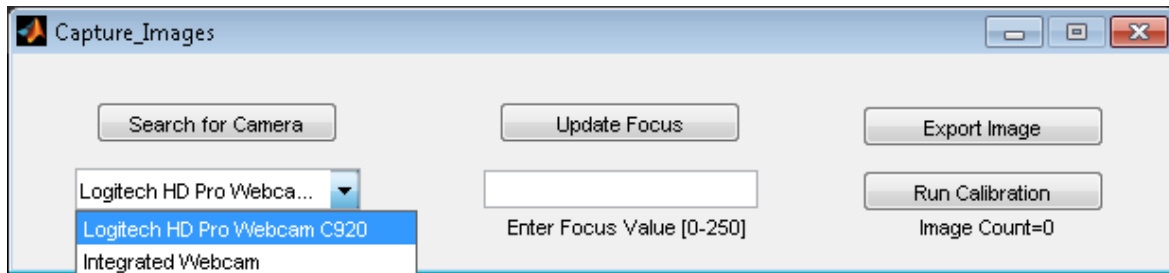


Figure 90: Image acquisition GUI for calibration of camera

The object used to calibrate the camera is a grid of white and black squares designed in the form of a checker board illustrated in Figure 91 . The small black patch, attached on the side of the grid, is used for laser positioning. Many of the checker board pattern is captured by the camera and the images are used to find the camera intrinsic and extrinsic properties. Camera intrinsic parameters, unique for any camera, are defining quantities that map the pixel positions with the image frame coordinates while the extrinsic parameters relate the camera to a world reference frame.

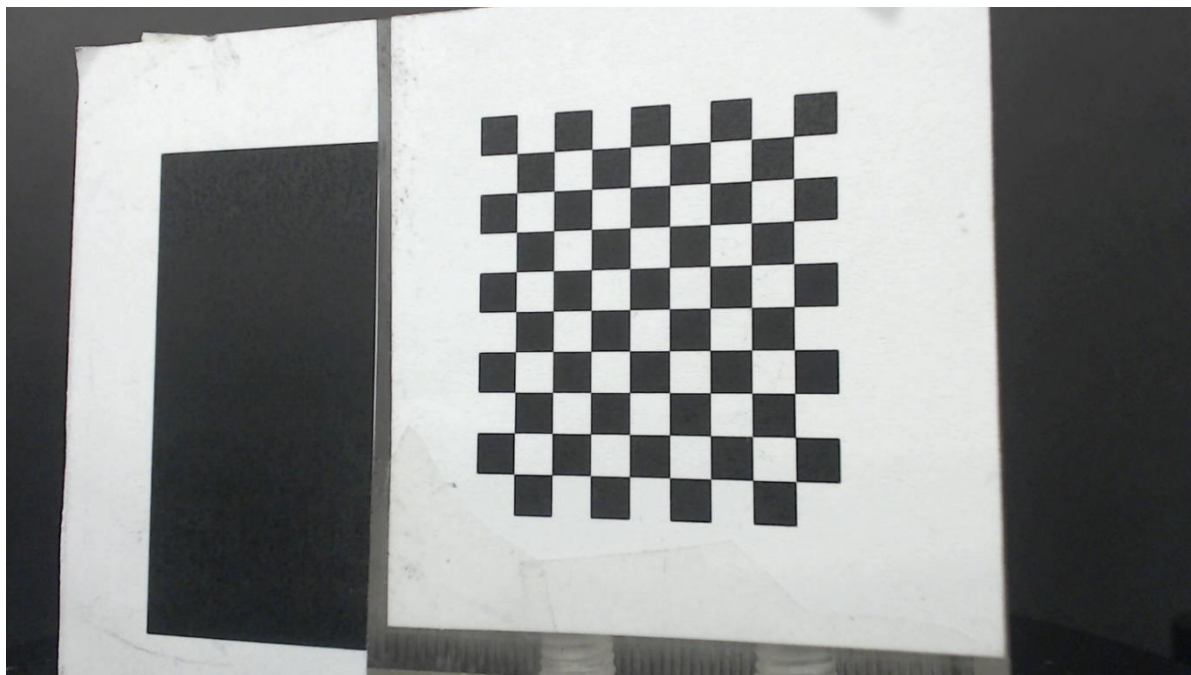


Figure 91: Calibration pattern that looks like checker board is used along with small dark patch used for laser setting.

The captured images are calibrated with the aid of MATLAB camera calibration application built from methods established in literature[139–141]. The application recognizes the internal square corners and records the pixel locations. The detected corners of a sample image are shown in Figure 92 .

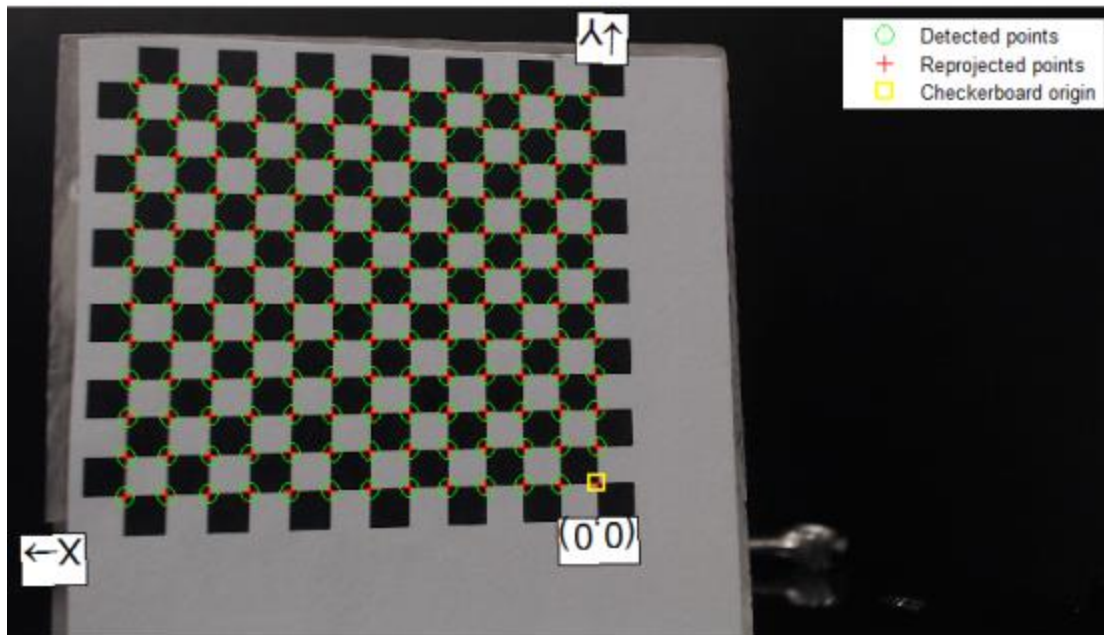


Figure 92: Detected pixel location of the square corners used for camera calibration

In derivation of an optical model, stored information from a camera that relates a 2-dimensional image to the real 3-dimensional spaces is formulated. For calibration of the optical device used in this work, a verifiably accurate model is necessary. For this research, an optical camera having a 1/3" 1920x1080 full High Definition sensor with a glass Carl Zeiss lens is used. Calibration needs to be implemented with a geometry of pre-calibrated dimension that is to be placed within the viewing space of the scanner's camera. The pinhole camera model is applied together with a distortion model of polynomial nature for the modeling of detected calibration quantities to relate pixel points with image spatial coordinates. Tangential distortion is not considered because of its negligible impact in the system. The radial distortion model applied

originated from Zhang [139] where raw distorted image points $(\tilde{x}_p, \tilde{y}_p)$ are related to the ideal pinhole points (x_p, y_p) in the expression given in Equation 18.

$$\begin{aligned} \tilde{x}_p &= x_p + x \left[k_1(x_p^2 + y_p^2) + k_2(x_p^2 + y_p^2)^2 \right] \\ \tilde{y}_p &= y_p + y \left[k_1(x_p^2 + y_p^2) + k_2(x_p^2 + y_p^2)^2 \right] \end{aligned} \quad (18)$$

Here, the quantities k_1 and k_2 are the distortion coefficients. While the focal point is taken as the origin of the image points, the images of the square calibration grid with points (x_p, y_p) are mapped to a world 3D reference frame points $(X_0, Y_0, 0)$ on the plane using the relation given by Zhang [139]:

$$s \begin{bmatrix} x_p \\ y_p \\ 1 \end{bmatrix} = \begin{bmatrix} f_x & 0 & c_x \\ 0 & f_y & c_y \\ 0 & 0 & 1 \end{bmatrix} \cdot E \cdot \begin{bmatrix} X_0 \\ Y_0 \\ 0 \\ 1 \end{bmatrix}; \quad (E = [R \ T]) \quad (19)$$

The quantities f_x and f_y are the focal length in pixel units, c_x and c_y represent the location of the pixel principal axis also in pixel and s is a scaling factor used to match quantities on both sides of the equation. These quantities constitute the intrinsic parameters of a camera [140] that characterize its internal workings. The matrix E is comprised of extrinsic parameters which contains the Rotation matrix R and translation T of camera relative to the world reference on calibration pattern's plane. These parameters are obtained through optimization (using Levenberg-Marquardt algorithm) of the intrinsic, extrinsic and the distortion constants by minimization of the deviations between reconstructed image of the model points with the measured ones. Figure 94 gives the mean error of the reconstructed image points from calibration compared to the real images in pixels.

The reconstructed calibration patterns from extrinsic transformations are plotted in Figure 93a. The variation in the optimal values of focus and central axis are shown in Figure 93b. For every scan carried the appropriate focus for the stand-off distance should be chosen, and the corresponding intrinsic parameter should be applied. Obtained after optimization of the camera parameters, the plot relates the pixel locations with the known square sizes in the 3D world. The deviation in pixel between the detected pixel locations and the reconstructed location using the

intrinsic and extrinsic parameters found in Figure 94, gives an average deviation that is around 0.32 pixels which is acceptable for the application.

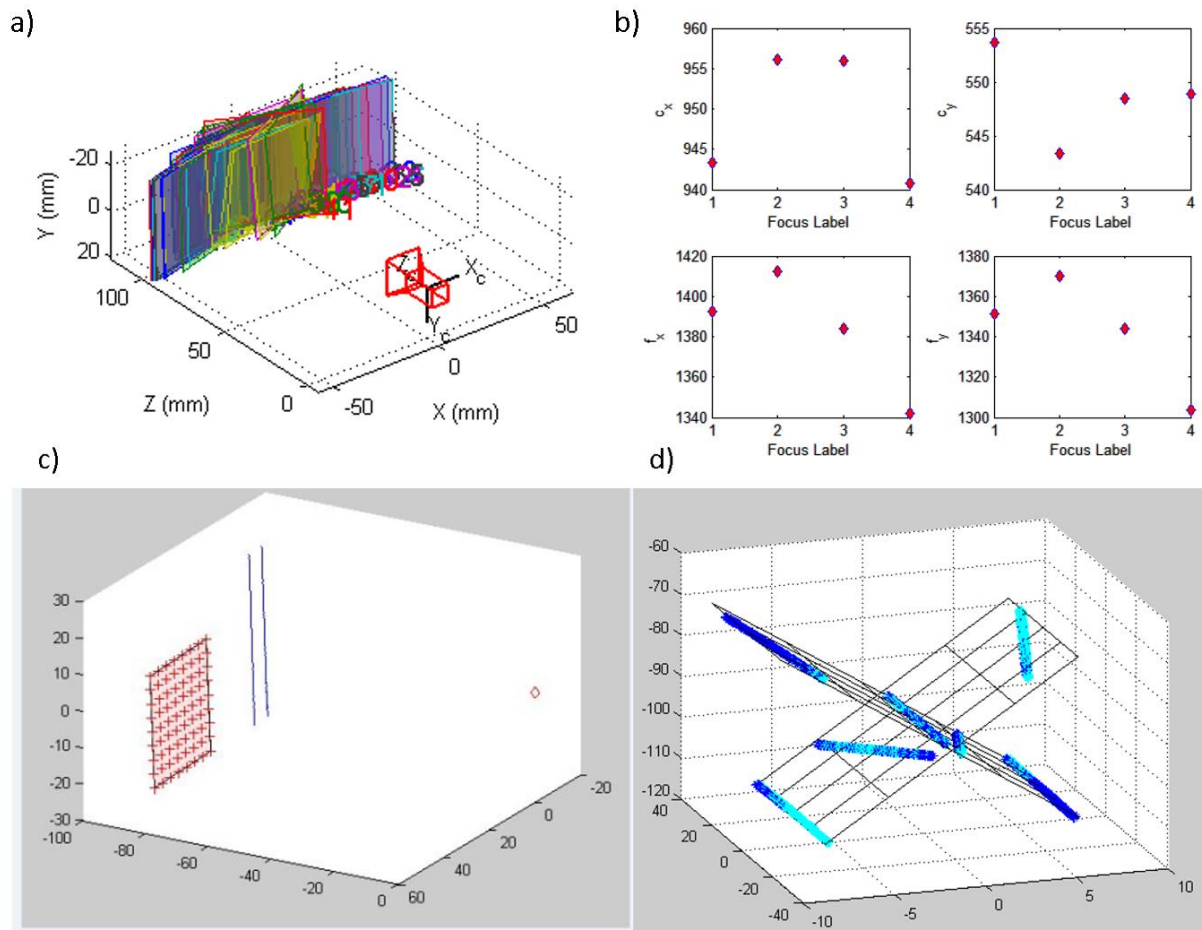


Figure 93: a) Reconstructed calibration patterns at several locations to visualize extrinsic parameters. b) Variation of some intrinsic parameters at different focus at stand off distance between 50mm to 120mm. c) The reconstructed lasers on the plane of calibrator. d) Computed laser beam planes used using reconstructed lines.

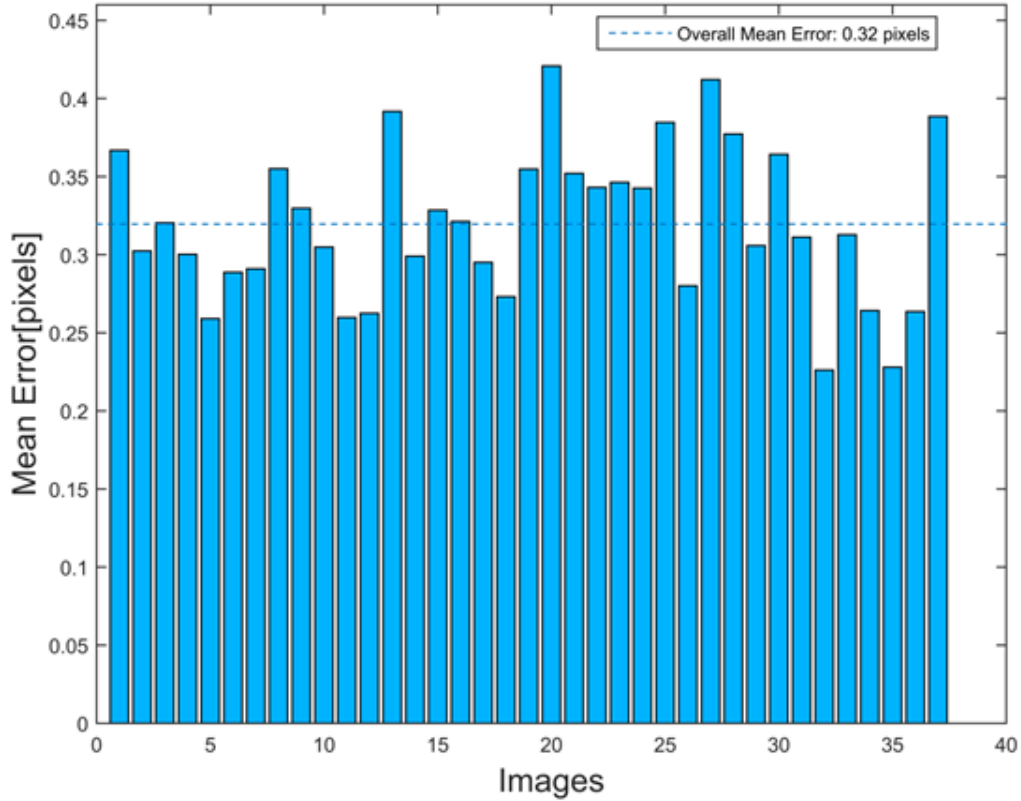


Figure 94: Mean deviation of reconstructed pixel points from the detected points which indicates accuracy of the camera model

6.1.2 Calibration of lasers, and motion axes

The effects of errors and tolerances in manufacturing can lead to the geometric measurements in the assembled scanner deviate by up to the order of hundreds of micrometers. The alternative way of exact measurement and alignment of some parts to fit strict dimensional tolerance such as the location of the focal point and axis will require very costly methods. Hence, the scanning motion which is restricted to rotation about Spin and Lift axes can be used in calibration and assessment of the scanner dimensions and configuration of measuring elements. Since a measurement is to be rigidly fixed to the turntable, merely knowing the orientation of the base turntable is enough to relate the work-piece frame. In addition, it is assumed that laser plane and camera axis remain unchanged with respect to each other during the scanning process.

The obtained points $(X, Y, Z)_C$ from a scanning session are at an instantaneous i step of spin with respect to point C on camera. The measurement needs to be transformed to the frame

attached to the measured part (Frame S). The chosen part reference frame is at the point S, which represents the intersection of Spin and Lift axes. The new set of points for each step at an arbitrary spin angle of θ_i at a fixed lift configuration ϕ is given below (Equation 20) and shown in the Figure 95 .

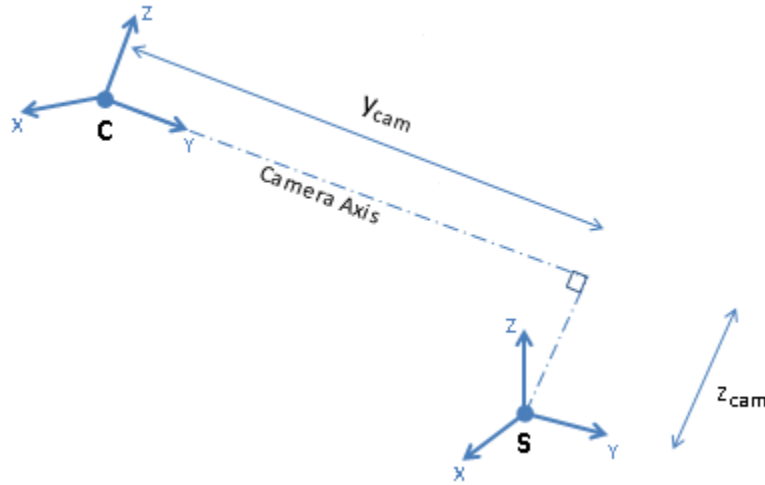


Figure 95: Sketch showing camera and scanner object frame

$$\begin{bmatrix} X_i \\ Y_i \\ Z_i \\ 1 \end{bmatrix}_S = \begin{bmatrix} \cos(\theta_i) & \sin(\theta_i) & 0 & 0 \\ -\sin(\theta_i) & \cos(\theta_i) & 0 & 0 \\ 0 & 0 & 1 & 0 \\ 0 & 0 & 0 & 1 \end{bmatrix} \cdot \begin{bmatrix} 1 & 0 & 0 & 0 \\ 0 & \cos(\phi) & \sin(\phi) & 0 \\ 0 & -\sin(\phi) & \cos(\phi) & 0 \\ 0 & 0 & 0 & 1 \end{bmatrix} \cdot \begin{bmatrix} 1 & 0 & 0 & X_{cam} \\ 0 & 1 & 0 & Y_{cam} \\ 0 & 0 & 1 & Z_{cam} \\ 0 & 0 & 0 & 1 \end{bmatrix} \cdot \begin{bmatrix} X \\ Y \\ Z \\ 1 \end{bmatrix}_C \quad (20)$$

Equation 20 provides the general motion transformation equation of the scanner where $(X_{cam}, Y_{cam}, Z_{cam})$ is the displacement vector of the camera reference point C from the stationary point S.

The rest of the calibration section focuses on the methods of deriving an accurate and optimal values of the parameters $\langle \phi, \beta, y_l, X_{cam}, Y_{cam}, Z_{cam} \rangle$. The position of the Spin axis is found by fitting series rotated planar calibration points obtained at about 40 instances on the calibration grid into circles. The circles are then used to extract the center points that serves as pints on the

axis. The mentioned Equation 19 is used to find the extrinsic values of R and T that is used for a different purpose here. Since the camera is fixed for each lift configuration, the extracted points from the pattern rotation should fit into circles. The center points of those circles should then represent the axis of rotation, hence the Spin axis. The collected points on the axis can be used to determine the location and direction of the Spin axis. To achieve this, principal component analysis (PCA) is used together with a singular value decomposition (SVD) algorithm to obtain axis vector where cumulative distances to axis points remain minimal [142]. The evaluated fitting of axes for 7 lift positions shown in Figure 96a were obtained for changed lift angles using the lift motor. The lift angle can be evaluated from the following dot product of Spin axis normal vector and the camera y-axis ($n_{cam,y} = \langle 0,1,0 \rangle$) unit vector provided in Equation 21.

$$\phi = \cos^{-1}(n_{cam,y} \cdot n_{spin}) \quad (21)$$

The accuracy of these angular measurements can be analyzed by checking maximum deviations of axis points from the axis. The angles and the associated uncertainties are provided in Figure 96b.

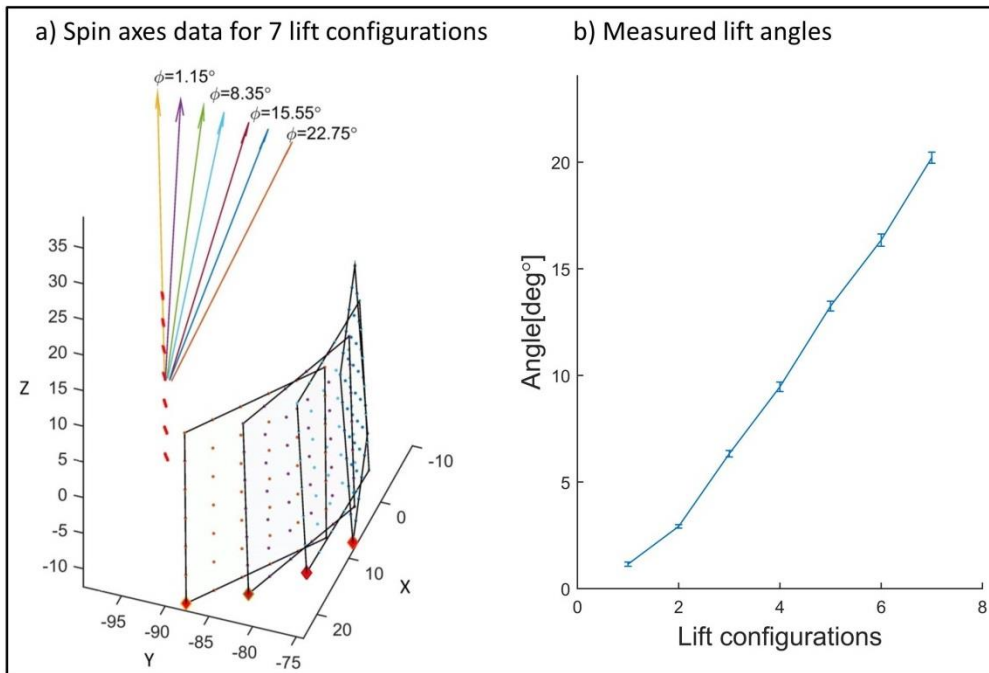


Figure 96: a) Spin axis of 7 configurations with some calibration planes and center points of 1st Lift. b) Measured lift angles from fitted Spin axis data with their confidence interval

A procedure similar to one mentioned is used is carried out for identifying the Lift axis where the camera is lifted at various locations, and the same patterns are recorded. After Lift axis is defined also identified by point data, the intersection of Spin and Lift axis is assumed as midpoint of the perpendicular distance between the axes to account for uncertainties in measurements. This distance should be very small for the axes to be considered to be intersecting axes. It is possible for the axes to not intersect, in the case of high error in manufacturing and assembly. For non-intersecting axes, an additional point must be introduced to the transformation relation so that each axis has a point where rotation is carried out. In the assembled scanner case, the axes intersect at the point S, that is found to be at $(X_{cam}, Y_{cam}, Z_{cam})$ from the camera reference, obtained using imaging feedback discussed.

The laser beam plane is adjusted by detecting laser lines on the planar surface at different locations within the field of view. Image of the calibration pattern taken without laser stripe and those when the laser is switched on provide the basis for definition of the location of the laser points that are on the laser plane. The capture laser lines are shown in Figure 93c. A multiple of these points are captured at various poses of the planar calibrator. The laser lines used to find laser planes are shown in Figure 93d. The laser is adjusted manually until lines obtained from the laser fit into a plane that is found to be with normal in the XY plane of the camera. After the alignment, the values of the two variables β and y_l can also be determined directly from the defined laser beam planes. The summary of the method and procedures used in for calibrations of motion and lasers is provided in Figure 97.

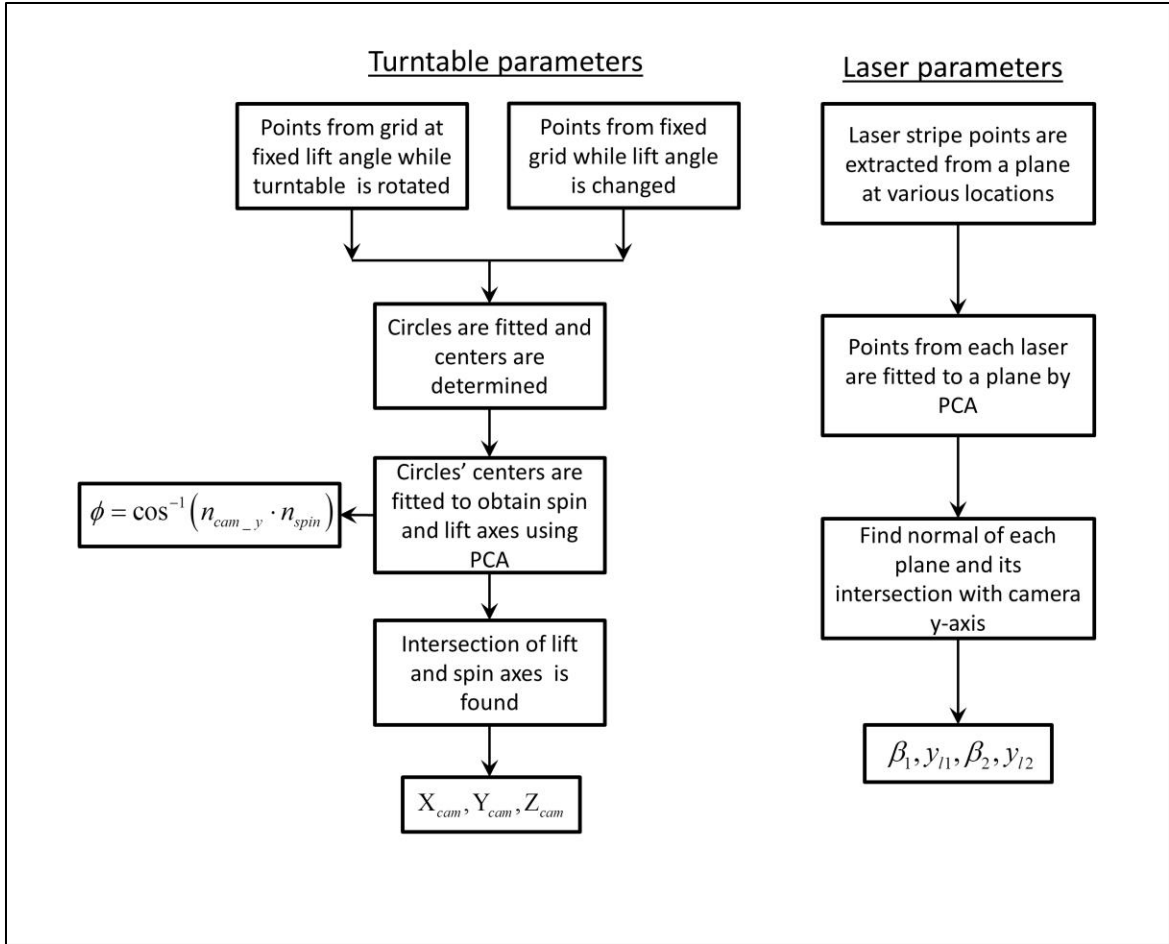


Figure 97: Procedure of calibration of the scanner variables using camera, lasers and a planar calibration grid

6.2 Triangulation model

A pinhole Camera model relates set of laser reflection points from captured images in pixels to the original collection of points in Space at the an instant. For the image to obey the pinhole hole, relevant image distortion model obtained during calibration is used to transform image points to an undistorted from.

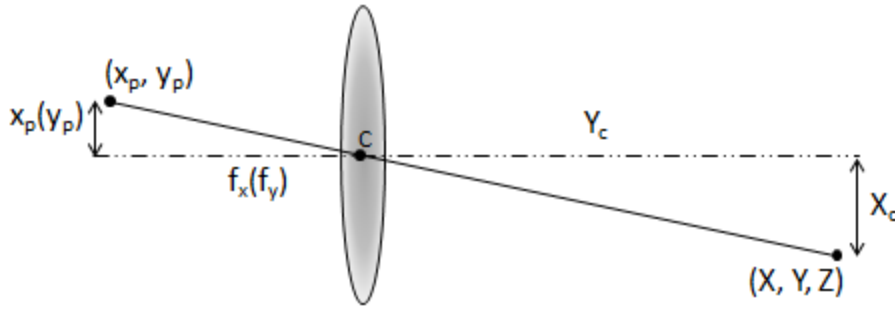


Figure 98: Pinhole camera model relation between pixel and world position

The relation between undistorted pixel locations and world points are $\frac{X_c}{Y_c} = \frac{x_p}{f_x}$ and $\frac{Z_c}{Y_c} = \frac{y_p}{f_y}$.

There is distinction between the calibration carried out the process carried out in the previous calibration sub-section and the model introduced in this sub-section. The calibration performed is only to determine the camera properties that relate it with the image taken; there is need for an additional relation between the location of the part during scanning motion and the image frame. Image points of laser scan must be represented in a fixed 3D world frame. The laser points extraction from images are discussed in the following section. From the basic pinhole model, two equations that relate undistorted image laser points (x_p, y_p) to world points (X_c, Y_c, Z_c) in camera frame located at point C are:

$$X_c = \frac{x_p}{f_x} Y_c \quad , \quad Z_c = \frac{y_p}{f_y} Y_c \quad (22)$$

To find the complete 3D location of a point, it is required to have 3 equations. Hence, an extra equation is afforded by the fact that all the detected points must lay on the laser beam plane. The triangle formed by laser, camera and detected laser point forms the principle of triangulation [143], the technique behind most laser 3D scanners that are not of the time-of-flight nature. The geometric relation in on the diagram in Figure 99 provides the following relation. This third relation arising from the triangulation phenomenon is what govern the laser 3D scanners that equips them with the ability to measure the depth of a 2D image.

$$X_c = (Y_l - Y_c) \tan(\beta) \quad (23)$$

From Equations 22 and 23 rearrangement, Equation 24 gives the complete 3D position of the pixel laser dot.

$$\left. \begin{aligned} X_c &= \frac{Y_l \tan(\beta) x_p}{x_p + f_x \tan(\beta)} ; Y_c = \frac{Y_l \tan(\beta)}{\frac{x_p}{f_x} + \tan(\beta)} ; Z_c = \frac{Y_l \tan(\beta) y_p}{\frac{x_p f_y}{f_x} + f_y \tan(\beta)} \end{aligned} \right\} \quad (24)$$

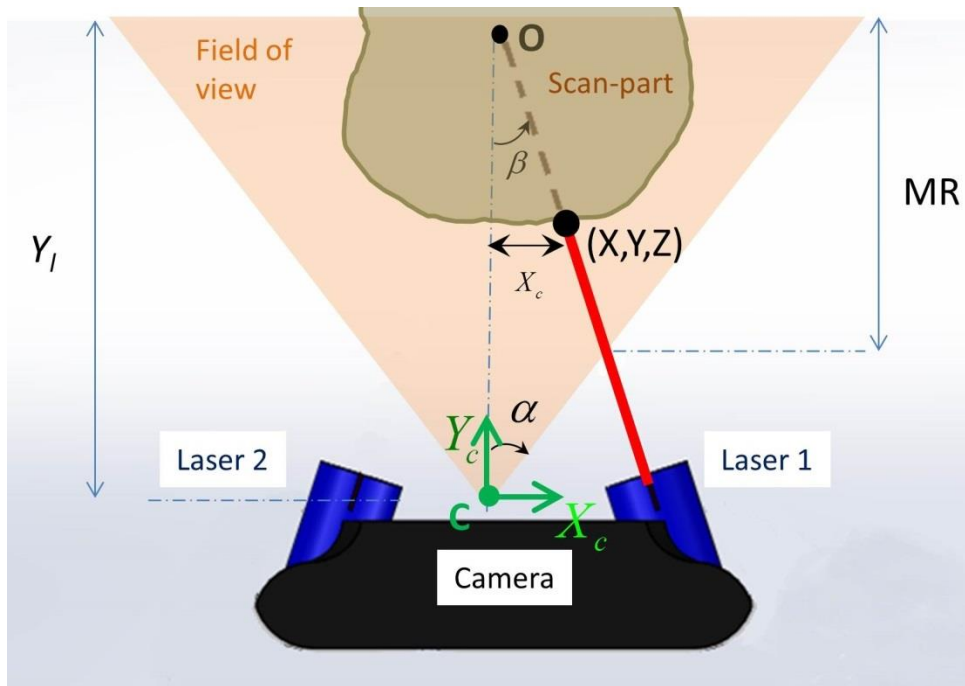


Figure 99: Triangulation diagram showing measurable range (MR), field of view, laser 1 plane and sample point (X, Y, Z)

6.3 Laser stripe extraction using image processing:

It is important to understand how the laser line beam behaves and its interaction with a part to be able to devise a proper method of reconstruction of the laser beam positions on an object. The observe laser width by the camera is not equal to the incident beam width. This way the laser width appears to the camera is sketched in Figure 100 .

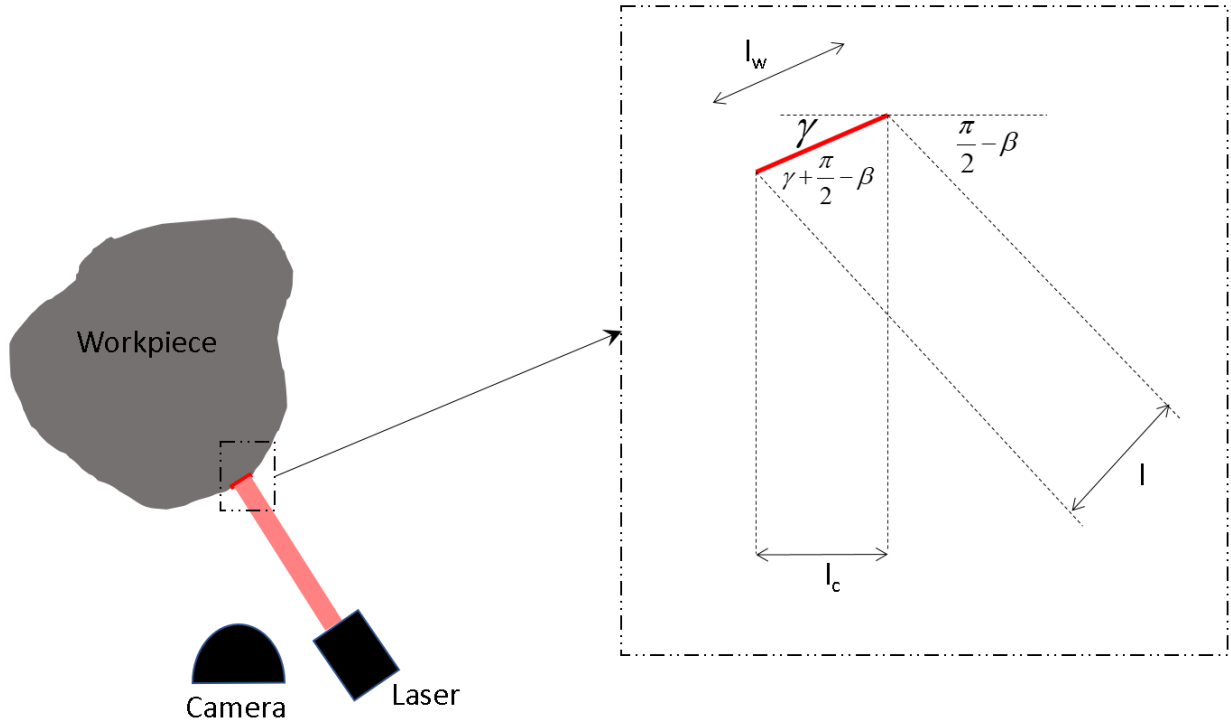


Figure 100: laser width resolved as how it appears on the camera

Where l is the laser beam thickness, l_w is the thickness of the projected beam on part, l_c is width of the reflected beam as seen by the camera, β is the laser triangulation angle and α the angle between camera and the local surface normal of the object. The view laser width can be found using the following relations.

$$l = l_w \cos(\beta - \alpha) \Rightarrow l_w = \frac{l}{\cos(\beta - \alpha)} \quad (25)$$

$$l_c = \frac{l \cos(\gamma)}{\cos(\beta - \gamma)} \quad (26)$$

The need for turn-table and other positioning apparatus is to keep the local surface normal not too far away from the camera view angle.

The limitation on the object size and measurable range of a triangulation 3D scanning system is computed using from the diagram in Figure 101 . For a camera with field of view angle of FOV , the maximum object radial size R_{max} and scanner measurable range MR are given in Equations 27 and 28.

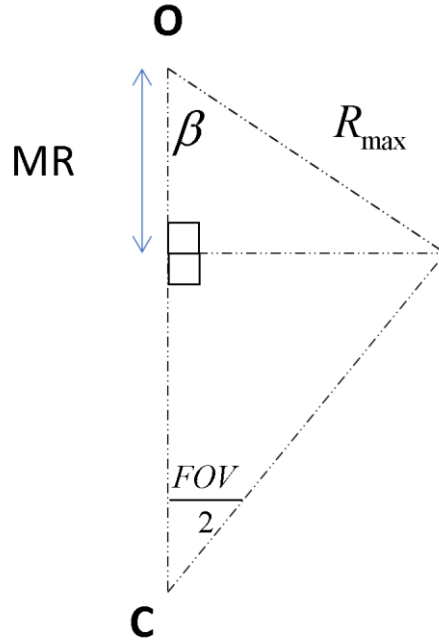


Figure 101: Sketch showing measurable range and camera field of view

$$R_{max} = \frac{\tan\left(\frac{FOV}{2}\right)y_o}{\tan(\beta) \tan\left(\frac{FOV}{2}\right)} [1 + \tan^2(\beta)]^{\frac{1}{2}} \quad (27)$$

$$MR = \frac{y_o \tan\left(\frac{FOV}{2}\right)}{\tan\left(\frac{FOV}{2}\right) + \tan(\beta)} \quad (28)$$

The intensity of the red channel of the line laser used when reflected from a black planar surface at two offset distances is given in Figure 102 . The laser width is generally observed to be between 5-12 pixels. The thresholding method will usually choose those region with high intensity of light and separate them the other regions. Operations will only be carried out on the selected regions to produce a stripe that represent the central line of the laser beam as projected on the 3D object. Testing the laser scanner on a dark surface is a means of understanding the least intense light reflection from objects and the variation of the intensity as the reflected incident angle diverge from the camera. At the close range of 27mm, there is no change in the level of intensity observed but that begins to change when the range reaches 50mm and above. The Lambertian model

assumed here has the intensity that decreases by a factor of cosine of the angle the reflected light makes with the camera axis.

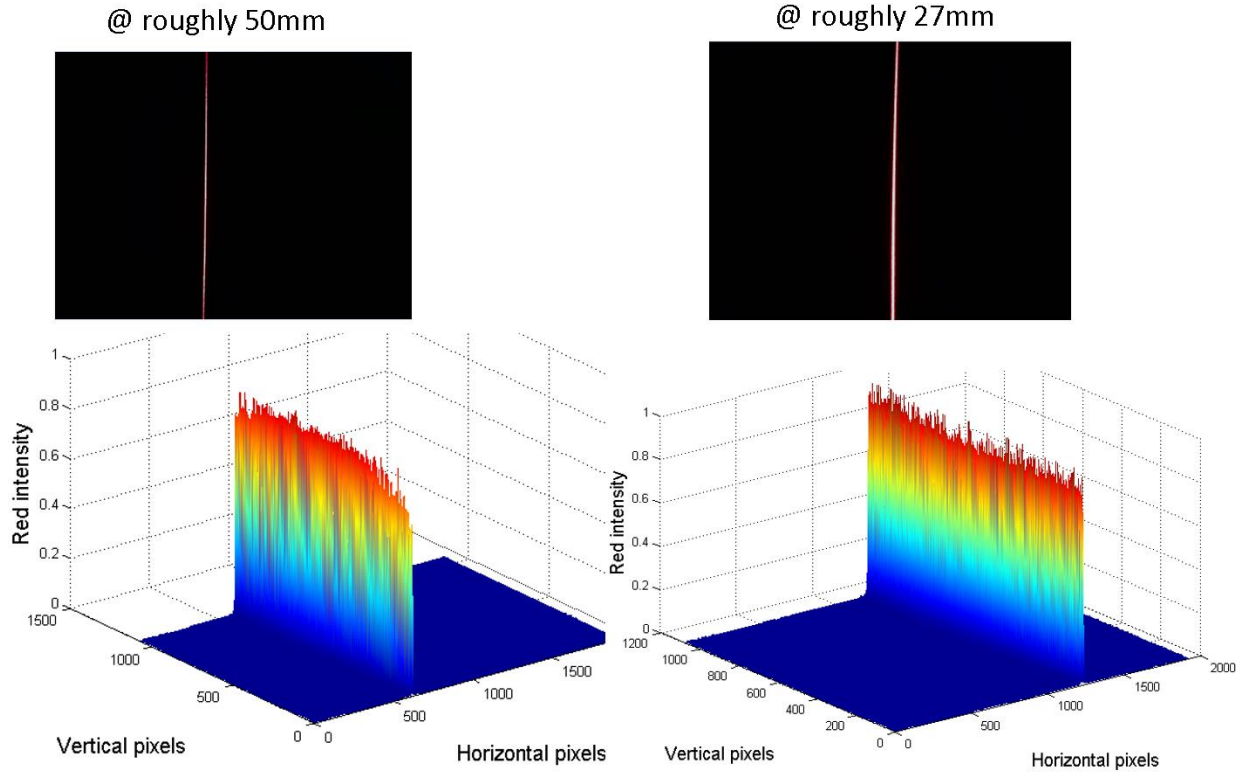


Figure 102: Raw red channel image sensor signal at two distances showing reflected laser beam

Before extraction of stripe curve, the image undergoes some preprocessing. To uniform out noise, a gaussian kernel h is convoluted with gray-scale image $I(i, j)$ in the given equation. The gray scale image is generated from a combination of the 3 channels of the colored image (red, blue and green) RGB.

$$I(i, j) \cdot h = \sum_{k=1}^{n_1} \sum_{l=1}^{n_2} h(k, l) I(i - k, j - l) \quad (29)$$

Where $k \in \{1, 2 \dots n_1\}$, $l \in \{1, 2 \dots n_2\}$ for $n_1 \times n_2$ sized filter

$$h(k, l) = \frac{e^{-\frac{(k^2+l^2)}{2\sigma^2}}}{\sum_{n_1} \sum_{n_2} e^{-\frac{(k^2+l^2)}{2\sigma^2}}} \quad (30)$$

The size $n_1 \times n_2$ and mean σ are to be determined according to line width and intensity [120]. The gray-scale image is convoluted with the kernel discretely. The improvement on the image can be seen in the Figure 103 . The resulting image with filter is smoother and has less errors from noise.

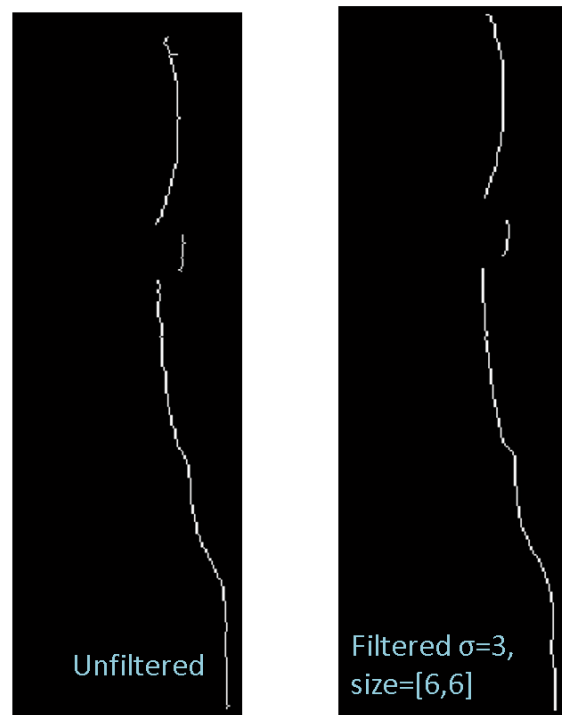


Figure 103: Filter and unfiltered images compared

Images with laser stripes need to be processed and the intersection between the measured object and the laser plane should be obtained and stored for further manipulations. The 3D scanner is prepared to work in normal lighting to prevent having use a dark working space. To reduce the effects of surrounding light, the scanner works at low exposure settings (variable based on the scanning environment). With the proper setting, the image background is usually completely dark. The external lighting should be as uniform as it can be, and exposure should be adjusted for every changes in the scanning condition.

Concerning the several reflectance model, as suggested in some papers [144,145], reflectance can be divided into diffuse lobe, specular lobe and specular spike. With uncertainty

associated with the specular lobe and spike reflection models, reflections are assumed to have purely Lambertian diffuse lobe[145] and specular reflections are avoided as much as possible during scan. For instance, shiny metallic objects are thinly painted matte white before scanning to avoid spike of light that hides small features on the image. The contributions of the paint on the reflected image can be seen in Figure 104, where the image of a painted aluminum sample is compared with the same part before painting.

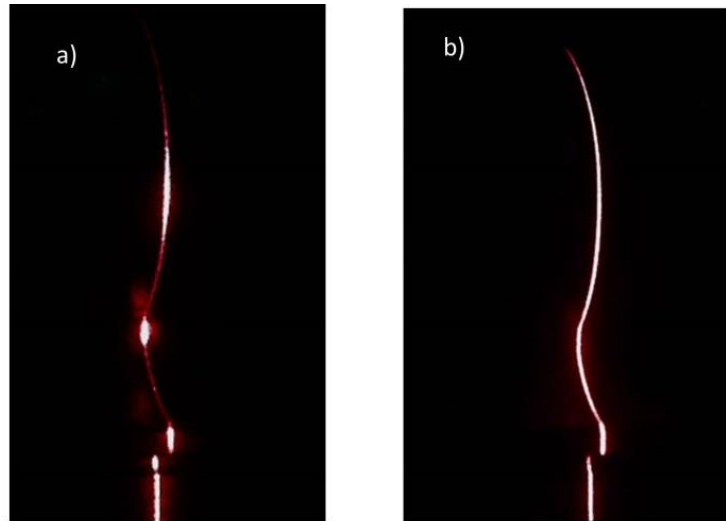


Figure 104: a) Image shiny aluminum part and b) Image after it is painted

Another important way the reflection on the object can temper with the image of real object outline is when some of the light goes into the object. The effect of a translucent surface on the scan result can be seen in Figure 105 . In the figure, a rat bone is reconstructed with and without painting. Translucent surface, like the bone take some of the incident light and creates a glowing light within the object making scan results less accurate.

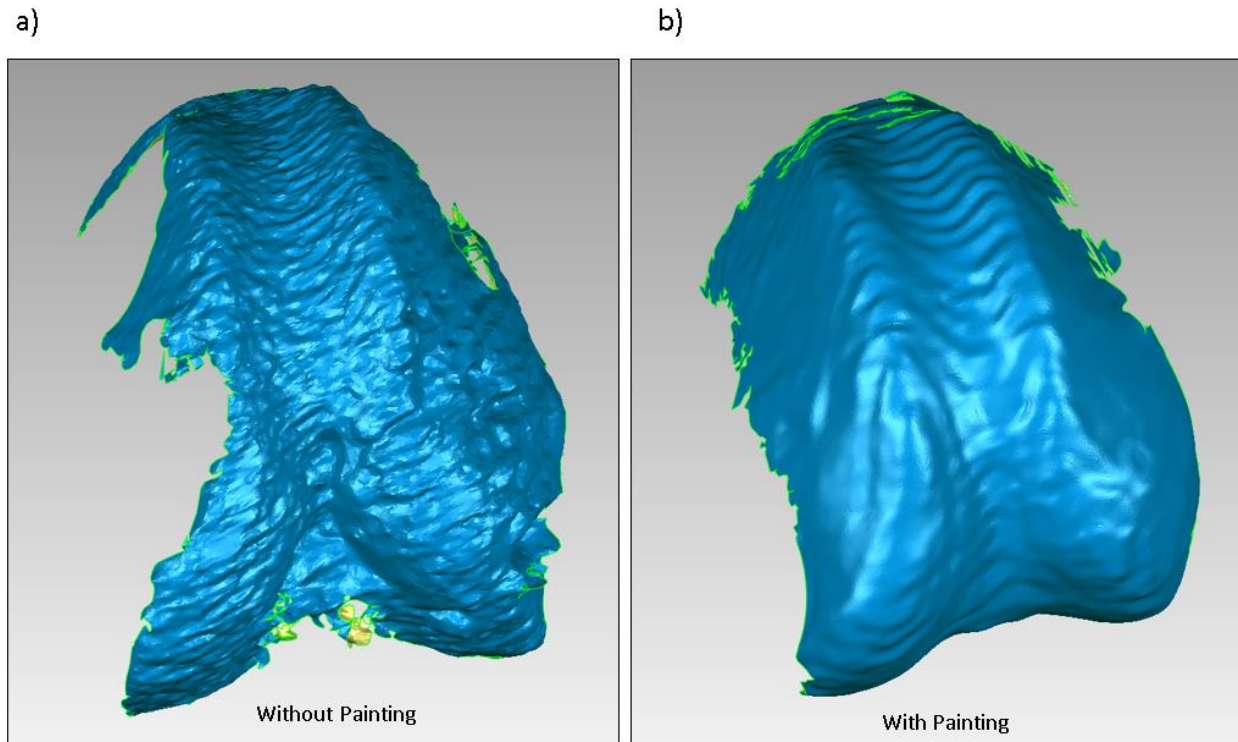


Figure 105: Reconstruction of rat knee without painting in (a) and with painting in (b)

The contrast of the image is adjusted in each color channel to eliminate the background noise. The resulting RGB image is then converted to an intensity image on which stripe extraction can be executed. Method of laser stripe extraction where each row is analyzed separately to extract stripe is considered in literature ([120,146]). The selected pixels in a row that pass the threshold criterion together with their intensities are used in determining the laser stripe point. The chosen pixel location of the stripe does not have to be a discrete pixel position, as Usamentiaga et al. [146] and Forest et al. [147] suggested using subpixel approximation methods such as Gaussian and center of mass where the methods show performance in similar range.

In this work, thresholding of intensity image is carried out locally within an appropriately sized window that trails along the laser stripe. The local thresholding is chosen because for regions where the normal angle is wide compare to laser incidence direction and the camera view direction tend to have low intensity, so the use of a single threshold limit will eliminate those points. The process begins by a rough segmentation that is carried out to isolate regions that exceed a certain threshold. The initial threshold is chosen to be very low strength, so as to allow all relevant portions

of the image to be included. For this purpose, the threshold value is chosen to be a fraction of Otsu global threshold [148] to get a binary image. A morphological filling of the generated binary image is performed after which identification of regions is carried out and the image's connected-components are labeled accordingly. The values of the areas of these components are stored and the mid-point path is found row by row for each connected objects in the image. Decision on which region to use have to be made when more than one connected components are found on a row, one with larger area is preferred since it is less likely to be a result of noise. With the mid-points defined, thresholding limits are found locally for each small window with their dimensions variably chosen according to stripe width. This window is illustrated in Figure 106, where it is moved along the mid-point path until each row is fully segmented.

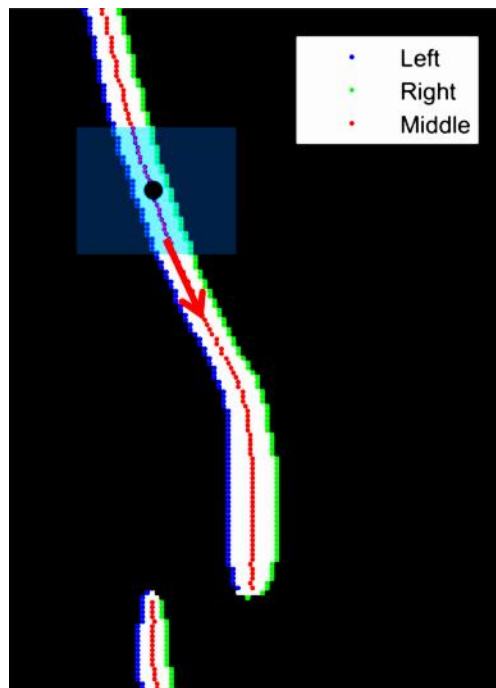


Figure 106: Local threshold method carried out in a local vicinity window

From the data obtained from the image, there are random noise emanating from image sensor and laser itself [149]. A way of mitigating the random noise is by convolution of the image with a Gaussian kernel whose deviation is varied based on stripe width and intensity for each image [120]. There are many ways of identification of the laser line from a binary or grayscale image.

The use of four methods (median, mean, gaussian and thinning methods) of curve extraction have been formulated and tested. Median did not give an accurate result as the weighted mean and gaussian approaches which provided reconstruction accuracy in the same magnitude.

For all scan results published here, two methods of peak intensity determination methods are used—the Gaussian peak and centroid methods. For the centroid method, the center-of-intensity are used as laser intersection points with the workpiece. The method of point extraction used is dependent on local vicinity of each row used for computing centroids, due to local thresholding. So, unlike row independent methods [146], the row signals are not entirely independent of each other. As for the Gaussian beam model, the Gaussian peak extraction strategy fits the row data into a normal distribution function and the peak point is found. Qi et al [149] explains the Gaussian method further. For reference additional reference, Colak et. al[150] studied various stripe detection methods—like GA, GD, CM, Max, etc—to compared the deviations in measurements.

After the curve is extracted from each image, a cubic spline or NURBS can be interpolated piece-wisely given the condition whether the surface scanned has holes or not. Figure 107 shows the two cases where holes are either filled or not using spline interpolation. The interpolated points will be resampled and processed into mesh. The interpolation makes it possible to reconstruct parts at subpixel level. However excessive interpolation can introduce non-existent texture on the reconstructed surface, such as the one shown in Figure 108 .

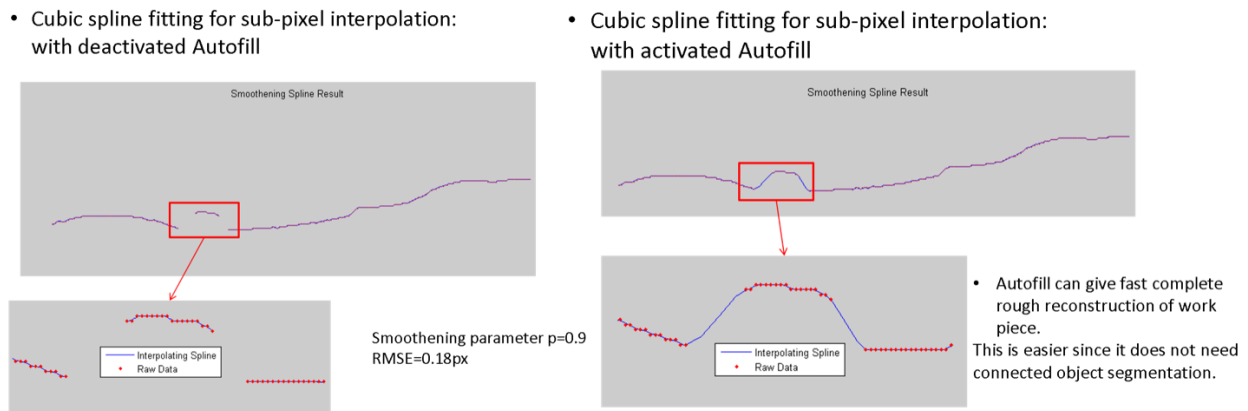


Figure 107: Cubic spline fitting of stripe points with and without filling of holes

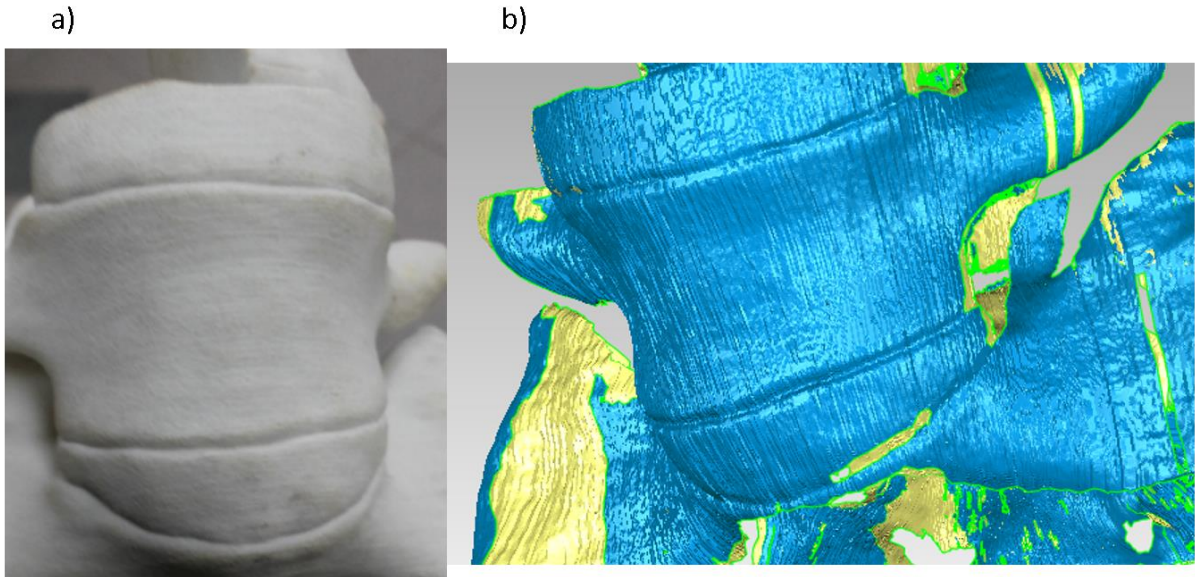


Figure 108: Demonstration of how artificial texture can be introduced to the reconstructed part by over-interpolation

Local threshold segmentation is applied in place of global threshold. Global thresholding sometimes removes portions of scanned object that are not bright enough as can be seen in Figure 109 . The region was marked by a global Otsu threshold where important portion is cut off. Because of this, a local Otsu threshold is implemented. The effect of this method can be seen in the reconstructed model in Figure 110 .



Figure 109: Omitted portion when applying global thresholding

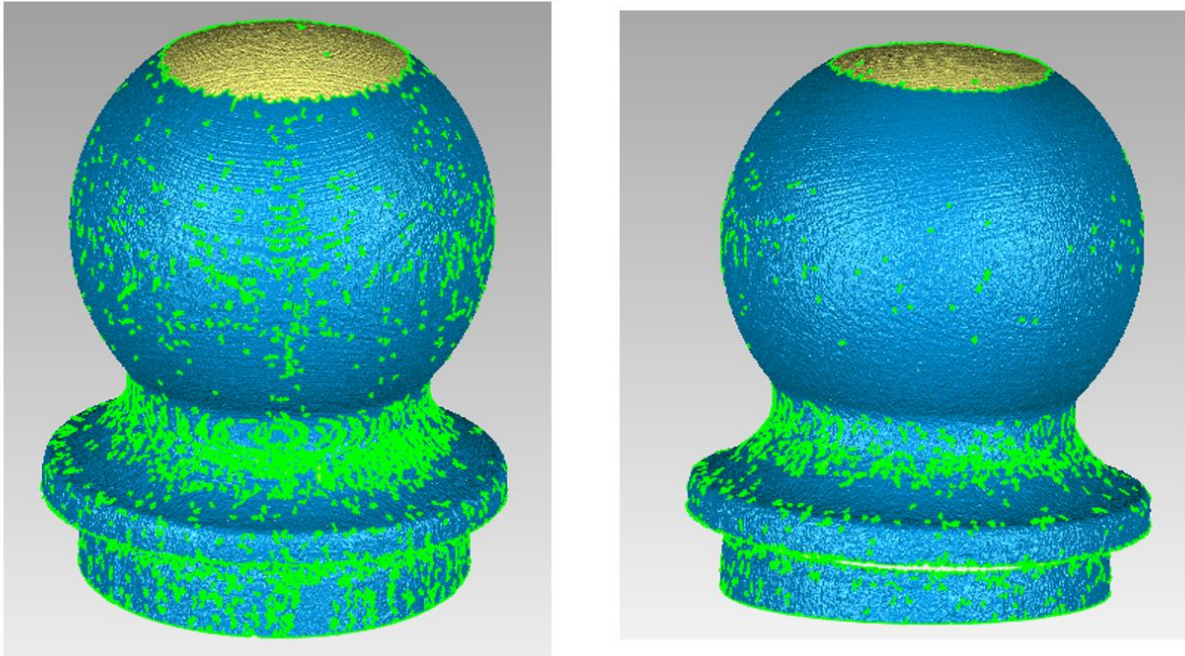


Figure 110: Part on the left, reconstructed using global threshold shows more missing portions than the one on the right that is reconstructed using local thresholding

A normal estimation procedure described in Figure 111 has been developed. The normal direction is assumed to be perpendicular to the interpolating spline and in the laser plane. It is computed using the gradient of the spline and is transformed by rotations θ and ϕ . The estimation of normal vectors may serve as aid in mesh processing to improve the mesh creation.

Normal Estimation

- With gradient $\langle dx, dy \rangle$; $\langle -dy, dx \rangle$ is always normal to the curve and is directed outward if $x > 0$
- This normal vector together with the curve must be transformed to 3D space. It is assumed that the vectors all lie in laser plane.

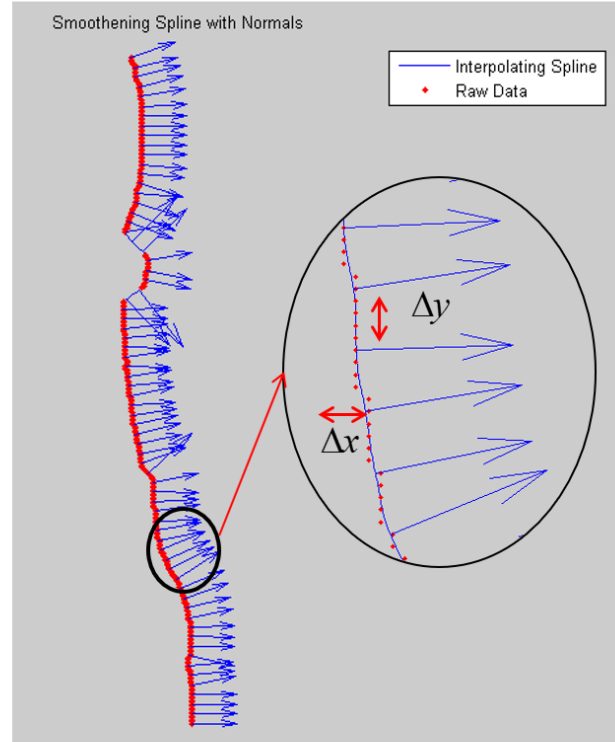


Figure 111: Normal estimation from image gradient

The obtained normal directions in pixel n_{px} and n_{py} are transformed to 3D world using pinhole and triangulation relations covered previously. The instantaneous normal (n'_x, n'_y, n'_z) are expressed in Equation 31 below.

$$\left\{ \begin{array}{l} n'_y = \frac{y_{cam} \tan(\beta)}{\tan(\beta) + \frac{n_{px}}{f_x}} \\ n'_x = \frac{n_{px}}{f_x} \cdot n'_y \text{ and } n'_z = \frac{n_{py}}{f_y} \cdot n'_y \end{array} \right\} \quad (31)$$

The normal direction need to be transformed to the original frame of the object. This is carried out in Equation 32 below

$$\begin{bmatrix} n_x \\ n_y \\ n_z \end{bmatrix} = \begin{bmatrix} \cos(\theta) & -\sin(\theta)\cos(\phi) & -\sin(\theta)\sin(\phi) \\ \sin(\theta) & \cos(\theta)\cos(\phi) & \cos(\theta)\sin(\phi) \\ 0 & -\sin(\phi) & \cos(\phi) \end{bmatrix} \cdot \begin{bmatrix} n'_x \\ n'_y \\ n'_z \end{bmatrix} \quad (32)$$

Where:

$[n_x, n_y, n_z]^T$ is normal in 3D,

$[n'_x, n'_y, n'_z]^T$ is normal at instant of capture.

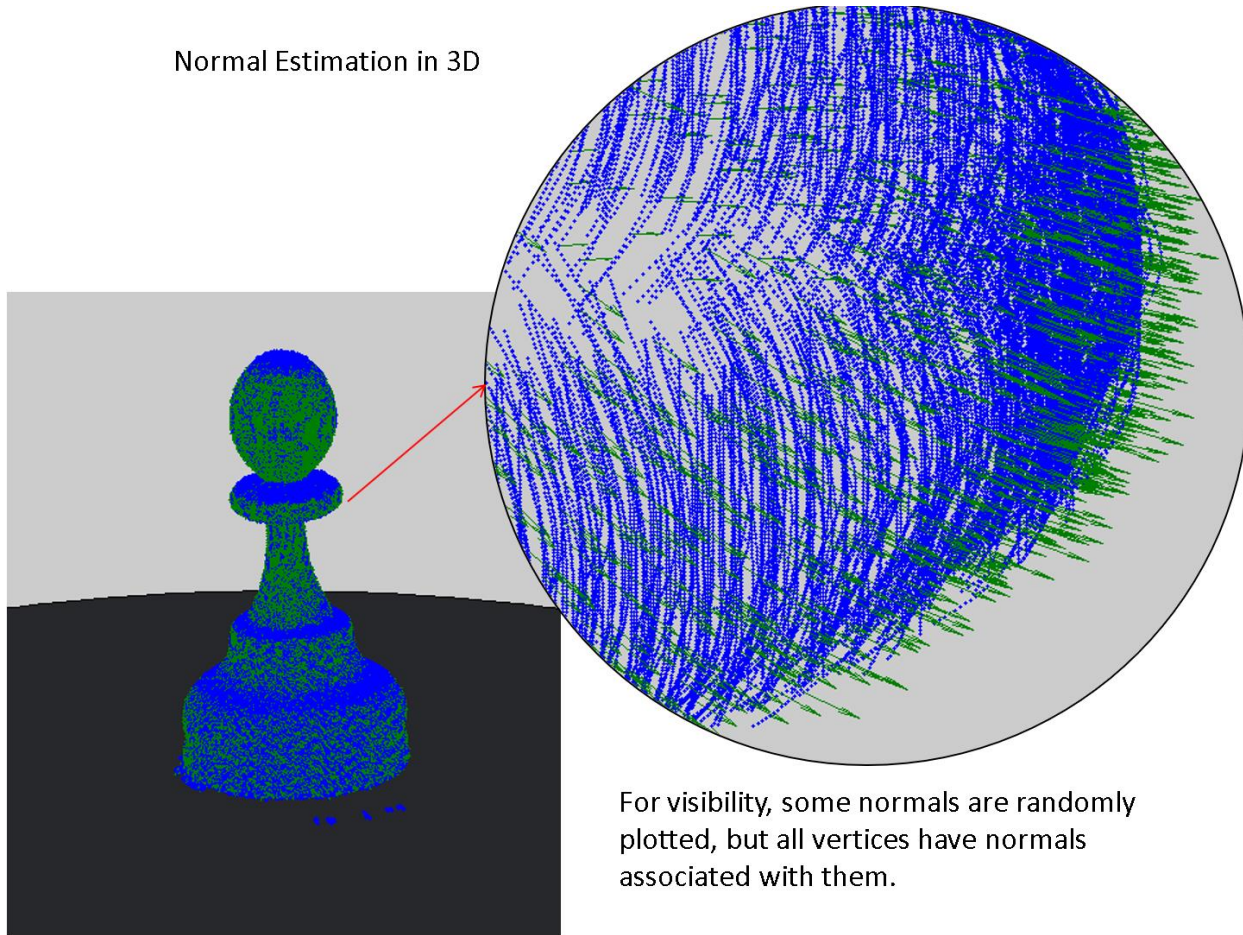
β is angle of laser plane,

$[f_x, f_y]$ are focal length in pixel,

$[n_{px}, n_{py}]$ is normal in image plane.

y_{cam} is relative camera y-position from spinner.

Normal Estimation in 3D



For visibility, some normals are randomly plotted, but all vertices have normals associated with them.

Figure 112: Sample point cloud with some normal directions indicated in green arrows

The normals are finally normalized to magnitude of unity. The resulting normal directions are demonstrated on a point cloud in the Figure 112 . The normal are plotted for random points for clarity. With cloud point and normal defined, a small script was written in MATLAB to create PLY file format of mesh defined progressively from stripe points. The constructed meshes are illustrated in Figure 113 . The file structure of the generated PLY file is shown in Figure 114 . More advanced mesh generation schemes are available [151–153] and commercial products exist that can smoothen, resample and improve the point cloud and generate mesh from it.

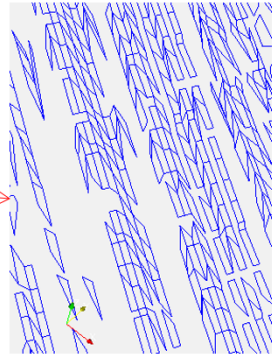
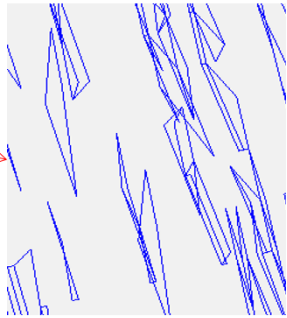
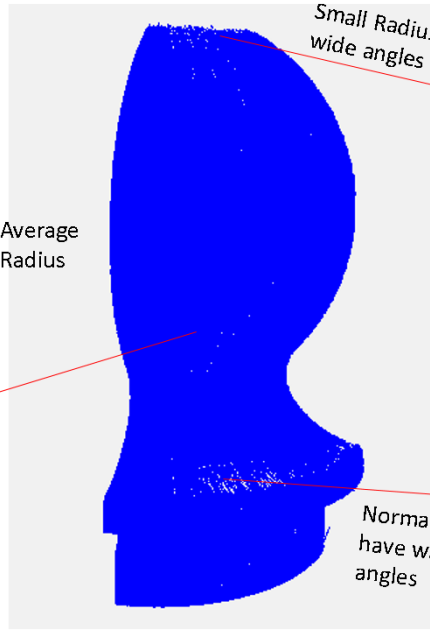
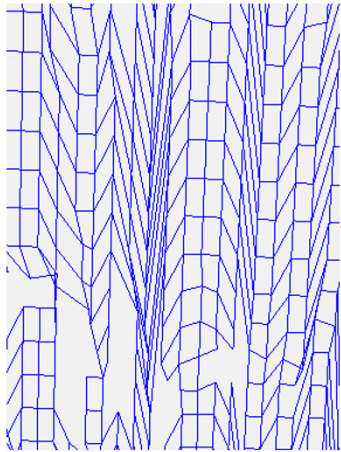
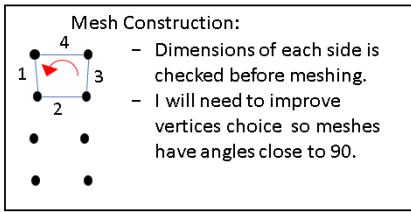


Figure 113: Mesh generation showing polygons at various locations

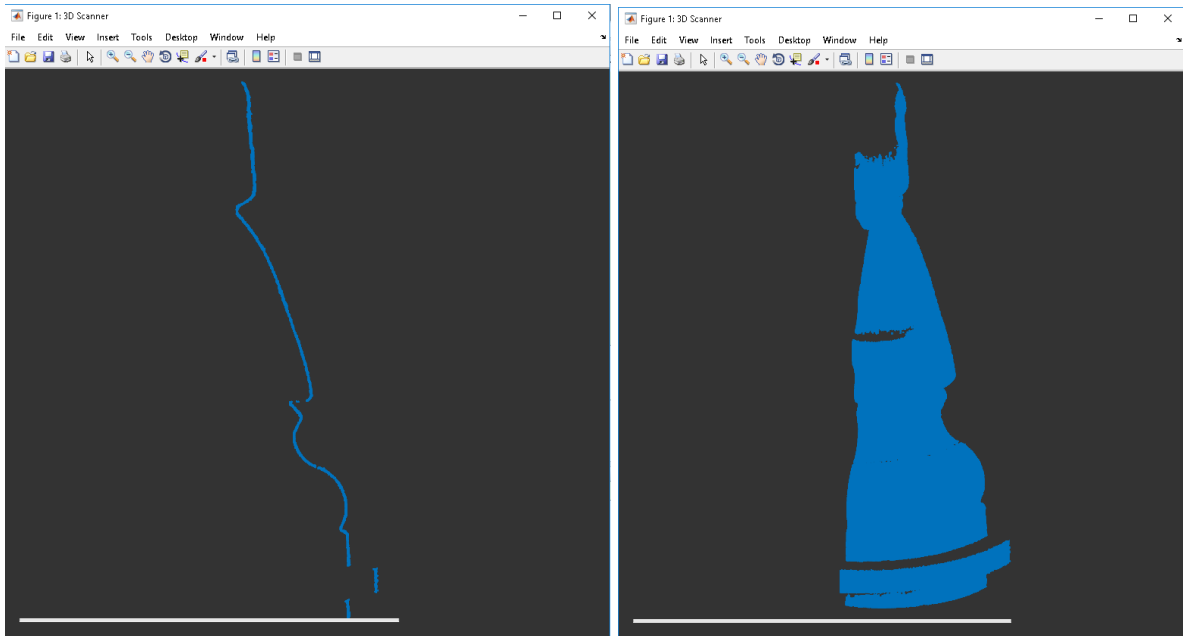
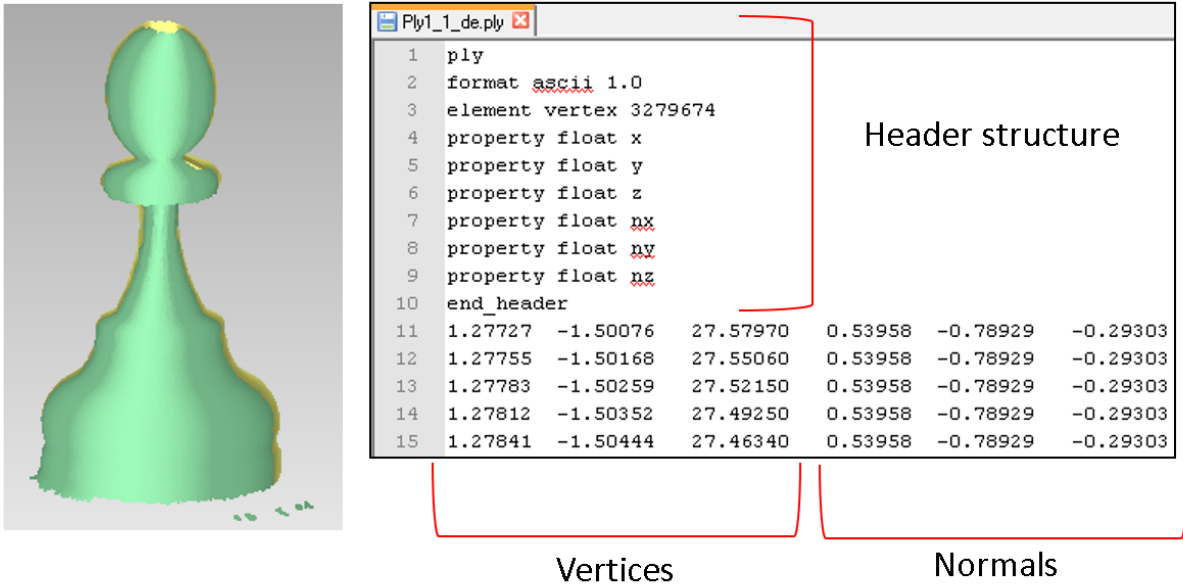


Figure 114: PLY file structure generated using points and normal vectors and the real-time point cloud processing application in MATLAB

6.4 Evaluation of Measurements

Initial measurements are comparable on mesh processing software. Specific geometric dimension can be compared using the measurement tools available in point cloud and mesh CAD software. For instance, the diameter of a cam sample is reconstructed and measured using two separate scans from the two lasers. Figure 115 shows the outcome of the measurement compared with the exact diameter of the part. The standard deviation shows how much the scanner's measurement vary. It is necessary to carry out a more rigorous and standard measurement evaluation and analysis.

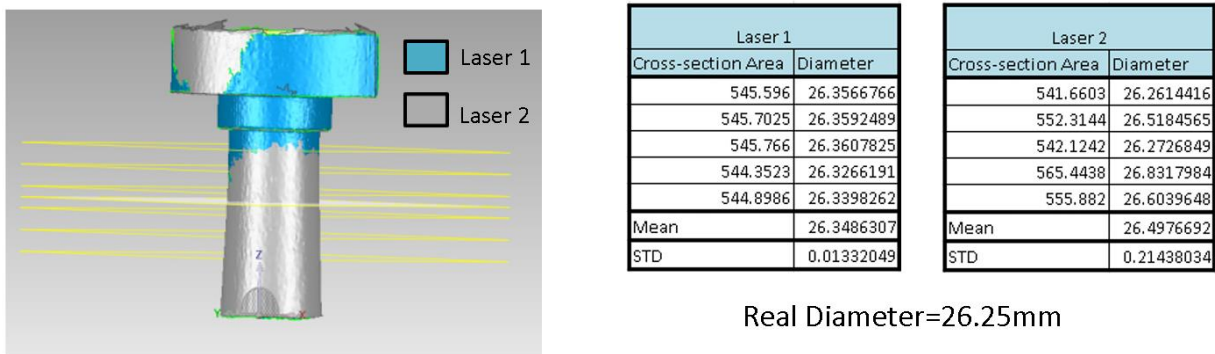


Figure 115: Preliminary evaluation of dimensions of reconstructed part

To obtain full information on the accuracy of measurement, the effects of the scanner parameters are considered. In this section, the determined parameters of the scanner are evaluated within some confidence intervals using the calibration data. A standard uncertainty analysis of the 3D scanner measurement is carried out using “Guide on the expression of uncertainty in measurement” (GUM)[154]. The goal is to find the effects of variations within the uncertainty interval in each of the influencing parameters of $\mathbf{u} = \langle \phi, \beta, \gamma_l, X_{cam}, Y_{cam}, Z_{cam} \rangle$ and how they affect the resulting error in measured points. For this, the points are first expressed explicitly as function of \mathbf{u} . The model of measured points (points from an object scan usually have between 10 thousand to 5 million points) that is a function of \mathbf{u} and the image leads to an overdetermined system. The relation linking the parameters directly to the measured points is found in Equation 33 for each i step of stripe angle by substitution and reorganization of Equations 27, 28 and 30.

$$\begin{bmatrix} X \\ Y \\ Z \end{bmatrix}_i = R(\theta_i)P(u) = R(\theta_i) \begin{bmatrix} \frac{x_p}{f_x} y_l \Gamma(\beta) - X_{cam} \\ \left[\cos(\phi) + \frac{y_p}{f_y} \sin(\phi) \right] y_l \Gamma(\beta) - Y_{cam} \cos(\phi) - Z_{cam} \sin(\phi) \\ \left[\frac{y_p}{f_y} \cos(\phi) - \sin(\phi) \right] y_l \Gamma(\beta) + Y_{cam} \sin(\phi) - Z_{cam} \cos(\phi) \end{bmatrix} \quad (33)$$

With $P(u)$ expressed as the second term in Equation 33, the following Equations 34 and 35 define the expressions $R(\theta)$ and $\Gamma(\beta)$ respectively.

$$R(\theta) = \begin{bmatrix} \cos(\theta) & \sin(\theta) & 0 \\ -\sin(\theta) & \cos(\theta) & 0 \\ 0 & 0 & 1 \end{bmatrix} \quad (34) \quad \Gamma(\beta) = \frac{\tan(\beta)}{\frac{x_p}{f_x} + \tan(\beta)} \quad (35)$$

Taking the derivative of Equation 33 yields the changes in position due to perturbations in the variables.

$[\partial x \quad \partial y \quad \partial z]^T_i = R(\theta_i) \cdot J_{P,u} \cdot \partial u$, where the Jacobian matrix is defined in Equation 36 below.

$$J_{P,u} = \begin{bmatrix} 0 & \frac{x_p y_l \Gamma'(\beta)}{f_x} & \frac{x_p \Gamma(\beta)}{f_x} & -1 & 0 & 0 \\ \left(-s(\phi) + \frac{y_p c(\phi)}{f_y} \right) \Gamma(\beta) y_l + y_s s(\phi) - z_s c(\phi) & \left(c(\phi) + \frac{y_p s(\phi)}{f_y} \right) \Gamma'(\beta) y_l & \left(c(\phi) + \frac{y_p s(\phi)}{f_y} \right) \Gamma(\beta) & 0 & -c(\phi) & -s(\phi) \\ \left(-c(\phi) - \frac{y_p s(\phi)}{f_y} \right) \Gamma(\beta) y_l + y_s c(\phi) + z_s s(\phi) & \left(-s(\phi) + \frac{y_p c(\phi)}{f_y} \right) \Gamma'(\beta) y_l & \left(-s(\phi) + \frac{y_p c(\phi)}{f_y} \right) \Gamma(\beta) & 0 & s(\phi) & -c(\phi) \end{bmatrix} \quad (36)$$

Where Equation 37 defines $\Gamma'(\beta)$.

$$\Gamma'(\beta) = \frac{x_p}{f_x \cos^2(\beta) \left[\frac{x_p}{f_x} + \tan(\beta) \right]^2} \quad (37)$$

The Jacobian of the scanner model is used in the optimization process covered later in this section.

6.4.1 Uncertainty analysis of measured points

With the scanner model of measurement derived, it becomes necessary to evaluate the uncertainty associated with values measured with the scanner. The obtained measurement model depends on the image pixels that has been undistorted and preprocessed, all known relations and quantifiable models of the studied 3D scanner parameters discussed has been considered.

Guide on the expression of uncertainty in measurement (GUM) and International vocabulary on metrology (VIM), provide an international standard of evaluation and expression of measurement uncertainty[154,155]. These standards require a model of measurement reflecting the relation between influencing quantities and the output. In the case of this work, the model of the scanner is given in Equation 33 and the inputs are the six variables in the array \mathbf{u} . Based on the guidelines dictated by GUM, the model of measurement must include all influencing quantities with known corrections included. Also, the standard uncertainty of the desired quantity can be analyzed based on the standard deviation of each of the input. This standard deviation of inputs can be estimated from a distribution of possible values obtained by experimentation or observation. Probability distribution frequencies maybe based on direct observations or other knowledge, such as calibration data. GUM section 4.3 provides the guidelines for estimate of inputs whose values have not being obtained by repeated observation. This is the guideline used for the input data of the scanner, where estimation is done by calibration.

The uncertainties values of the input quantities are estimated using calibration data which can be used to obtain the probability distribution function (PDF) of the values (GUM type B uncertainty evaluation). During the calibration process, since the values of parameters in \mathbf{u} are calibrated through fitting of points from the camera-laser scanner system, the deviations of the points from the fitted model gives a statistical basis for estimation of variance. From the calibration data and their deviations, the best estimate of measurement and the dispersion in the measurement of each input parameter can be evaluated, such as ϕ error bar plotted in Figure 96b. When the best estimate of the inputs and their uncertainties are available, a Gaussian PDF is recommended. Using the standard deviation that is taken at 68% level of confidence, the scanner inputs estimates of the generated PDFs and the standard deviations are given in Table 1.

Table 1: Properties of the scanner parameters used as input PDFs for uncertainty propagation

	ϕ [rad]	β_1 [rad]	y_{l1} [mm]	X_{cam} [mm]	Y_{cam} [mm]	Z_{cam} [mm]	β_2 [rad]	y_{l2} [mm]
Estimates	0.0248	0.3517	93.050	-2.634	98.330	-2.662	-0.3344	91.055
Uncertainties (68% level of confidence)	0.005	0.010	0.15	0.040	0.040	0.040	0.008	0.15

GUM recommends the use of the law of propagation of uncertainty with Taylor's series truncation to propagate input PDFs to obtain uncertainty of measurand. However, there is provision of alternative for complex measurement models; a practical and more general tool such as Monte Carlo simulation is applicable[156]. Monte Carlo simulation works by random sampling of large combinations (minimum of 10^6 samples by GUM) of each input PDF values, using which the measurand quantities are found by applying the complete system model thereby generating the output PDF. The coordinate points X, Y, Z and radial deviation measured from a known sphere are studied as measurands using image points from the sphere at various locations. The average radial deviation alongside the overall Monte Carlo simulation of uncertainty propagation process is presented in Figure 116. The distribution of the other measurands of the sample sphere are given in the position coordinates X, Y, Z are shown in Figures 117a, 117b and 117c. The deviation of the sample points from the sphere surface are expected to be distributed in a way that the mean will be about zero rather than the -0.247 shown in Figure 116. As a result, the subsequent subsection deals with ways to minimize such deviations by optimization.

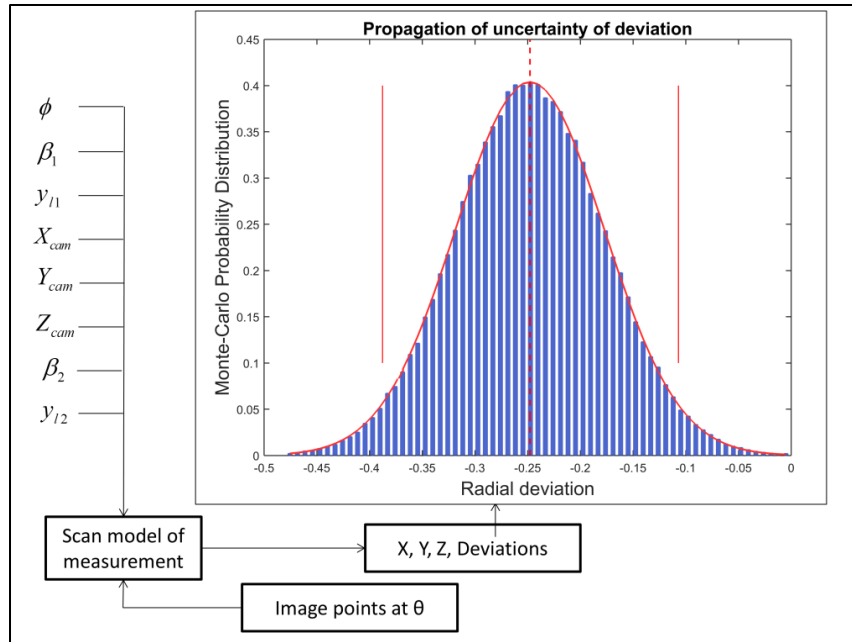


Figure 116: Monte Carlo simulation of uncertainty propagation showing average sample distribution of radial deviation

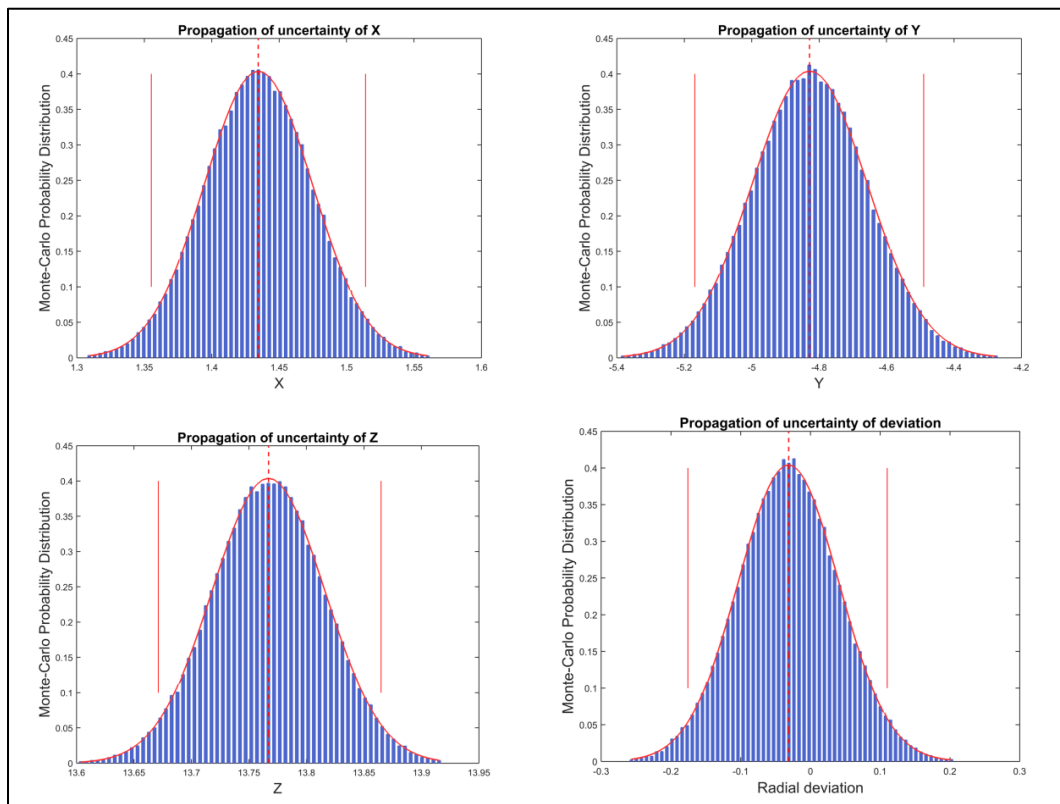


Figure 117: Results of uncertainty propagation in X, Y, Z are shown in plots a, b, and c with 2-sigma confidence interval marked. The average least squares optimized radial deviation PDF of sample points on the sphere is shown in d.

6.4.3 Least squares optimization

The deviations of many scanned points from a known geometric relation are minimized by varying the values of the variables in \mathbf{u} . Evaluation of the values of the variables from Equation 33 when given numerous solution of the points from a known geometry is a difficult problem. Such systems do not have a unique solution; hence, estimation is sought by using least squares techniques.

The input variables for the two-lasers-system are $u_1 = \langle \phi, \beta_1, \gamma_{l1}, X_{cam}, Y_{cam}, Z_{cam} \rangle$ and $u_2 = \langle \phi, \beta_2, \gamma_{l2}, X_{cam}, Y_{cam}, Z_{cam} \rangle$, cumulatively making 8 distinct parameters. It should be noted that calibrated estimates of these quantities do not guarantee to give the best measurement since small adjustments in each value will represent a probable another estimate. The calibration was made not considering the entire 3D scanning model, it is therefore expected that the initial calibration estimate might not be optimal. As stated in the last subsection, the use of the calibrated estimates produced a radial measurement estimate that is about 0.25mm deviated. Therefore, there is a need for a method of optimizing the parameters so that the measurements give less deviation.

A known spherical sample is used as reference benchmark for optimization of the scanner parameters. In essence, any known geometry can be used for this purpose. Iuliano et al[157] proposed using a geometry that is made from combination of basic surfaces to assess accuracy from the objects. However, the benchmark geometry must be known precise within an acceptable and tighter tolerance. For this work, the sphere is measured with a contact type CMM with uncertainty less than 3 micrometers. The CMM measurement of around 60 points on the sphere shows a maximum deviation of about 4.5 micrometers. Taking the radius of the sphere r , and that it is known with an uncertainty of less than 5 micrometers. The following expressions in Equation 38 are minimized to find the optimal u_1 and u_2 variables. The minimization is based on some known relations verifiable geometrically. Each of the expressions should be zero if the scanner works at an absolute accuracy, hence combination of parameter values that leads to the value of the functions should be the optimum.

The solution is to diminish deviations that are given by the following expressions in Equations 38 and 39. For each i step of turntable rotation:

$$\left. \begin{aligned} f_1^i(u_1) &= \|R(\theta_i)P(u_1) - X_{cnt1}(u_1)\| - r \\ f_2^i(u_2) &= \|R(\theta_i)P(u_2) - X_{cnt2}(u_2)\| - r \\ f_3^i(u_1, u_2) &= \|X_{cnt1}(u_1) - X_{cnt2}(u_2)\| \end{aligned} \right\} \quad (38)$$

The least square problems are therefore defined as:

$$\min_{u_1} \sum_i \|f_1^i(u_1)\|^2, \min_{u_2} \sum_i \|f_2^i(u_2)\|^2, \sum_i \min_{u_1, u_2} \|f_3^i(u_1, u_2)\|^2 \quad (39)$$

Where X_{cnt1} and X_{cnt2} are centers of fitted spheres of laser 1 and laser 2 measurements respectively. The spheres are fitted using geometric least square fitting [158]. The least squares solution minimizes the sum of squares of the deviations of thousands of points extracted from the images.

The least square problem is solved by using bounded trust-region-reflective algorithm available on MATLAB® platform with optimization toolbox [159,160]. It works by generating simpler sub-problems which serve as estimation within a smaller trust-region. The optimal results are given in Table 2 with the original values computed by calibration outlined in Section 6.1. The total residual factor, which is proportional to the sum of distances of the points from the fitted sphere, decreases by more than 50 times as given in Table 2. The residual represents increases with increases in the total error from all the extracted points. Moreover, by comparison of Figure 116 and Figure 117d, the radial deviation is observed to diminish considerably.

Table 2: Scanner variables before and after optimization using a spherical benchmark

	ϕ [rad]	β_1 [rad]	y_{l1} [mm]	X_{cam} [mm]	Y_{cam} [mm]	Z_{cam} [mm]	β_2 [rad]	y_{l2} [mm]	Residuals Factor
Computed	0.0248	0.3517	93.050	- 2.634	98.330	- 2.662	- 0.3344	91.055	6793.7
Optimized	0.0201	0.3662	92.701	- 2.670	98.345	- 2.687	- 0.3394	90.390	117.3

Figure 118 shows the fitted spheres using each of the two lasers and the corresponding error distributions of the first laser are shown in Figures 119a and 119b.

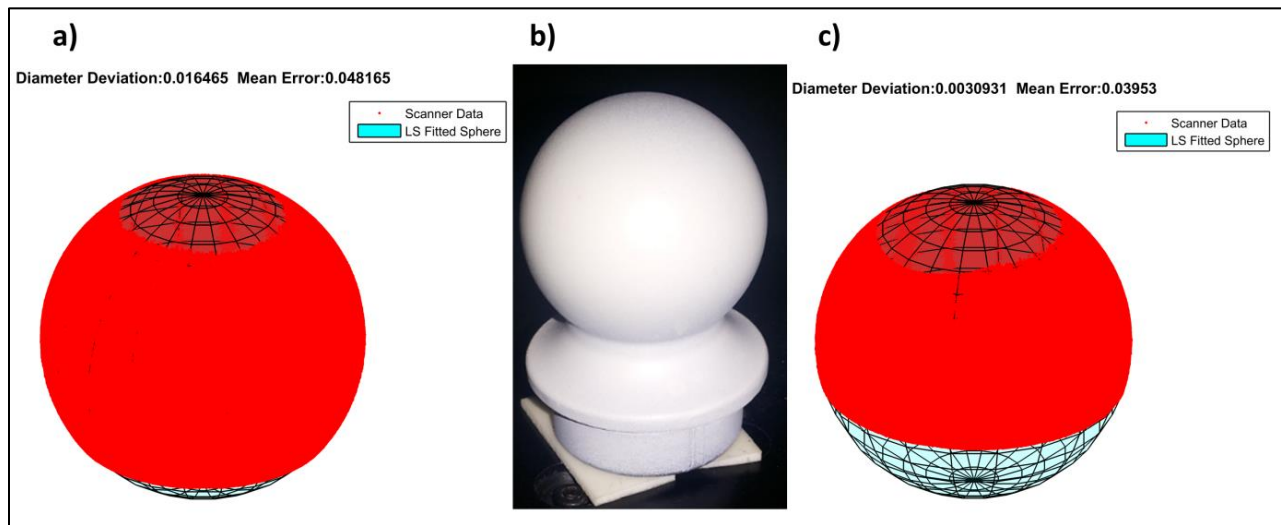


Figure 118: a) First laser scan fitted on sphere after optimization. b) Painted aluminum specimen. c) Second laser scan fitted on sphere after optimization

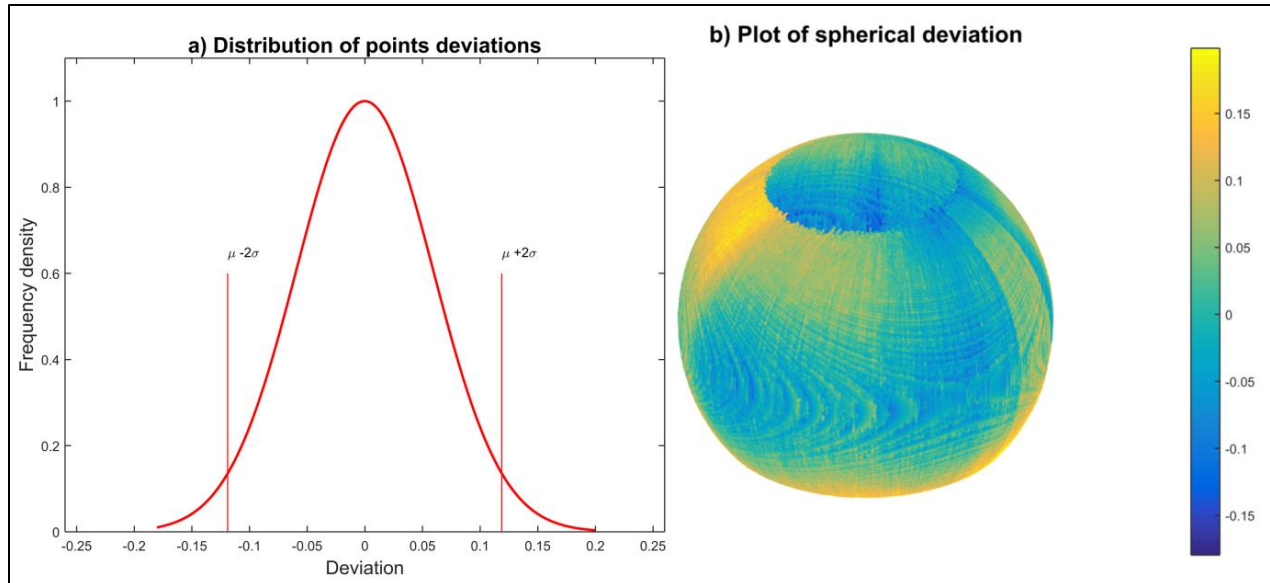


Figure 119: a) Frequency distribution of point radial deviations on sphere. b) Radial deviations of scan points on the sphere

6.5 Mesh Fusion and CAD conversion

Combination of reconstruction results are carried out either in mech or point cloud stages. After fusion of data obtained at other lift angles using both lasers, the completely reconstructed sphere specimen is shown in Figure 120b. A more complex fused mesh of scan object from this scanner is shown in Figure 120c-d. In order to avoid overlap of surfaces, only region with incomplete data should be patched to the first scan. This can be accomplished by filtering subsequent scans to allow only missed regions before joining data together. An easier way of patching scan data can be carried out using commercial mesh modeling software. Further adjustments of points can be made using constraint iterative closest point (ICP) algorithms to ensure data sets are properly merged. It is found that significant decrease in number of iterations are required when ICP is carried out using point of geometric features [161]. The geometric feature ICP(GF-ICP) method converges faster.

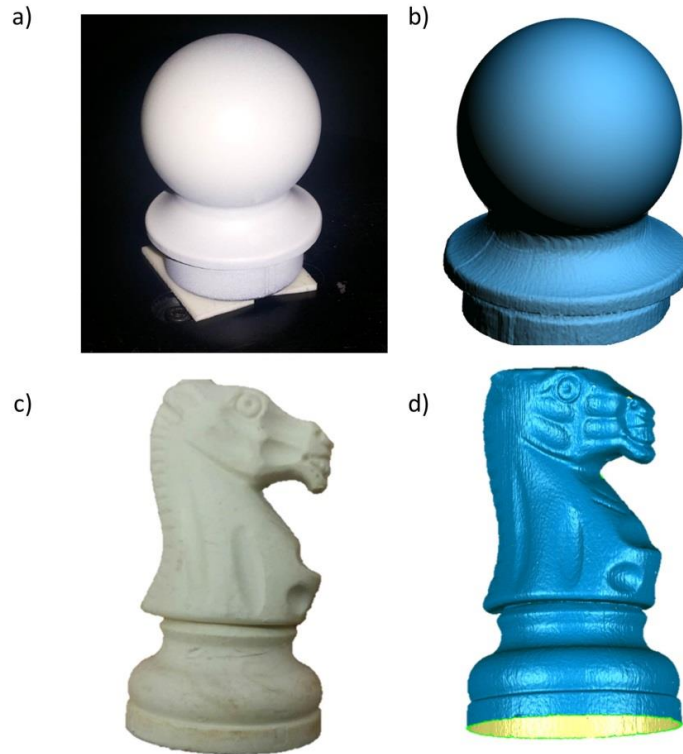


Figure 120: a) and b) are the sphere image and its fused mesh respectively. c) and d) are image and fused meshes of a knight piece respectively.

Apart from measuring a spherical object, a planar part is also measured. The error distribution of plane data using obtained scanner parameters is plotted in Figure 121c. Some papers [124,127,162] used spherical and planar objects joined together and compare the distance D between the plane and the center of the sphere. To compare results with those papers, a rigidly joined sphere and plane model illustrated in Figure 121 is measured by contact type CMM with Renishaw MH 20 probe. The same model is scanned on the laser scanner five times. The reference CMM result is $D_0=8.032\text{mm}$ while scanner gave average distance $D_s=7.988\text{mm}$. The overall standard deviation in measurements of the designed scanner ranges between 40 to 70 micrometers while results within 2-sigma probability region stand at 90 to 130 micrometers.

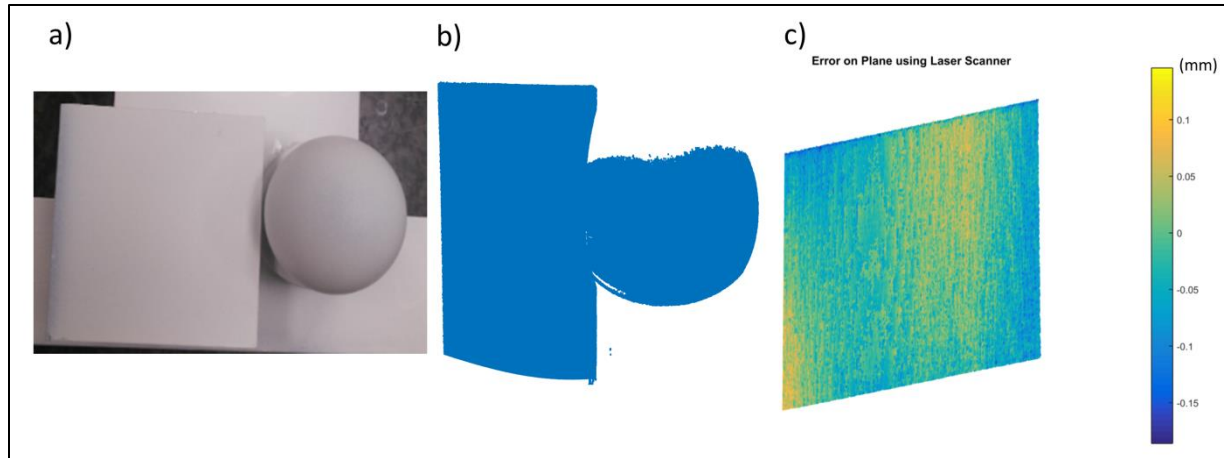


Figure 121: a) Plane and sphere model used for measurement b) Reconstructed model used to measure D_s c) Error distribution of plane data

Acquired points can be organized into mesh. Even though meshing is out of the scope of this work, a simple meshing method has been tested by connecting neighboring vertices [163]. This mesh could be further processed into any CAD format that can be opened in solid modeling softwares. Advanced mesh processing such as smoothening and resampling can be carried using software like Geomagic studio and Meshlab. Accuracy of the laser scanner can be improved by better calibrations, use of more flexible mechanism to keep the camera closer to workpiece and use of laser with thinner beam width.

6.6 Conclusion

A prototype of 3D laser scanning is developed to facilitate inexpensive reverse engineering at various object view angles by the positioned imaging sensor. An indispensable feature of any 3D scanner is measurement accuracy which should be reliably quantified and improved. Being that the uncertainties of measured points using a laser scanner originate from the part geometry dependent form deviation, laser uncertainty, lens imperfection, non-uniform illumination and camera-laser system positioning, evaluation and improvement of accuracy can be rather challenging. A formal study on uncertainty of measured points is carried out by propagation of uncertainties in influencing parameters of the scanner.

A method of finding motion axes and their intersection with respect to the camera reference frame was developed for the scanner prototype. The parameters that define relative position and

orientation of the camera-laser system with the rotation table are studied, providing knowledge for derivation of the scanner measurement model. To eliminate the systematic error contributed by uncertainties in these parameters, their values are optimized using least squares. The error in measurements of the improved scanner is measured on some geometric samples and found to be comparable with uncertainties from other studies.

BIBLIOGRAPHY

- [1] Cointegration AA, Tsoku JT, Mosikari TJ, Xaba D, Modise T. An Analysis of the Relationship between Manufacturing Growth and Economic Growth in South Africa : A Cointegration Approach 2017;11:433–8. doi:10.14505//jarle.v8.4(26).19.
- [2] United-Nations-Industrial-Development-Organization. The Importance of Manufacturing in Economic Development: Has this changed? vol. 12. 2016.
- [3] Swift KG, Booker JD. Manufacturing Process Selection Handbook. 2013. doi:10.1093/oxfordhb/9780199757183.013.0001.
- [4] Esmaeilian B, Behdad S, Wang B. The evolution and future of manufacturing: A review. J Manuf Syst 2016;39:79–100. doi:10.1016/j.jmsy.2016.03.001.
- [5] Nassehi A, Newman S, Dhokia V, Zhu Z, Asrai RI. Using formal methods to model hybrid manufacturing processes BT - Enabling Manufacturing Competitiveness and Economic Sustainability. In: ElMaraghy HA, editor., Berlin, Heidelberg: Springer Berlin Heidelberg; 2012, p. 52–6.
- [6] Boothroyd G, Dewhurst P, Knight, A W. Product Design for Manufacture and Assembly. Third. CRC Press; 2010.
- [7] Ben S, Colin S, Barry W, John P, Jorg B. Factory of the future - Advanced manufacturing technologies, including 3-D printing, will disrupt how we manufacture. 2013.
- [8] Toffler A. The third wave LK - <https://kocuniversity.on.worldcat.org/oclc/7213361>. New York SE - Xv, 537 Pages ; 18 Cm: Bantam Books; 1981.
- [9] IfM. Ten future digital supply chain scenarios 2016:3–4. https://www.ifm.eng.cam.ac.uk/uploads/Research/CIM/Scope_of_ten_future_DSC_scenarios.pdf (accessed October 28, 2018).
- [10] Cotteleer MJ. 3D opportunity: Additive manufacturing paths to performance, innovation, and growth. SIMT Addit Manuf Symp 2014:23. doi:10.1080/02607476.2010.497366.
- [11] Jiang R, Kleer R, Piller FT. Predicting the future of additive manufacturing: A Delphi study

- on economic and societal implications of 3D printing for 2030. *Technol Forecast Soc Change* 2017;117:84–97. doi:10.1016/j.techfore.2017.01.006.
- [12] Gibson I, Rosen D, Stucker B. *Additive Manufacturing Technologies*. vol. 44. 2015. doi:10.1007/978-1-4939-2113-3.
- [13] DMRC. *Thinking ahead the Future of Additive Manufacturing - Analysis of Promising Industries*. 2011.
- [14] Kurfess T, Cass WJ. Rethinking Additive Manufacturing and Intellectual Property Protection. *Res Manag* 2014;57:35–42. doi:10.5437/08956308X5705256.
- [15] Weller C, Kleer R, Piller FT. Economic implications of 3D printing: Market structure models in light of additive manufacturing revisited. *Int J Prod Econ* 2015;164:43–56. doi:10.1016/j.ijpe.2015.02.020.
- [16] Huang SH, Liu P, Mokasdar A, Hou L. Additive manufacturing and its societal impact: A literature review. *Int J Adv Manuf Technol* 2013;67:1191–203. doi:10.1007/s00170-012-4558-5.
- [17] Domingues J, Marques T, Mateus A, Carreira P, Malça C. An Additive Manufacturing Solution to Produce Big Green Parts from Tires and Recycled Plastics. *Procedia Manuf* 2017;12:242–8. doi:10.1016/j.promfg.2017.08.028.
- [18] Esteve F. *A Guide to Successful Rapid Manufacturing*. Smithers Rapra for the KTRM Project Consortium; 2012.
- [19] Monzón MD, Ortega Z, Martínez A, Ortega F. Standardization in additive manufacturing: activities carried out by international organizations and projects. *Int J Adv Manuf Technol* 2014;76:1111–21. doi:10.1007/s00170-014-6334-1.
- [20] AM Platform. *Additive Manufacturing: Strategic Research Agenda*. vol. 17. 2014. doi:10.1302/0301-620X.100B4.BJJ-2017-0662.R2.
- [21] Wits WW, García JRR, Becker JMJ. How Additive Manufacturing Enables more Sustainable End-user Maintenance, Repair and Overhaul (MRO) Strategies. *Procedia CIRP* 2016;40:694–9. doi:10.1016/j.procir.2016.01.156.

- [22] Lin CH, Chen JJ, Wu CH, Lee HY, Liu YH. Image analysis system for acquiring three-dimensional contour of foot arch during balanced standing. *Comput Methods Programs Biomed* 2004;75:147–57. doi:10.1016/j.cmpb.2003.12.003.
- [23] Wang CS. An analysis and evaluation of fitness for shoe lasts and human feet. *Comput Ind* 2010;61:532–40. doi:10.1016/j.compind.2010.03.003.
- [24] Pirotti F, Guarnieri A, Vettore A. State of the art of ground and aerial laser scanning technologies for High-resolution topography of the Earth Surface. *Eur J Remote Sens* 2013;46:66–78. doi:10.5721/EuJRS20134605.
- [25] Kedzierski M, Fryskowska A. Terrestrial and aerial laser scanning data integration using wavelet analysis for the purpose of 3D building modeling. *Sensors (Switzerland)* 2014;14:12070–92. doi:10.3390/s140712070.
- [26] Afazov S, Okioga A, Holloway A, Denmark W, Triantaphyllou A, Smith SA, et al. A methodology for precision additive manufacturing through compensation. *Precis Eng* 2017;50:269–74. doi:10.1016/j.precisioneng.2017.05.014.
- [27] S. Scott C (Stratasys, Inc. MM. APPARATUS AND METHOD FOR CREATING THREE-DIMENSIONAL OBJECTS. US00521329A, 1979. doi:10.2116/bunsekikagaku.28.3_195.
- [28] Matsuzaki R, Ueda M, Namiki M, Jeong T-K, Asahara H, Horiguchi K, et al. Three-dimensional printing of continuous-fiber composites by in-nozzle impregnation. *Sci Rep* 2016;6:23058. doi:10.1038/srep23058.
- [29] Love LJ, Kunc V, Rios O, Duty CE, Elliott AM, Post BK, et al. The importance of carbon fiber to polymer additive manufacturing. *J Mater Res* 2014;29:1893–8. doi:10.1557/jmr.2014.212.
- [30] Blather JE. Manufacture of contour relief maps. US473901, 1892.
- [31] Housholder R. Molding process. US4247508, 1981.
- [32] Hull CW, Arcadia C. Apparatus for Production of Three-Dimensional Objects By Stereolithography. 4,575,330, 1984. doi:US005485919A.
- [33] Thompson MK, Moroni G, Vaneker T, Fadel G, Campbell RI, Gibson I, et al. Design for

- Additive Manufacturing: Trends, opportunities, considerations, and constraints. *CIRP Ann - Manuf Technol* 2016;65:737–60. doi:10.1016/j.cirp.2016.05.004.
- [34] Schmidt M, Merklein M, Bourell D, Dimitrov D, Hausotte T, Wegener K, et al. Laser based additive manufacturing in industry and academia. *CIRP Ann* 2017;66:561–83. doi:10.1016/j.cirp.2017.05.011.
- [35] Bourell DL. Perspectives on Additive Manufacturing. *Annu Rev Mater Res* 2016;46:1–18. doi:10.1080/1070289X.2012.699879.
- [36] Pham DT, Gault RS. A comparison of rapid prototyping technologies. *Int J Mach Tools Manuf* 1998;38:1257–87. doi:10.1016/S0890-6955(97)00137-5.
- [37] Huang Y, Leu MC. *Frontiers of Additive Manufacturing Research and Education*. 2014.
- [38] Mohamed OA, Masood SH, Bhowmik JL. Optimization of fused deposition modeling process parameters: a review of current research and future prospects. *Adv Manuf* 2015;3:42–53. doi:10.1007/s40436-014-0097-7.
- [39] Lieneke T, Denzer V, Adam GAO, Zimmer D. Dimensional Tolerances for Additive Manufacturing: Experimental Investigation for Fused Deposition Modeling. *Procedia CIRP* 2016;43:286–91. doi:10.1016/j.procir.2016.02.361.
- [40] Bank HS. Development of a Hybrid and Open Architected Controlled Laser Workstation by. Koc University August, 2011.
- [41] Klift F Van Der, Koga Y, Todoroki A, Ueda M, Hirano Y. 3D Printing of Continuous Carbon Fibre Reinforced Thermo-Plastic (CFRTP) Tensile Test Specimens. *Open J Compos Mater* 2016:18–27.
- [42] Markforged. MarkForged inc. Mechanical Properties 2015:2015.
- [43] P. K. Mallick (Mech. Eng U of M. Fiber-Reinforced Composites. Third. CRC Press; 2007.
- [44] Tymrak BM, Kreiger M, Pearce JM. Mechanical properties of components fabricated with open-source 3-D printers under realistic environmental conditions. *Mater Des* 2014;58:242–6. doi:10.1016/j.matdes.2014.02.038.
- [45] Ahn S, Montero M, Odell D, Roundy S, Wright PK. Anisotropic material properties of fused

- deposition modeling ABS. *Rapid Prototyp J* 2002;8:248–57. doi:10.1108/13552540210441166.
- [46] Rodríguez JF, Thomas JP, Renaud JE. Design of Fused-Deposition ABS Components for Stiffness and Strength. *J Mech Des* 2003;125:545. doi:10.1115/1.1582499.
- [47] MarkForged develops 3D printer for carbon fibre. *Reinf Plast* 2015;59:12. doi:10.1016/j.repl.2014.12.027.
- [48] Brenken B, Barocio E, Favaloro A, Kunc V, Pipes RB. Fused filament fabrication of fiber-reinforced polymers: A review. *Addit Manuf* 2018;21:1–16. doi:10.1016/j.addma.2018.01.002.
- [49] Directional Composites through Manufacturing Innovation 2018. <http://www.dicomi.eu/#>.
- [50] Layegh K. SE, Yigit IE, Lazoglu I. Analysis of tool orientation for 5-axis ball-end milling of flexible parts. *CIRP Ann - Manuf Technol* 2015;64:97–100. doi:10.1016/j.cirp.2015.04.067.
- [51] Upcraft S, Fletcher R. The rapid prototyping technologies. *Assem Autom* 2003;23:318–30. doi:10.1108/01445150310698634.
- [52] Nee AYC, Fuh JYH, Miyazawa T. On the improvement of the stereolithography (SL) process. *J Mater Process Technol* 2001;113:262–8. doi:10.1016/S0924-0136(01)00634-3.
- [53] Doubrovski Z, Verlinden JC, Geraedts JMP. Optimal design for additive manufacturing: Opportunities and challenges. *Proc ASME Des Eng Tech Conf* 2011;9:1–12. doi:10.1115/DETC2011-48131.
- [54] Kshitiz Upadhyay, Ravi Dwivedi AKS. Determination and Comparison of the Anisotropic Strengths of Fused Deposition Modeling P400 ABS. *Adv. 3D Print. Addit. Manuf. Technol.*, 2017, p. 95–100. doi:10.1007/978-981-10-0812-2.
- [55] Yerazunis WS, Barnwell JCI, Nikovski DN. Strengthening ABS, Nylon, and Polyester 3D Printed Parts by Stress Tensor Aligned Deposition Paths and Five-Axis Printing. *Solid Free Fabr Symp* 2016:1259–71. doi:10.1021/acsnano.6b02108.
- [56] Isa MA, Yiğit IE, Lazoglu I. Analysis of Build Direction in Deposition-Based Additive

- Manufacturing of Overhang Structures. *Solid Free. Fabr. 2018 Proc. 29th Annu. Int.*, 2018.
- [57] Song X, Pan Y, Chen Y. Development of a Low-Cost Parallel Kinematic Machine for Multidirectional Additive Manufacturing. *J Manuf Sci Eng* 2015;137:021005. doi:10.1115/1.4028897.
- [58] Curran C. The road ahead for 3-D printing. *Pwc Next In Tech* 2016. <http://usblogs.pwc.com/emerging-technology/the-road-ahead-for-3d-printing/> (accessed November 1, 2018).
- [59] 5axismaker. 5AXISMAKER Machine 2018. <http://www.5axismaker.com/5axis/>.
- [60] Shen H, Huiadong D, Shuhua Y, Fu J. Fused deposition modeling 5-axis additive manufacturing: machine design, fundamental printing methods and critical process characteristics. *Rapid Prototyp J* 2017. doi:10.1108/RSR/-10-2016-0070.
- [61] Scott L, Neufeld R, Bob K, Erik Z. Marlin 3D Printer Firmware. Github Repos 2017. <https://github.com/MarlinFirmware/Marlin> (accessed December 23, 2016).
- [62] RAMPS 1.4 Assembly Guide n.d. https://www.reprap.org/mediawiki/images/0/06/RAMPS_dossier.pdf (accessed November 1, 2018).
- [63] Graves S, Rocholl J, Marlin H, Clear K, Labs BE, Rostock T. Johann C . Rocholl (Rostock) Style Delta Robot Kinematics 2012.
- [64] Gaynor AT, Meisel NA, Williams CB, Guest JK. Topology Optimization for Additive Manufacturing: Considering Maximum Overhang Constraint. *15th AIAA/ISSMO Multidiscip Anal Optim Conf* 2014:1–8. doi:10.2514/6.2014-2036.
- [65] Wulle F, Coupek D, Schäffner F, Verl A, Oberhofer F, Maier T. Workpiece and Machine Design in Additive Manufacturing for Multi-Axis Fused Deposition Modeling. *Procedia CIRP* 2017;60:229–34. doi:10.1016/j.procir.2017.01.046.
- [66] Mohd Ariffin MKA, Sukindar NA, Baharudin BTHT, Jaafar CNA, Ismail MIS. Slicer Method Comparison Using Open-source 3D Printer. *IOP Conf Ser Earth Environ Sci* 2018;114. doi:10.1088/1755-1315/114/1/012018.

- [67] Vincent Khau, Eleanor lourey SN. 3D Printing Tips and Tech 2015.
- [68] Lee K, Jee H. Slicing algorithms for multi-axis 3-D metal printing of overhangs. *J Mech Sci Technol* 2015;29:5139–44. doi:10.1007/s12206-015-1113-y.
- [69] Bin Ishak I, Fisher J, Larochelle P. Robot Arm Platform for Additive Manufacturing Using Multi-Plane Toolpaths. Vol 5A 40th Mech Robot Conf 2016:V05AT07A063. doi:10.1115/DETC2016-59438.
- [70] Zhao G, Ma G, Feng J, Xiao W. Nonplanar slicing and path generation methods for robotic additive manufacturing. *Int J Adv Manuf Technol* 2018:1–11. doi:10.1007/s00170-018-1772-9.
- [71] Zhao H ming, He Y, Fu J zhong, Qiu J jiang. Inclined layer printing for fused deposition modeling without assisted supporting structure. *Robot Comput Integr Manuf* 2018;51:1–13. doi:10.1016/j.rcim.2017.11.011.
- [72] Vanek J, Galicia JAG, Benes B. Clever Support: Efficient Support Structure Generation for Digital Fabrication. *Comput Graph Forum* 2014;33:117–25. doi:10.1111/cgf.12437.
- [73] Yu-xin M, Li-fang W, Jian-kang Q, Runyu W. An Optimized Scheme to Generating Support Structure for 3D Printing. In: Zhang Y-J, editor. *Image Graph.*, Cham: Springer International Publishing; 2015, p. 571–8.
- [74] Zhao J. Determination of optimal build orientation based on satisfactory degree theory for RPT. *Proc - Ninth Int Conf Comput Aided Des Comput Graph CAD/CG 2005* 2005;2005:225–30. doi:10.1109/CAD-CG.2005.32.
- [75] Pandey PM, Thrimurthulu K, Reddy NV. Optimal part deposition orientation in FDM by using a multicriteria genetic algorithm. *Int J Prod Res* 2004;42:4069–89. doi:10.1080/00207540410001708470.
- [76] Paul R, Anand S. Optimization of layered manufacturing process for reducing form errors with minimal support structures. *J Manuf Syst* 2015;36:231–43. doi:10.1016/j.jmsy.2014.06.014.
- [77] Mirzendehtdel AM, Suresh K. Support structure constrained topology optimization for

- additive manufacturing. *CAD Comput Aided Des* 2016;81:1–13. doi:10.1016/j.cad.2016.08.006.
- [78] Gaynor AT, Guest JK. Topology optimization considering overhang constraints: Eliminating sacrificial support material in additive manufacturing through design. *Struct Multidiscip Optim* 2016;54:1157–72. doi:10.1007/s00158-016-1551-x.
- [79] Kallevik G. 5-axis 3D Printer-Designing a 5-axis 3D printer. University of Oslo, 2015.
- [80] Lee K, Jee H. Slicing algorithms for multi-axis 3-D metal printing of overhangs. *J Mech Sci Technol* 2015;29:5139–44. doi:10.1007/s12206-015-1113-y.
- [81] Redwood B, Schöffner F, Garret B. The 3D Printing Handbook. *3D Hubs* 2017:304.
- [82] Gao W, Zhang Y, Ramanujan D, Ramani K, Chen Y, Williams CB, et al. The status, challenges, and future of additive manufacturing in engineering. *CAD Comput Aided Des* 2015;69:65–89. doi:10.1016/j.cad.2015.04.001.
- [83] Huang Y, Leu MC, Mazumder J, Donmez A. Additive Manufacturing: Current State, Future Potential, Gaps and Needs, and Recommendations. *J Manuf Sci Eng* 2015;137:014001. doi:10.1115/1.4028725.
- [84] Wulle F, Coupek D, Schäffner F, Verl A, Oberhofer F, Maier T. Workpiece and Machine Design in Additive Manufacturing for Multi-Axis Fused Deposition Modeling. *Procedia CIRP* 2017;60:229–34. doi:10.1016/j.procir.2017.01.046.
- [85] Chen JSS, Feng HY. Optimal layer setup generation in layered manufacturing with a given error constraint. *J Manuf Syst* 2011;30:165–74. doi:10.1016/j.jmsy.2011.07.001.
- [86] Jin YA, Li H, He Y, Fu JZ. Quantitative analysis of surface profile in fused deposition modelling. *Addit Manuf* 2015;8:142–8. doi:10.1016/j.addma.2015.10.001.
- [87] Chakraborty D, Aneesh Reddy B, Roy Choudhury A. Extruder path generation for Curved Layer Fused Deposition Modeling. *CAD Comput Aided Des* 2008;40:235–43. doi:10.1016/j.cad.2007.10.014.
- [88] Llewellyn-Jones T, Allen R, Trask R. Curved Layer Fused Filament Fabrication Using Automated Toolpath Generation. *3D Print Addit Manuf* 2016;3:236–43.

doi:10.1089/3dp.2016.0033.

- [89] Allen RJA, Trask RS. An experimental demonstration of effective Curved Layer Fused Filament Fabrication utilising a parallel deposition robot. *Addit Manuf* 2015;8:78–87. doi:10.1016/j.addma.2015.09.001.
- [90] Jin Y, Du J, He Y, Fu G. Modeling and process planning for curved layer fused deposition. *Int J Adv Manuf Technol* 2017;91:273–85. doi:10.1007/s00170-016-9743-5.
- [91] Singamneni S, Roychoudhury A, Diegel O, Huang B. Modeling and evaluation of curved layer fused deposition. *J Mater Process Technol* 2012;212:27–35. doi:10.1016/j.jmatprotec.2011.08.001.
- [92] Castelino K, D’Souza R, Wright PK. Toolpath optimization for minimizing airtime during machining. *J Manuf Syst* 2003;22:173–80. doi:10.1016/S0278-6125(03)90018-5.
- [93] Guo Q, Sun Y, Jiang Y, Yan Y, Zhao B, Ming P. Tool path optimization for five-axis flank milling with cutter runout effect using the theory of envelope surface based on CL data for general tools. *J Manuf Syst* 2016;38:87–97. doi:10.1016/j.jmsy.2015.11.003.
- [94] Keating S, Oxman N. Compound fabrication: A multi-functional robotic platform for digital design and fabrication. *Robot Comput Integr Manuf* 2013;29:439–48. doi:10.1016/j.rcim.2013.05.001.
- [95] Le VT, Paris H, Mandil G. Process planning for combined additive and subtractive manufacturing technologies in a remanufacturing context. *J Manuf Syst* 2017;44:243–54. doi:10.1016/j.jmsy.2017.06.003.
- [96] Jones R, Haufe P, Sells E, Iravani P, Olliver V, Palmer C, et al. Reprap - The replicating rapid prototyper. *Robotica* 2011;29:177–91. doi:10.1017/S026357471000069X.
- [97] Mani K, Kulkarni P, Dutta D. Region-based adaptive slicing. *CAD Comput Aided Des* 1999;31:317–33. doi:10.1016/S0010-4485(99)00033-0.
- [98] Willem F. B, Frederik W. J, Frits H. P. Design and Display of Solid Models. *Adv. Comput. Graph. VI-Images Synth. Anal. Interaction*, 2005, p. 1–57. doi:10.1016/B978-0-12-227741-2.50028-1.

- [99] Piegl L, Tiller W. The NURBS Book. 2nd ed. Springer; 1997. doi:10.1007/978-3-642-59223-2.
- [100] COX MG. The Numerical Evaluation of B-Splines*. IMA J Appl Math 1972;10:134–49.
- [101] de Boor C. On calculating with B-splines. J Approx Theory 1972;6:50–62. doi:[https://doi.org/10.1016/0021-9045\(72\)90080-9](https://doi.org/10.1016/0021-9045(72)90080-9).
- [102] de Boor C. A Practical Guide to Spline. vol. Volume 27. 1978. doi:10.2307/2006241.
- [103] Jin GQ, Li WD, Tsai CF, Wang L. Adaptive tool-path generation of rapid prototyping for complex product models. J Manuf Syst 2011;30:154–64. doi:10.1016/j.jmsy.2011.05.007.
- [104] Jin Y an, He Y, Fu J zhong, Gan W feng, Lin Z wei. Optimization of tool-path generation for material extrusion-based additive manufacturing technology. Addit Manuf 2014;1:32–47. doi:10.1016/j.addma.2014.08.004.
- [105] Ju T, Goldman R. Morphing Rational B-spline Curves and Surfaces Using Mass Distributions. Eurographics, 2003, p. 0–7.
- [106] Piegl L, Tiller W. Symbolic operators for NURBS. CAD Comput Aided Des 1997;29:361–8. doi:10.1016/S0010-4485(96)00074-7.
- [107] Affouard A, Duc E, Lartigue C, Langeron JM, Bourdet P. Avoiding 5-axis singularities using tool path deformation. Int J Mach Tools Manuf 2004;44:415–25. doi:10.1016/j.ijmachtools.2003.10.008.
- [108] Grandguillaume L, Lavernhe S, Tournier C. A tool path patching strategy around singular point in 5-axis ball-end milling. Int J Prod Res 2016;54:7480–90. doi:10.1080/00207543.2016.1196835.
- [109] Makhanov SS, Anotaiapaiboon W. Advanced Numerical Methods to Optimize Cutting Operations of Five-Axis Milling Machines. 2007. doi:10.1007/978-3-540-71121-6.
- [110] Dong Y, Su F, Sun G, Liu Y, Zhang F. A feature-based method for tire pattern reverse modeling. Adv Eng Softw 2018;124:73–89. doi:10.1016/j.advengsoft.2018.08.008.
- [111] Walker SM, Schwyn DA, Mokso R, Wicklein M, Müller T, Doube M, et al. In Vivo Time-Resolved Microtomography Reveals the Mechanics of the Blowfly Flight Motor. PLoS Biol

- 2014;12. doi:10.1371/journal.pbio.1001823.
- [112] Salzmann M, Fua P. Deformable Surface 3D Reconstruction from Monocular Images. vol. 2. 2010. doi:10.2200/S00319ED1V01Y201012COV003.
- [113] Li L, Schemenauer N, Peng X, Zeng Y, Gu P. A reverse engineering system for rapid manufacturing of complex objects. *Robot Comput Integr Manuf* 2002;18:53–67. doi:10.1016/S0736-5845(01)00026-6.
- [114] Javaid M, Haleem A, Kumar L. Current status and applications of 3D scanning in dentistry. *Clin Epidemiol Glob Heal* 2018:0–1. doi:10.1016/j.cegh.2018.07.005.
- [115] Paulus S, Schumann H, Kuhlmann H, Léon J. High-precision laser scanning system for capturing 3D plant architecture and analysing growth of cereal plants. *Biosyst Eng* 2014;121:1–11. doi:10.1016/j.biosystemseng.2014.01.010.
- [116] Henrichsen A. 3D Reconstruction and Camera Calibration from 2D Images by. *Camera* 2000;10:133.
- [117] Chan VH, Samaan M. Spherical/cylindrical laser scanner for geometric reverse engineering 2004:33. doi:10.1117/12.525181.
- [118] Abdel-Bary EBRAHIM Professor M. 3D Laser Scanners' Techniques Overview. *Int J Sci Res Index Copernicus Value Impact Factor* 2013;14611:2319–7064.
- [119] Petrov M, Talapov A, Robertson T, Lebedev A, Zhilyaev A, Polonskiy L. Optical 3D digitizers: Bringing life to the virtual world. *IEEE Comput Graph Appl* 1998;18:28–37. doi:10.1109/38.674969.
- [120] Molleda J, Usamentiaga R, García DF, Bulnes FG, Espina A, Dieye B, et al. An improved 3D imaging system for dimensional quality inspection of rolled products in the metal industry. *Comput Ind* 2013;64:1186–200. doi:10.1016/j.compind.2013.05.002.
- [121] Blais F, Beraldin JA. Recent developments in 3D multi-modal laser imaging applied to cultural heritage. *Mach Vis Appl* 2006;17:395–409. doi:10.1007/s00138-006-0025-3.
- [122] Popov I, Onuh S, Dotchev K. Dimensional error analysis in point cloud-based inspection using a non-contact method for data acquisition. *Meas Sci Technol* 2010;21:075303.

doi:10.1088/0957-0233/21/7/075303.

- [123] Zhou L, Waheed a., Cai J. Correction technique to compensate the form error in 3D profilometry. *Measurement* 1998;23:117–23. doi:10.1016/S0263-2241(98)00014-1.
- [124] Isheil a., Gonnet J-P, Joannic D, Fontaine J-F. Systematic error correction of a 3D laser scanning measurement device. *Opt Lasers Eng* 2011;49:16–24. doi:10.1016/j.optlaseng.2010.09.006.
- [125] Curless B, Levoy M. Better optical triangulation through spacetime analysis. *Proc IEEE Int Conf Comput Vis* 1995. doi:10.1109/ICCV.1995.466772.
- [126] Drenik M, Kampel M. An evaluation of low cost scanning versus industrial 3D scanning devices. *Proc - 1st Int Congr Image Signal Process CISP 2008* 2008;3:756–60. doi:10.1109/CISP.2008.762.
- [127] Xi F, Liu Y, Feng HY. Error compensation for three-dimensional line laser scanning data. *Int J Adv Manuf Technol* 2001;18:211–6. doi:10.1007/s001700170076.
- [128] Davis J, Chen X. A laser range scanner designed for minimum calibration complexity. *Proc Third Int Conf 3-D Digit Imaging Model* 2001:91–8. doi:10.1109/IM.2001.924412.
- [129] Fan X, Zhang L, Brown B, Rusinkiewicz S. Automated view and path planning for scalable multi-object 3D scanning. *ACM Trans Graph* 2016;35:1–13. doi:10.1145/2980179.2980225.
- [130] Sliwa T. Using high-speed camera to discriminate projective line with an adverse illumination. *Proc SPIE* 2003;5011:140–8. doi:10.1117/12.474014.
- [131] Goodman TS, Buel WB, Anantha V, Steiner RJ. *Laser Scanning Systems and Methods*. 20150043225A1, 2015.
- [132] Winkelbach S, Molkenstruck S, Wahl FM. Low-Cost Laser Range Scanner and Fast Surface Registration Approach. *Pattern Recognit.*, vol. 10496, 2006, p. 718–28. doi:10.1007/978-3-319-66709-6.
- [133] Matter & Form. *Matter and Form 3D Scanner*. 3D Scanner 2018. <https://matterandform.net/scanner>.

- [134] Isa MA, Lazoglu I. Design and analysis of a 3D laser scanner. *Meas J Int Meas Confed* 2017;111. doi:10.1016/j.measurement.2017.07.028.
- [135] Jiri C, Pazdera I. The New Stepper Driver for Low-Cost Arduino Based 3D Printer with Dynamic Stepper Control. *Adv Intell Syst Comput* 2018;644:v. doi:10.1007/978-3-319-65960-2.
- [136] Hawryluk M, Ziemia J. Application of the 3D reverse scanning method in the analysis of tool wear and forging defects. *Meas J Int Meas Confed* 2018;128:204–13. doi:10.1016/j.measurement.2018.06.037.
- [137] No Title. Toshiba TB6600HQ Bipolar Stepper Mot Driv 2015. <http://www.cuteminds.com/en/elettronicagen/elettronica/46-controller-bipolare-toshiba-tb6600hq-hg>.
- [138] Toshiba. Toshiba TB6600HG n.d. <https://toshiba.semicon-storage.com/us/product/linear/motordriver/detail.TB6600HG.html> (accessed October 1, 2018).
- [139] Zhang Z. A Flexible New Technique for Camera Calibration (Technical Report) 2002;22:1330–4.
- [140] Heikkila J, Silven O. A four-step camera calibration procedure with implicit imagecorrection. *Proc IEEE Comput Soc Conf Comput Vis Pattern Recognit* 1997. doi:10.1109/CVPR.1997.609468.
- [141] Tsai RY. A Versatile Camera Calibration Techniaue for High-accuracy 3D Machine Vision Metrology Using Off-the-shelf TV Camera and Lenses. *IEEE J Robot Autom* 1987. doi:10.1109/JRA.1987.1087109.
- [142] Jolliffe IT. *Principal Component Analysis, Second Edition* n.d.
- [143] França JGDM, Gazziro M a., Ide AN, Saito JH. A 3D scanning system based on laser triangulation and variable field of view. *Proc - Int Conf Image Process ICIP* 2005;1:425–8. doi:10.1109/ICIP.2005.1529778.
- [144] Wang Y, Feng H-Y. Modeling outlier formation in scanning reflective surfaces using a laser

- stripe scanner. *Measurement* 2014;57:108–21. doi:10.1016/j.measurement.2014.08.010.
- [145] Shree K. Nayar, Katsushi Ikeuchi TK. *Surface Reflection: Physical and Geometrical Perspectives*. *IEEE Trans Pattern Anal Mach Intell* 1991;13.
- [146] Usamentiaga R, Molleda J, García DF. Fast and robust laser stripe extraction for 3D reconstruction in industrial environments. *Mach Vis Appl* 2012;23:179–96. doi:10.1007/s00138-010-0288-6.
- [147] Forest J, Salvi J, Cabruja E, Pous C. Laser stripe peak detector for 3D scanners. A FIR filter approach. *Proc - Int Conf Pattern Recognit* 2004;3:646–9. doi:10.1109/ICPR.2004.1334612.
- [148] Otsu N. A Threshold Selection Method from Gray-Level Histograms. *IEEE Trans Syst Man Cybern* 1979;C:62–6.
- [149] Qi L, Zhang Y, Zhang X, Wang S, Xie F. Statistical behavior analysis and precision optimization for the laser stripe center detector based on Steger’s algorithm. *Opt Express* 2013;21:13442–9. doi:10.1364/OE.21.013442.
- [150] Colak S, Fresse V, Alata O, Gautrais T. Comparative study of laser stripe detection algorithms for embedded real-time suitability in an industrial quality control context Comparative study of laser stripe detection algorithms for embedded real-time suitability in an industrial quality control c 2018.
- [151] Nagata F, Takeshita K, Watanabe K, Habib MK. Generation of triangulated patches smoothed from original point cloud data with noise and its application to robotic machining. 2016 *IEEE Int Conf Mechatronics Autom IEEE ICMA 2016* 2016;1:535–40. doi:10.1109/ICMA.2016.7558620.
- [152] Löhner R, Oñate E. An advancing front point generation technique. *Commun Numer Methods Eng* 1998;14:1097–108. doi:10.1002/(SICI)1099-0887(199812)14:12<1097::AID-CNMI183>3.0.CO;2-7.
- [153] Bénéière R, Subsol G, Gesquière G, Le Breton F, Puech W. A comprehensive process of reverse engineering from 3D meshes to CAD models. *CAD Comput Aided Des* 2013;45:1382–93. doi:10.1016/j.cad.2013.06.004.

- [154] JCGM. Evaluation of measurement data — Guide to the expression of uncertainty in measurement 2008.
- [155] JCGM. JCGM 200 : 2012 International vocabulary of metrology – Basic and general concepts and associated terms (VIM) 3rd edition Vocabulaire international de métrologie – Concepts fondamentaux et généraux et termes associés (VIM) 3 e édition 2012.
- [156] Cox M, Harris P. EVALUATION OF MEASUREMENT UNCERTAINTY BASED ON THE PROPAGATION OF DISTRIBUTIONS 2003;46:9–14.
- [157] Iuliano L, Minetola P, Salmi A. Proposal of an innovative benchmark for comparison of the performance of contactless digitizers. Meas Sci Technol 2010;21:105102. doi:10.1088/0957-0233/21/10/105102.
- [158] Ahn SJ, Rauh W. Geometric Least Squares Fitting of Circle and Ellipse. Int J Pattern Recognit Artif Intell 1999;13:987–96. doi:10.1142/S0218001499000549.
- [159] Thomas F. Coleman YL. An Interior Trust Region Approach for Nonlinear Minimization Subject to Bounds. Soc Ind Appl Math 1996;6.
- [160] Mathworks C. Optimization Toolbox TM User ' s Guide R 2015 a 2015.
- [161] He Y, Liang B, Yang J, Li S, He J. An iterative closest points algorithm for registration of 3D laser scanner point clouds with geometric features. Sensors (Switzerland) 2017;17. doi:10.3390/s17081862.
- [162] Feng HY, Liu Y, Xi F. Analysis of digitizing errors of a laser scanning system. Precis Eng 2001;25:185–91. doi:10.1016/S0141-6359(00)00071-4.
- [163] Woo H, Kang E, Wang S, Lee KH. A new segmentation method for point cloud data. Int J Mach Tools Manuf 2002;42:167–78. doi:10.1016/S0890-6955(01)00120-1.